



저작자표시-비영리-변경금지 2.0 대한민국

이용자는 아래의 조건을 따르는 경우에 한하여 자유롭게

- 이 저작물을 복제, 배포, 전송, 전시, 공연 및 방송할 수 있습니다.

다음과 같은 조건을 따라야 합니다:



저작자표시. 귀하는 원저작자를 표시하여야 합니다.



비영리. 귀하는 이 저작물을 영리 목적으로 이용할 수 없습니다.



변경금지. 귀하는 이 저작물을 개작, 변형 또는 가공할 수 없습니다.

- 귀하는, 이 저작물의 재이용이나 배포의 경우, 이 저작물에 적용된 이용허락조건을 명확하게 나타내어야 합니다.
- 저작권자로부터 별도의 허가를 받으면 이러한 조건들은 적용되지 않습니다.

저작권법에 따른 이용자의 권리는 위의 내용에 의하여 영향을 받지 않습니다.

이것은 [이용허락규약\(Legal Code\)](#)을 이해하기 쉽게 요약한 것입니다.

[Disclaimer](#)

의학박사 학위논문

**Mechanistic Elucidation and Biochemical
Modulation of the Autophagic Arg/N-
Degron Pathway for ER-phagy and
Targeted Proteolysis**

자가포식 아르기닌/N-말단 범칙이 선택적 소포체 분해와
표적분해기술에 적용되는 기전 설명과 생화학적 조절

2021년 8월

서울대학교 대학원

의과학과 의과학 전공

지 창 훈

자가포식 아르기닌/N-말단 법칙이
선택적 소포체 분해와 표적분해에
적용되는 기전 설명과 생화학적 조절

지도 교수 권 용 태

이 논문을 의학박사 학위논문으로 제출함
2021년 8월

서울대학교 대학원
의과학과 의과학 전공
지 창 훈

지창훈의 의학박사 학위논문을 인준함
2021년 7월

위 원 장 _____ 목인희 _____

부위원장 _____ 권용태 _____

위 원 _____ 예상규 _____

위 원 _____ 이민재 _____

위 원 _____ 최철용 _____

Mechanistic Elucidation and Biochemical Modulation of the Autophagic Arg/N- Degron Pathway for ER-phagy and Targeted Protein Degradation

Advisor Yong Tae Kwon

Submitted as Thesis for Doctor of Philosophy
in Medical Science at the Department of Biomedical Sciences, Seoul
National University Graduate School
Chang Hoon Ji

Approved by Thesis Committee:
July 2021

Chairman	<u>Inhee Mook-Jung</u>
Vice-chairman	<u>Yong Tae Kwon</u>
Fellow	<u>Sang Kyu Ye</u>
Fellow	<u>Min Jae Lee</u>
Fellow	<u>Cheol Yong Choi</u>

Abstract

Mechanistic Elucidation and Biochemical Modulation of the Autophagic Arg/N-Degron Pathway for ER- phagy and Targeted Protein Degradation

Chang Hoon Ji

Major in Biomedical Sciences

Department of Biomedical Sciences

Seoul National University Graduate School

The N-degion pathway is a proteolytic determinant system that dictates the half-lives of its substrates based on the identity of their N-terminal amino acid residues and/or post-translational modifications. Among the many branches of the N-degion pathway, the arginylation branch can direct substrates for not only proteasomal but also autophagic degradation by virtue of their N-terminal arginine (Nt-Arg) residue. In so doing, the Arg/N-degion pathway regulates global cellular proteostasis.

The first part of this thesis will detail a broad overview and general background of the intracellular protein degradation mechanisms for protein quality control, and especially how the Arg/N-degion pathway is intertwined with these mechanisms. The two major degradative machineries are the ubiquitin-proteasome system (UPS) and the autophagy-lysosome pathway (ALP), which respectively degrade proteins via the proteasome and the lysosome. Among these, autophagy can degrade virtually all cellular materials, ranging from DNA to organelles and pathogens, as a selective form of cellular

defense and maintenance.

First, molecular mechanisms and physiological ramifications of how the autophagic Arg/N-degron pathway mediates endoplasmic reticulum (ER) protein quality control and homeostasis (by selective degradation of the endoplasmic reticulum) will be discussed. Arg/N-degron-mediated ER-phagy facilitates ubiquitin-dependent sequestration and degradation of not only the ER membrane but also the ER lumen and internal proteins. This mechanism can provide a novel avenue of therapeutic targeting against ER proteinopathies whose hallmark proteins aggregate and accumulate within the ER lumen, rendering them inaccessible to the proteasome.

Next, based on my work on Arg/N-degron-dependent biochemical modulation of ER-phagy using small-molecule p62 ligands, I present the development of a targeted protein degradation (TPD) platform based on the autophagic Arg/N-degron pathway and its utility against pathological protein species. This platform was coined as AUTOPhagy-TARgeting Chimera, or AUTOTAC. Targeted protein degradation, as opposed to functional silencing of proteins, siRNA-mediated interference or mAb therapy, provides a myriad of pharmacological and biological advantages. AUTOTAC is an unique modality even in targeted protein degradation, since it not only delivers the protein-of-interest to the autophagic membrane (a common feature of autophagic degraders) but also simultaneously boosts cellular autophagy.

Finally, I will conclude this thesis with an overall summary and discussion of my findings. Elucidating the biochemical and molecular mechanisms of the autophagic Arg/N-degron pathway will provide a framework for maintaining cellular proteostasis and combating proteopathies.

*Part of the contents in the Introduction section were published in [Ji CH & Kwon YT. 2017. Crosstalk and interplay between the ubiquitin-proteasome system and autophagy.

Molecules and Cells, **40**: 441-449] (please refer to CV).

The first part of the Results section was published in [Ji *et al.* 2019. The N-degron pathway mediates ER-phagy. *Molecular Cell*, **75: 1058-1072] (please refer to CV).

***The second part of the Results section is under revision for publication in *Nature Communications* (please refer to CV).

Keywords: Arg/N-degron pathway, protein quality control, selective macroautophagy, ER-phagy, targeted protein degradation, AUTOTAC

Student ID: 2014-25075

Table of Contents

Abstract	i
Table of Contents	iii
List of figures	vi
Acronyms and abbreviations	xi
Introduction	1
<i>Overview & background</i>	
Results.....	15
<i>The N-degron pathway mediates ER-phagy</i>	<i>15</i>
p62 mediates ER-phagy and ER homeostasis	16
Modulation of p62-mediated ER-phagy by Nt-arginylation	17
TRIM13 is the ER-associated receptor of p62 in ER-phagy	18
Modulation of TRIM13 by Nt-arginylation.....	20
Identification of TRIM13 as a platform for ER-phagy.....	21
Development of chemical N-degrons that modulate ER-phagy	23
The N-degron Arg mediates ER proteostasis via ER-phagy	24
Figures	27
Materials & Methods	80
<i>Targeted protein degradation via the autophagy-lysosome system: AUTOTAC (autophagy-targeting chimera).....</i>	<i>97</i>
Development of the AUTOTAC platform	98
Targeted degradation of soluble proteins by AUTOTAC	99
Therapeutic efficacy of AUTOTAC in cancer signaling	101
AUTOTAC targets Ub-conjugated misfolded protein aggregates to the lysosome.....	102
Degradation of pathological neurodegeneration-associated aggregates using AUTOTAC	103

AUTOTAC mediates the eradication of tau aggregates from mouse brains	105
Figures.....	107
Materials & Methods	147
Discussion	162
<i>Summary & follow-up</i>	
References.....	170
Abstract (in Korean)	182
Acknowledgements	184

List of figures

Introduction

Fig. 1. Protein quality control – re-folding, sequestration & degradation	12
Fig. 2. Crosstalk and interplay between the ubiquitin-proteasome system and the autophagy-lysosome pathway.....	13
Fig. 3. The Arg/N-degron pathway as a determinant of proteolysis by the ubiquitin-proteasome system or autophagy-lysosome pathway.....	14

Results

The N-degron pathway mediates ER-phagy

Fig. 4. Autophagy-dependent formation of ER membrane-derived vesicles containing ER luminal proteins during autophagy	27
Fig. 5. p62 is required for autophagic sequestration and targeting of ER membrane-derived vesicles containing ER luminal proteins.....	28
Fig. 6. ER luminal proteins are constitutively degraded via macroautophagy	29
Fig. 7. p62 facilitates constitutive lysosomal degradation of ER-resident luminal proteins	30
Fig. 8. p62 mediates proteotoxicity-mediated autophagic turnover of ER luminal proteins	31
Fig. 9. Autophagy protects cells from proteotoxicity-induced ER stress	32
Fig. 10. p62 maintains integrity of ER architecture via autophagy	33
Fig. 11. p62 desensitizes cells to ER stress-induced apoptosis	34
Fig. 12. The Nt-Arg residue selectively binds p62	35
Fig. 13. The Nt-Arg residue induces p62 self-oligomerization	36
Fig. 14. ATE1-mediated Nt-arginylation enables recruitment of p62 and ER membrane-derived vesicles.....	37
Fig. 15. Nt-arginylation is required for autophagic targeting of ER luminal proteins...	38
Fig. 16. The Nt-Arg residue regulates constitutive lysosomal turnover of the ER membrane and luminal proteins.....	39

Fig. 17. The Arg/N-degron pathway mediates proteotoxicity-induced autophagic turnover of ER luminal proteins	40
Fig. 18. Proteotoxic stress induces cytosolic retrotranslocation and Nt-arginylation of ER chaperones	41
Fig. 19. The N-degron Arg of Nt-arginylated ER chaperones binds p62	42
Fig. 20. Nt-arginylated ER chaperones are degraded by autophagy under proteotoxic stress	43
Fig. 21. Nt-arginylated ER chaperone BiP generated via the ubiquitin fusion technique binds p62.....	44
Fig. 22. Nt-arginylation-mediated autophagy protects cells from proteotoxicity-induced ER stress and apoptosis	45
Fig. 23. Nt-arginylation maintains ER morphological integrity.....	46
Fig. 24. K63-ubiquitination is selectively associated with p62-dependent ER-phagy ...	47
Fig. 25. The ER transmembrane E3 ligase TRIM13 is K63-ubiquitinated during autophagy but K48-ubiquitinated for the UPS	48
Fig. 26. TRIM13 recruits K63-Ub chains during ER-phagy	49
Fig. 27. TRIM13 mediates autophagic targeting and lysosomal degradation of the ER membrane and luminal proteins.....	50
Fig. 28. TRIM13 levels are dynamically regulated upon ER stress	51
Fig. 29. The p62-Nt-arginylation circuit mediates TRIM13 stability.....	52
Fig. 30. Oligomeric species of TRIM13 are degraded by autophagy.....	53
Fig. 31. TRIM13 forms an autophagy-degraded complex with p62	54
Fig. 32. Constructs of p62 and TRIM13 for domain mapping studies	55
Fig. 33. The p62-PB1 domain promotes formation of the p62-TRIM13 complex	56
Fig. 34. Auto-ubiquitination of TRIM13 and its recognition by the p62-UBA domain implement autophagic flux of the p62-TRIM13 complex.....	57
Fig. 35. The Arg/N-degron destabilizes TRIM13.....	58
Fig. 36. Nt-arginylation targets oligomeric and aggregated TRIM13 species for autophagic clearance.....	59
Fig. 37. The Arg/N-degron and its recognition via the p62-ZZ domain is required for autophagic clearance of the p62-TRIM13 complex	60
Fig. 38. p62 facilitates ER-phagy independent of previously-identified receptors	61

Fig. 39. TRIM13 recruits the mammalian PI3K complex	62
Fig. 40. The TRIM13-p62 circuit is associated to the omegasome formation site.....	63
Fig. 41. Chemical structure of Nt-Arg-mimicking p62-ZZ ligands	64
Fig. 42. p62-ZZ ligands induce self-oligomerization of p62 and accelerate cellular autophagy flux	65
Fig. 43. p62-ZZ ligands promote autophagosomal and lysosomal delivery of ER-derived vesicles.....	66
Fig. 44. Synthetic activation of the p62-ZZ domain recruits p62 to ER-derived vesicles	67
Fig. 45. Synthetic mimicry of Nt-Arg deliver entire ER fragments to the lysosome	68
Fig. 46. p62-ZZ ligands induce autophagic degradation of ER-resident proteins.....	69
Fig. 47. Nt-Arg-mimicry directly rescues ER stress, morphological aberrations and apoptosis caused by Nt-arginylation deficiency	70
Fig. 48. Chemical activation of Nt-arginylation generally inhibits ER stress-induced apoptosis	71
Fig. 49. Nt-Arg-mimicry facilitates autophagic proteolysis of the p62-TRIM13 complex	72
Fig. 50. The aggregation-prone misfolded ER protein species ATZ directly up-regulates cytosolic Nt-Arg and TRIM13 levels	73
Fig. 51. The p62-Nt-Arg pathway targets aggregation-prone ATZ for autophagy	74
Fig. 52. Arg/N-degron-mediated ER-phagy is selective for ATZ.....	75
Fig. 53. p62-ZZ ligands promote autophagic degradation of aggregation-prone ATZ...	76
Fig. 54. Synthetic mimicry of Nt-Arg targets ATZ via ER-phagy.....	77
Fig. 55. TRIM13 mediates autophagic degradation of ATZ.....	78
Fig. 56. Graphical abstract of Arg/N-degron-mediated ER-phagy	79
 <i>Targeted protein degradation via the autophagy-lysosome system: AUTOTAC (autophagy-targeting chimera)</i>	
Fig. 57. Mechanism-of-action and chemical structures of autophagy-targeting ligands	107
Fig. 58. Molecular docking models of ATLs to the p62-ZZ domain.....	108

Fig. 59. ATLS bind p62 and induce its self-oligomerization	109
Fig. 60. ATLS induce p62-associated autophagosome formation.....	110
Fig. 61. ATLS induce global autophagic flux and p62 degradation.....	111
Fig. 62. Mechanism-of-action and chemical structures of oncoprotein-targeting AUTOTACs.....	112
Fig. 63. Oncoprotein-targeting AUTOTACs promote high molecular-weight self-oligomerization of p62.....	113
Fig. 64. ER β -targeting AUTOTAC sdegrades ER β in a dosage-dependent manner....	114
Fig. 65. AR-targeting AUTOTAC degrades AR in a dosage-dependent manner	115
Fig. 66. MetAP2-targeting AUTOTAC degrades MetAP2 in a dosage-dependent manner	116
Fig. 67. Oncoprotein-targeting AUTOTACs induce selective degradation of their targets	117
Fig. 68. AR-targeting AUTOTAC targets AR to the autophagosome	118
Fig. 69. ER β -targeting AUTOTAC targets ER β and p62 to the autophagosome.....	119
Fig. 70. MetAP2-targeting AUTOTAC accelerates autophagic flux of MetAP2.....	120
Fig. 71. AUTOTAC-induced degradation is mediated by p62 and macroautophagy...	122
Fig. 72. Domain deletion constructs of p62 and their autophagosomal targeting	123
Fig. 73. AUTOTAC-dependent targeted protein degradation does not require ubiquitination.....	123
Fig. 74. Oncoprotein-targeting AUTOTACs exhibit enhanced inhibition of oncogenic signaling cascades.....	124
Fig. 75. Oncoprotein-targeting AUTOTACs selectively impede cancer cell proliferation	125
Fig. 76. Anti-oncoprotein AUTOTACs selectively impede cancer cell migration.....	126
Fig. 77. Mechanism-of-action an chemical structures of proteinopathy-targeting AUTOTACs.....	127
Fig. 78. Aggregate-targeting AUTOTACs promote high molecular-weight self-oligomerization of p62.....	128
Fig. 79. PBA-based AUTOTACs selectively accelerates lysosomal flux of ubiquitin-conjugated protein aggregates	129

Fig. 80. PBA-based AUTOTACs selectively deliver ubiquitin-conjugated protein aggregates to p62-associated autophagic membranes.....	130
Fig. 81. Anle138b-based AUTOTAC targets ubiquitin-conjugated protein aggregates to p62 bodies for autophagic clearance	131
Fig. 82. Dosage-dependent & selective degradation of mutant tauP301L by PBA-based AUTOTACs	132
Fig. 83. Dosage-dependent & selective degradation of mutant tauP301L by Anle138b-based AUTOTAC.....	133
Fig. 84. Anti-aggregate AUTOTACs rapidly degrade mutant tauP301L.....	134
Fig. 85. PBA-based AUTOTACs selectively sequester and target tauP301L for macroautophagy.....	135
Fig. 86. PBA-based AUTOTACs accelerate lysosomal flux of insoluble mutant tauP301L.....	136
Fig. 87. PBA-based AUTOTACs rescue autophagic flux of hyper-phosphorylated mutant tauP301L.....	137
Fig. 88. PBA-based AUTOTACs specifically target high-molecular, aggregated species of mutant tauP301L for degradation.....	138
Fig. 89. AUTOTAC-induced interaction between tauP301L and p62 is independent of ubiquitin chain recognition.....	139
Fig. 90. PBA-based AUTOTACs selectively accelerate autophagic proteolysis of mutant HttQ97 as opposed to wild-type HttQ25	140
Fig. 91. Dosage-dependent & selective degradation of mutant HttQ97 by Anle138b-based AUTOTAC.....	141
Fig. 92. Schematic illustration of the brain-specific hTauP301L-BiFC murine model and PBA-based AUTOTAC injection regimen	142
Fig. 93. PBA-based AUTOTAC degrades insoluble mutant tauP301L in murine brains	143
Fig. 94. PBA-based AUTOTAC eliminates both total and phosphorylated mutant tauP301L oligomers and aggregates in murine brains.....	144
Fig. 95. Schematic of the mechanism-of-action of AUTOTAC	146

Acronyms and abbreviations

A1AT: Alpha1-antitrypsin
AKT: Protein kinase B
ALP: Autophagy-Lysosome Pathway
AR: Androgen receptor
ATL: Autophagy-Targeting Ligand
ATZ/NHK: Alpha1-antitrypsin mutant Z/null Hong Kong
AUTOTAC: Autophagy-Targeting Chimera
ATE1: Arginyltransferase 1
ATD: Alpha1-antitrypsin deficiency
ATG: Autophagy-related gene/protein
Baf. A1: Bafilomycin A1
BiFC: Bipartite Fluorescence Complementation
BiP: Binding Immunoglobulin Protein
CHOP: C/EBP Homologus Protein
CRT: Calreticulin
DC₅₀: Degradation concentration 50
Degron: Degradation signal
DHT: Dihydrotestosterone
D_{max,24h}: Maximal clearance at 24 hours
E2: Estradiol
EGFR: Epidermal growth factor receptor
ERAD: ER-Associated Degradation
ER β : Estrogen receptor beta
ERK: Extracellular signal-regulated kinase
ER-phagy: selective autophagic degradation of the endoplasmic reticulum
HCQ: Hydroxychloroquine
Htt: Huntingtin
ICC: Immunocytochemistry
IP: Immunoprecipitation
KDEL: Lys-Asp-Glu-Leu
LIR domain: LC3-Interacting Region domain
MEF: Mouse embryonic fibroblast
MetAP2: Methionine aminopeptidase 2
MG132: Carbobenzoxy-Leu-Leu-leucinal
Mitophagy: selective autophagic degradation of the mitochondria
Nt-Arg: N-terminal Arginine
P62/SQSTM1: Ubiquitin-binding protein p62/Sequestosome-1
PARP: Poly (ADP-ribose) polymerase
PB1 domain: Phox and Bem1 domain
PDI: Protein Disulfide Isomerase
PI3K: Phosphatidylinositol 3-kinase
PPI: Protein-protein interaction
pQc: Protein quality control
PROTAC: Proteolysis-Targeting Chimera
RFP-GFP: Red Fluorescent Protein – Green Fluorescent Protein
RHD: Rel homology domain
SAR: Structure-Activity Relationship
SDS-PAGE: Sodium Dodecyl-Sulfate Polyacrylamide gel
SLR: Sequestosome1-Like Receptor
TBL: Target-Binding Ligand

TPD: Targeted Protein Degradation
TRIM13: Tripartite motif protein 13
Ub: Ubiquitin
UBD/UBA: Ubiquitin-Binding Domain/Ubiquitin-Associated
UPR: Unfolded Protein Response
UPS: Ubiquitin-Proteasome System
VPS34: Phosphatidylinositol 3-kinase VPS34
WB: Western blotting
WIPI2: WD-repeat domain phosphoinositide-interacting protein 2

Introduction

Overview & background

At any given moment in time, up to 30% of all nascent peptide chains can be misfolded (1, 2). Given that the structure of a protein determines its function, such misfolding usually induces loss-of-function toxicity (1, 2). Additionally, this misfolding also exposes hydrophobic motifs that otherwise are thermodynamically hidden within the confines of the protein structure; these exposed hydrophobic patches then aggregate with similar counterparts in an attempt to lower entropy (1-3). Such aggregates can be and are indeed responsible for gain-of-function toxicity, including but not limited to sequestration of other normal proteins, uncontrolled interaction with, and inhibition of, other proteins and organelles (1-3).

Cells employ a triage of decision-making cascades, collectively termed protein quality control (pQc), in order to combat such loss-of-function and gain-of-function toxicity arising from protein misfolding and aggregation (Fig. 1) (1-3). The first step in protein quality control is the selective recognition of misfolded proteins by molecular chaperones such as heat shock protein 70 (HSP70) or C-terminus of Hsc70-interacting protein (CHIP)(2). Molecular chaperones achieve such selectivity by specifically binding to the exposed hydrophobic patches that misfolded proteins usually exhibit, and actively consume ATP in order to re-fold these proteins into their native conformation (4). At the same time, if and inevitably when this re-folding attempt fails, the cell initiates both sequestration and degradation of these misfolded and/or aggregated proteins (1). Sequestration of pathological protein species, not unlike the prison system, carries the obvious advantage of protecting the rest of the cell from them. Simultaneously, removal of these pathological species from the general cellular populace allows molecular chaperones an easier access to attempt the re-folding process. Moreover, the resulting class of pseudo-organelles (e.g., aggresome) consisting of these pathological protein species also provides an energy-efficient method of cargo collection for degradation by autophagy (to be discussed later) (5).

The final step and *pièce de résistance* in protein quality control is protein degradation, which not only removes defective and pathological cellular material but also recycles them for energy and nutrient metabolism (6, 7). Proteolysis also allows acute regulation of cellular functions by degrading critical key components of cellular signaling pathways. Protein degradation is largely classified into two major pathways, the ubiquitin-proteasome system (UPS) and the autophagy-lysosome pathway (ALP) (6-8). The UPS is a selective proteolytic system in which substrates are recognized and tagged with ubiquitin for processive degradation by the proteasome (7, 8). Autophagy is a bulk degradative system that uses lysosomal hydrolases to degrade proteins as well as various other cellular constituents (6, 9, 10). Since the inception of their discoveries, the UPS and autophagy were thought to be independent of each other in components, action mechanisms, and substrate selectivity. Recent studies, however, collectively suggest that cells operate a single proteolytic network comprising of the UPS and autophagy that share notable similarity in many aspects and functionally cooperate with each other to maintain proteostasis (11).

The ubiquitin-proteasome system (UPS) mediates ubiquitin-dependent degradation of short-lived proteins via the proteasome (8, 12, 13). In this enzymatic cascade, ubiquitin is activated and conjugated by the respective E1 and E2 enzymes, which is then transferred to the ubiquitin ligase E3, which recognizes and ubiquitinates substrates for proteasomal degradation via the chymotrypsin-like, trypsin-like, and caspase-like peptidase activities of the 26S proteasome. In addition to degradation of misfolded and unfolded proteins throughout the cell, the UPS is also involved in turnover of short-lived regulators of a myriad of cellular processes.

The autophagy-lysosome pathway (ALP, hereafter autophagy) is a catabolic process by which unwanted or cytotoxic substrates ranging from misfolded protein aggregates to organelles and pathogens are degraded by acidic hydrolases in the

lysosome (6, 11). Depending on how its substrates are delivered into the lysosome, autophagy can be classified as either macroautophagy, microautophagy, or chaperone-mediated autophagy (CMA). In microautophagy and CMA, substrates are respectively engulfed or shuttled by the heat shock cognate protein 70 (Hsc70) chaperone into the lysosome (6, 11). For macroautophagy, however, substrates are first encapsulated in an autophagic membrane called the phagophore, whose maturation into the autophagosome is followed by fusion with the lysosome (10, 14).

Autophagy can be further characterized as either bulk or selective depending on the purpose that it serves within the cell. Bulk autophagy is defined by relatively non-specific degradation of cellular materials for nutrient and energy metabolism, while selective autophagy is designated for specific elimination of unwanted or harmful cellular cargoes (such as misfolded proteins and their aggregates) (9, 15, 16). For macroautophagy, the targeting of cellular cargoes warrants specific receptors such as p62/SQSTM1 (Sequestosome-1) and Sequestosome-Like Receptors (SLR) such as NBR1 that bind both ubiquitin chains on cargoes via their ubiquitin (Ub)-associated (UBA) domains and LC3 on the inner part of autophagic membranes via an LC3-interacting region (LIR) domain (17, 18)

. Regardless of what degradative machinery is used, proteolysis is carried out with extreme selectivity towards its substrates. Central to both the UPS and autophagy is ubiquitination, i.e., the conjugation of the 76-amino acid protein ubiquitin to the lysine (Lys) residues of other proteins (2, 13, 19). Ubiquitination can generate degradation signals (degrons) on substrates destined for destruction by the proteasome or lysosome or, alternatively, modulate their non-proteolytic processes (20). Ubiquitin can be conjugated to a substrate as a monomer at a single (monoubiquitination) or multiple (multi-monoubiquitination) Lys residues. A ubiquitin moiety can be further conjugated by another ubiquitin via any of its seven Lys residues (Lys6, Lys11, Lys27,

Lys29, Lys33, Lys48, and Lys63) or, alternatively, the N-terminal methionine (Met1) (12). Moreover, a single ubiquitin polymer often contains mixed ubiquitin linkages, in which ubiquitin is conjugated with other ubiquitin through two or more different linkages. Ubiquitin can also be modified at two or more sites, forming a branched conjugate (21). Additive to the complexity of the ubiquitin code, recent studies show that ubiquitin on substrates can be modified by ubiquitin-like modifiers such as SUMO, NEDD8, and ISG15 (22, 23) or small molecule chemicals such as phosphate and acetate (24). The ubiquitin linkages and their modifications generate distinct structures and recruit specific downstream effectors, generating a countless variation in information for the substrates (25).

Ubiquitin chains can serve as proteasomal ‘tags’ which are selectively bound by the ubiquitin-binding domains (UBDs) of adaptors (7, 8). UBDs decode the distinct structures of ubiquitin chains and transfer the information on the substrates to downstream machinery. Some UBD-containing adaptors link the substrates to the proteasome (e.g., RPN10 and RPN13) or autophagic vacuoles (e.g., p62/SQSTM-1/Sequestosome-1 and neighbor of BRCA1 gene 1 (NBR1)). The recognition of ubiquitin chains by UBD adaptors can induce the removal of damaged or surplus subcellular organelles such as mitochondria or invading pathogens (26). Thus, ubiquitination can induce acute degradation by both the proteasome and the lysosome, functioning as a common denominator shared by the UPS and autophagy under the umbrella of a single proteolysis network that is under constant crosstalk and interplay (Fig. 2).(12, 13, 26)

While ubiquitination functions as a degradation tag for substrates, the degradative machineries require an extra layer of selectivity in that they must specifically recognize the to-be-degraded substrate. Such selectivity is achieved by the presence of degradation signals (degrons) within the substrate itself. Degrons can range

from entire motifs such as D-boxes, KEN box sequences, ABBA motifs or PEST sequences to single amino acid-residues, such as the N-degron or the C-degron pathway (27). Additionally, degrons may be either ubiquitin-dependent or ubiquitin-independent.

Among these degrons, the N-degron pathway dictates the *in vivo* half-life of substrate proteins based on the identity of their N-terminal amino acid residues (following any co- or post-translational cleavage). Known destabilizing N-terminal amino acid, termed N-degrons, include positively charged (Arg, Lys, and His) and bulky hydrophobic (Phe, Trp, Tyr, Leu, and Ile) residues exposed on the N-termini (28). Amongst these, the N-terminal Arg can be generated through post-translational incorporation of the amino acid L-Arg to N-terminal Asp or Glu (29, 30). In the classical N-end rule pathway, the N-terminal Arg of arginylated substrates is recognized by recognition components, called N-recognins, such as the UBR box family (UBR1, UBR2, UBR4 and UBR5), leading to substrate ubiquitination and proteasomal degradation (31).

The recently-discovered autophagic Arg/N-degron pathway mediates autophagic proteolysis and modulates the activity of the autophagic adaptor p62 as well as autophagosome biogenesis (Cha-Molstad et al., 2016). In this circuit, the accumulation of autophagic cargoes such as ubiquitinated proteins and aggregates induces the N-terminal arginylation of ER-resident chaperones such as BiP/GRP78, calreticulin, and protein disulfide isomerase, resulting in the cytosolic accumulation of their arginylated species. Amongst these, arginylated BiP, R-BiP, is associated with misfolded proteins, and its N-terminal Arg binds the ZZ domain of p62. This N-end rule interaction induces a conformational change of p62, exposing its PB1 and LC3-interacting domains, which accelerates its self-oligomerization and targeting to autophagosomes (Cha-Molstad, Sung et al., 2015). In addition, p62, whose ZZ domain is occupied with N-terminal Arg, acts as an autophagic inducer that facilitates autophagosome biogenesis (32). Thus, the

autophagic p62 is an N-recognin of the N-end rule pathway that modulates macroautophagy in response to proteotoxicity. However, the exact ramifications and physiological relevance, including pharmacological modulation, of the autophagic Arg/N-degron pathway have not yet been fully explored.

Macroautophagy is a catabolic process by which cytoplasmic constituents such as misfolded proteins and organelles are sequestered by autophagosomes and digested by lysosomal hydrolases (6, 10). The targeting of autophagy cargoes involves specific receptors such as p62/Sequestosome-1 and Neighbor of BRCA gene 1 (NBR1) (17, 18, 33) whose UBA and LIR domains enable recognition of both ubiquitin (Ub) chains on protein cargoes and LC3 on autophagosomes, respectively (11, 26). Selective autophagy by LIR-containing receptors facilitates the removal of various subcellular organelles such as mitochondria, peroxisomes, and the endoplasmic reticulum (ER) (6, 9). Organellophagy typically initiates when autophagic adaptors bind both polyubiquitinated transmembrane receptors and LC3 on autophagic membranes (15, 34, 35). Alternatively, membrane-associated receptors may directly – via their LIR domains – or indirectly bind LC3 on autophagic membranes (36-38). Like many organelles, the ER is also subject to both constitutive and stress-induced turnover (9, 39). Recent studies identified several ER membrane-associated receptors, such as reticulophagy regulator 1 (FAM134B), reticulon 3 (RTN3), and translocation protein SEC62 (Sec62), whose LIR domains directly recruit phagophores to facilitate ER-phagy (40-43). However, mechanisms for a Ub-and adaptor-dependent ER-phagy, akin to the PINK1-Parkin pathway in mitophagy, have yet to be discovered. Moreover, the physiological significance of ER-phagy in general has yet to be elucidated.

Perturbations in the normal functions and homeostasis of the ER, due to factors such as accumulation of misfolded proteins and their aggregates in the ER lumen, lead to ER stress (44, 45). To cope with this stress, cells operate adaptive quality control

systems, such as the unfolded protein response (UPR) (1). The initial objective of the UPR is to re-establish ER homeostasis via the chaperone-mediated refolding of misfolded proteins during inhibition of general protein translation (4, 5, 46). Simultaneously, the cell employs protein quality control systems such as ERAD (ER-Associated Degradation) for ubiquitination and proteasomal degradation of soluble misfolded proteins (3, 47). Should ER stress persist, however, the UPR then induces programmed cell death, which modulates the pathogenesis of neurodegenerative diseases, metabolic disorders and cancer among others (48-50). Thus, targeting ER stress is a highly promising therapeutic avenue of research, with chemical chaperones and small molecule inhibitors of specific UPR pathways showing clinical efficacy in a variety of disease models (51-53). However, given that the UPR can play both cytoprotective and cytotoxic roles (54) and that pathological aggregates trapped within the ER lumen are resistant to re-folding or proteasomal degradation (5), alternative mechanisms to alleviate ER stress and restore ER homeostasis are becoming increasingly important. The existence of ER-associated proteinopathies, such as α 1-antitrypsin deficiency and cystic fibrosis, whose hallmark proteins aggregate within the ER lumen and/or cause chronic ER stress, further underscores the importance of a degradation mechanism of the ER and its contents for ER proteostasis (16, 55, 56). The need for such a mechanism is also highlighted given that ER stress from impaired ER protein quality control mediates the pathogenesis of a myriad of diseases, even those whose hallmark aggregation-prone proteins are outside the ER (e.g., neurodegenerative diseases and type-II diabetes) (54, 57). As such, selective degradation of not only damaged ER compartments but also these ER-resident misfolded proteins and their aggregates may directly ameliorate ER stress and prevent UPR-induced apoptosis.

Thus, in the first part of this thesis, I show that the N-recognin p62 of the N-degron rule pathway mediates ER-phagy. During ER-phagy, its activity is modulated

through the interaction with the Nt-Arg of arginylated substrates such as R-BiP. Activated by the Nt-Arg, p62 targets the ER transmembrane receptor tripartite motif containing 13 (TRIM13), which is ubiquitinated via the K63 linkage, for autophagy. This N-degron-dependent ER-phagy also mediates ER autophagic protein quality control for the ER stress response and for pathogenic misfolded protein aggregates such as α 1-antitrypsin mutant Z.

In the central dogma, the genetic information in DNA is transcribed into RNA, which in turn is translated to protein. Recent advances in genetic bioengineering, exemplified by CRISPR, TALEN and siRNA, have enabled selective destruction and functional silencing of DNA and RNA (58, 59). In contrast to the universally applicable nature of DNA and RNA editing, there are currently no general tools by which proteins are selectively recognized and targeted for destruction. Functional silencing of proteins via small molecule inhibitors, while highly penetrant, rapid and straightforward, is limited to approximately only a fifth of the entire human proteome (60). Such a technology, if available, will be readily applied as research tools and agents to selectively downregulate target proteins in cultured cells and in living organisms such as mice and flies. Selective degradation of disease-associated proteins also provides an attractive opportunity to develop degrader-type drugs.

Targeted protein degradation (TPD) is the latest of emerging modalities in drug discovery and development and typically employs heterobifunctional chimeric molecules comprised of a target binder linked to a degradation-inducing moiety, which offer an attractive therapeutic means to eradicate disease-associated proteins, especially those belonging to the once-considered ‘undruggable’ proteome (60-64). Current TPD technology, as exemplified by PROteolysis-TArgeting Chimera (PROTAC), is limited to inducing the ubiquitination of target substrate for its degradation (65). Despite its advantages, however, ubiquitin (Ub)-dependent PROTAC is largely confined to a

limited set of target proteins and of E3 ligases, due to technical difficulties in forming a substrate-PROTAC-E3 ternary complex (66). These technical challenges, which to date has ruled out the possibility of a pan-ubiquitinating and promiscuous E3 ligase for PROTACs, limit the meaningful clinical targets of PROTAC to a handful of otherwise short-lived ubiquitinated substrates, especially oncoproteins (65, 67, 68). Moreover, Ub-dependent PROTAC may not be an ideal TPD platform to degrade misfolded and aggregation-prone pathological protein species, such as those of neurodegenerative proteinopathies, as these protein species are typically resistant to unfolding and subsequent degradation by the proteasome due to size limitations (69). These challenges of the existing TPD modalities necessitate a generally applicable TPD platform independent of Ub and the proteasome. While recent efforts – such as harnessing S-guanylation-inducing molecular tags or targeting extracellular and secreted/membrane proteins directly to the lysosome via peptidic tags – attempt to address degradation of PROTAC-resistant cargoes, no degrader technology yet exists for directly targeting proteins and their aggregates to the autophagosome in an Ub-independent and receptor-mediated manner (69).

Consequently, in the second part of this thesis, I report the development of a generally applicable chemical tool, AUTOTAC, by which a broad range of cellular proteins can be selectively recognized and targeted to autophagic membranes for lysosomal degradation. Central to the mode of action in AUTOTAC is the ability of ATL to induce a conformational activation of otherwise inactive p62 into an autophagy-compatible form. Upon binding to ATL, p62 exposes PB1 and LIR domains, which respectively facilitates p62 self-polymerization in complex with targets and its interaction with LC3 on autophagic membranes. As ATL-mediated autophagic activation of p62 does not need to form a tertiary complex with targets, AUTOTAC can

induce the degradation of a broad range of cellular proteins including their misfolded aggregates.

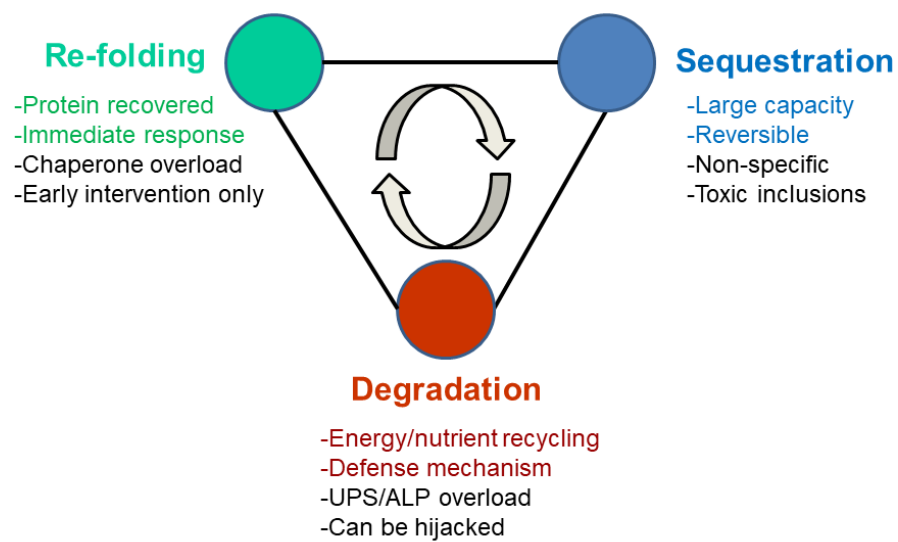


Fig. 1. Protein quality control – triage of re-folding, sequestration & degradation

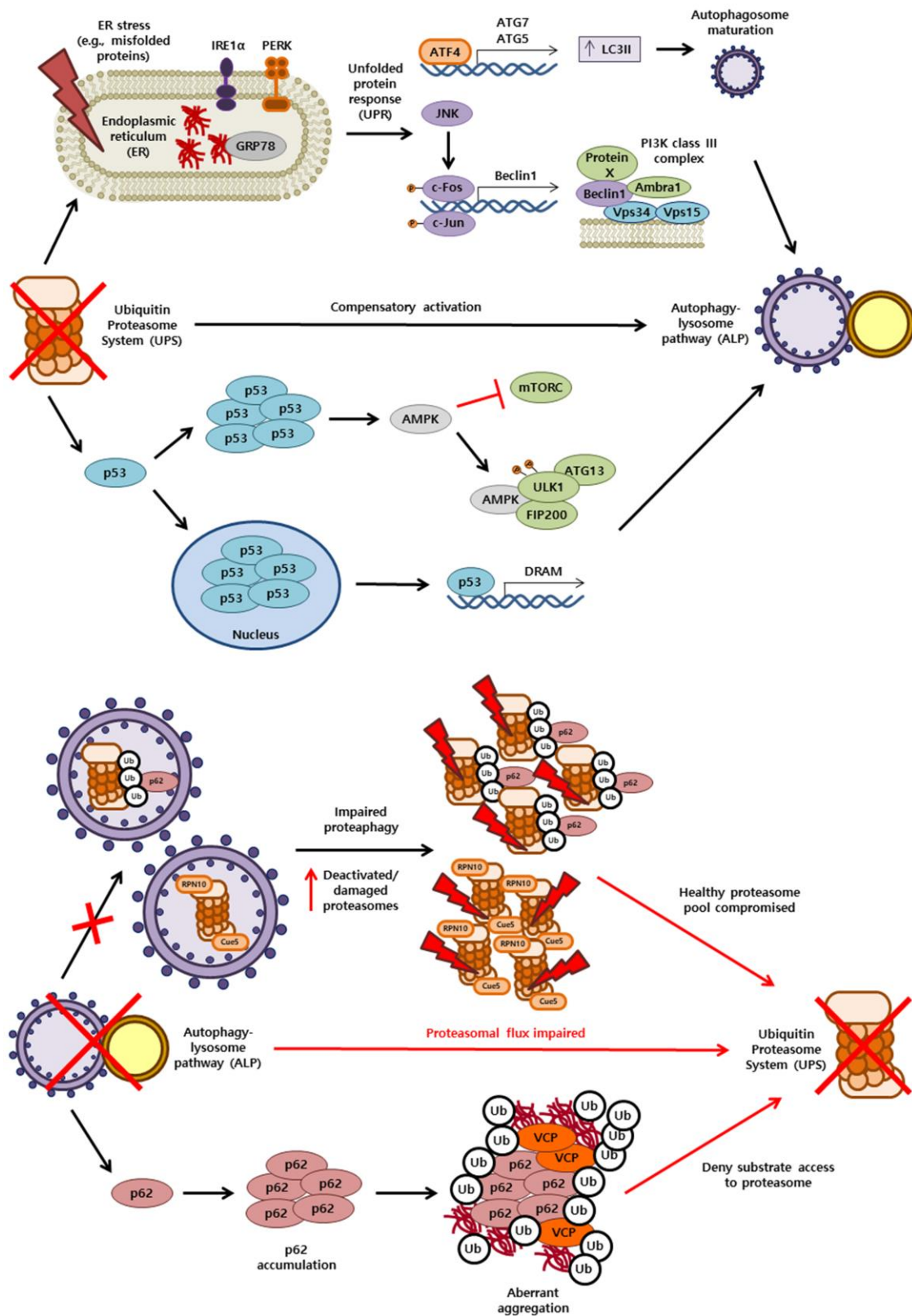


Fig. 2. Crosstalk and interplay between the ubiquitin-proteasome system and the autophagy-lysosome pathway

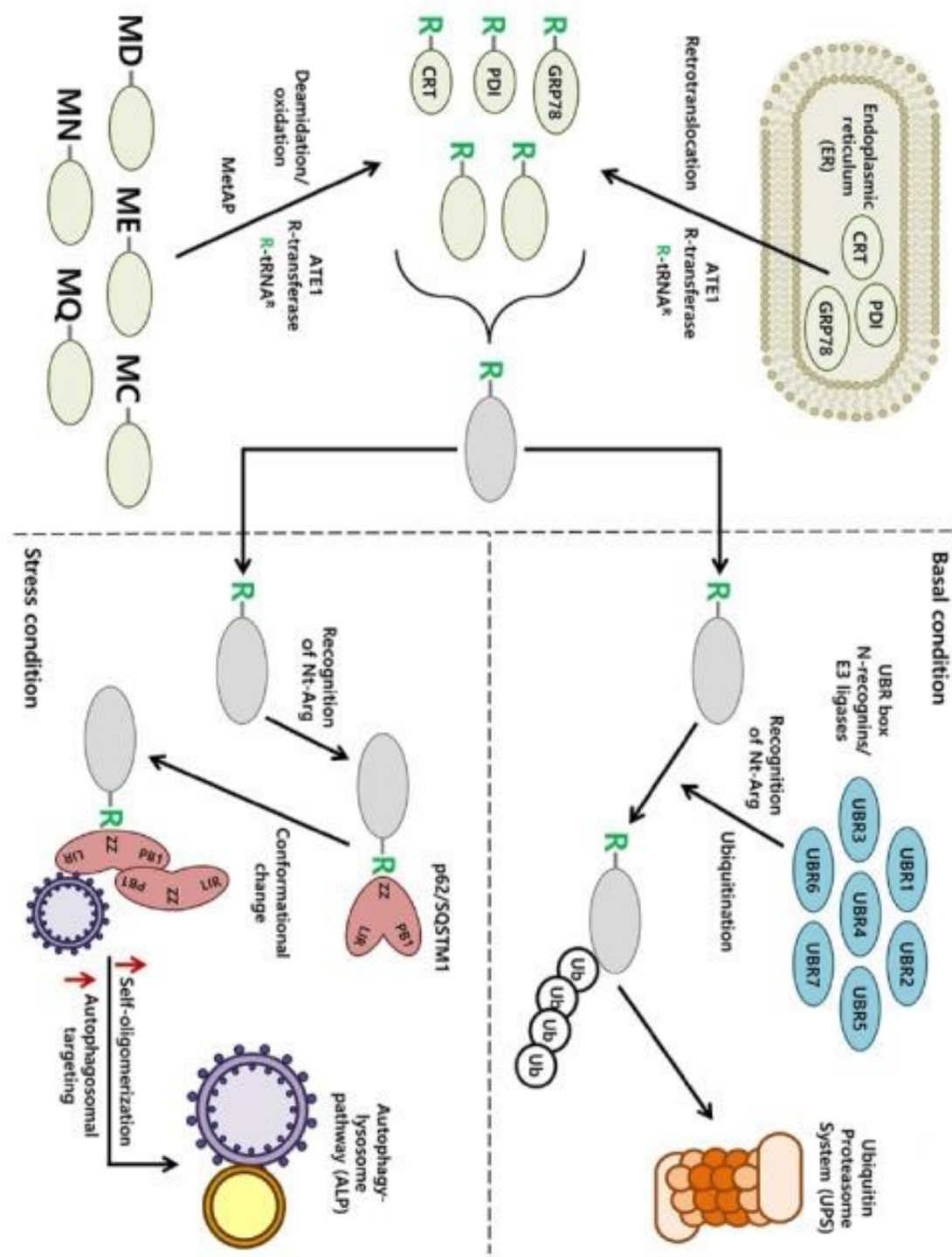


Fig. 3. The Arg/N-degron pathway as a determinant of proteolysis by the ubiquitin-proteasome system or autophagy-lysosome pathway

Results

The N-degron pathway mediates ER-phagy

p62 mediates ER-phagy and ER homeostasis

To elucidate the role of p62 in ER-phagy as an N-recogin, I monitored its localization in comparison with those of ER-residing proteins using immunostaining analyses. The p62 stainings marked the ER, forming puncta that colocalized with the ER transmembrane protein calnexin as well as proteins containing the KDEL (Lys-Asp-Glu-Leu) sequence, an ER-retention signal (Fig. 4A). I therefore determined whether p62-associated ER compartments are subject to autophagic degradation. Autophagic flux assays using bafilomycin A1 showed that these puncta containing ER proteins were targeted to LC3-GFP⁺ autophagic vacuoles (Fig. 4B). Autophagic targeting (Fig. 5) of the ER membrane (Fig. 5A) and luminal proteins (Fig. 5B), as well as their macroautophagic (Fig. 6A, 6B and 6C) but not proteasomal degradation (Fig. 6B) of ER proteins was inhibited by p62 knockdown (Fig. 7) as strongly as by chemical inhibition of autophagy or Atg5 knockdown (Fig. 6) as opposed to proteasomal inhibition (Fig. 6). As these results suggest that p62-dependent macroautophagy mediates ER-phagy in normally growing cells, I subsequently asked whether p62 mediates the autophagic degradation of ER compartments in stressed cells. When cells were challenged with the proteasome inhibitor MG132, p62 knockdown impaired the turnover of BiP (Fig. 8) as well as other KDEL proteins (Fig. 8). These results suggest that p62 mediates ER-phagy in normal as well as stressed cells.

Next, I examined whether p62 modulates the homeostasis of the ER. Immunoblotting analyses showed that autophagic inhibition rendered cells hypersensitive to ER stress as indicated by the increased level of CHOP (Fig. 9). When p62 was depleted, the ER as a whole, as stained by calnexin and KDEL, lost its morphological integrity and spontaneously swollen (Fig. 10A). The expanded ER was broken down into morphologically abnormal fragments (Fig. 10B), which were devoid of LC3⁺ vacuoles (Fig. 10B). Consistently, p62-deficient cells were hypersensitive to

various ER stressors, triggering ER stress and apoptosis as determined by CHOP levels and PARP1 cleavage (Fig. 11). These results suggest that p62-mediated macroautophagy plays a protective role in the ER homeostasis.

Modulation of p62-mediated ER-phagy by Nt-arginylation

I have previously shown that the Nt-Arg of arginylated proteins binds p62 and induces its oligomerization (32, 70). I therefore determined whether the Nt-Arg of arginylated proteins binds p62 during ER-phagy and modulates its activity. As expected, *in vitro* pulldown assays confirmed that the Nt-Arg of the ER chaperones BiP (Fig. 12A), CRT (Fig. 12B) and ERdj5 (Fig. 12C). *In vitro* oligomerization assays showed that the dipeptide Arg-Ala but not the control Ala-Arg induced p62 oligomerization (Fig. 13). When Nt-arginylation was inhibited using tannic acid, p62 punctate signals were delocalized from calnexin signals on the ER membrane as well as in the cytosol (Fig. 14), indicating that the Nt-Arg is required for the targeting of p62 to the ER. I then asked whether the Nt-Arg is indispensable for autophagic degradation of ER compartments. Indeed, autophagic targeting of KDEL⁺ proteins was abolished by inhibiting Nt-arginylation with not only tannic acid (Fig. 15A) but also ATE1 knockout (Fig. 15B). Moreover, either ATE1 knockdown (Fig. 16A) or inhibition (Fig. 16B) resulted in excessive accumulation of not only ER proteins such as BiP, CRT and PDI but also p62. A similar accumulation of these proteins was observed under ER stress caused by proteasomal inhibition (Fig. 17). These results suggest that the Nt-Arg of arginylated proteins binds p62, induces its polymerization – a key step in ER-phagy – and results in autophagic flux of not only p62 but various ER proteins.

Next, I assessed the importance of Nt-arginylation in ER homeostasis by monitoring ER stress responses and ER integrity. ER chaperones as well as their Nt-arginylated species accumulated in the cytosol under ER stress caused by various

challenges, ranging from misfolded protein accumulation and chaperone inhibition to impaired ER-Golgi trafficking and defective N-linked glycosylation (Fig. 18). These Nt-arginylated ER chaperones, which were confirmed to bind p62 (Fig. 19), were subject to autophagic turnover (Fig. 20), suggesting that cellular Nt-Arg levels respond to ER stress and are ultimately degraded by autophagy. To rule out the possibility that cytosolic and non-arginylated species of these ER chaperones binds p62 and modulate its activity, I constructed Ub-R/V-BiP-flag fusion (co-translationally cleaved to yield Arg- or Val-BiP-flag) proteins (71, 72) lacking their ER signal peptide and their ER retention signal KDEL peptide, ensuring their cytosolic localization (Fig. 21A). Co-IP analyses revealed that only Arg-BiP-flag interacts with p62 (Fig. 21B), indicating that the Nt-Arg residue of the arginylation-permissive ER chaperones is required for their binding with p62.

I then determined whether this response modulated ER homeostasis. Cells with ATE1 inhibition (Fig. 22A) or genetic ablation (Fig. 22B) were hypersensitive to autophagic inhibition and ER stress. This stress response was followed by decreased viability (Fig. 22C) and spontaneous ER expansion (Fig. 23A and 23B), leading to apoptotic death (Fig. 22A). These results highlight the essential role of Nt-arginylation-mediated ER-phagy in the homeostasis of the ER in normally growing cells as well as those under ER stress and, for the first time, implicate the N-degron pathway in degradation of non-proteinaceous cellular materials.

TRIM13 is the ER-associated receptor of p62 in ER-phagy

Given that p62 is an autophagic cargo adaptor that recognizes Ub chains on substrate proteins, I investigated whether ubiquitination was required for p62/Nt-Arg-dependent ER-phagy. To this end, I performed immunostaining analyses of different Ub linkage types. The results showed that the ER was marked by puncta positive for K63-

linked Ub chains, which were subject to autophagic turnover (Fig. 24A and 24B). The autophagic targeting of K63-linked Ub puncta was abolished in p62-deficient cells (Fig. 24A). In contrast, K48-linked signals appeared to be diffusive throughout the cells (Fig. 24B). These results implicate K63-linked ubiquitination in p62-mediated ER-phagy.

In search of an ER-associated receptor that binds p62 and whose K63-linked ubiquitination enables p62-dependent ER-phagy, I noted that the ER transmembrane E3 ligase TRIM13 ubiquitinates itself and other substrates via K63 linkage (73, 74). Indeed, autophagy flux assay showed that TRIM13 was degraded by macroautophagy and stabilized in ATG5 knockdown cells (Fig. 6) as well as those treated with tannic acid (Fig. 16). This led us to suspect that TRIM13 may be the receptor for p62 in Nt-arginylation-mediated ER-phagy. When the ubiquitinated species of TRIM13 (Fig. 25A) was selectively monitored, K63-ubiquitinated TRIM13 was the substrate of autophagy but not the proteasome (Fig. 25B and 25C). In contrast, K48-ubiquitinated TRIM13 was degraded by only the proteasome (Fig. 25D). Next, I determined whether TRIM13 is essential for ER-phagy. TRIM13 knockdown inhibited not only the localization of K63-Ub puncta on the ER but also their autophagic turnover (Fig. 26). TRIM13 knockdown also abolished autophagosomal targeting (Fig. 27A) and lysosomal degradation (Fig. 27B) of ER proteins. A similar result was obtained under prolonged proteasomal inhibition (Fig. 27C). TRIM13 protein levels were drastically upregulated by proteotoxic ER stress due to not only misfolded protein accumulation or chaperone inhibition but also impaired ER-Golgi trafficking or defective N-linked glycosylation (Fig. 28). These results suggest that TRIM13 is an ER-associated receptor which is polyubiquitinated via K63 linkage and required for efficient ER-phagy as both a constitutive and a stress response system.

Next, I examined whether the autophagic degradation of TRIM13 requires its interaction with p62. Cycloheximide degradation assays showed that p62 knockdown

drastically abolished the turnover of TRIM13 (Fig. 29B), which is normally short-lived (Fig. 29A). To determine whether TRIM13 is degraded as a monomer or oligomer, I performed *in vivo* oligomerization assays using non-reducing SDS-PAGE. When autophagy was blocked, TRIM13 accumulated as not a monomer but oligomeric species ranging mainly from dimers to tetramers (Fig. 30). Moreover, Co-IP assays showed that TRIM13 interacted with p62, which was strengthened upon autophagy inhibition (Fig. 31A, 31B and 31C). These results suggest that p62 binds ER-associated TRIM13, forming a complex, whose oligomerization is a prerequisite to their autophagic degradation and ER-phagy.

I also dissected the domain of p62 that binds TRIM13 using p62 deletion and TRIM13 point mutants (Fig. 32). Mapping analyses showed that PB1 domain was essential for binding TRIM13 (Fig. 33). Unexpectedly, the UBA domain of p62 was required not for binding TRIM13 but for autophagic flux of the TRIM13-p62 complex (Fig. 34A). Given that the UBA domain of p62 likely binds Ub chains on TRIM13, I tested whether auto-ubiquitination of TRIM13 via K63 linkage is essential for ER-phagy. The C13A TRIM13 mutant, a catalytically inactive E3 ligase (75), could not be assembled with K63-Ub chains (Fig. 34B), suggesting that the primary means by which TRIM13 is ubiquitinated is auto-ubiquitination. Importantly, the resulting mutant TRIM13-p62 complex was resistant to autophagic degradation (Fig. 34C). These results suggest that auto-ubiquitination of TRIM13 is essential but is not sufficient for ER-phagy.

Modulation of TRIM13 by Nt-arginylation

Given that the Nt-Arg binds and activates p62, I determined whether the N-degron Arg modulates TRIM13 via p62 in a *trans*-mode. Cycloheximide degradation assays showed that ATE1 knockdown inhibited the degradation of TRIM13 (Fig. 29).

Consistently, TRIM13 degradation was accelerated by overexpressing either ATE1 isoforms (Fig. 35A) or Arg-BiP-GFP (Fig. 35B), the latter being cotranslationally produced from the Ub-R/V-BiP-GFP fusion and lacking both the ER signal peptide and ER retention KDEL peptide (Fig. 32). In contrast, Val-BiP-GFP lacking the Nt-Arg did not induce TRIM13 degradation (Fig. 35). Non-reducing SDS-PAGE showed that upon ATE1 inhibition by tannic acid, TRIM13 lost its oligomeric status, leading to the uncontrolled formation of aggregates (Fig. 36). Thus, the Nt-Arg modulates the oligomerization of TRIM13 via p62.

Next, I determined whether the Nt-Arg is essential for the interaction of TRIM13 with p62 and its degradation. Following tannic acid treatment, p62 normally bound TRIM13, but TRIM13 and its complex with p62, which is normally degraded by autophagy, became metabolically stabilized (Fig. 37A). Consistently, co-IP analyses showed that p62-ZZ mutants that cannot bind the Nt-Arg normally bound TRIM13 (Fig. 37B). When the turnover of the p62-TRIM13 was monitored, TRIM13 in complex with p62 ZZ mutants was resistant to autophagic turnover, in contrast to wild-type p62 (Fig. 37B). This finding was validated using p62 mutants harboring point mutations (C142A/C145A or C151A/C154A) in the zinc finger of ZZ domain (Fig. 37C), which render p62 unable to bind Nt-Arg. These results suggest that Nt-Arg binding to p62 ZZ domain is essential for ER-phagy.

Identification of TRIM13 as a platform for ER-phagy

I asked how the p62/Nt-Arg/TRIM13 circuit induces membrane curvature and/or fragmentation for sequestration of ER-resident contents. I first analyzed the sequences of both p62 and TRIM13 but did not find any reticulon homology domains (RHD) that induce ER membrane curvature (76, 77). I then asked whether p62 interacts with previously identified RHD-carrying ER-phagy receptors, namely FAM134B and RTN3

(41, 42), and observed via co-IP analyses that neither FAM134B (Fig. 38A) nor RTN3 (Fig. 38B) binds p62 in either normal or autophagy-inhibited conditions.

Previous reports on Parkin-mediated mitophagy and ER-phagy in both yeast and mammals have identified mechanisms by which recruitment of autophagy initiation proteins to the organellophagy receptors mediates both autophagosome biogenesis and the delivery of organellar cargo therein (78, 79). Specifically, the closure of the isolation membrane unto itself also entraps the omegasome(s) from which it originated, trapping ER-resident and membrane proteins in the process (14, 80). Given that many TRIM proteins function as platforms for not only selective autophagy cargo recognition but also autophagosome biogenesis (81, 82), I asked whether TRIM13 can selectively induce membrane curvature and/or fragmentation via autophagy induction during ER-phagy. Co-IP analyses revealed that TRIM13 interacts with both Beclin-1 and VPS34 (Fig. 39), members of the mammalian PI3K complex which can sense and induce membrane curvature and expansion of the isolation membrane originating from the omegasome during autophagosome nucleation (83, 84). Moreover, these interactions were strengthened upon ER stress conditions (Fig. 39). Consistent with these results, upon ER stress by tunicamycin treatment, TRIM13 formed punctate structures that co-localized with not only p62 (Fig. 40A) but also the omegasome marker WIPI2 (Fig. 40B) and phagophore marker ATG12 (Fig. 40C). Given my data that TRIM13 (Fig. 30, 36) along with p62 (Fig. 13) is degraded as an oligomer, I suggest that oligomeric TRIM13 may serve as a platform on or near the omegasome for both the Beclin-1/VPS34 complex and p62, for eventual engulfment by the isolation membrane/phagophore. This 'TRIM13-osome' may physically mark the site of ER-phagy via phagophore nucleation and anchor p62 for autophagosomal targeting of TRIM13-marked ER compartments.

Development of chemical N-degrons that modulates ER-phagy

To develop a pharmacological means to modulate ER-phagy, I synthesized chemical mimics of the Nt-Arg (Fig. 41) based on recent work (32) and tested whether these ligands modulate p62 functions for ER-phagy. Compared with negative controls, the ligands selectively enhanced oligomerization and aggregation of p62 (Fig. 42A) as well as cellular autophagic flux (Fig. 42B). Colocalization analysis using exogenous LC3-GFP (Fig. 43A and 43B) or stably-expressed RFP-GFP-LC3 (Fig. 43C) revealed that they facilitated autophagosomal and lysosomal targeting of ER luminal proteins (Fig. 44A) and the ER membrane (Fig. 44B) as punctate signals positive for p62. To confirm that the ligands induced delivery of entire parts of the ER (ER-phagy), as opposed to clusters of ER proteins (aggrephagy), to autolysosomes, I performed transmission electron microscopy (Fig. 45). Upon treatment with YOK1104, HEK293T cells readily exhibited an abundance of autophagosomes and autolysosomes (Fig. 45, 1st column) coupled with short and fragmented ER scattered throughout the cytosol (Fig. 45, 1st and 2nd column). Importantly, compared with those of control cells, autolysosomes in YOK1104-treated cells displayed an accumulation of ER fragments within their interior (Fig. 45), indicating that the ligands induced delivery of entire ER compartments. Next, I tested whether the ligands can induce autophagic degradation of the ER and its contents via ER-phagy. Immunoblotting analyses showed that YOK1104 readily facilitated the degradation of BiP and PDI as well as TRIM13 following their up-regulation by proteotoxic ER stress (Fig. 46A). Autophagy flux assays confirmed that YOK1104 drives TRIM13 to autophagic degradation (Fig. 46B). These results suggest that the p62 ligands accelerate ER-phagy.

I tested whether the chemical N-degrons could restore ER homeostasis by virtue of ER-phagy. Indeed, YTK1105 rescued tannic acid-treated cells from ER stress and apoptosis in an autophagy-dependent manner (Fig. 47A). In cells treated with tannic

acid, the ER was spontaneously swollen into aberrant morphology, which was readily restored by YTK1105 (Fig. 47B). To test whether this efficacy depends on p62, I compared YTK1105 with the general autophagy inducer rapamycin. In contrast to YTK1105, no such rescue effects were observed with rapamycin (Fig. 47B). Importantly, p62 ligands also rescued cells from various types of ER stress and consequent apoptosis (Fig. 48A, 48B and 48C), indicating that p62-ZZ ligands have the potential to ameliorate ER stress.

I investigated the mechanisms by which p62 ligands accelerate ER-phagy. Co-IP coupled with autophagy flux analysis using TRIM13 pulldown indicated that YOK1104 enhanced autophagic degradation of the TRIM13-p62 complex (Fig. 49A). I therefore examined whether p62 ligands induced TRIM13 degradation as a monomer or an oligomer using non-reducing SDS-PAGE. YOK1104 selectively induced the degradation of oligomeric but not that of monomeric species of TRIM13 (Fig. 49B). Collectively, these data demonstrate that the chemical N-degrons facilitate autophagic degradation of the TRIM13-p62 complex as an oligomeric form, providing a pharmaceutical means to modulate ER-phagy and maintain ER homeostasis.

The N-degron Arg mediates ER protein quality control via ER-phagy

Soluble misfolded proteins generated within the ER lumen are sorted out by molecular chaperones and delivered to ERAD for ubiquitination and proteasomal degradation (1). However, little is known about how ERAD-resistant insoluble aggregates trapped within the ER lumen are degraded. I tested whether the N-degron Arg facilitates sequestration and autophagic degradation of insoluble misfolded aggregates accumulating in the ER lumen by using the Z variant (E342K; ATZ) of α 1-antitrypsin (A1AT) (56, 85) as a model misfolded and pathologically aggregation-prone substrate of the metabolic proteinopathy α 1-antitrypsin deficiency (ATD). In ATD,

which is the most common inherited metabolic liver disease, ATZ is misfolded and aggregated within the ER lumen of hepatocytes, whose chronic accumulation results in ER stress and consequent apoptosis of hepatocytes, leading to liver cirrhosis and even hepatocellular carcinoma (86, 87). While the soluble monomeric species of ATZ are degraded by the proteasome via ERAD, its insoluble aggregated species is targeted to autophagy (56, 88, 89). I confirmed that ectopic expression of ATZ, like that with proteotoxic ER stress, induced Nt-arginylation of BiP (Fig. 50A) following its retrotranslocation to the cytosol (Fig. 50B). Consistent with the data that ER stress from chemical proteotoxicity up-regulates TRIM13 levels, ectopic expression of ATZ also up-regulated TRIM13 protein levels (Fig. 50C). Moreover, RNA interference of either *p62* (Fig. 51A) or *ATE1* (Fig. 51B) abolished autophagic targeting of ATZ and resulted in the accumulation of ATZ and its fragments (Fig. 51C). In contrast to aggregation-prone ATZ, the soluble and ERAD substrate null Hong Kong (NHK) variant of A1AT (87) was not affected by p62 knockdown (Fig. 52). These results suggest that N-degron-dependent ER-phagy selectively responds to the presence of ER-resident insoluble aggregates and sequesters and targets them for autophagic degradation.

I determined the efficacy of synthetic p62 ligands in accelerating N-degron-dependent ER-phagy for ER protein quality control of ATZ. Treatment with the p62-ZZ ligand promoted lysosomal degradation of ATZ in an autophagy-dependent manner (Fig. 53A), especially in the detergent-insoluble fraction (Fig. 53B). Moreover, a recent study showed that ATZ can be ubiquitinated by an ER transmembrane E3 ligase upon retrotranslocation and targeted to p62-dependent macroautophagy for lysosomal degradation (90), as a form of autophagic ERAD and/or aggrephagy. I thus investigated whether the p62/N-degron/TRIM13 circuit promotes ATZ degradation via ER-phagy and not autophagic ERAD or aggrephagy. Crucially, p62 ligand-induced ATZ puncta were strongly positive for the ER membrane (Fig. 54). Moreover, the expression of

TRIM13 led to autophagic clearance of ATZ (Fig. 55B) without a physical interaction between the two (Fig. 55A), which would have been needed for autophagic ERAD or aggrephagy of ATZ following its retrotranslocation and ubiquitination. I conclude that ATZ aggregates in the ER lumen are degraded by ER-phagy via the p62/Nt-Arg/TRIM13 circuit, whose response to the presence of ATZ aggregates, via induction of Nt-arginylation and TRIM13 levels, mediates ER proteostasis. These results not only provide a pharmaceutical means to eliminate pathogenic aggregates from the ER and alleviate ER stress but also suggest that the N-degron pathway mediates autophagic ER protein quality control.

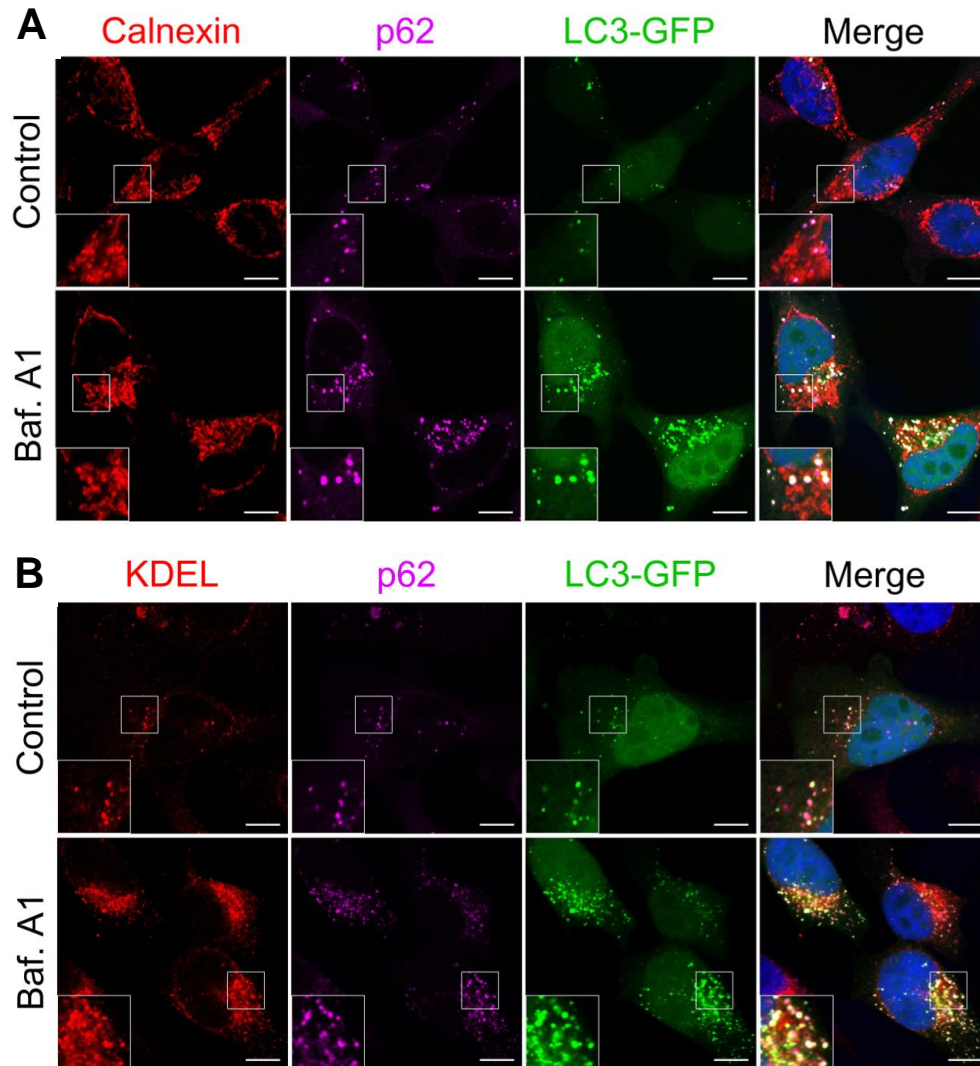


Fig. 4. Autophagy-dependent formation of ER membrane-derived vesicles containing ER luminal proteins during autophagy. (A) ICC of p62, calnexin and LC3-GFP puncta in HeLa cells transfected with LC3-GFP treated with Baf. A1 (200 nM, 6 h). Scale bar, 10 μ m. (B) Same as A, but with KDEL instead of calnexin.

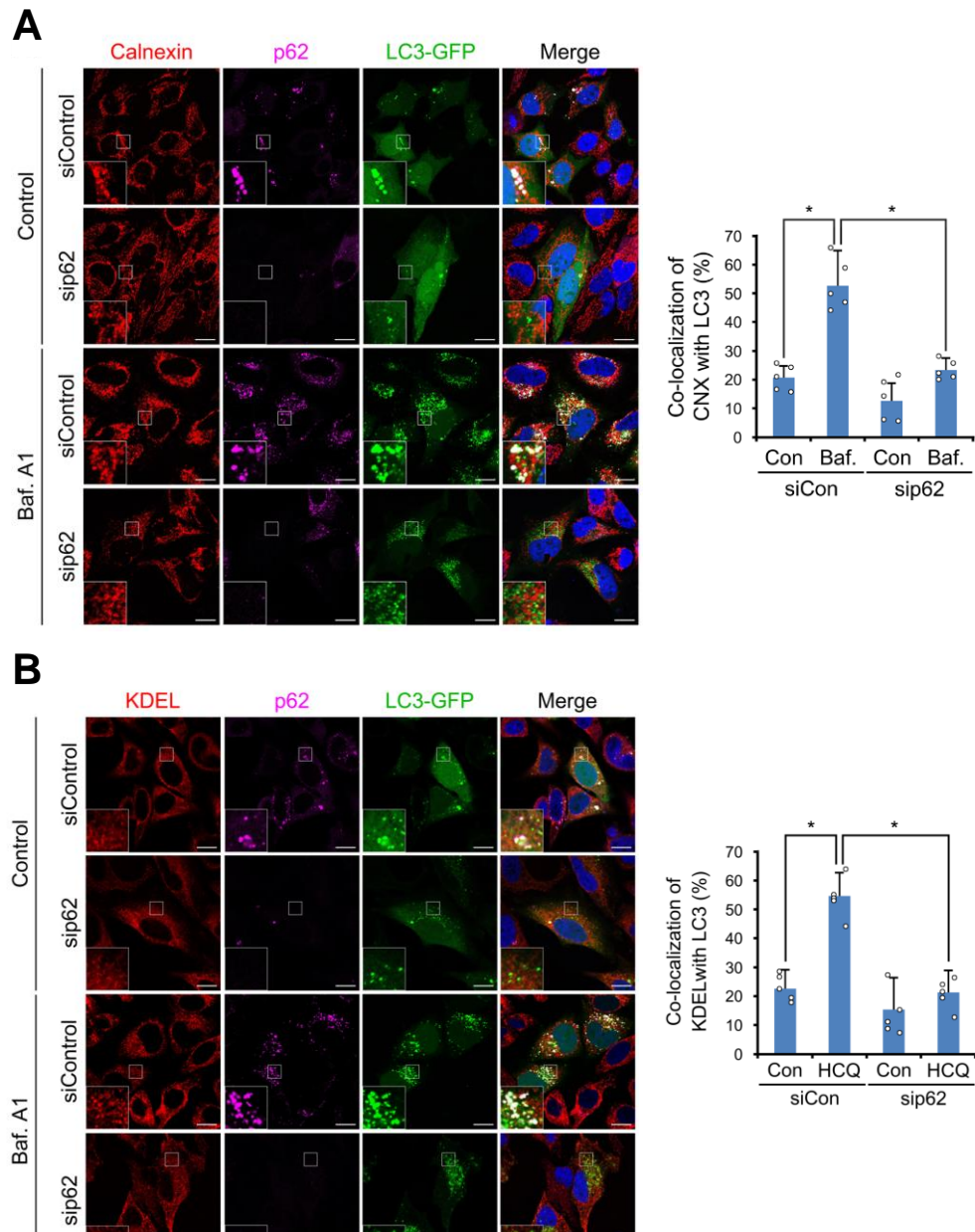


Fig. 5. p62 is required for autophagic sequestration and targeting of ER membrane-derived vesicles containing ER luminal proteins. (A) ICC of p62, calnexin and LC3-GFP puncta in HeLa cells under siRNA-mediated knockdown of *p62*, transfected with LC3-GFP and treated with Baf. A1 (200 nM, 6 h). Scale bar, 10 μ m. Quantification: n=50 cells. (B) Identical to A but with KDEL instead of calnexin.

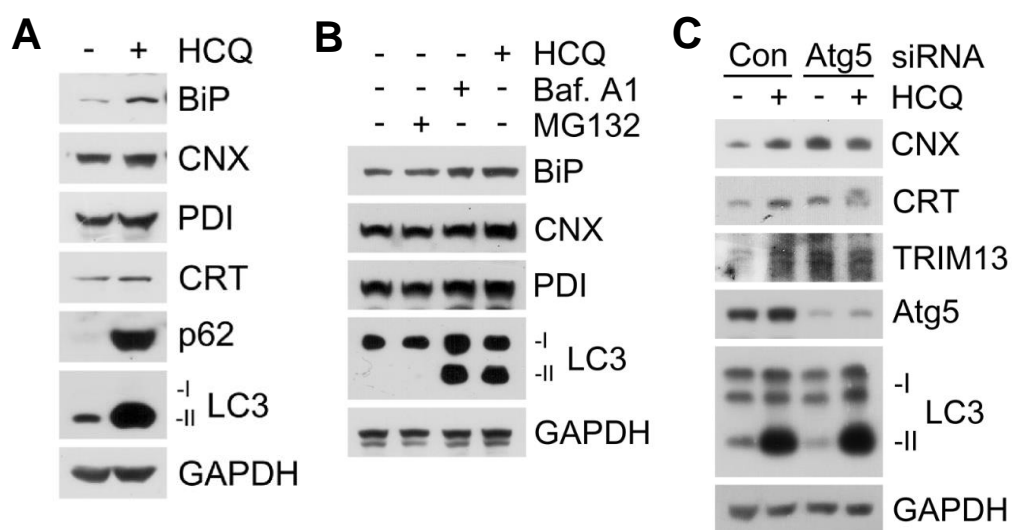


Fig. 6. ER-resident luminal proteins are constitutively degraded via macroautophagy. (A) WB in HeLa cells treated with HCQ (10 μ M, 24 h). (B) WB in HeLa cells treated with HCQ (10 μ M, 24 h), MG132 (10 μ M, 6 h) or Baf. A1 (200 nM, 6 h). (C) WB in HeLa cells under RNA interference of *ATG5* (40 nM, 48 h) and treated with HCQ (10 μ M, 24 h).

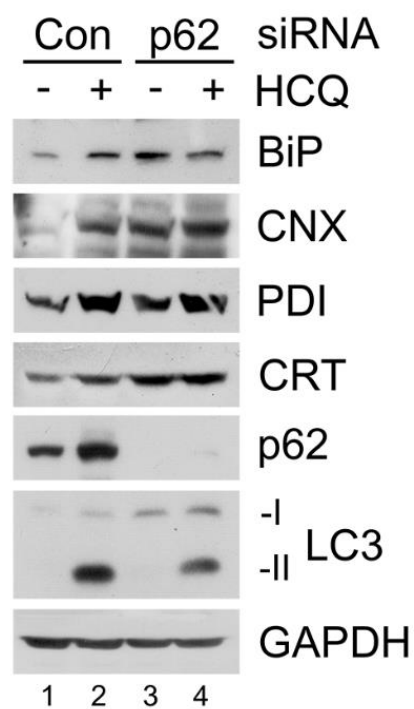


Fig. 7. p62 facilitates constitutive lysosomal degradation of ER-resident luminal proteins. WB in HeLa cells under siRNA-mediated knockdown of p62 and treated with HCQ (10 μ M, 24 h).

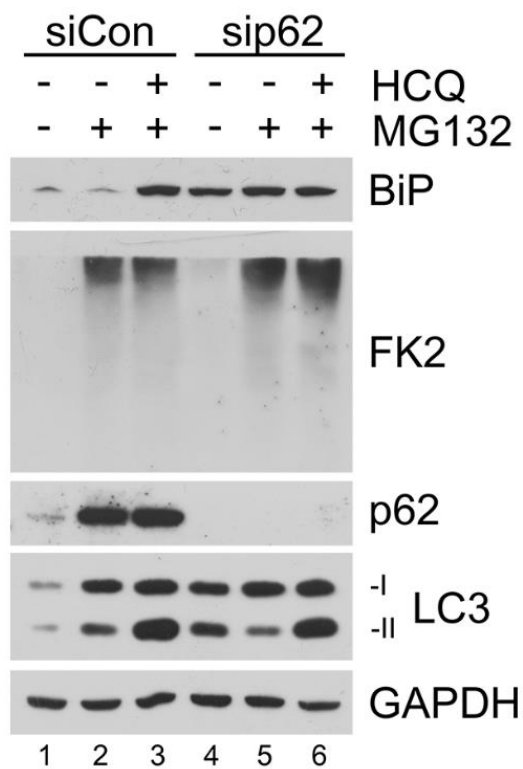


Fig. 8. p62 mediates proteotoxicity-mediated autophagic turnover of ER lumenal proteins. WB in HeLa cells treated with MG132 (2 μ M, 18 h), HCQ (10 μ M, 24 h), or both under *p62* siRNA compared to control.

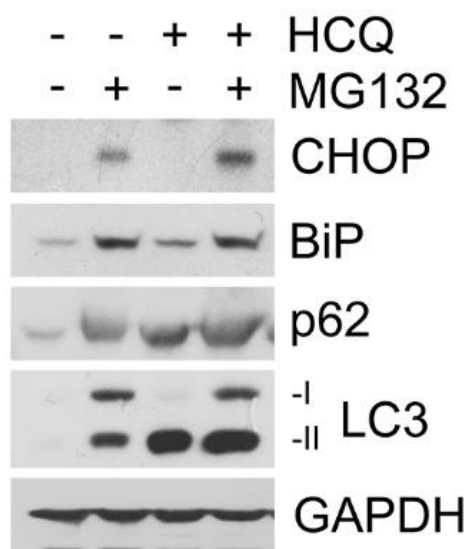


Fig. 9. Autophagy protects cells from proteotoxicity-induced ER stress. WB of HeLa cells treated with MG132 (2 μ M, 18 h), HCQ (10 μ M, 24 h), or both.

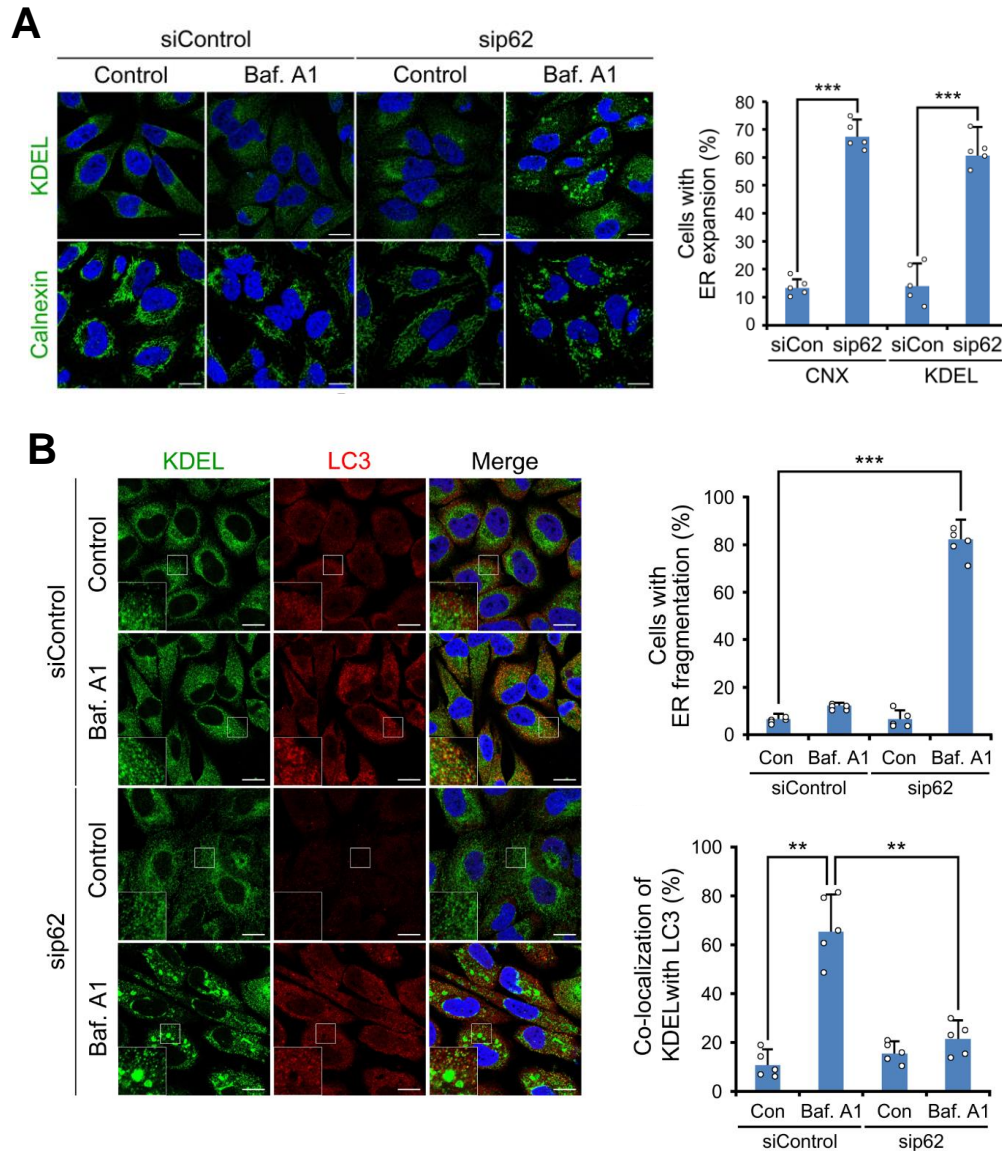


Fig. 10. p62 maintains integrity of ER architecture via autophagy. (A) ICC in HeLa cells of KDEL and calnexin signals under *p62* siRNA compared to control (48 h) treated with bafilomycin A1 (200 nM, 24 h). Scale bar, 10 μ m. Quantification: n= 40 cells. (B) ICC in HeLa cells of KDEL signals under *p62* siRNA compared to control (40 nM, 48 h) treated with bafilomycin A1 (200 nM, 24 h). Scale bar, 10 μ m. Quantification: n= 40 cells.

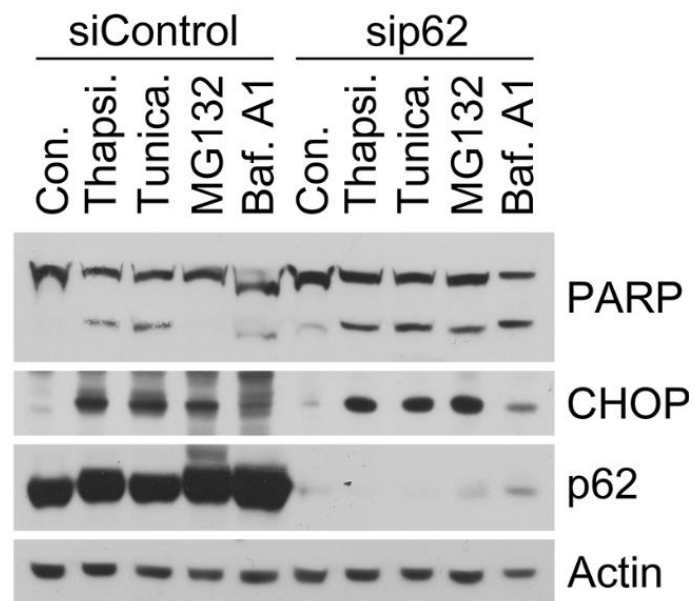


Fig. 11. p62 desensitizes cells to ER stress-induced apoptosis. WB of HeLa cells treated with thapsigargin (200 nM, 18 h), tunicamycin (0.1 μ g/mL, 18 h), MG132 (2 μ M, 18 h), or Baf. A1 (200 nM, 18 h) under *p62* or control siRNA (48 h).

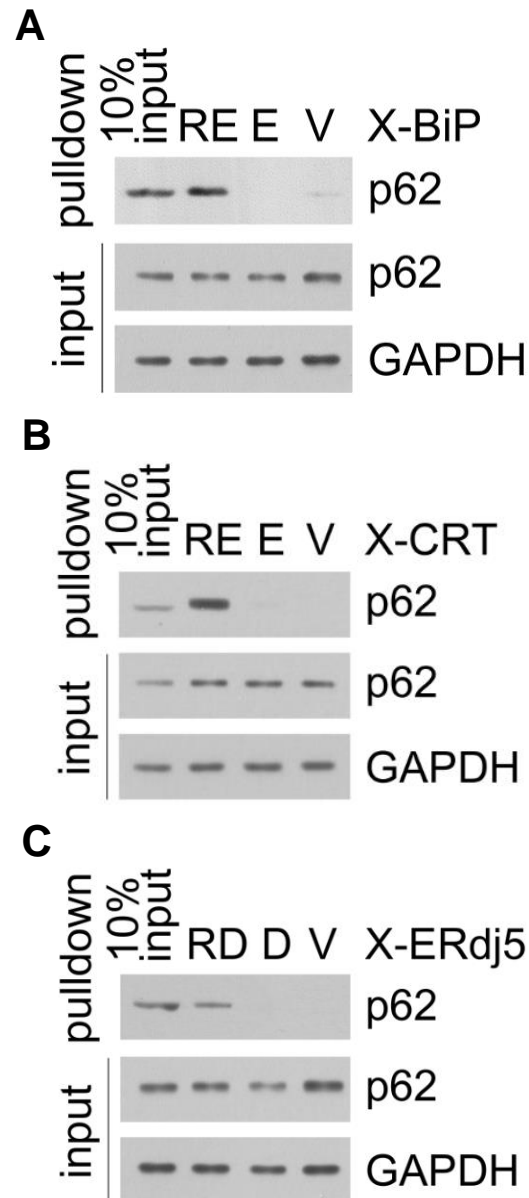


Fig. 12. The Nt-Arg residue selectively binds p62. (A) *In vitro* pulldown assay of X-BiP (X = E, V, or RE) peptide of the first 12 amino acid sequence of BiP following signal peptide cleavage. (B,C) Identical to A, but with X-CRT and X-ERdj5, respectively.

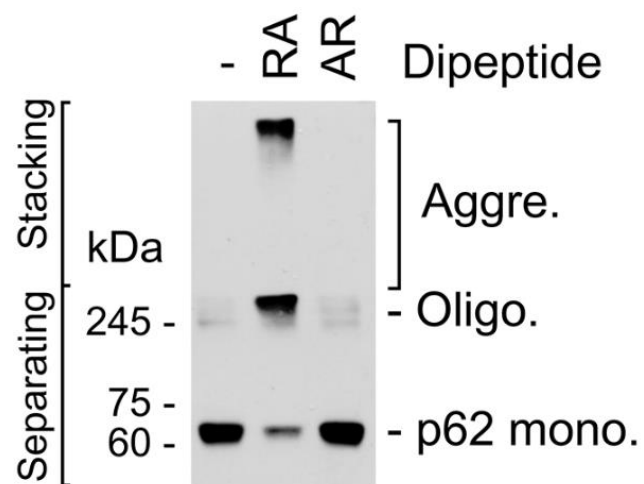


Fig. 13. The Nt-Arg residue induces p62 self-oligomerization. *In vitro* p62 oligomerization assay in HEK293T cells incubated with Arg-Ala or Ala-Arg dipeptides (50 mM, 2 h).

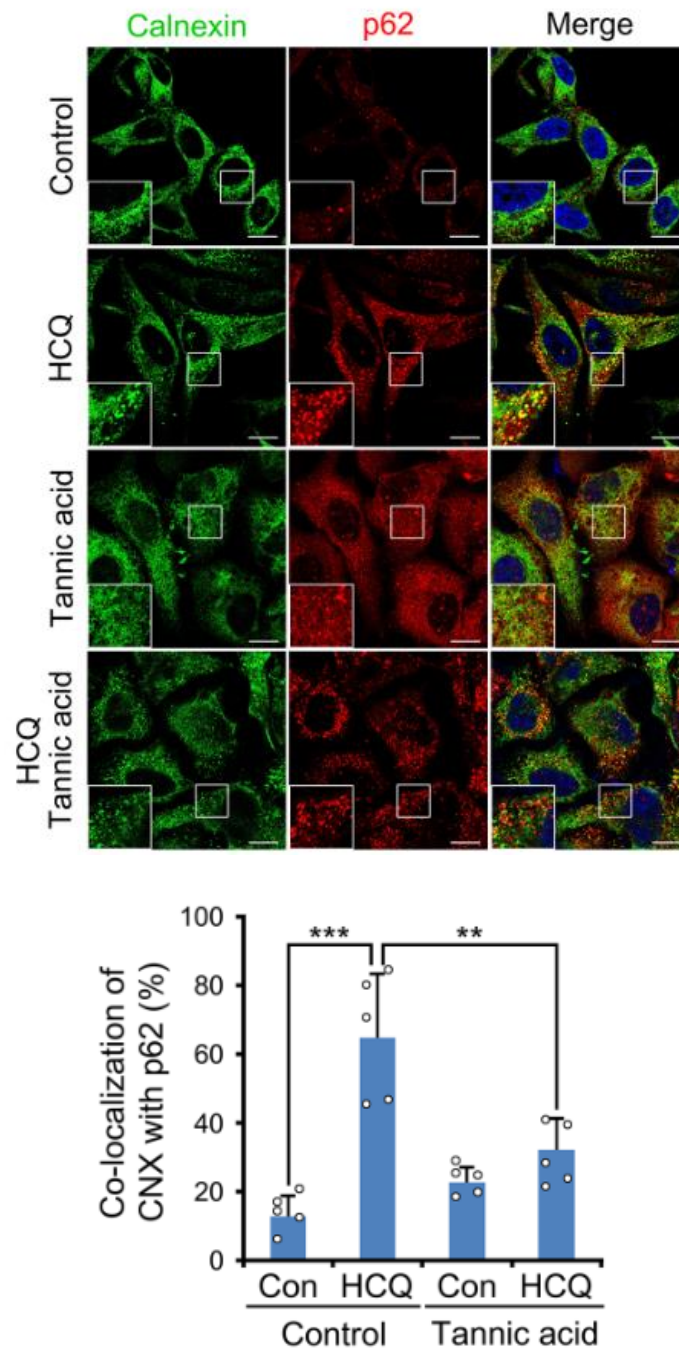


Fig. 14. ATE1-mediated Nt-arginylation enables recruitment of p62 and ER membrane-derived vesicles. (C) ICC of p62 and calnexin in HeLa cells treated with HCQ (10 μ M, 24 h), tannic acid (30 μ M, 24 h), or both. Scale bar, 10 μ m. **(D)** Quantification: n=50 cells.

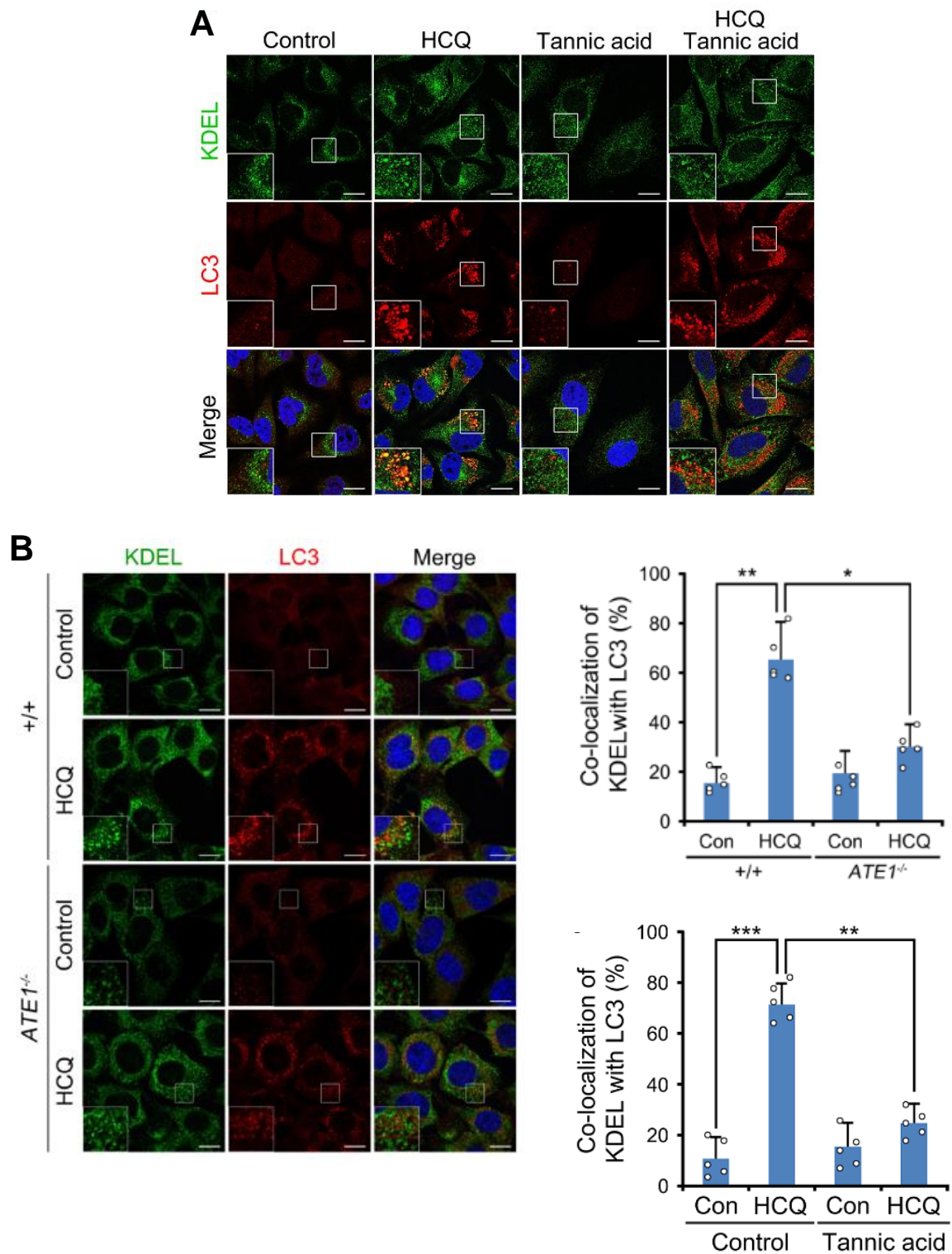


Fig. 15. Nt-arginylation is required for autophagic targeting of ER luminal proteins. (A) ICC of KDEL in HeLa cells treated with HCQ (10 μ M, 24 h), tannic acid (30 μ M, 24 h), or both. Scale bar, 10 μ m. Quantification: n=50 cells. (B) ICC of KDEL in wild-type or *ATE1*^{-/-} MEFs treated with HCQ (10 μ M, 24 h). Scale bar, 10 μ m. Quantification: n=50 cells.

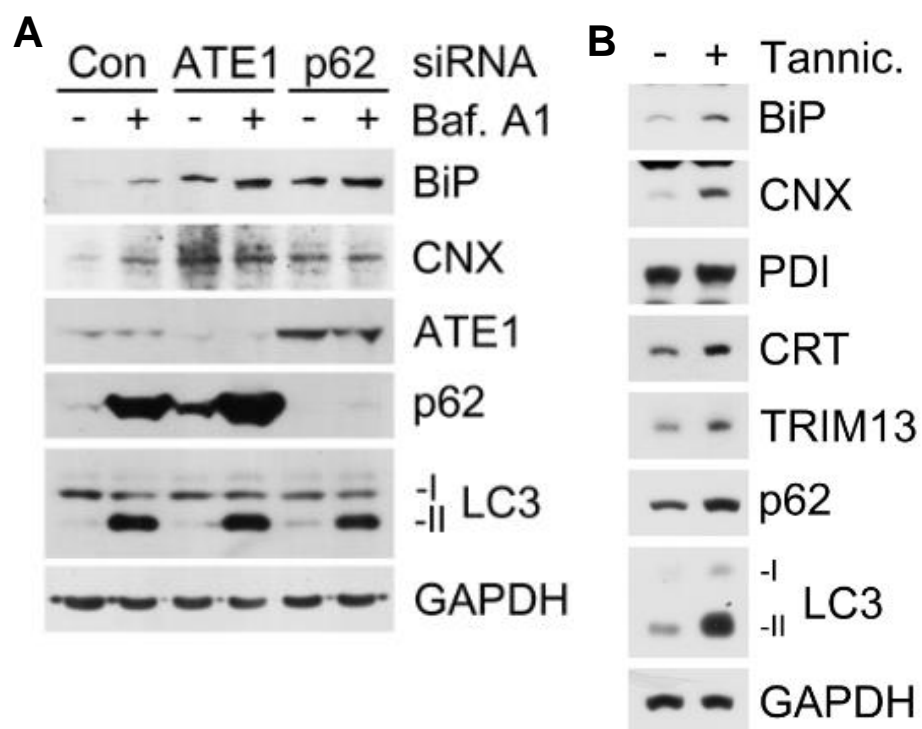


Fig. 16. The Nt-Arg residue regulates constitutive lysosomal turnover of the ER membrane and luminal proteins. (A) WB of HeLa cells under control, *p62*, or *ATE1* knockdown (48 h) and treated with bafilomycin A1 (200 nM, 7 h). **(B)** WB in HeLa cells treated with tannic acid (30 μ M, 24 h).

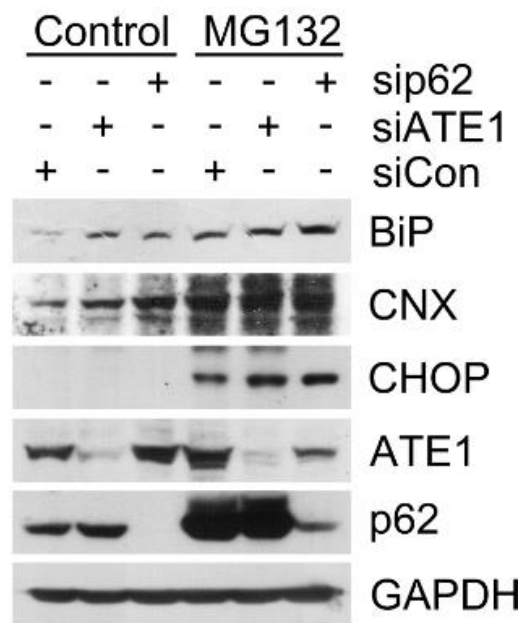


Fig. 17. The Arg/N-degron pathway mediates proteotoxicity-induced autophagic turnover of ER luminal proteins. WB in HeLa cells under siRNA-mediated interference of *p62* or *ATE1* compared to control (40 nM, 48 h) and treated with MG132 (2 μ M, 24 h).

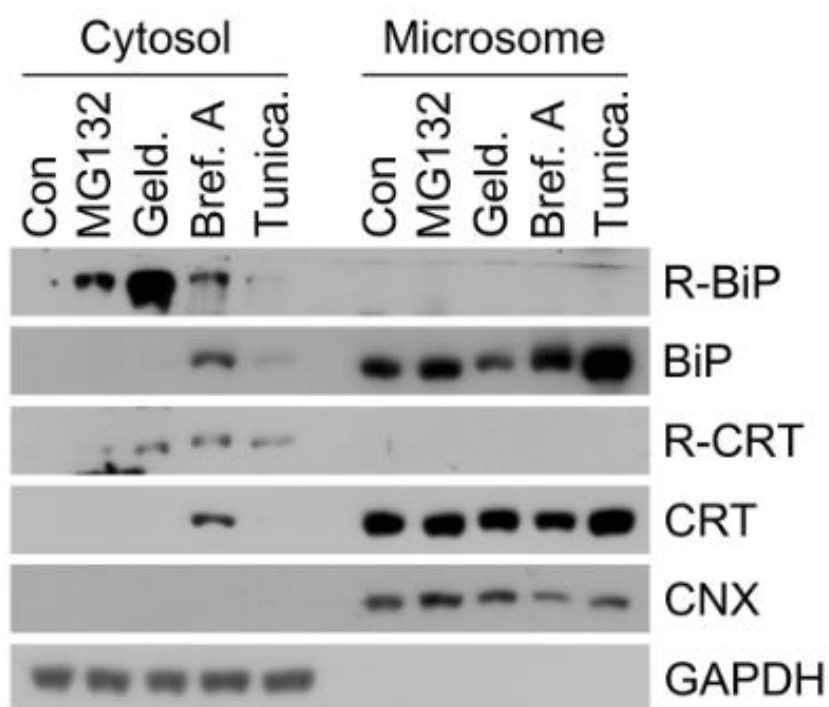


Fig. 18. Proteotoxic stress induces cytosolic retrotranslocation and Nt-arginylation of ER chaperones. Subcellular fractionation of HeLa cells treated with MG132 (2 μ M, 24 h), geldanamycin (1 μ M, 24 h), brefeldin A (0.3 μ M, 24 h), or tunicamycin (0.25 μ g/mL, 24 h).

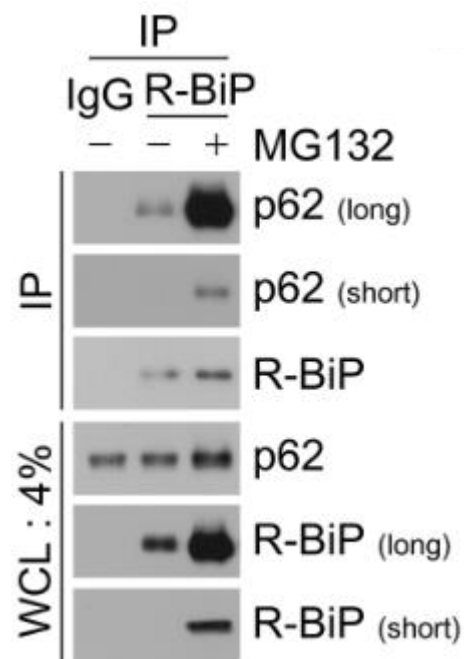


Fig. 19. The N-degron Arg of Nt-arginylated ER chaperones binds p62. Endogenous co-IP assay in HEK293T cells treated with MG132 (2 μ M, 24 h) or DMSO.

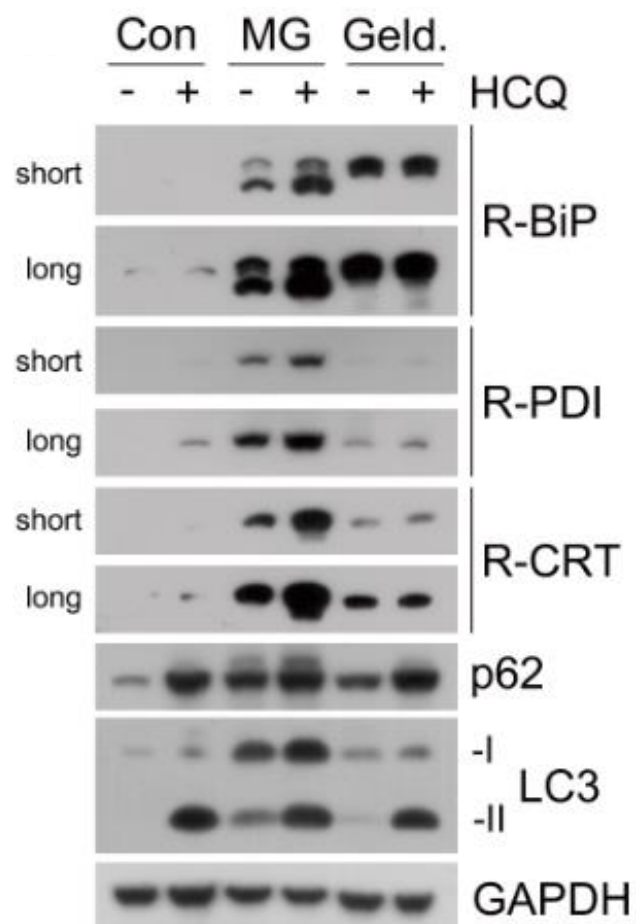


Fig. 20. Nt-arginylated ER chaperones are degraded by autophagy under proteotoxic stress. WB in HeLa cells treated with MG132 (2 μ M, 24 h) or geldamycin (1 μ M, 24 h) in the absence or presence of HCQ (10 μ M, 24 h).

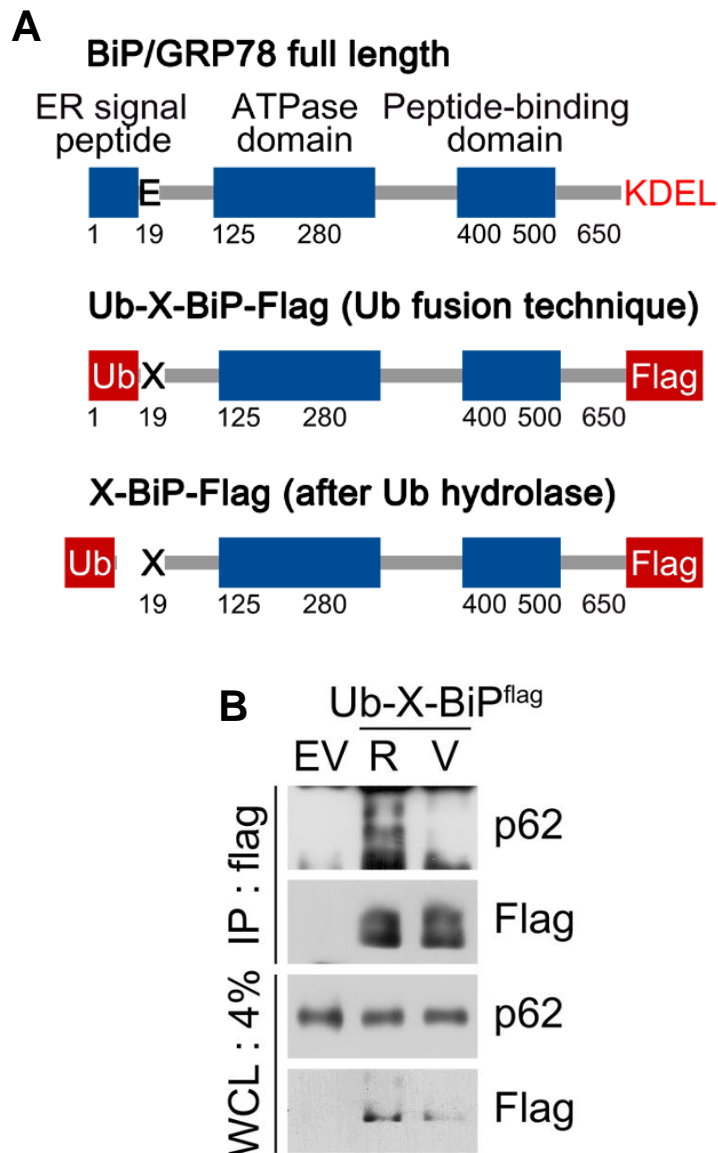


Fig. 21. Nt-arginylated ER chaperone BiP generated via the ubiquitin fusion technique selectively binds p62. (A) Cytosolic Ub-X-BiP-flag (X=R,V) constructs using the Ub fusion technique. (B) Co-IP assay in HEK293T cells expressing Ub-X-BiP-flag (X=R,V).

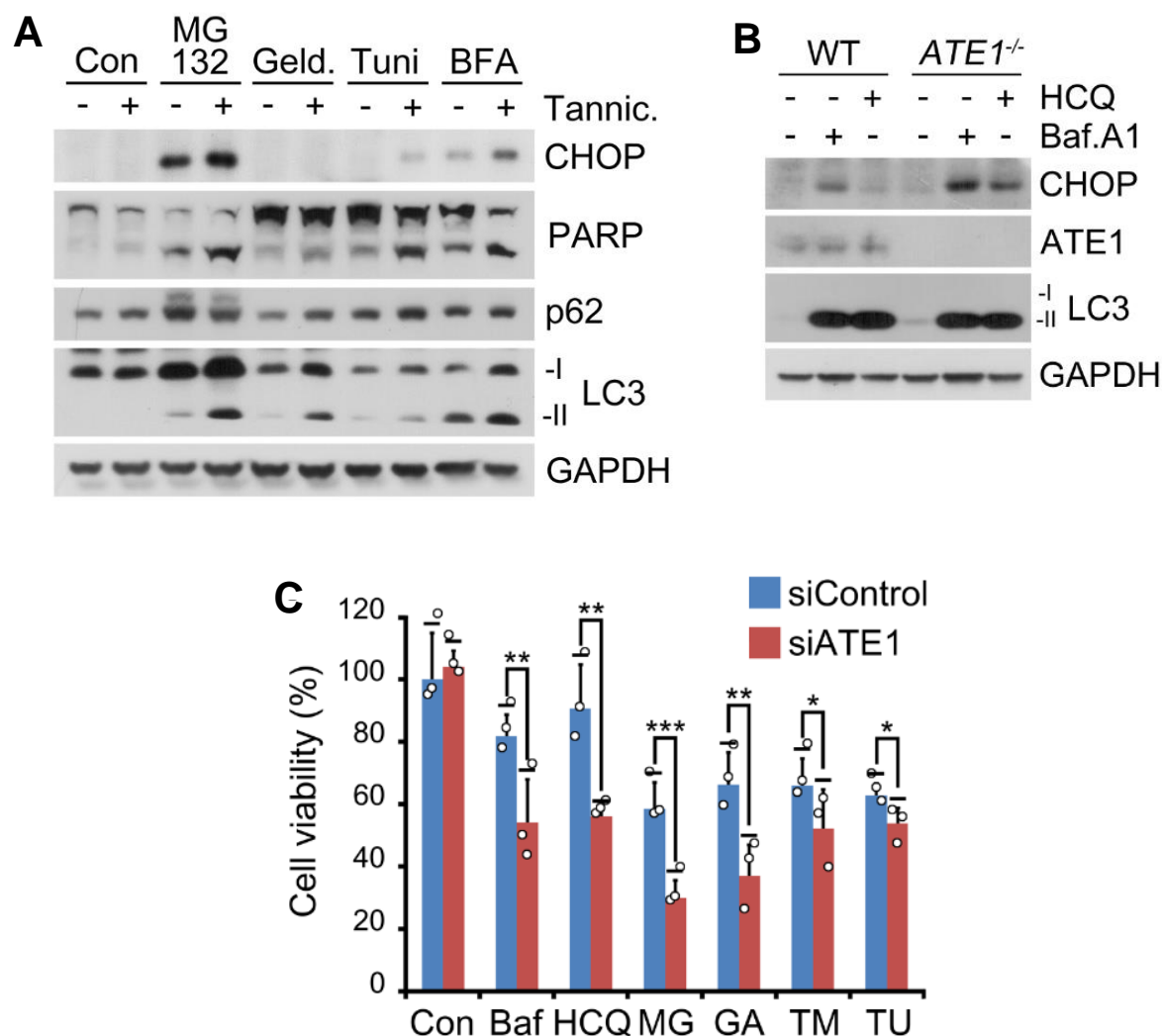


Fig. 22. Nt-arginylation-mediated autophagy protects cells from proteotoxicity-induced ER stress and apoptosis. (A) WB of HeLa cells treated with MG132 (1 μ M, 24 h), geldanamycin (500 nM, 24 h), tunicamycin (0.25 μ g/mL, 24 h) or brefeldin A (0.3 μ M, 24 h) with or without tannic acid (25 μ M, 24 h). (B) WB of wild-type and *ATE1*^{-/-} MEFs treated with prolonged autophagy inhibition (bafilomycin A1; 200 nM, 24 h or HCQ; 25 μ M, 24 h). (C) WST-based cell viability assay of HeLa cells under RNA interference of *ATE1* or control, treated with baf. A1 (200 nM, 24 h), HCQ (10 μ M, 24 h), MG132 (1 μ M, 24 h), geldanamycin (1 μ M, 24 h), thapsigargin (200 nM, 24 h), or tunicamycin (0.1 μ g/mL, 24 h).

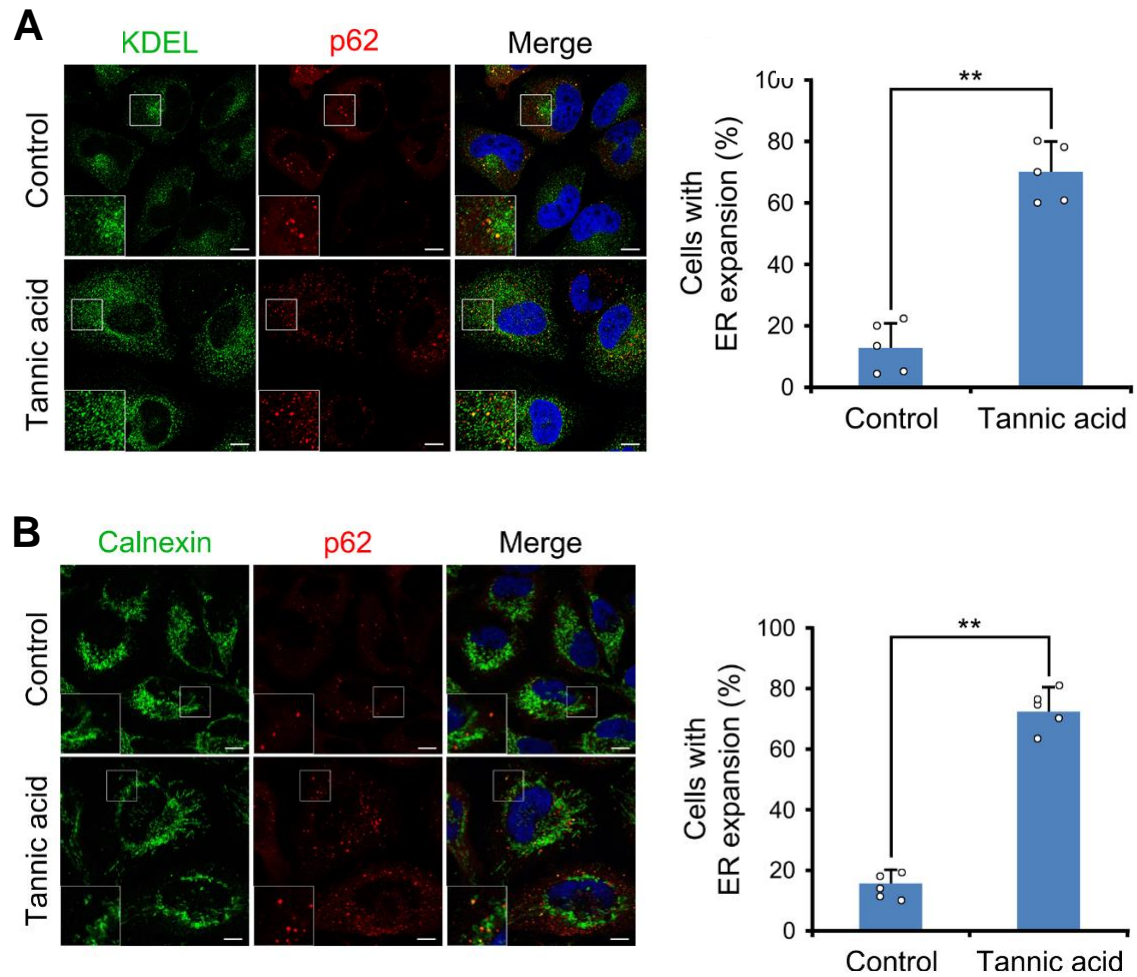


Fig. 23. Nt-arginylation maintains integrity of ER architecture. (A) ICC of KDEL signals in HeLa cells treated with tannic acid (30 μ M, 24 h) or control. Scale bar, 5 μ m. Quantification: n=50 cells. **(B)** Identical to **A**, but with calnexin instead of KDEL.

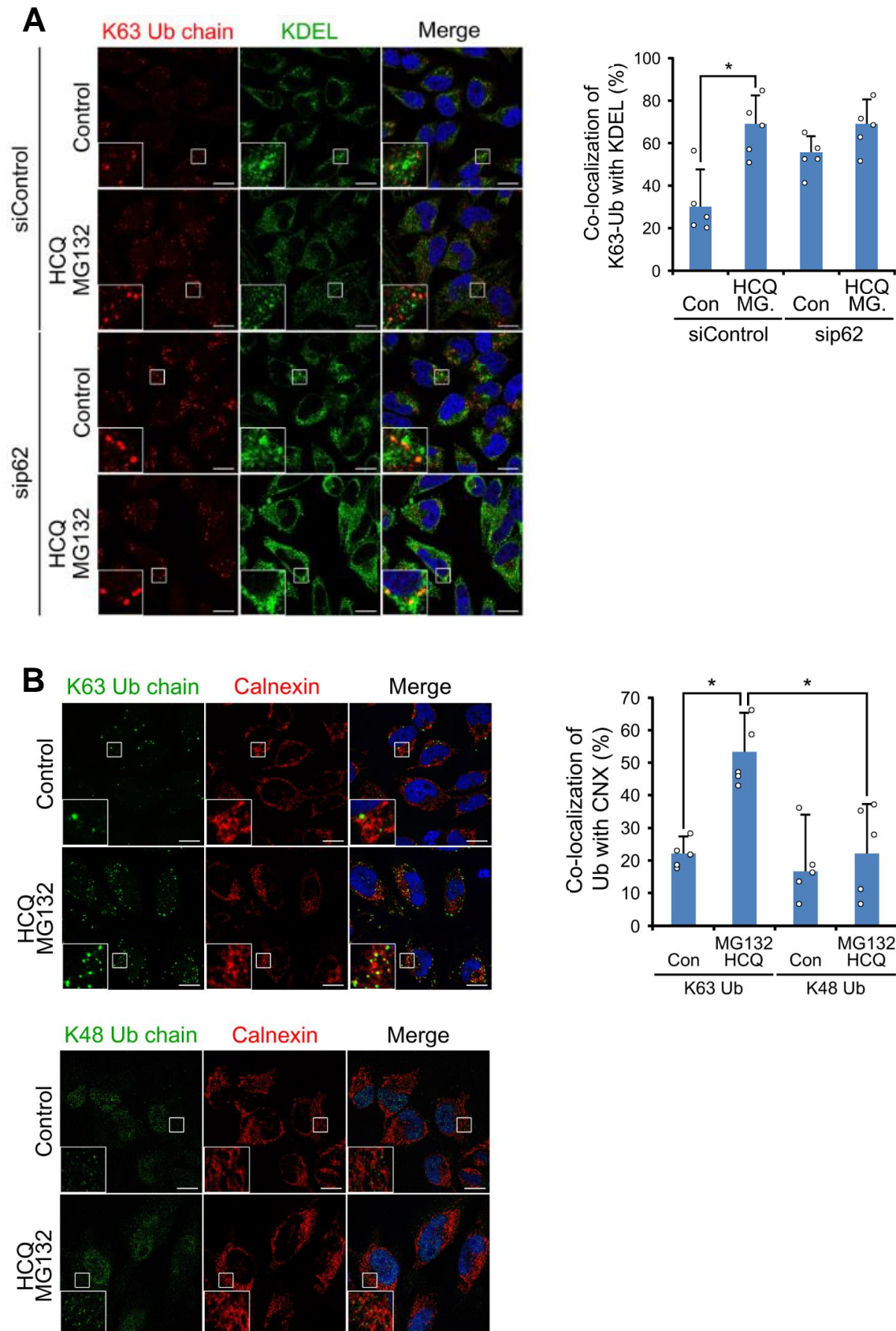


Fig. 24. K63-ubiquitination is selectively associated with ER-phagy. (A) ICC of K63-linked poly-Ub chains and KDEL in HeLa cells treated with MG132 (2 μ M, 18 h) and HCQ (10 μ M, 18 h) under control or *p62* knockdown (48 h). Scale bar, 10 μ m. Quantification: *n*=40 cells. (B) ICC of calnexin with K48-Ub or K63-Ub puncta structures in HeLa cells co-treated with MG132 (2 μ M, 18 h) and HCQ (10 μ M, 24 h) compared to DMSO. Scale bar, 10 μ m. Quantification: *n*=50 cells.

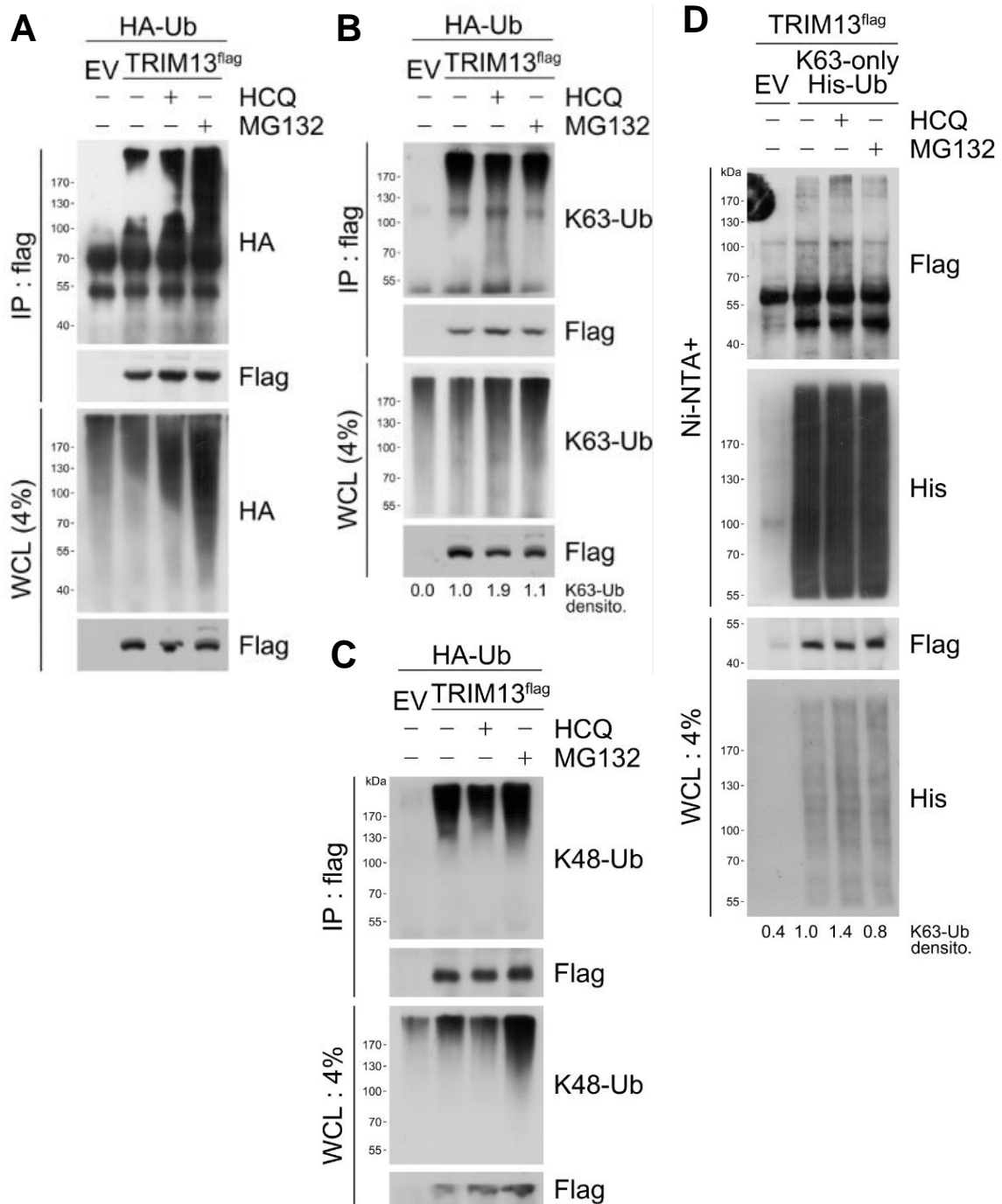


Fig. 25. The ER transmembrane E3 ligase TRIM13 is K63-ubiquitinated during autophagy but K48-ubiquitinated for the UPS. (A,B,C) Denaturation IP assay in HEK293T cells co-transfected (24 h) with TRIM13-flag or negative control empty vector (EV) and HA-Ub, followed by HCQ (10 μ M, 24 h) or MG132 (10 μ M, 6 h) treatment. (D) Denaturation IP assay in HEK293T cells co-transfected (24 h) with TRIM13-flag or negative control empty vector (EV) and K63-only His-Ub and treated with HCQ (10 μ M, 24 h) and MG132 (10 μ M, 6 h). Densitometry values of TRIM13-flag conjugated to K63-only His-Ub were quantified by ImageJ.

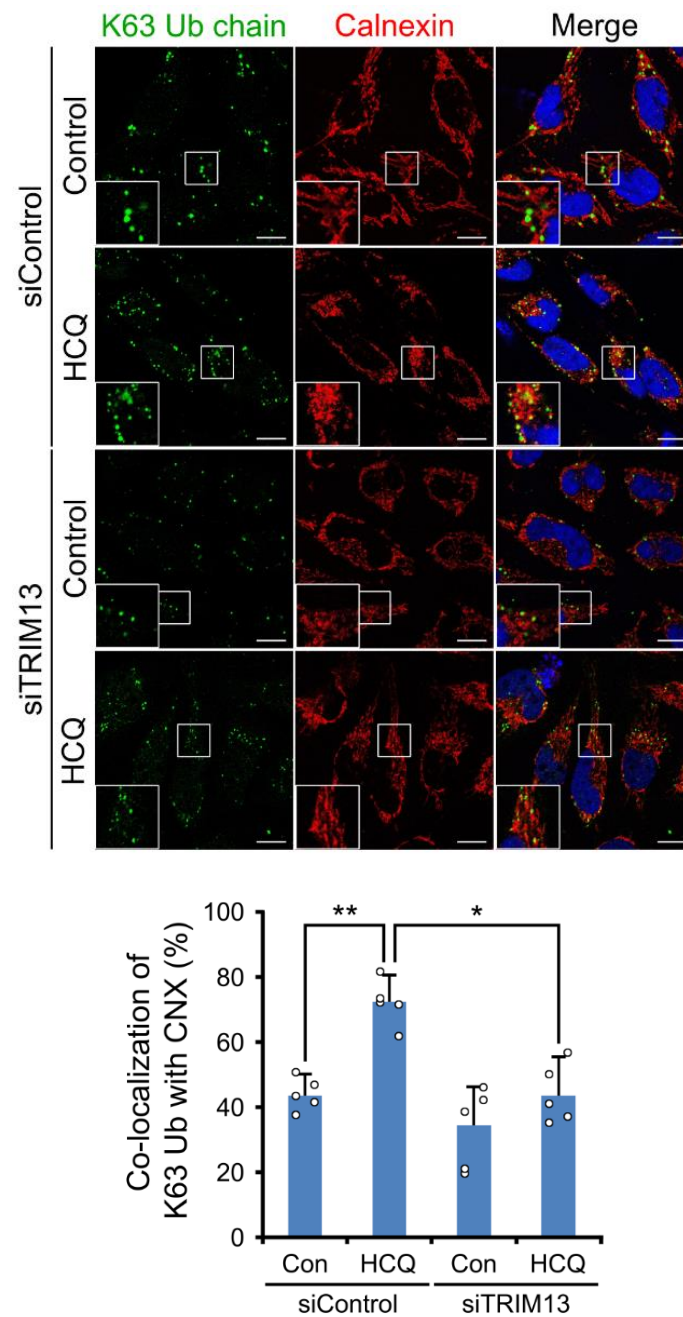


Fig. 26. TRIM13 is required for the involvement of K63-Ub chains during ER-phagy. ICC of calnexin and K63-Ub puncta structures in HeLa cells treated with or without HCQ (10 μ M, 24 h). Scale bar, 10 μ m. Quantification: n=50 cells.

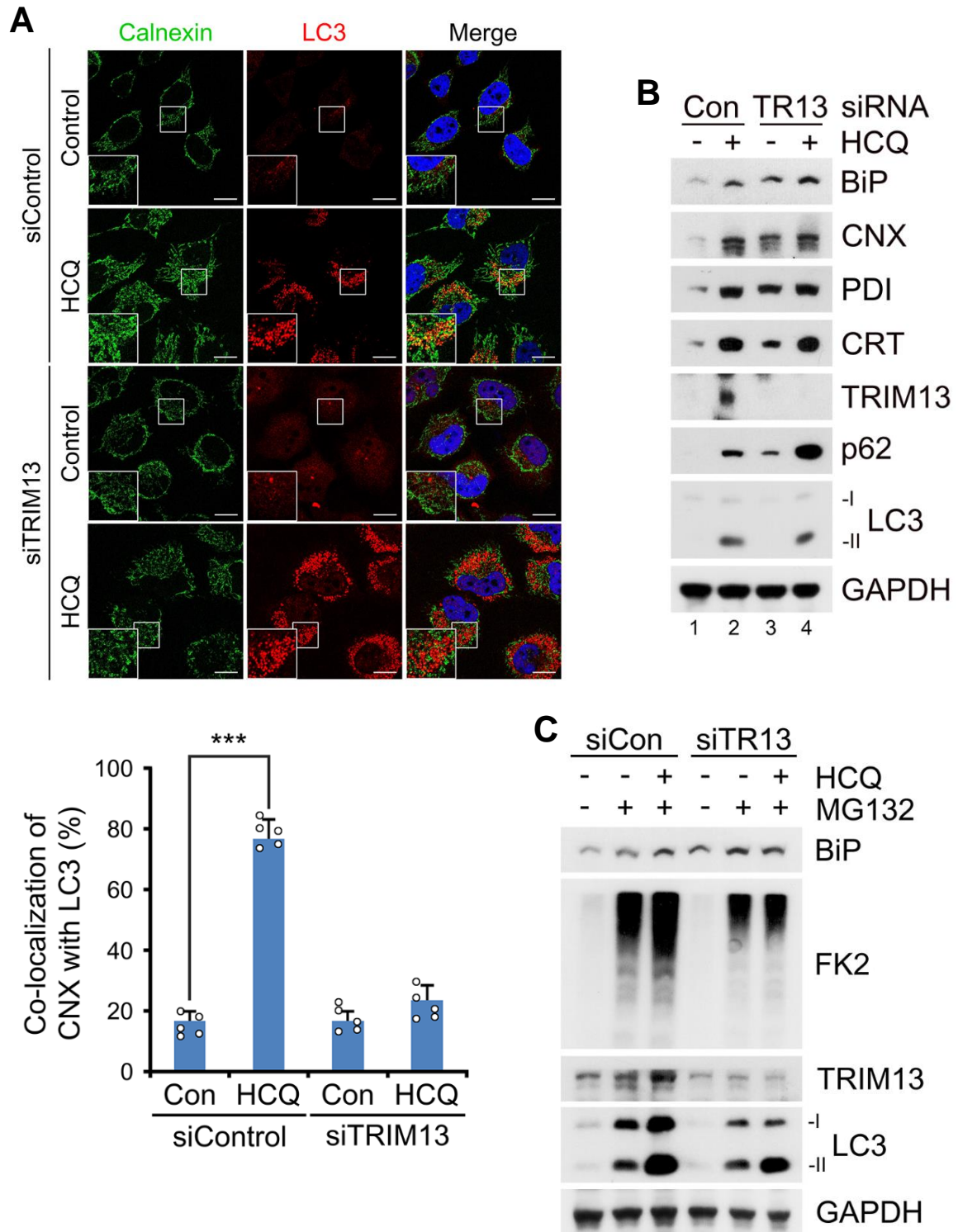


Fig. 27. TRIM13 mediates autophagic targeting and lysosomal degradation of the ER membrane and luminal proteins. (A) ICC of LC3 and calnexin in HeLa cells treated with HCQ (10 μ M, 24 h) under control or *TRIM13* knockdown (48 h). Scale bar, 10 μ m. Quantification: n=50 cells. (B) WB in HeLa cells under control or *TRIM13* knockdown (48 h) treated with or without HCQ (10 μ M, 24 h). (C) Same as in B but treated with MG132 (2 μ M, 18 h) with or without HCQ (10 μ M, 24 h).

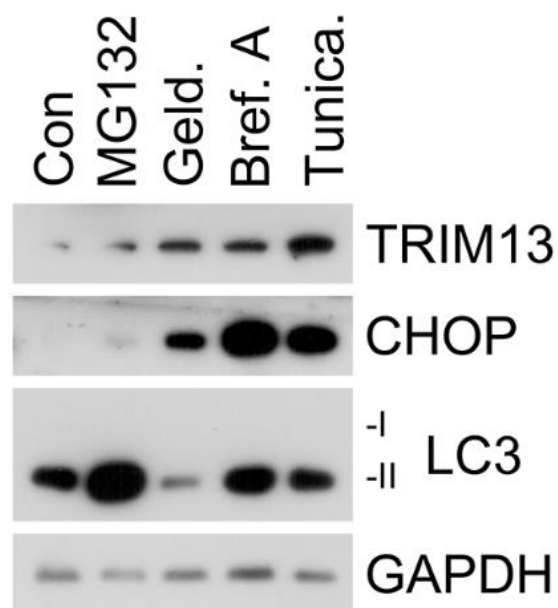


Fig. 28. TRIM13 levels are dynamically regulated upon ER stress. WB of HeLa cells treated with MG132 (2 μ M, 24 h), geldanamycin (1 μ M, 24 h), brefeldin A (0.3 μ M, 24 h), or tunicamycin (0.25 μ g/mL, 24 h).

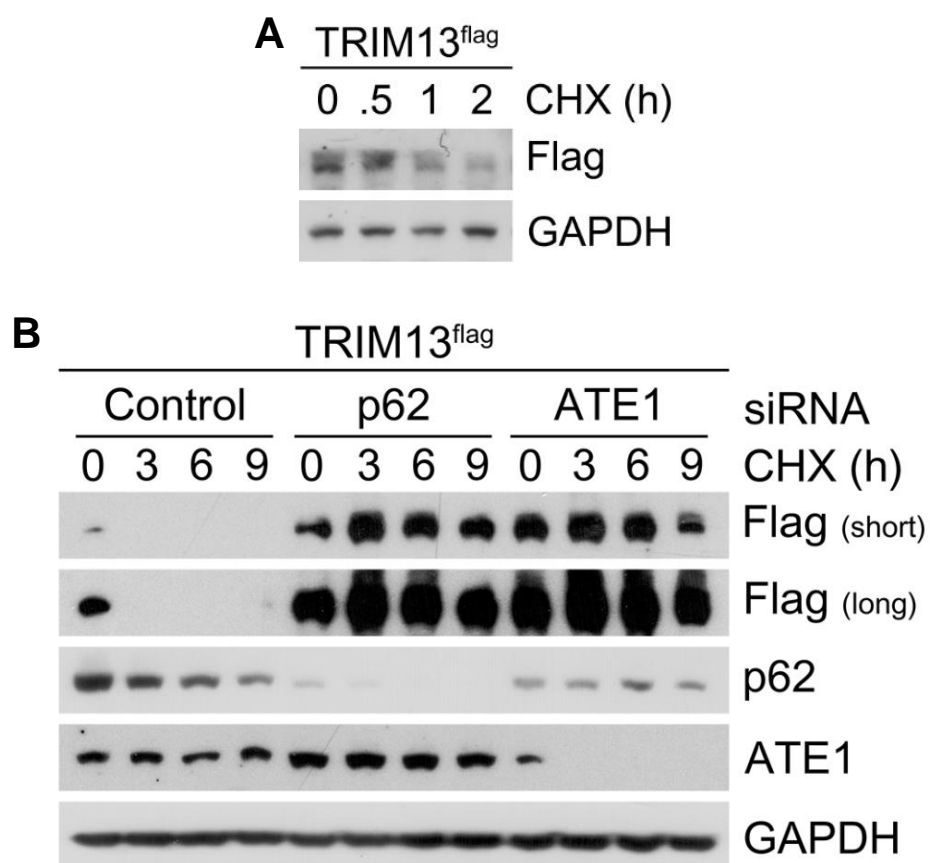


Fig. 29. The p62-Nt-arginylation circuit mediates TRIM13 stability. (A) Cycloheximide chase assay in HeLa cells expressing TRIM13-flag (24 h) for the indicated time points. (B) CHX chase assay in HeLa cells expressing TRIM13-flag under siRNA-mediated knockdown of p62 or ATE1 (48 h).

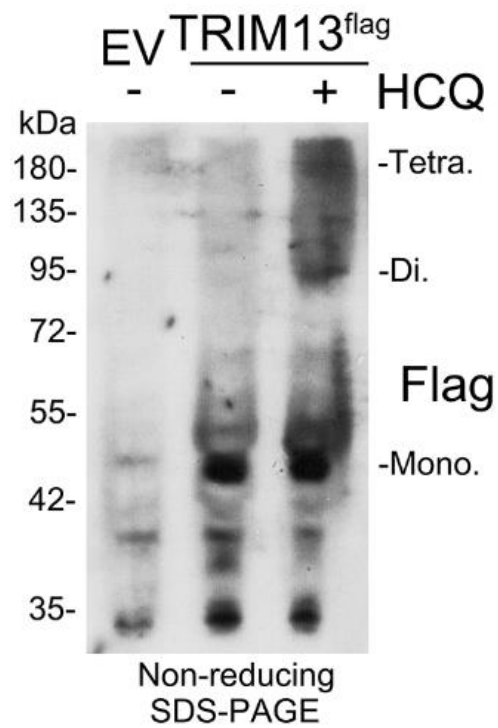


Fig. 30. Oligomeric species of TRIM13 are degraded by autophagy. *In vivo* oligomerization assay of TRIM13-flag in HEK293T cells treated with or without HCQ (10 μ M, 24 h).

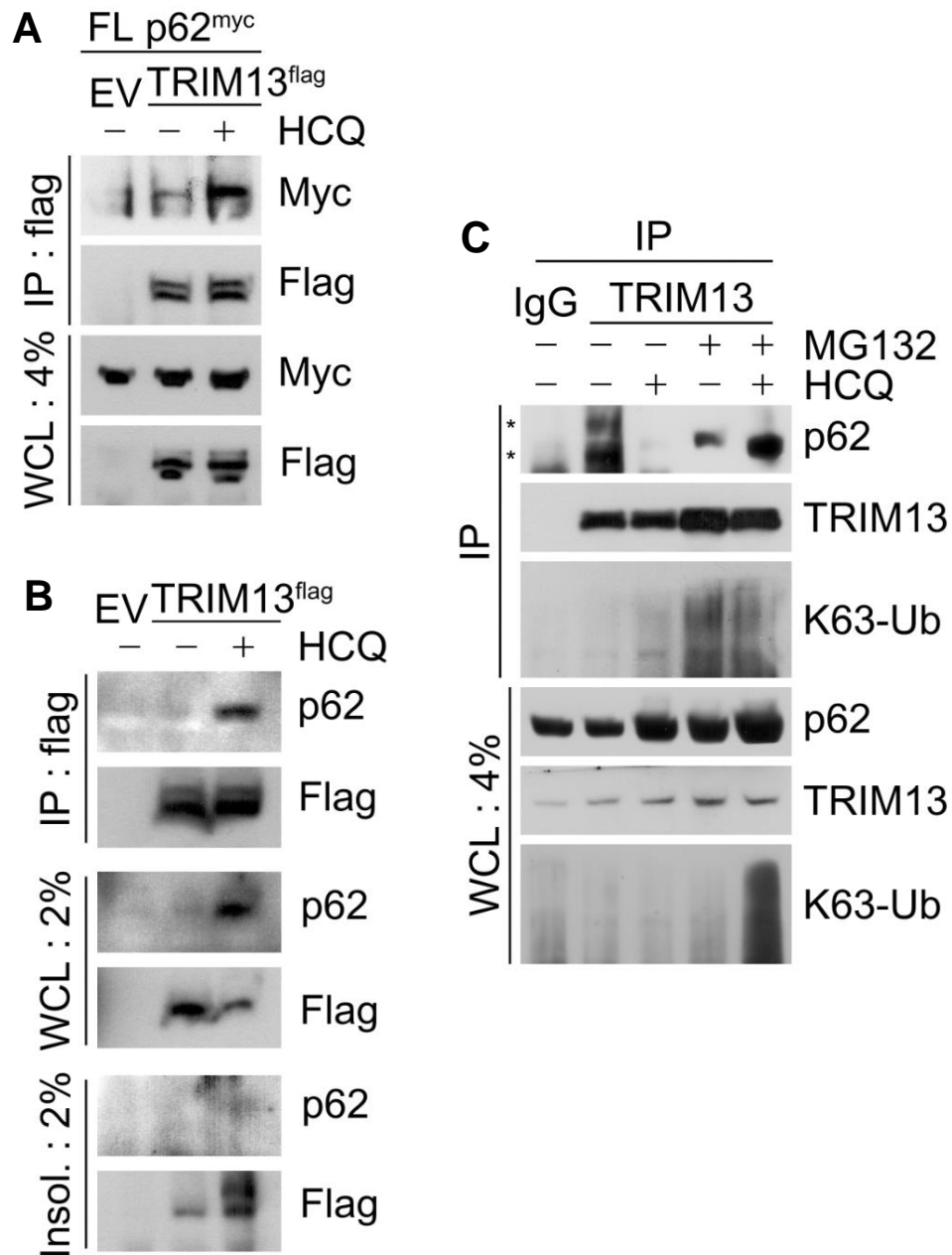


Fig. 31. TRIM13 forms an autophagy-degraded complex with p62. (A) Co-IP assay in HEK293T cells co-transfected (24 h) with full-length p62-myc and TRIM13-flag or negative control empty vector (EV), treated with HCQ (10 μ M, 24 h) or negative control. (B) Co-IP assay in HEK293T cells expressing TRIM13-flag and treated with or without HCQ (10 μ M, 24 h). (C) Endogenous co-IP assay in HEK293T cells treated with HCQ (10 μ M, 24 h), MG132 (2 μ M, 24 h), or both.

p62 full length



p62 Δ PB1



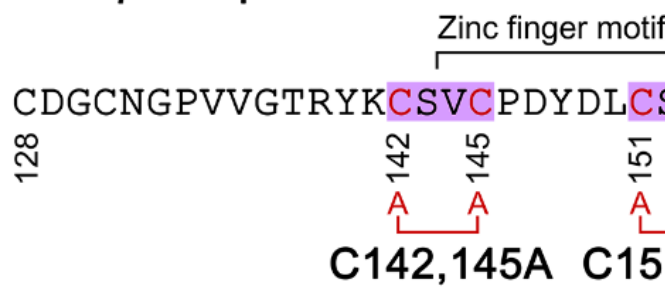
p62 Δ ZZ



p62 Δ UBA



H. sapiens p62 ZZ domain



TRIM13 full length



H. sapiens TRIM13 RING domain

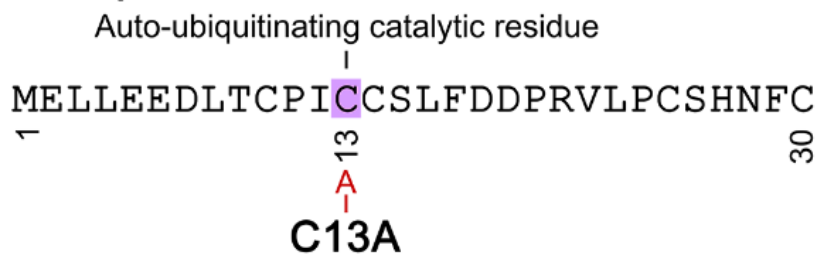


Fig. 32. Constructs of p62 and TRIM13 for domain mapping studies.

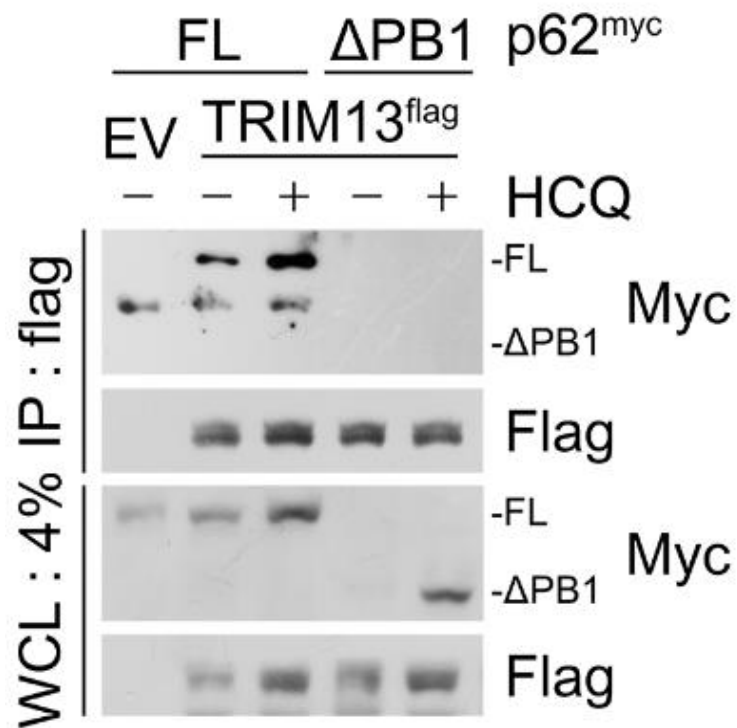


Fig. 33. The p62-PB1 domain promotes p62-TRIM13 complex formation. Co-IP assay in HEK293T cells co-transfected (24 h) with full-length or ΔPB1 p62-myc and TRIM13-flag or negative control empty vector (EV), treated with HCQ (10 μM, 24 h) or negative control.

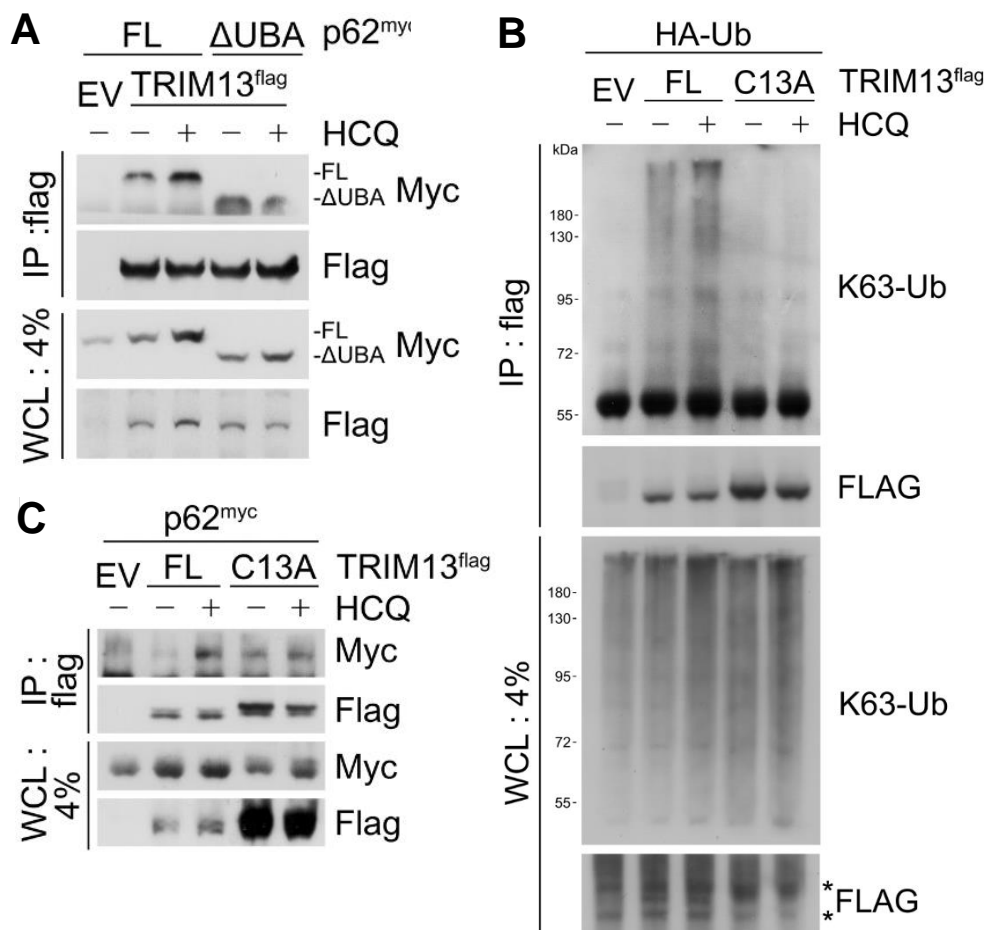


Fig. 34. Auto-ubiquitination of TRIM13 and its recognition by the p62-UBA domain implement autophagic flux of the p62-TRIM13 complex. (A) Co-IP assay in HEK293T cells co-transfected (24 h) with full-length or Δ UBA p62-myc and TRIM13-flag or negative control empty vector (EV), treated with HCQ (10 μ M, 24 h) or negative control. (B) Denaturation IP assay in HEK293T cells co-transfected with wild-type or C13A TRIM13-flag and HA-Ub and treated with HCQ (10 μ M, 24 h). (C) Same as in A but for wild-type or C13A point mutant TRIM13-flag with full-length p62.

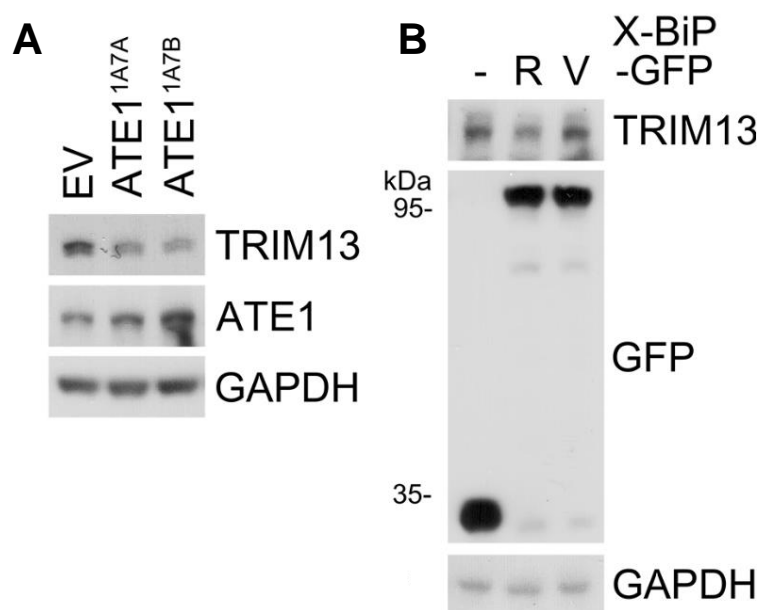


Fig. 35. The Arg/N-degron destabilizes TRIM13. (A,B) WB in HeLa cells transiently expressing murine ATE1 isoforms or Ub-X-BiP-GFP (X=R,V), respectively.

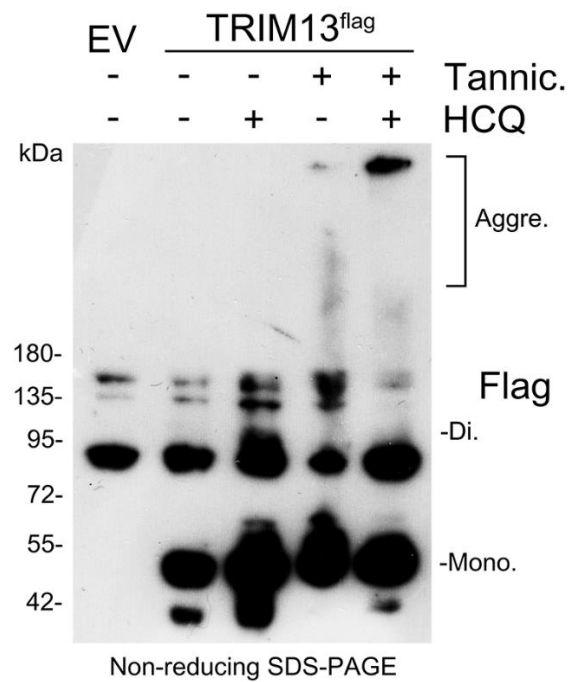


Fig. 36. Nt-arginylation targets oligomeric and aggregated TRIM13 species for autophagic clearance. *In vivo* oligomerization assay of TRIM13-flag in HEK293T cells treated with HCQ (10 μ M, 24 h),

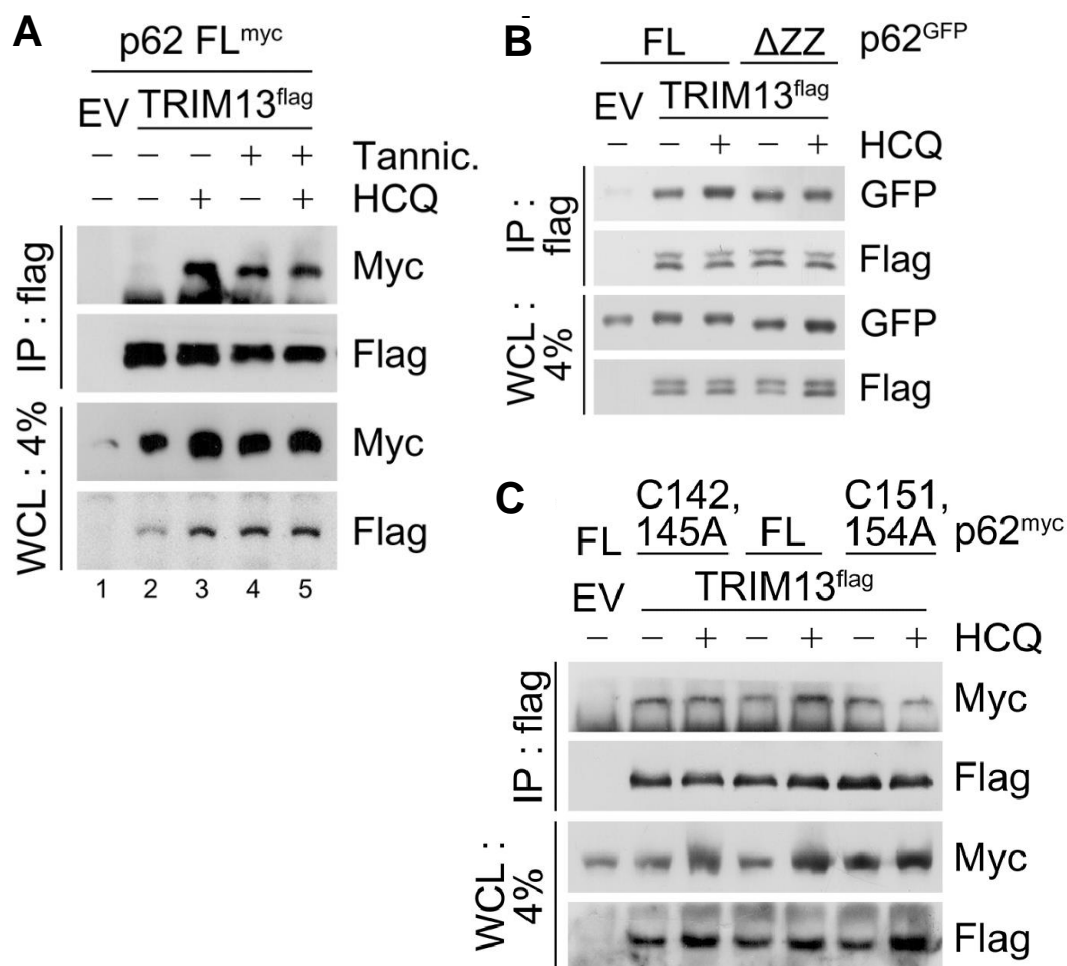


Fig. 37. The Arg/N-degron and its recognition via the p62-ZZ domain is required for autophagic clearance of the p62-TRIM13 complex. (A) Co-IP assay in HEK293T cells co-transfected (24 h) with p62-myc and TRIM13-flag and treated with HCQ (10 μ M, 24 h), tannic acid (30 μ M, 24 h) or both. (B) Co-IP assay in HEK293T cells co-transfected (24 h) with full-length or Δ ZZ p62-myc and TRIM13-flag and treated with HCQ (10 μ M, 24 h), (C) Identical to B but for full-length compared with ZZ domain zinc finger motif mutant C142,145A or C151,154A p62-myc.

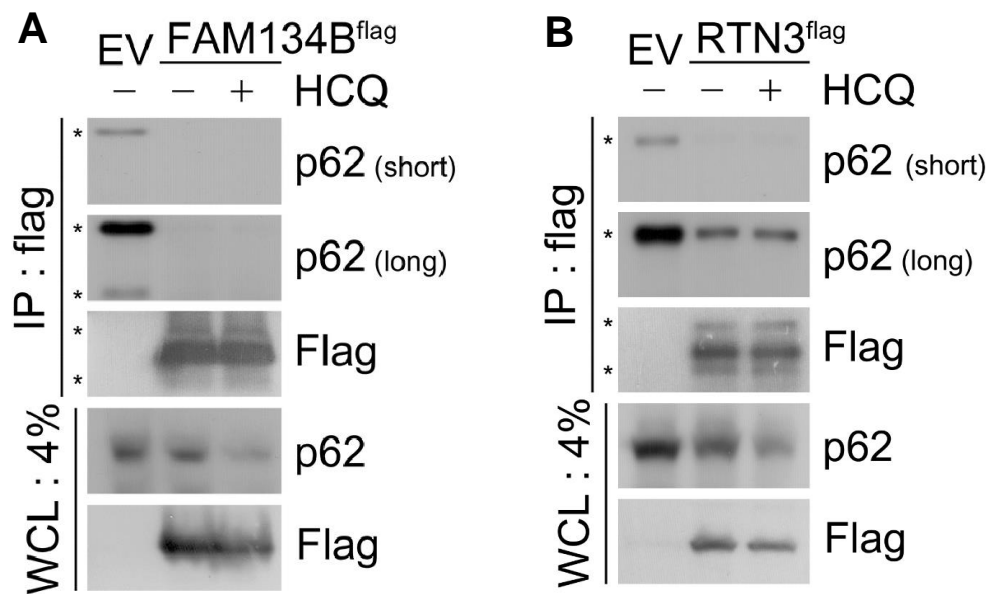


Fig. 38. p62 facilitates ER-phagy independent of previously-identified receptors. (A,B) Co-IP assay in HEK293T cells expressing FAM134B-flag or RTN3-flag and treated with or without HCQ (10 μ M, 24 h).

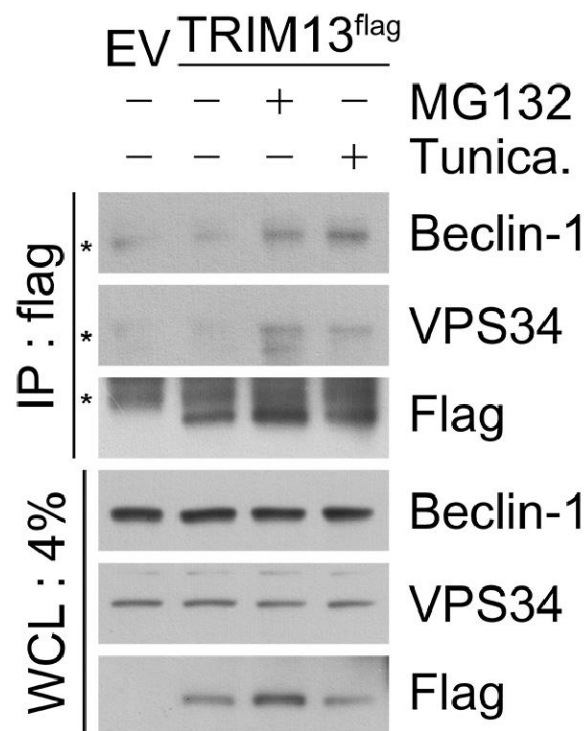


Fig. 39. TRIM13 recruits the mammalian PI3K complex. Co-IP assay in HEK293T cells expressing TRIM13-flag and treated with MG132 (2 μ M, 24 h) or tunicamycin (0.25 μ g/mL, 24 h).

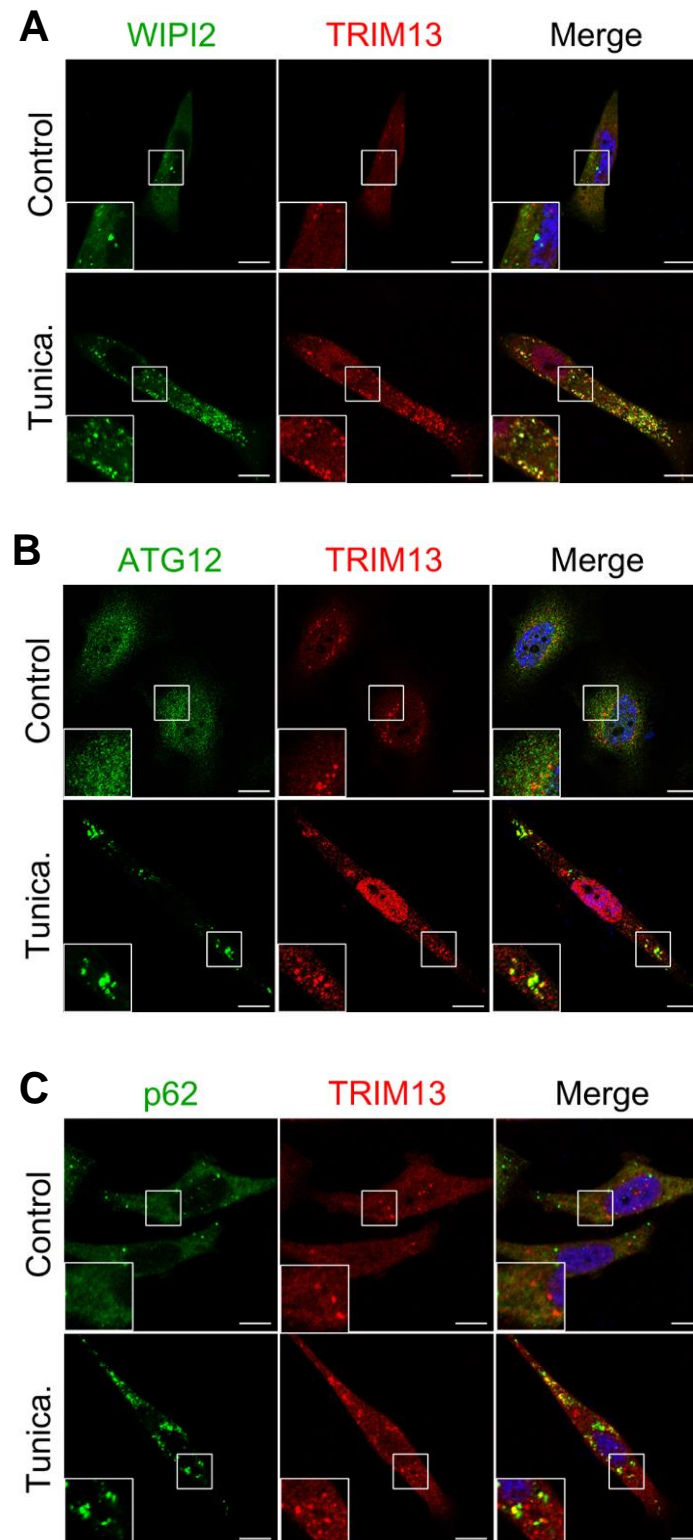


Fig. 40. The TRIM13-p62 circuit is associated to the omegasome formation site. (A,B,C) ICC of endogenous TRIM13 with WIPI2, ATG12 or p62, respectively, in HeLa cells treated with tunicamycin (0.1 μ g/mL, 18 h) or DMSO negative control. Scale bar, 10 μ m.

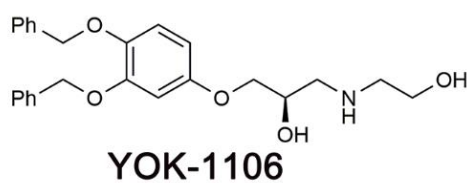
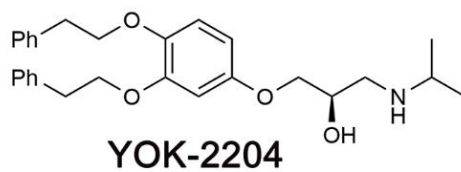
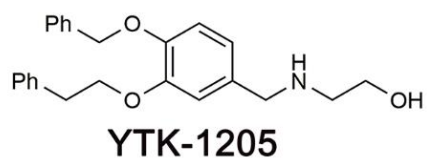
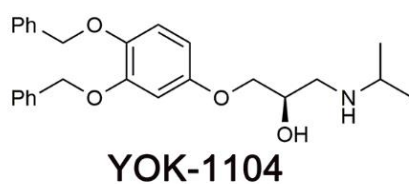
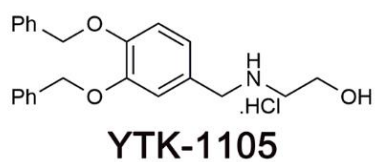


Fig. 41. Chemical structure of Nt-Arg-mimicking p62-ZZ ligands

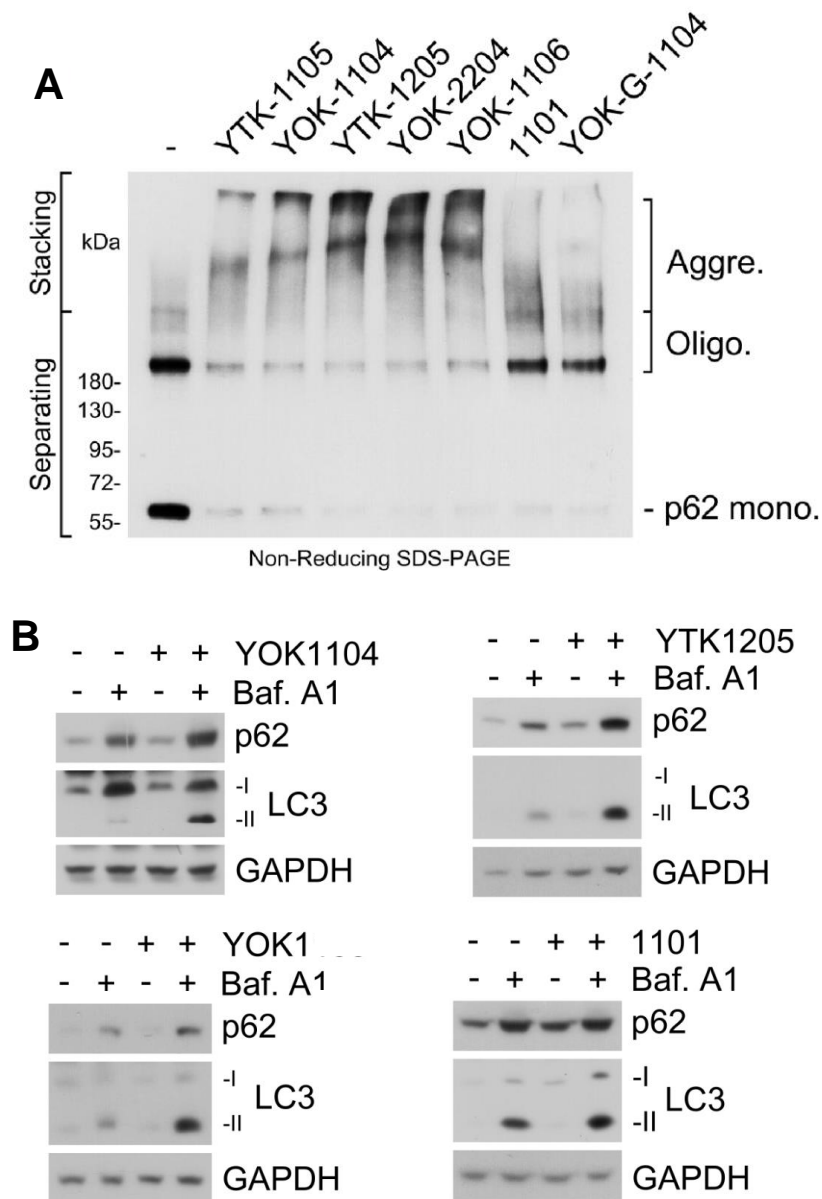


Fig. 42. p62-ZZ ligands induce p62 self-oligomerization and cellular autophagy flux. (A) *In vitro* p62 oligomerization assay in HEK293T cells incubated with the p62-ZZ ligands or negative control ligands 1101 and YOK-G-1104 (all 1 mM, 2 h). (B) WB of HEK293T cells treated with YOK1104, YOK1106, YTK1205 or 1101 (2.5 μ M, 5 h) in the absence or presence of HCQ (10 μ M, 24 h).

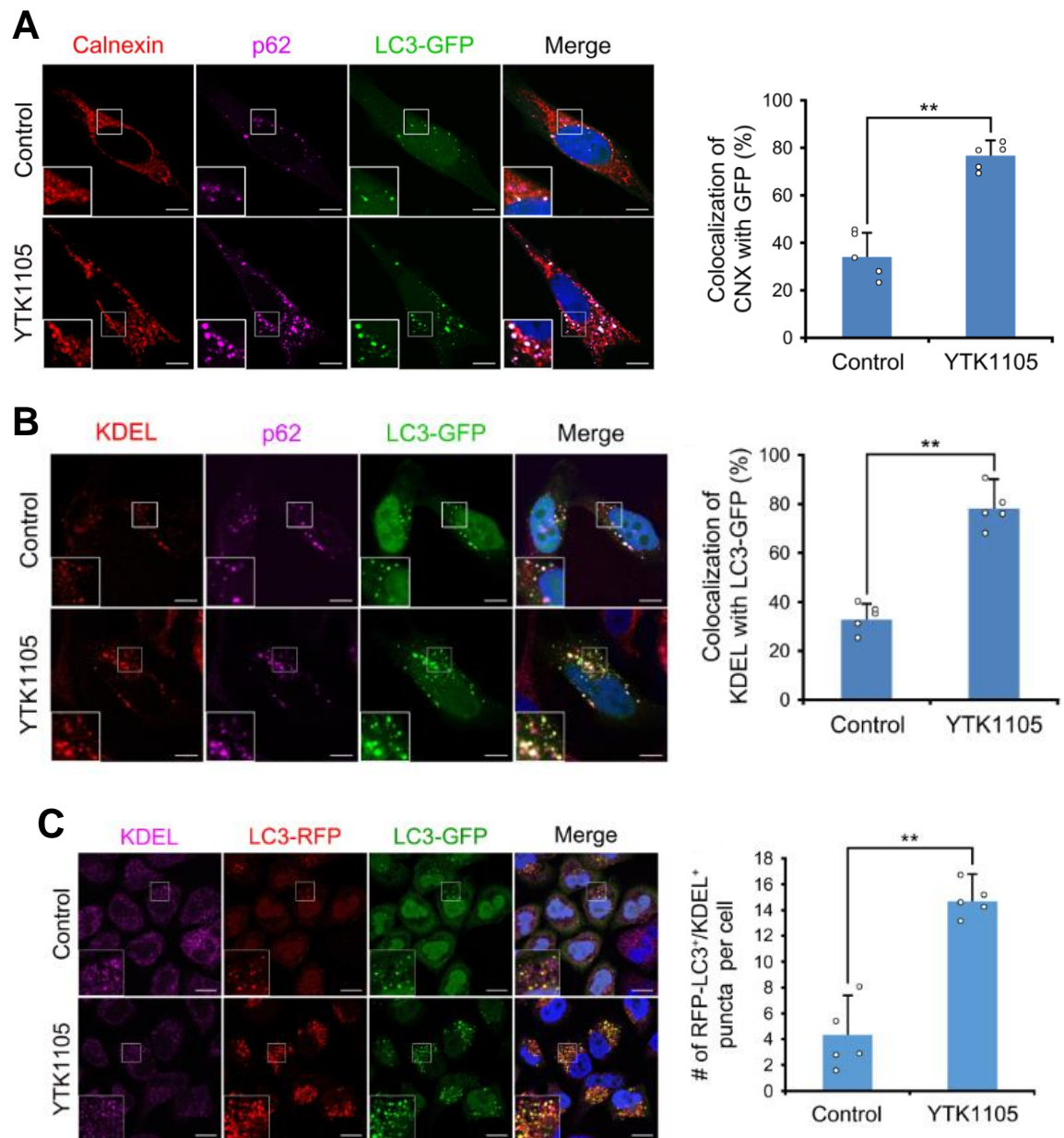


Fig. 43. p62-ZZ ligands promote autophagosomal and lysosomal delivery of ER-derived vesicles. (A,B) ICC of calnexin or KDEL with p62 and LC3-GFP puncta structures in HeLa cells transfected with LC3-GFP and treated with YTK1105 (2.5 μ M, 9 h). Scale bar, 10 μ m. Quantification: n=50 cells. **(C)** ICC of KDEL in HeLa cells stably expressing RFP-GFP-LC3 and treated with YTK1105 (2.5 μ M, 5 h). Scale bar, 10 μ m. Quantification: n=50 cells.

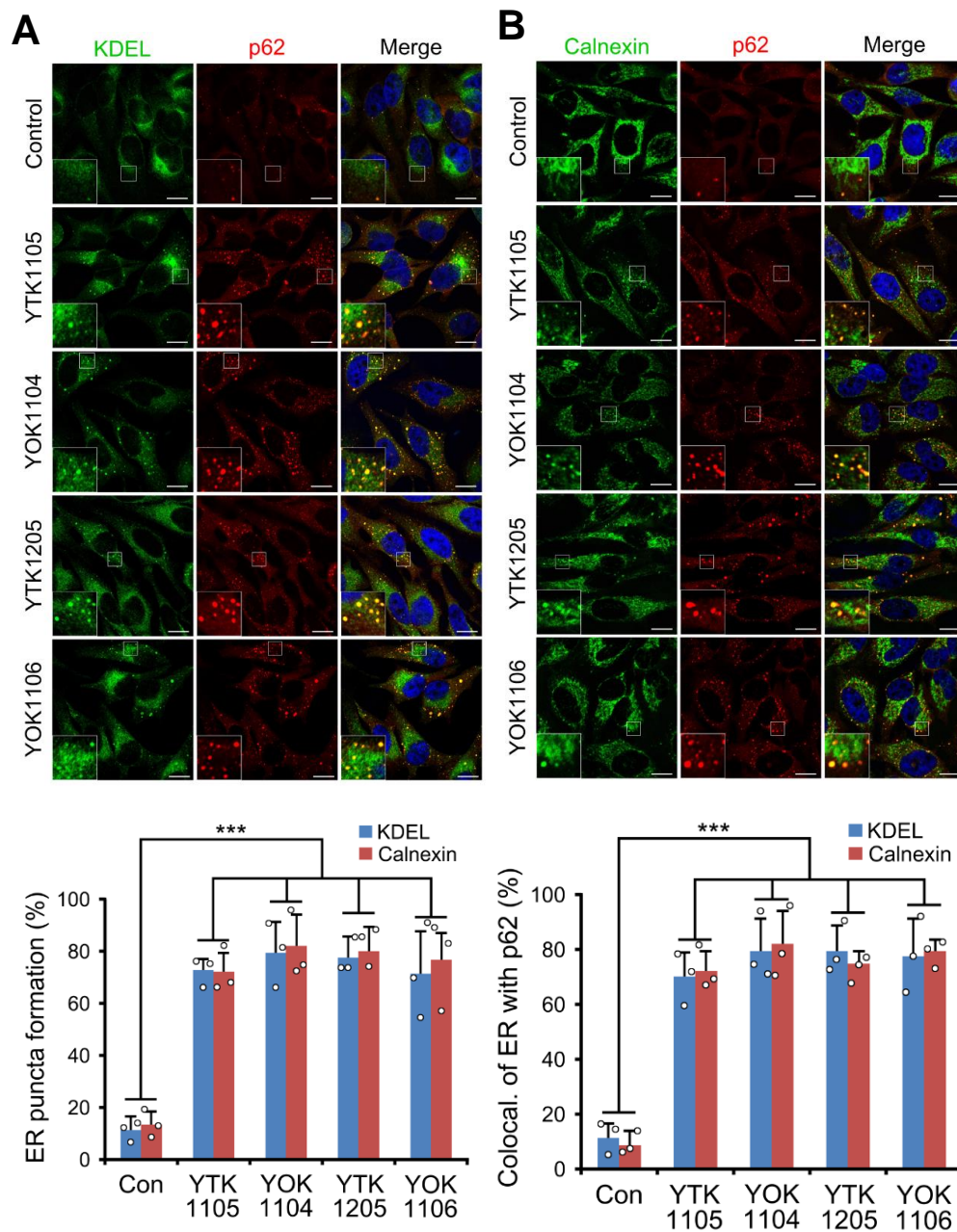


Fig. 44. Synthetic activation of the p62-ZZ domain recruits p62 to ER-derived vesicles. (A, B) ICC of p62 with KDEL or calnexin in HeLa cells treated with YTK1105 (2.5 μ M, 5 h), YOK1104 (2.5 μ M, 5 h), YTK2205 (2.5 μ M, 5 h), or YOK1106 (2.5 μ M, 5 h). Scale bar, 10 μ m. Quantification: n=50 cells.

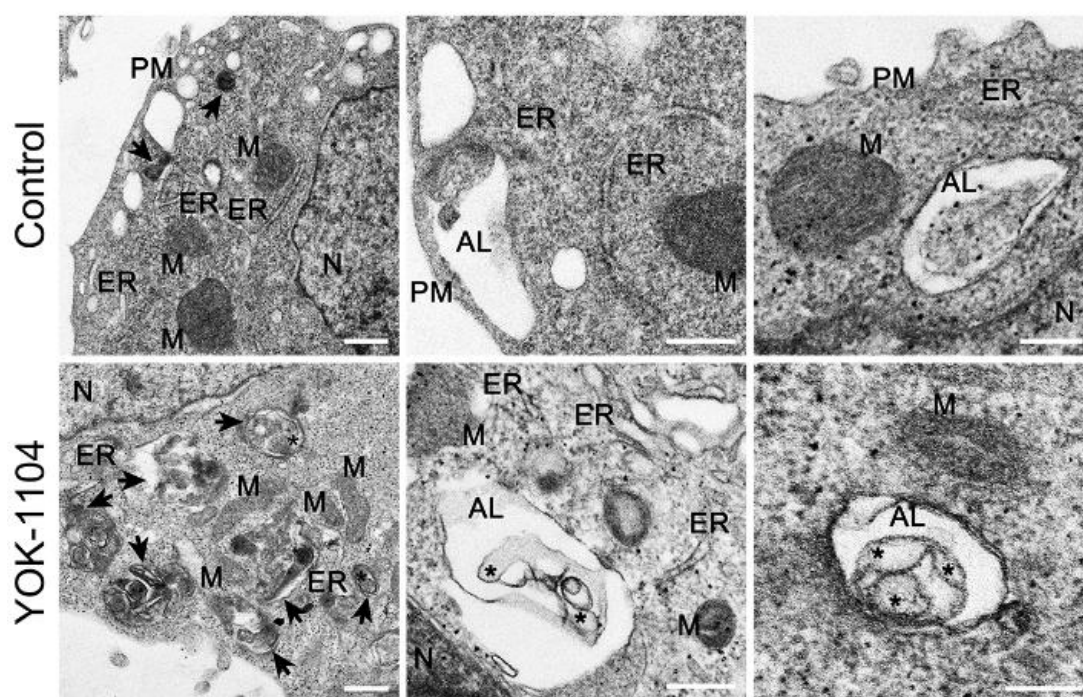


Fig. 45. Synthetic mimicry of Nt-Arg deliver entire ER fragments to the lysosome. TEM of HEK293T cells treated with YOK1104 (2.5 μ M, 6 h) or control DMSO. Autolysosomes are indicated by arrows and asterisks label ER fragments inside autolysosomes. Scale bars, 500 nm (1st & 2nd column), 200 nm (3rd column).

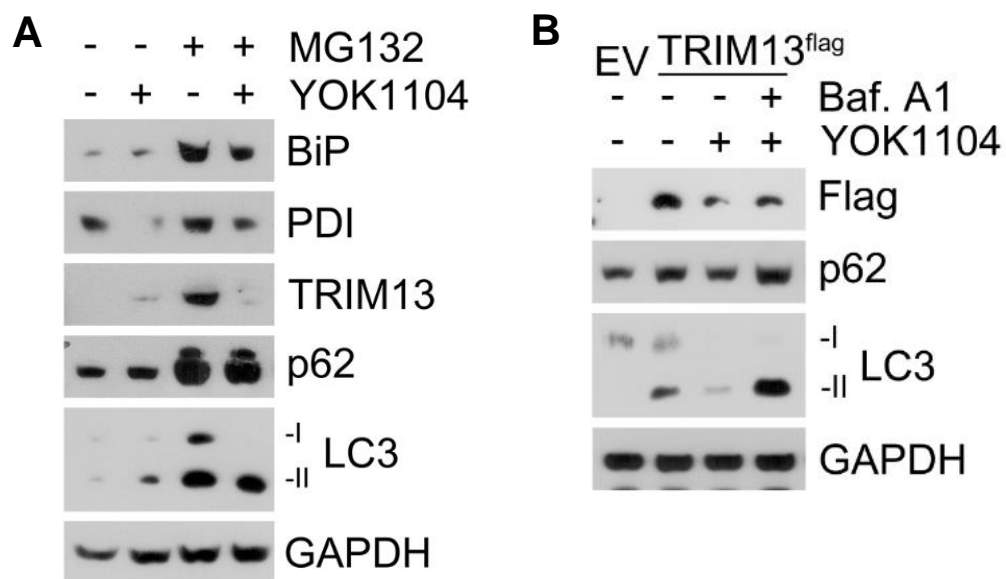


Fig. 46. p62-ZZ ligands induce autophagic degradation of ER-resident proteins. (A) WB of HeLa cells treated with MG132 (2 μ M, 24 h), YOK1104 (2.5 μ M, 4 h), or both. (B) WB of HeLa cells transfected with TRIM13-flag or negative control empty vector (EV) and treated with YOK1104 (2.5 μ M, 4 h) with or without bafilomycin A1 (200 nM, 6 h).

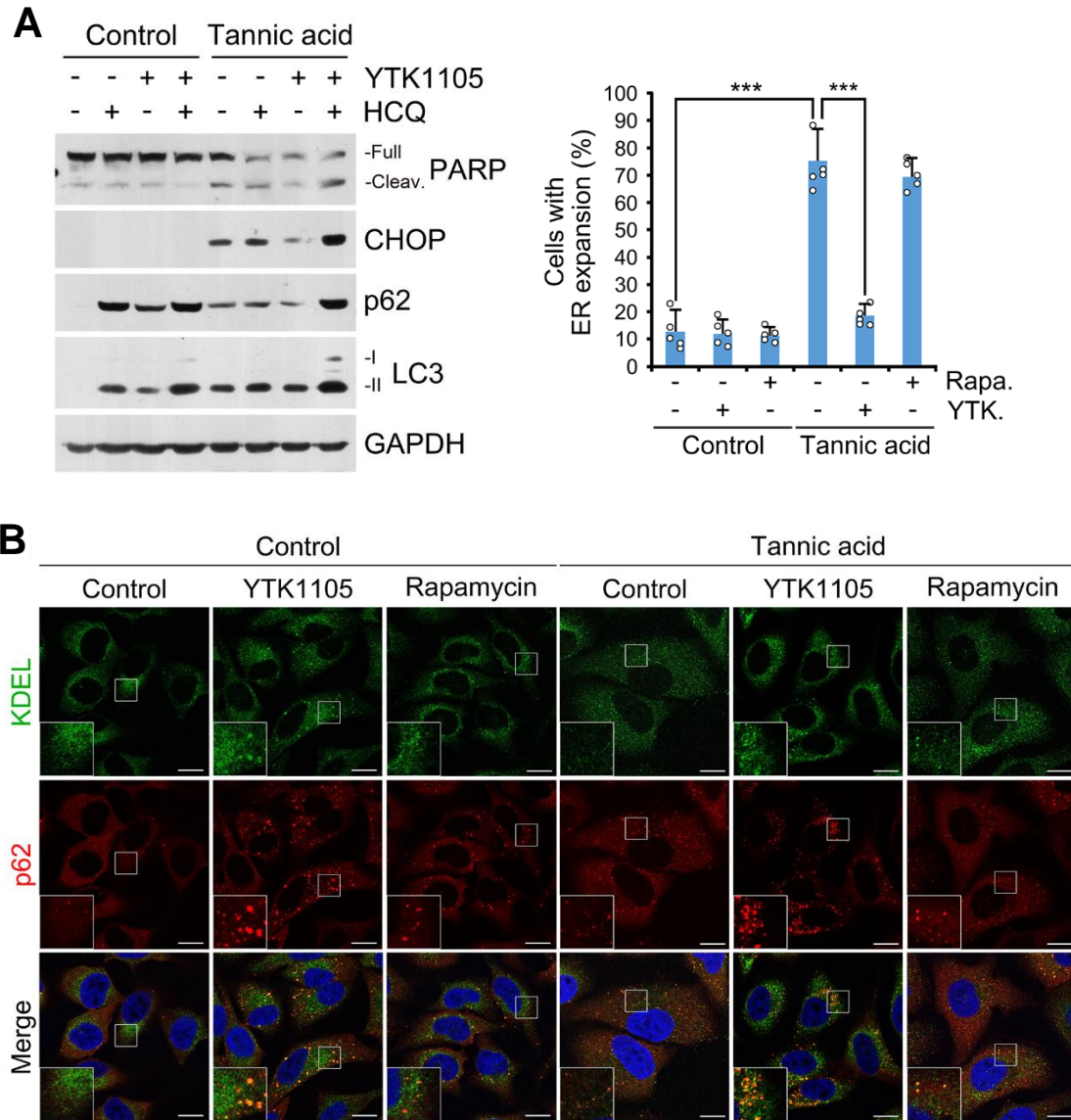


Fig. 47. Nt-Arg-mimicry directly rescues ER stress, morphological aberrations and apoptosis caused by Nt-arginylation deficiency. (A) WB of HeLa cells after treatment with HCQ (10 μ M, 24 h), YTK1105 (5 μ M, 9 h), or both in the presence or absence of tannic acid (30 μ M, 24 h). **(B)** ICC of KDEL signals in HeLa cells after treatment with YTK1105 (2.5 μ M, 5 h) or rapamycin (2 μ M, 18 h), all with or without tannic acid (30 μ M, 24 h). Scale bar, 10 μ m. Quantification: n=50 cells.

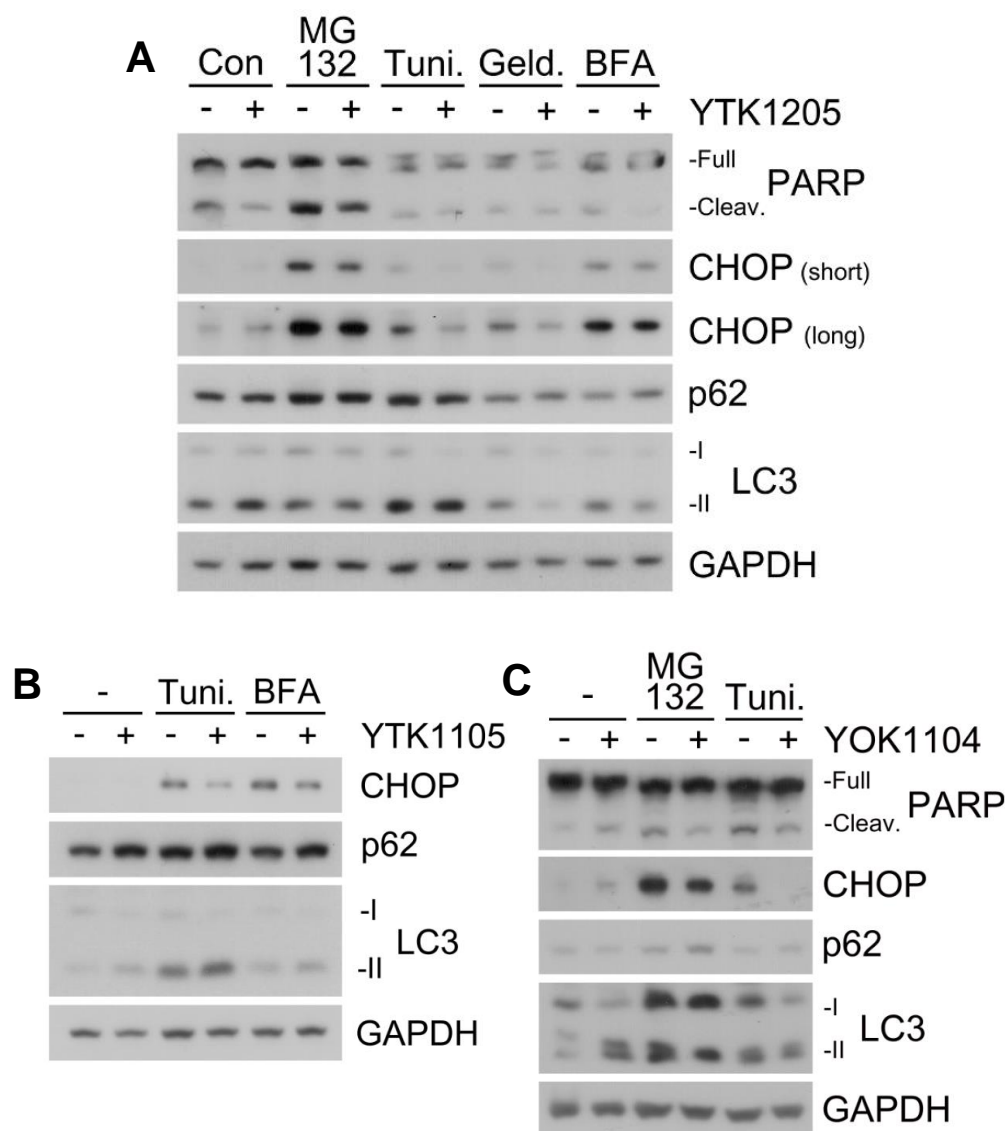


Fig. 48. Chemical activation of Nt-arginylation generally inhibits ER stress-induced apoptosis. (A) WB of HEK293T cells after treatment with MG132 (0.5 μ M, 18 h), tunicamycin (0.25 μ g/mL, 18 h), geldanamycin (500 nM, 18 h) or brefeldin A (0.3 μ M, 18 h) with or without YTK1205 (2.5 μ M, 24 h). (B) WB of HEK293T cells treated with tunicamycin (0.25 μ g/mL, 24 h) or brefeldin A (0.3 μ M, 24 h) in the presence or absence of YTK1105 (5 μ M, 24 h). (C) Identical to BN but with MG132 (1 μ M, 24 h) or tunicamycin (0.25 μ g/mL, 24 h) used in the presence or absence of YOK1104 (5 μ M, 24 h).

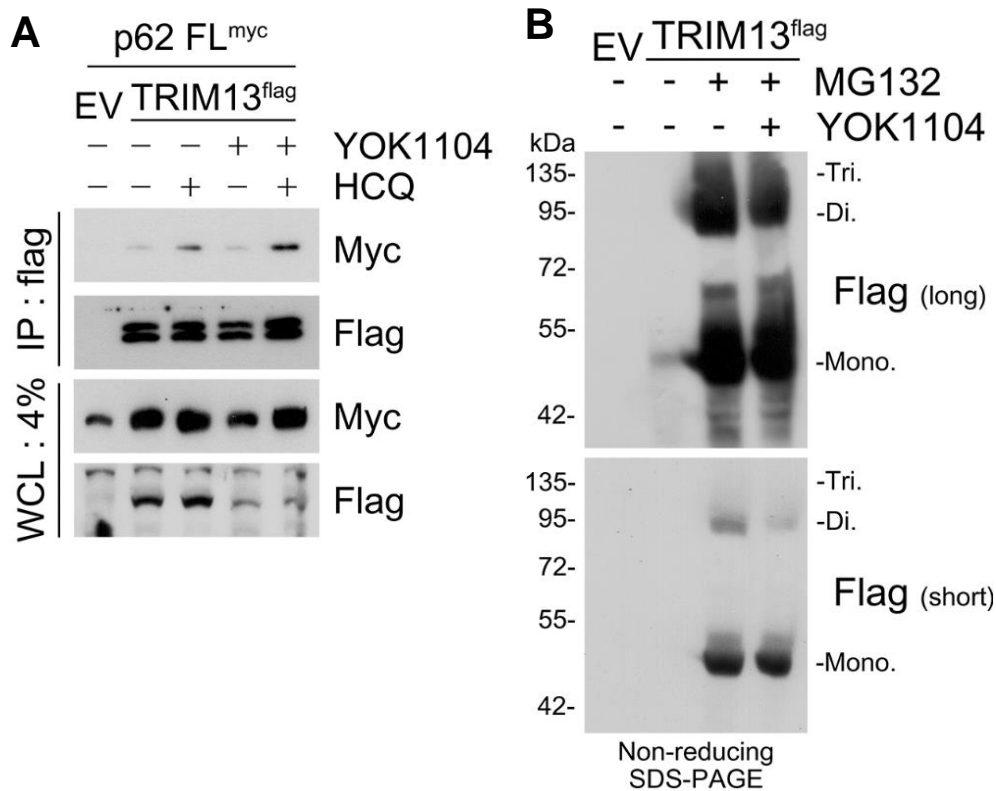


Fig. 49. Nt-Arg-mimicry facilitates autophagic proteolysis of the p62-TRIM13 complex. (A) Co-IP assay in HEK293T cells co-transfected (24 h) with p62-myc and TRIM13-flag or negative control empty vector (EV) and treated with HCQ (10 μ M, 24 h), YOK1104 (2.5 μ M, 4 h), or both. (B) *In vivo* oligomerization assay of TRIM13-flag in HEK293T cells treated with MG132 (2 μ M, 24 h) with or without YOK1104 (2.5 μ M, 4 h).

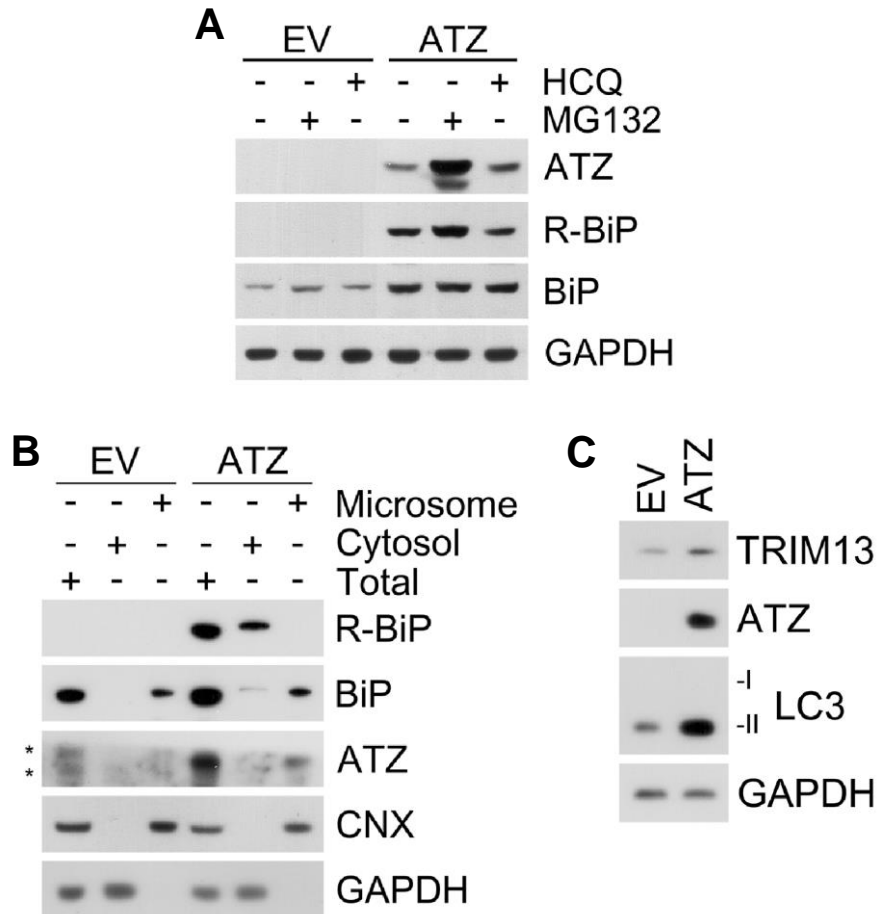


Fig. 50. The aggregation-prone misfolded ER protein species ATZ directly up-regulates cytosolic Nt-Arg and TRIM13 levels. (A) WB of HeLa cells transfected with ATZ or empty vector (EV) and treated with MG132 (2 μ M, 18 h) or HCQ (10 μ M, 24 h). **(B)** Subcellular fractionation of HeLa cells transfected with ATZ. **(C)** WB of HeLa cells ectopically expressing ATZ or empty vector.

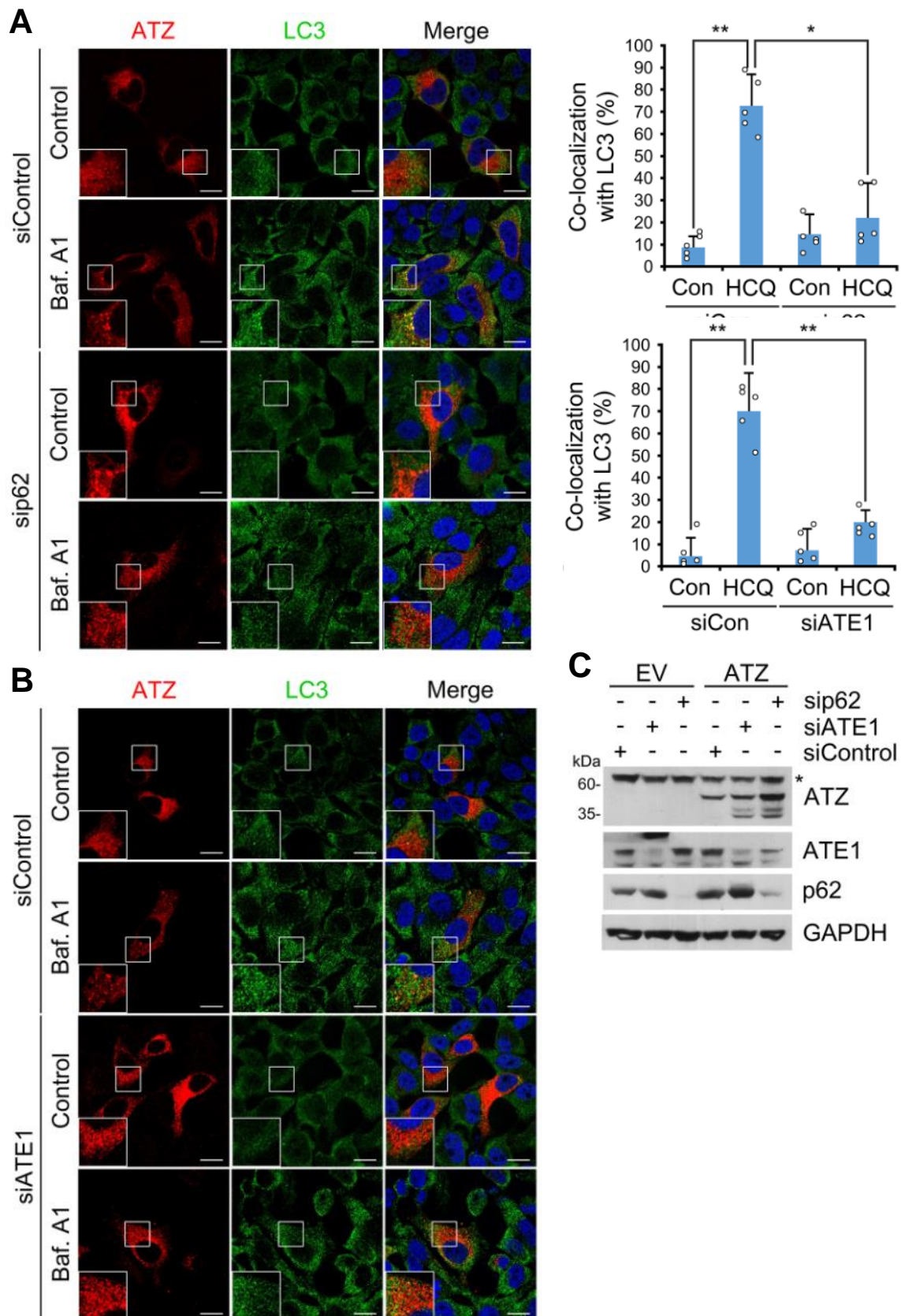


Fig. 51. The p62-Nt-Arg pathway targets aggregation-prone ATZ for autophagy. (A,B) ICC of ATZ and LC3 in HeLa cells transfected with ATZ and treated with Baf. A1 (200nM, for 7 h) under *p62* or *ATE1* interference compared to control (48 h). Scale bar, 10 μ m. Quantification: n=50 cells. (C) WB of HeLa cells transfected with ATZ or control under siRNA-mediated knockdown of *p62* or *ATE1* (48 h).

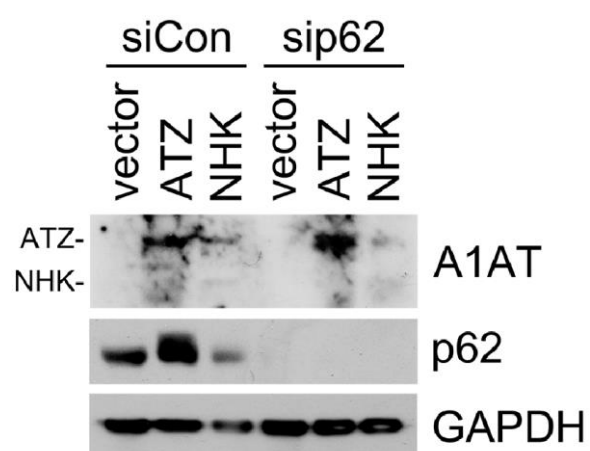


Fig. 52. Arg/N-degron-mediated ER-phagy is selective for ATZ. WB of ATZ and NHK under siRNA-mediated knockdown (48 h) of control and *p62* in HeLa cells.

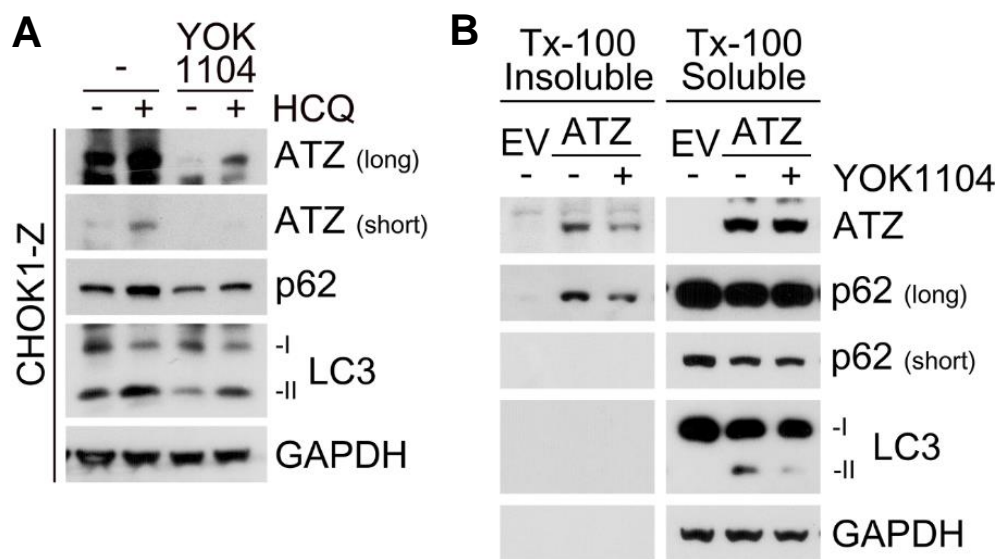


Fig. 53. p62-ZZ ligands promote autophagic degradation of aggregation-prone ATZ. (A) CHOK1-Z cells stably expressing ATZ were treated with HCQ (10 μ M, 24 h), YOK1104 (2.5 μ M, 5 h), or both for WB. (B) Triton X-100 insoluble/soluble fractionation assay in HEK293T cells transfected with ATZ and treated with YOK1104 (2.5 μ M, 3 h) for immunoblotting analysis.

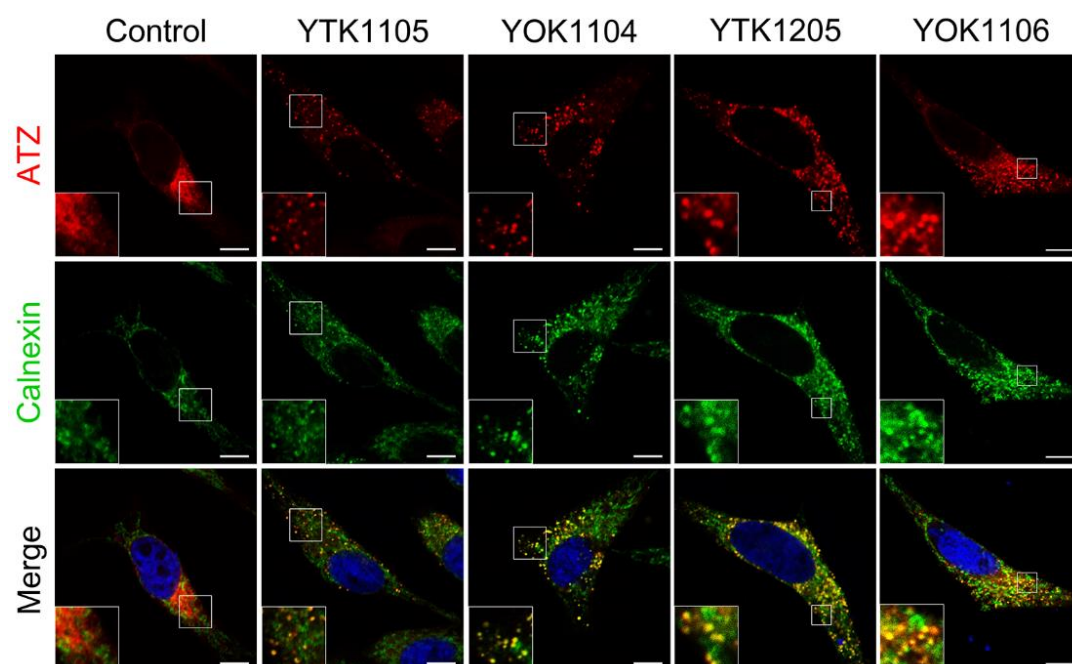


Fig. 54. Synthetic mimicry of Nt-Arg targets ATZ via ER-phagy Co-localization assay of ATZ and calnexin in ATZ-transfected HeLa cells treated with p62-ZZ ligands (5 μ M, 9 h). Scale bar, 10 μ m.

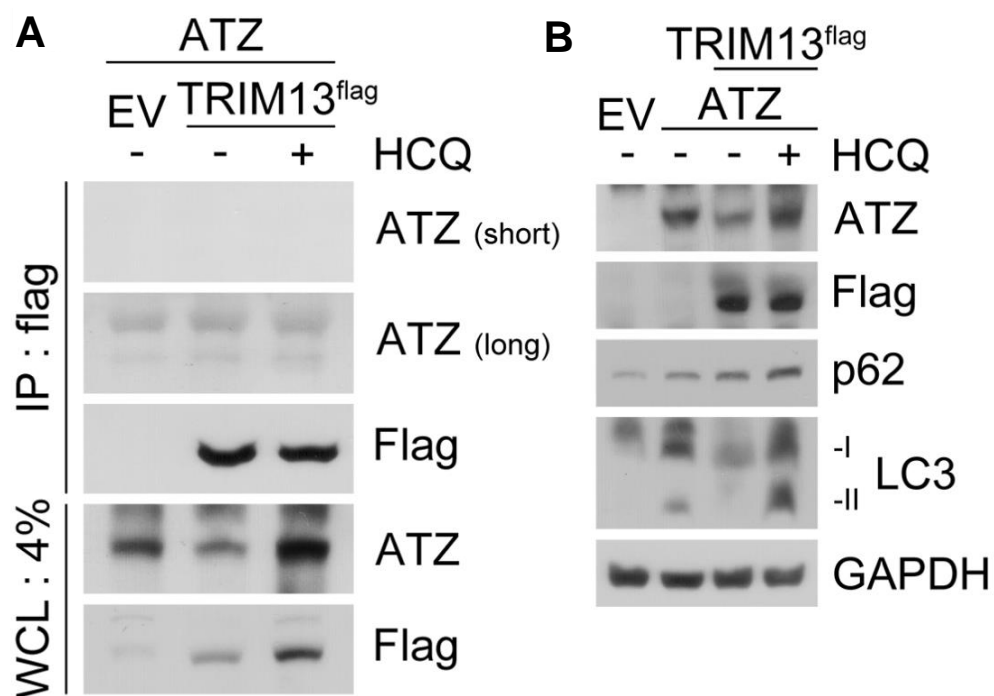


Fig. 55. TRIM13 mediates autophagic degradation of ATZ. (A) Co-IP assay in HEK293T cells co-transfected (24 h) with TRIM13-flag and ATZ, followed by treatment with HCQ (10 μ M, 24 h). (B) WB in HeLa cells co-transfected (24 h) with ATZ and TRIM13-flag, subsequently treated with or without HCQ (10 μ M, 24 h).

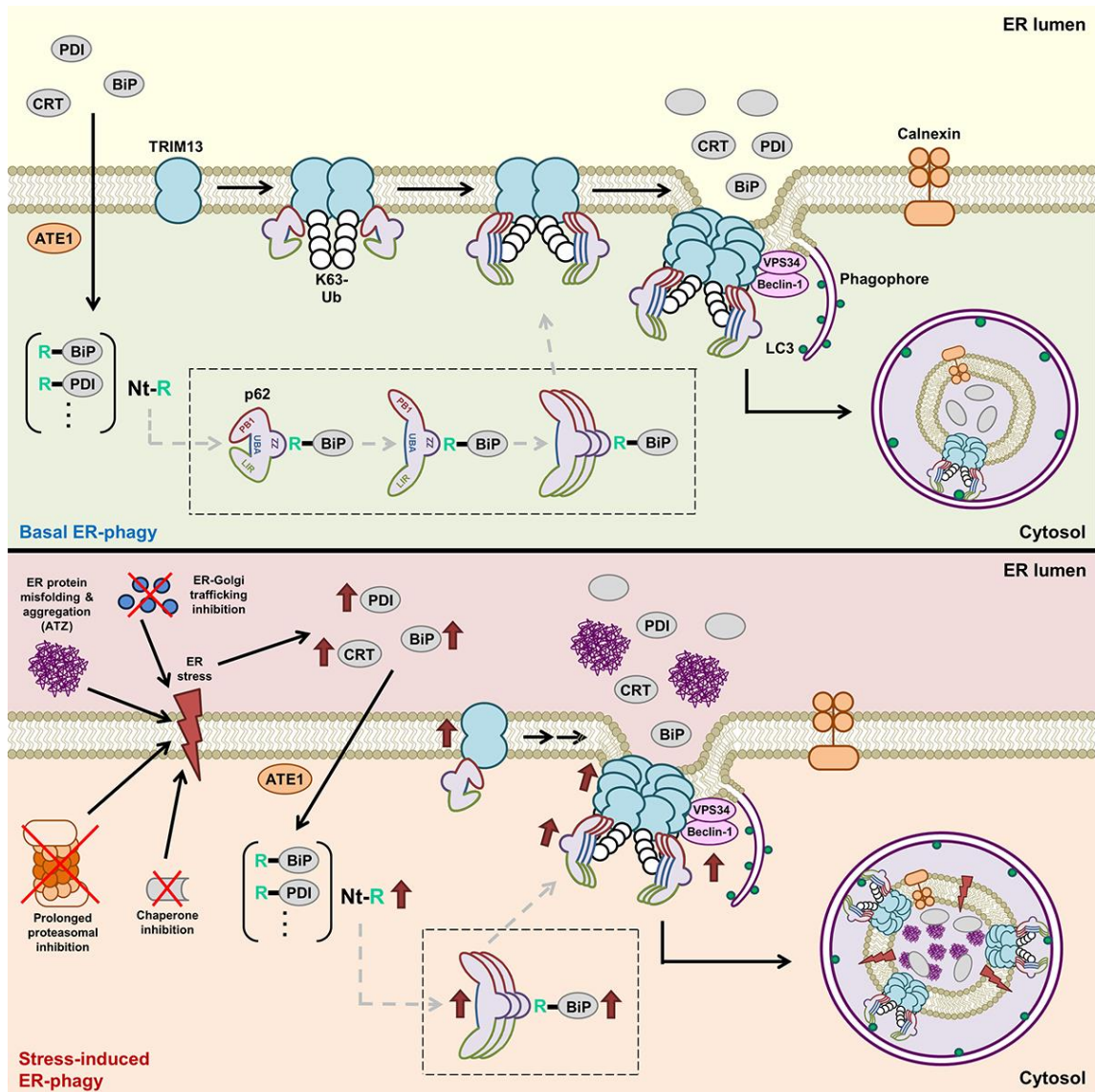


Fig. 58. Graphical abstract of Arg/N-degron-mediated ER-phagy

MATERIALS & METHODS

Cell culture

HeLa, HEK293, HEK293T, +/+, *ATE1*^{-/-}, *p62*^{-/-} and *ATG5*^{-/-} mouse embryonic fibroblast (MEF), RFP-GFP-LC3 stable HeLa and ATZ-expressing stable CHOK1-Z cell lines were cultured in Dulbecco's Modified Eagle's Medium (DMEM; Gibco) supplemented with 10% Fetal Bovine Serum (FBS; Gibco) and antibiotics (100 units/mL penicillin and 100 µg/mL streptomycin) in a 5% CO₂ incubator. For knockout MEFs and stable cell lines, absence or presence of intended target protein(s) was confirmed by immunoblotting and/or immunocytochemistry.

Cloning and site-directed mutagenesis

The recombinant p62 plasmids were constructed as previously described (32). Briefly, PCR amplification of a full-length human *p62* cDNA fragment from the hMU012675 clone (21C Frontier Human Gene Bank) was followed by subcloning into the pcDNA3.1/*myc*-His plasmid (Thermo Fisher Scientific) at *EcoRI*/*XhoI* sites. The ΔPB1 and ΔUBA domain p62 mutants were generated in an identical manner. Site-directed mutagenesis was performed using the QuickChange II XL Site-Directed Mutagenesis Kit according to the manufacturer's instructions (Agilent) to produce amino acid substitutions (Cys to Ala) in the zinc finger motifs of the p62-ZZ domain. Alternatively, full-length p62-GFP and the ΔZZ domain mutant p62-GFP plasmids were subcloned as described above but into the pEGFP-N1 plasmid (Clontech) at *EcoRI*/*XhoI* sites. The plasmids encoding ATE1 R-transferase isoforms were constructed as previously described (29). To construct Ub-X-BiP-flag, corresponding cDNA fragments from Ub-X-BiP-GFP plasmid (71) were subcloned into pcDNA3.1 at *HindIII*/*BamHI* site using PCR amplification. For recombinant full-length human TRIM13-flag plasmid, HEK293T cells were subjected to total RNA isolation using TRIzol (Thermo Fisher

Scientific) followed by reverse transcriptase PCR to obtain full-length human *TRIM13* cDNA. This cDNA was then subcloned into the pcDNA3.1-3xflag plasmid (Thermo Fisher Scientific) at *EcoRI/XhoI* sites. Site-directed mutagenesis was performed to produce amino acid substitution (Cys to Ala) at the 13th residue of TRIM13.

Transfection

Plasmids were transfected into HeLa, HEK293 and HEK293T cells using the Lipofectamine 2000 Transfection Reagent according to the manufacturer's instructions (Invitrogen). Alternatively, for transfection into MEFs, Lipofectamine 3000 with Plus Reagent was used. siRNAs were transfected into HeLa, HEK293 and HEK293T cells using the Lipofectamine RNAiMAX Transfection Reagent (Invitrogen). For co-transfection of plasmids and siRNAs, Lipofectamine 2000 was used.

Generating antibodies to the arginylated species of E¹⁹-BiP, E¹⁸-CRT and D¹⁸-PDI

Rabbit polyclonal antibodies to the arginylated forms of E¹⁹-BiP, E¹⁸-CRT and D¹⁸-PDI were generated using the respective peptide sequences REEEDKKEDVGC, REPAVYFKEQ, and RDAPEEEDHVL, as previously described (71). Briefly, rabbits via a custom service at AbFrontier, Inc. (South Korea) were immunized with the above peptides and boosted with incomplete Freund's adjuvant at 3-week intervals. Rabbit antisera was then purified using immobilized protein A specific to IgG, after which two-step affinity chromatography of negative and then of positive purification was applied. Antibody specificity was confirmed via immunoblotting.

Western blotting (WB)

Cell pellets were washed with phosphate-buffered saline (PBS) and lysed in SDS-based sample buffer (277.8 mM Tris-HCl, pH 6.8, 4.4% LDS, 44.4% (v/v) glycerol) with

beta-mercaptoethanol. Alternatively, cell pellets or protein supernatants were lysed in 5X Laemmli sample buffer. Using SDS-PAGE, whole cell lysates were separated and transferred onto polyvinylidene difluoride membranes at 100 V for 2 h at 4°C. Subsequently, the membrane was blocked with 4% skim milk in PBS solution for 30 min at room temperature and incubated overnight with primary antibodies, followed by incubation with host-specific HRP-conjugated secondary antibodies (1:10000 dilution). For signal detection, a mixture of ECL solution (Thermo Fisher Scientific) was applied onto the membrane and captured using X-ray films.

***In vitro* peptide pulldown assay**

A set of synthetic 12-mer peptides corresponding to the N-terminal sequences of the ER chaperones BiP, CRT and ERdj5 following their signal peptide cleavage, was C-terminally biotin-conjugated by Dr. Jeong Kyu Bang at Korea Research Institute of Bioscience and Biotechnology. (South Korea). The X¹⁹-BiP peptide (X-EEDKKEDVGTK-biotin) has Arg-Glu¹⁹ (permanently arginylated), Glu¹⁹ (native), or Val¹⁹ (Asp-to-Val mutant) at the N terminus. The X¹⁹-CRT peptide (X-PAVYFKEQFLK-biotin) has Arg-Glu¹⁹ (permanently arginylated), Glu¹⁹ (native), or Val¹⁹ (Asp-to-Val mutant) at the N terminus. The X⁹⁴-ERdj5 peptide (X-QDFYSLLGYSK-biotin) has Arg-Asp⁹⁴ (permanently arginylated), Asp⁹⁴ (native), or Val⁹⁴ (Asp-to-Val mutant) at the N terminus. To cross-link the above peptides with resin beads, C-terminally biotin-conjugated peptides were mixed with high-capacity streptavidin agarose resin (Thermo Fisher Scientific) at a ratio of 0.5 mg of peptide per 1 mL of settled resin and incubated on a rotator at 4°C overnight. After washing five times with PBS, the peptide-bead conjugates were diluted with PBS at a 1:1 ratio. To prepare protein extracts, cells were collected by centrifugation and lysed by freezing and thawing at least 10 times in hypotonic buffer [10 mM KCl, 1.5 mM MgCl₂, and 10

mM Hepes (pH 7.9)] with a protease inhibitor mix (Sigma). After centrifugation at $14,300 \times g$ at 4°C for 15 min, proteins were quantified using a BCA protein assay kit (Thermo Fisher Scientific). Total protein (200 μg) diluted in 300 μL of binding buffer [0.05% Tween-20, 10% glycerol, 0.2 M KCl, and 20 mM Hepes (pH 7.9)] were mixed with 50 μL of peptide-bead resin and incubated at 4°C for 2 h on a rotator. The protein-bound beads were collected by centrifugation at $2,400 \times g$ for 3 min and washed five times with binding buffer. The beads were resuspended in 25 μL of SDS sample buffer, heated at 95°C for 5 min, and subjected to SDS/PAGE and immunoblotting.

Chemical synthesis and analytical data of Nt-Arg-mimicking compounds

Ligands to the p62-ZZ domain – YTK1105, YOK1104, YTK1205, YOK2204 and YOK1106, as well as the negative control ligands 1101 and YOK-Gly-1104 – were synthesized as follows.

*1.1 Synthesis of 3,4-bis(benzyloxy)benzaldehyde **1101**:* to the stirred solution of 3,4-dihydroxybenzaldehyde **1** (1.00 g, 7.25 mmol) in dry DMF (10 mL) was added anhydrous K_2CO_3 (5.00 g, 36.23 mmol) added, followed by benzyl bromide (2.1 mL, 18.11 mmol). The mixture was stirred at room temperature for 2 h. Additional K_2CO_3 (2.4 g, 17.3 mmol) was added, and the mixture was heated to 70°C for 30 min and then cooled to room temperature. The mixture was partitioned between H_2O and ether (120 mL each). The organic layer was separated, and the water layer was extracted with ether (3×50 mL). The pooled organic layers were washed with H_2O (2×50 mL) and saturated aqueous NaCl (50 mL). The combined organic layers were dried over anhydrous NaSO_4 and the solvent was evaporated in *vacuo*. The resulting residue was purified by silica gel column chromatography using (7:3 hexane/ethyl acetate) to yield 3,4-bis(benzyloxy)benzaldehyde **1101** (2.19 g, 95%) as Cream-colored solid. ^1H NMR (CDCl_3) δ 9.81 (s, 1 H), 7.54-7.30 (m, 12 H), 7.04 (1H, d, $J = 9.0$ Hz), 5.27 (s, 2 H),

5.23 (s, 2 H); ESIMS m/z : 319.3[M+H]⁺.

1.2 Synthesis of 2-((3,4-bis(benzyloxy)benzyl)amino)ethan-1-ol hydrochloride YTK-1105: 3,4-bis(benzyloxy)benzaldehyde **1101** (3.18 g, 10 mmol) was dissolved in dry ethanol (20 mL), and ethanolamine (0.61 g, 10 mmol) was added. The reaction mixture was stirred for 12 h at 60°C. The reaction solution was cooled to room temperature. NaBH₄ (0.57 g, 15 mmol) was added slowly in portions, and the resulting solution was stirred for another 12 h. The solvent was evaporated in vacuum, and the residue was dissolved in water and extracted with ethyl acetate. The organic layers were combined and dried with anhydrous Na₂SO₄, filtered, and evaporated *in vacuo*. The residue was purified by flash column to generate the desired product 2-((3,4-bis(benzyloxy)benzyl)amino)ethan-1-ol (2.0 g, 56%). ¹H NMR (400 MHz, CDCl₃): δ 7.52–7.33 (m, 10H), 7.01–6.84 (m, 3H), 5.20 (s, 2H), 5.17 (s, 2H), 3.71 (s, 2H), 3.64 (t, J = 4.8, 2H), 2.93 (s, 2H), 2.72 (t, J = 4.8, 2H). 2-((3,4-bis(benzyloxy)benzyl)amino)ethan-1-ol (1.0 g, 2.75 mmol) was dissolved in absolute methanol (25 mL), and pumped HCl gas for 1 h. The mixture was stirred for another 2 h, evaporated to about 1 mL and added hexane to get the solid, which was filtered and dried to give the final compound 2-(3,4-bis(benzyloxy)benzyl)amino)ethan-1-ol hydrochloride **YTK-1105** (720 mg, 65%). ¹H NMR (400 MHz, DMSO-d₆): δ 8.83 (bs, 2H), 7.52–7.46 (m, 5H), 7.31–7.32 (m, 1H), 7.26–7.20 (m, 5H), 7.12–7.10 (m, 1H), 7.05–7.03 (m, 1H), 5.24–5.22 (m, 1H), 5.14 (s, 2H), 5.11 (s, 2H), 4.07 (s, 2H), 3.67–3.63 (m, 2H), 2.90 (s, 2H). ¹³C NMR (400 MHz, CDCl₃): δ 149.0, 148.2, 137.4, 133.3, 128.5, 127.8, 127.5, 127.4, 121.3, 115.4, 115.2, 71.5, 71.3, 60.8, 53.2, 50.7. LC–MS (ESI): m/z 364.3 [M+H]⁺.

1.3. Synthesis of 3,4-bis(benzyloxy)phenol 2: m-Chloroperbenzoic acid (0.78 g, 4.5 mmol) was added to a stirred solution of the 3,4-bis(benzyloxy)benzaldehyde **1101** (1 g, 3.0 mmol) in dichloromethane (15 mL), and the mixture was stirred at room

temperature for 4 h and then diluted with ethyl acetate. The organic solution was successively washed with saturated aqueous Na₂CO₃ solution and brine. The solvent was evaporated in *vacuo* to give corresponding formiate. NaOH (6 *N*) was added to a stirred solution of crude formiate in MeOH (15 mL). After stirring at room temperature for 30 min, was added 10% aq HCl solution. The reaction mixture was diluted with ethyl acetate (50 mL), washed with brine and dried over anhydrous Na₂SO₄. The flash chromatography (7:3 hexane/ethyl acetate) furnished the 3,4-bis(benzyloxy)phenol **2** (0.83 g, 86% (for 2 steps)) as solid. ¹H-NMR (CDCl₃, 300 MHz): δ 7.25–7.42 (m, 10H), 6.80 (d, 1H, *J* = 9.0 Hz), 6.48 (d, 1H, *J* = 3.0 Hz), 6.29 (dd, 1H, *J* = 3.0 and 9.0 Hz), 5.08 (d, 4H, *J* = 15 Hz), 4.55 (s, 1H); ESIMS *m/z*: 307.25 [M+H]⁺.

1.4 Synthesis of 2-((3,4-bis(benzyloxy)phenoxy)methyl)oxirane 3: to a mixture of 3,4-dibenzyloxy phenol **2** (100 mg, 0.33 mmol) in ethyl alcohol (5 mL), aqueous potassium hydroxide (22 mg, 0.40 mmol, 1 mL water) and (*R*)-epichlorohydrin (41 μ L, 0.50 mmol) were added. The resulting mixture was stirred for 15 h at room temperature. The solvent was removed under reduced pressure, and the residue dissolved in water and extracted with ethyl acetate. The organic extract was washed with brine and dried over Na₂SO₄. The solvent was evaporated to afford the crude product, which was purified by column chromatography using (7:3 hexane/ethyl acetate) yielded 2-((3,4-bis(benzyloxy)phenoxy)methyl)oxirane **3** (83 mg, 70%) as white solid.

1.5. Synthesis of (R)-1-(3,4-bis(benzyloxy)phenoxy)-3-(isopropylamino)propan-2-ol YOK-1104: to the solution of 2-((3,4-bis(benzyloxy)phenoxy)methyl)oxirane **3** (15 mg, 0.004 mmol) in MeOH (2 mL) was added isopropyl amine (0.21 mL, 2.6 mmol), and the mixture was vigorously stirred at room temperature for 4 h (TLC-monitoring). Then, the solvent was removed under reduced pressure. The resulting residue was extracted with CH₂Cl₂ (3 \times 10 mL). The combined organic layers were washed with brine (10 mL), dried over anhydrous Na₂SO₄ and concentrated under reduced pressure.

The obtained crude product was purified by column chromatography (CH₂Cl₂/MeOH, 10:1) to give pure (R)-1-(3,4-bis(benzyloxy)phenoxy)-3-(isopropylamino)propan-2-ol **YOK-1104** (72 mg, 86%) as a white powder and confirmed with ESIMS m/z: 423.5 [M+H]⁺.

1.6. *Synthesis of (R)-1-(3,4-bis(benzyloxy)phenoxy)-3-((2-hydroxyethyl)amino)propan-2-ol YOK-R-1106:* to the stirred solution of epoxide **3** (40 mg, 0.11 mmol) in EtOH (2 mL) was added isopropyl amine (18 μ L, 0.22 mmol), and the mixture was vigorously stirred at room temperature for 4 h (TLC-monitoring). Then, the solvent was removed under reduced pressure. The resulting residue was extracted with CH₂Cl₂ (3 \times 10 mL). The combined organic layers were washed with brine (10 mL), dried over anhydrous Na₂SO₄ and concentrated under reduced pressure. The obtained crude product was purified by column chromatography (CH₂Cl₂/MeOH, 10:1) to give pure (R)-1-(3,4-bis(benzyloxy)phenoxy)-3-((2-hydroxyethyl)amino)propan-2-ol **YOK-R-1106** (41 mg, 86%) as a white powder and confirmed with ESIMS m/z: 424.3 [M+H]⁺.

2.1. *Synthesis of 3,4-diphenethoxybenzaldehyde 4:* to the stirred solution of 3,4-dihydroxybenzaldehyde **1** (1.0 g, 7.25 mmol) in dry DMF was added (2-bromoethyl) benzene (2.48 mL, 18.1 mmol), followed by anhydrous K₂CO₃ (5.0 g, 36.2 mmol). The mixture was stirred at room temperature for 2 h. Additional K₂CO₃ (2.4 g, 17.3 mmol) was added, and the mixture was heated to 70°C for 30 min and then cooled to room temperature. The mixture was partitioned between H₂O and ether (120 mL each). The organic layer was separated, and the water layer was extracted with ether (3 \times 50 mL). The pooled organic layers were washed with H₂O (2 \times 50 mL) and saturated aqueous NaCl (50 mL). The pale, straw-colored extracts were dried over anhydrous sodium sulfate and concentrated after washing with hexanes (75 mL). The resulting residue was purified by silica gel column chromatography using (7:3 hexane/ethyl acetate) to yield

3,4-diphenethoxybenzaldehyde **4** (2.30 g, 92%) as Cream-colored solid. $^1\text{H-NMR}$ (CDCl_3 , 300 MHz): δ 9.84 (s, 1H), 7.43 (dd, 1H, $J = 3.0, 9.0$ Hz), 7.42 (s, 1H), 7.35 (d, 8H, $J = 6.0$ Hz), 7.31-7.24 (m, 2H), 6.96 (d, 1H, $J = 9.0$ Hz), 5.62 (s, 1H), 4.36 (td, 4H, $J = 3.0$ and 6.0 Hz), 3.17 (td, 4H, $J = 3.0$ and 6.0 Hz); ESIMS m/z : 347.3 $[\text{M}+\text{H}]^+$.

2.2. *Synthesis of 3,4-diphenethoxyphenol 5*: m-Chloroperbenzoic acid (0.40 g, 2.35 mmol) was added to a solution of the 3,4-diphenethoxybenzaldehyde **4** (0.5 g, 1.57 mmol) in dichloromethane (10 mL), and the mixture was stirred at room temperature for 4 h and then diluted with ethyl acetate. The organic solution was successively washed with saturated aqueous Na_2CO_3 solution and brine. The solvent was evaporated in *vacuo* to give corresponding formiate.

NaOH (6 N) was added to a stirred solution of crude formiate in MeOH (10 mL). After stirring at room temperature for 30 min, was added 10% aq HCl solution. The reaction mixture was diluted with ethyl acetate (50 mL), washed with brine and dried over anhydrous Na_2SO_4 . The flash chromatography (7:3 hexane/ethyl acetate) furnished the 3,4-diphenethoxyphenol **5** (0.40 g, 93%) as white solid. $^1\text{H-NMR}$ (CDCl_3 , 300 MHz): δ 7.22–7.35 (m, 10H), 6.76 (d, 1H, $J = 9.0$ Hz), 6.44 (d, 1H, $J = 3.0$ Hz), 6.30 (dd, 1H, $J = 3.0$ and 6.0 Hz), 4.74 (s, 1H), 4.13 (td, 4H, $J = 3.0$ and 9.0 Hz), 3.10 (td, 4H, $J = 3.0$ and 9.0 Hz).

2.3. *Synthesis of (R)-2-((3,4-diphenethoxyphenoxy)methyl)oxirane 6*: to a mixture of 3,4-diphenethoxyphenol **5** (0.35 g, 1.05 mmol) in ethyl alcohol (5 mL), aqueous potassium hydroxide (57.8 mg, 1.05 mmol, 100 μL water) and (R)-epichlorohydrin (1.13 mL, 5.0 mmol) were added. The resulting mixture was stirred for 15 h at room temperature. The solvent was removed under reduced pressure, and the residue dissolved in water and extracted with ethyl acetate. The organic extract was washed with brine and dried over Na_2SO_4 . The solvent was evaporated to afford the crude product, which was purified by column chromatography (silica gel 60-120 mesh),

with an ethyl acetate and n-hexane mixture in 1:4 ratio to generate the desired product (R)-2-((3,4-diphenethoxyphenoxy)methyl)oxirane **6** (0.33 g, 80%).

2.4. Synthesis of (R)-1-(3,4-diphenethoxyphenoxy)-3-(isopropylamino)propan-2-ol YOK-2204: to the stirred solution of (R)-2-((3,4-diphenethoxyphenoxy)methyl)oxirane **6** (100 mg, 0.26 mmol) in EtOH (2 mL) was added isopropyl amine (0.21 mL, 2.6 mmol), and the mixture was vigorously stirred at room temperature for 4 h (TLC-monitoring). Then, the solvent was removed under reduced pressure. The resulting residue was extracted with CH₂Cl₂ (3×10 mL). The combined organic layers were washed with brine (10 mL), dried over anhydrous Na₂SO₄ and concentrated under reduced pressure. The obtained crude product was purified by column chromatography (CH₂Cl₂/MeOH, 10:1) to give pure (R)-1-(3,4-diphenethoxyphenoxy)-3-(isopropylamino)propan-2-ol **YOK-2204** (99 mg, 86%) as a white powder. ¹H NMR (300 MHz, CDCl₃): δ 7.40-7.20 (m, 10H), 6.78 (d, 1H, *J* = 9.0 Hz), 6.52 (d, 1H, *J* = 3.0 Hz), 6.38 (dd, 1H, *J* = 3.0 and 9.0 Hz), 4.14 (dt, 4H, *J* = 9.0 and 15.0 Hz), 3.96-3.87 (m, 2H), 3.36 (brs, 2H), 3.11 (dt, 4H, *J* = 9.0 and 15.0 Hz), 3.01-2.92 (m, 2H), 2.80 (dd, 1H, *J* = 9.0 and 12.0 Hz), 1.19 (s, 3H), 1.17 (s, 3H) and also confirmed with ESIMS *m/z*: 424.3 [M+H]⁺.

3.1. Synthesis of 4-(benzyloxy)-3-hydroxybenzaldehyde 7: to a stirring solution of 3,4-dihydroxybenzaldehyde, **1** (2.5 g, 18.1 mmol) in anhydrous acetonitrile (30 mL), was added K₂CO₃ (2.5 g, 18.1 mmol) followed by benzyl bromide (2.15 mL, 18.1 mmol) slowly, at room temperature, under an inert (N₂) atmosphere. The reaction solvent was removed by evaporation under reduced pressure and to the resulting residue was added cold 10% NaOH solution and stirred for 10 min, after which ethyl acetate (100 mL) was added. The resulting biphasic mixture was separated and the aqueous layer was acidified with 4 N HCl and extracted with DCM (3 × 300 mL). The combined organic layer was washed with brine solution, water, dried over Na₂SO₄, and

concentrated under reduced pressure to obtain a residue, which was purified by crystallization using ethyl acetate to afford 4-(benzyloxy)-3-hydroxybenzaldehyde **7** (3.50 g, 85%) as a white powder. ^1H NMR (300 MHz, CDCl_3): δ 9.85 (s, 1H), 7.48-7.41 (m, 10H), 7.05 (d, 1H, $J = 9.0$ Hz), 5.90 (s, 1H), 5.22 (s, 2H); ESIMS m/z : 229 $[\text{M}+\text{H}]^+$.

3.2. Synthesis of 4-(benzyloxy)-3-phenethoxybenzaldehyde 8: to the stirred solution of 4-(benzyloxy)-3-hydroxybenzaldehyde **7** (2.50 g, 10.96 mmol) in dry DMF (10 mL) was slowly added anhydrous K_2CO_3 (2.90 g, 21.0 mmol), followed by (2-Bromoethyl)benzene (2.24 mL, 16.44 mmol). The mixture was heated to 70°C for 2 h and then cooled to room temperature. The mixture was partitioned between H_2O and ether (20 mL each). The organic layer was separated, and the water layer was extracted with ether (3×20 mL). The pooled organic layers were washed with H_2O (2×20 mL) and saturated aqueous NaCl (20 mL). The pale, straw-colored extracts were dried over anhydrous sodium sulfate and concentrated. The resulting residue was purified by silica gel column chromatography using EtOAc: Hexane (1:9) to yield 4-(benzyloxy)-3-phenethoxybenzaldehyde **8** (3.28 g, 90%) as Cream-colored solid. ^1H -NMR (CDCl_3 , 300 MHz): δ 9.84 (s, 1H), 7.48–7.26 (m, 12H), 7.02 (d, 1H, $J = 9.0$ Hz), 5.22 (s, 2H), 4.32 (t, 2H, $J = 6.0$ Hz), 3.19 (t, 2H, $J = 6.0$ Hz).

3.3. Synthesis of 2-((4-(benzyloxy)-3-phenethoxybenzyl)amino)ethan-1-ol YTK-1205: to a stirred solution of 4-(benzyloxy)-3-phenethoxybenzaldehyde **8** (100 mg, 0.30 mmol) in dry ethanol (5 mL), and 2-aminoethan-1-ol (91.5 μL , 1.5 mmol) was added and the reaction mixture was heated to 60°C . After completion of the aldehyde, the reaction mixture was cooled down to room temperature. NaBH_4 (17.1 mg, 0.45 mmol) was added slowly in portions, and the resulting solution was stirred for another 6 h. The solvent was evaporated in *vacuo*, and the residue was dissolved in water and extracted with ethyl acetate. The organic layers were combined and dried with Na_2SO_4 , filtered, and evaporated in vacuum. The residue was purified by flash column to generate the

desired product 2-((4-(benzyloxy)-3-phenethoxybenzyl)amino)-ethan-1-ol **YTK-1205** (97.7 mg, 86%). ^1H NMR (CD_3OD): δ 7.42-7.16 (m, 10H), 7.00 (d, 1H, $J = 3.0$ Hz), 6.95 (d, 1H, $J = 9.0$ Hz), 6.83 (dd, 1H, $J = 3.0$ and 9.0 Hz), 5.02 (s, 2H), 4.24 (t, 2H, $J = 6.0$ Hz), 3.71 (s, 2H), 4.04 (s, 2H), 3.66 (t, 2H, $J = 6.0$ Hz), 3.10 (t, 2H, $J = 6.0$ Hz), 2.71 (t, $J = 4.8$, 2H). ESIMS m/z : 378 $[\text{M}+\text{H}]^+$.

4.1. Synthesis of methyl (R)-(3-(3,4-bis(benzyloxy)phenoxy)-2-hydroxypropyl)glycinate YOK-Gly-1104: to the stirred solution of epoxide **3** (100 mg, 0.27 mmol) in EtOH (2 mL) was added glycine methyl ester hydrochloride (43.2 mg, 0.54 mmol), and the mixture was vigorously stirred at room temperature for 4 h (TLC-monitoring). Then, the solvent was removed under reduced pressure. The resulting residue was extracted with CH_2Cl_2 (3×10 mL). The combined organic layers were washed with brine (10 mL), dried over anhydrous Na_2SO_4 and concentrated under reduced pressure. The obtained crude product was purified by column chromatography ($\text{CH}_2\text{Cl}_2/\text{MeOH}$, 10:1) to give pure methyl (R)-(3-(3,4-bis(benzyloxy)phenoxy)-2-hydroxypropyl)glycinate **YOK-Gly-1104** (102 mg, 82%) as a white powder and confirmed with ESIMS m/z : 453 $[\text{M}+\text{H}]^+$.

Immunocytochemistry (ICC)

To observe cellular localization of proteins, cells were cultured on cover slips coated with poly-L-lysine (Sigma). The cells were fixed with 4% paraformaldehyde in PBS (pH 7.4) for 15 min at room temperature and washed three times with PBS for 5 min. The cells were permeabilized with 0.5% Triton X-100 in PBS solution for 15 min and washed three times with PBS for 5 min. The cells were blocked with 2% BSA in PBS solution for 1 h at room temperature. After blocking, the cells were incubated overnight at 4°C with primary antibody diluted in 2% BSA/PBS solution. Following incubation, the cells were washed three times for 10 min with PBS and incubated

with Alexa Fluor-conjugated secondary antibody diluted in 2% BSA/PBS for 30 min at room temperature. Subsequently, the coverslips were mounted on glass slides using a DAPI-containing mounting medium (Vector Laboratories). Confocal images were taken by laser scanning confocal microscope 510 Meta (Zeiss) and analyzed by Zeiss LSM Image Browser (ver. 4.2.0.121).

Co-immunoprecipitation

To study protein interactions, co-immunoprecipitation assays were performed. For exogenous co-IP, HEK293T cells were transfected with recombinant p62, BiP, TRIM13, FAM134B, RTN3 or ATZ using Lipofectamine 2000. For both endogenous and exogenous co-IP, cells were treated after 24 h with specified reagents for indicated incubation times. The cell pellets were scraped and pelleted by centrifugation, were resuspended and lysed in immunoprecipitation buffer [50 mM Tris-HCl pH 7.5, 150 mM NaCl, 0.5% Triton X-100, 1mM EDTA, 1mM phenylmethylsulfonyl fluoride (PMSF; Roche) and protease inhibitor cocktail (Sigma)] for 30 min on rotator at 4°C. Next, the supernatant and remaining pellet were passed through a 26-gauge 1 mL syringe 15 times and centrifuged at 13,000 g at 4°C and collected for the supernatant, to which I added normal mouse IgG (Santa Cruz) and Protein A/G-Plus agarose beads (Santa Cruz) to preclear the lysate at 4°C on a rotor overnight. Cell lysate was then incubated with M2 FLAG-affinity Gel agarose beads (Sigma) at 4°C on a rotor for 3 h. The gel beads were washed four times with IP buffer, resuspended in 2X Laemmli Sample Buffer, separated by SDS-PAGE and analyzed by immunoblotting with specified antibodies.

Denaturation-immunoprecipitation

To study ubiquitination of ectopically expressed or endogenous TRIM13, I carried out

denaturation immunoprecipitation assay. Briefly, cell pellets after trypsinization and centrifugation were resuspended in N-ethylmaleimide (NEM)-based buffer (10% SDS, 10 mM NEM in PBS), boiled at 100°C for 10 min and passed through a 26-gauge 1 mL syringe 15 times followed by centrifugation at 13,000 g at 4°C. The subsequent steps were identical to those during co-IP. Alternatively, His-tagged mutant Ub constructs were transiently co-transfected with that expressing TRIM13 into HEK293T cells using Lipofectamine 2000 for 24 h and subsequently treated with specified chemicals for indicated times. Cell pellet following trypsinization, collection and centrifugation was resuspended in 10 mM NEM solution in PBS with Ni-NTA+ beads (Sigma) in binding buffer (pH 8, 6 M guanidium chloride, 0.1 M Na₂HPO₄/NaH₂PO₄, 10 mM Tris pH 8, 10 mM beta-mercaptoethanol, 5 mM NEM, and 5 mM imidazole) for overnight incubation at 4°C. The beads were then washed with a series of wash buffers designated A (pH 8, 6 M guanidium chloride, 0.1 M Na₂HPO₄/NaH₂PO₄, 10 mM Tris pH 8, and 10 mM β-ME), B (pH 8, 8 M urea, 0.1 M Na₂HPO₄/NaH₂PO₄, 10 mM Tris pH 8, 10 mM β-ME), C (pH 6.3, 8 M urea, 0.1 M Na₂HPO₄/NaH₂PO₄, 10 mM Tris pH 8, 10 mM β-ME, 0.2% Triton X-100) and D (pH 6.3, 8 M urea, 0.1 M Na₂HPO₄/NaH₂PO₄, 10 mM Tris pH 8, 10 mM β-ME, 0.1% Triton X-100) at room temperature and incubated in elution buffer (2X Laemmli Sample Buffer, 0.72 M BME, and 200mM imidazole) for 20 min. Samples were boiled for 10 min at 100°C and loaded for SDS-PAGE and immunoblotting analysis.

ER expansion visualization and measurement

Using confocal microscopy of cells analyzed by immunocytochemistry, ER expansion was visualized by considered when KDEL- or calnexin-labelled ER occupied more than 80% of cell area. Furthermore, the ER area measurements were calculated by ImageJ (NIH, Bethesda, v1.52) and the background threshold was

manually defined and set for all images. ER area was calculated and marked from the total cell area as a fraction after borders of each cell were set.

***In vitro* p62 oligomerization**

HEK293 cells were transiently transfected with a plasmid encoding p62-myc/his fusion proteins, resuspended in lysis buffer [50 mM Hepes (pH 7.4), 0.15 M KCl, 0.1% Nonidet P-40), 10% glycerol, and a mixture of protease inhibitors and phosphatase inhibitor (Abcam)] and lysed by 10 cycles of freezing and thawing, followed by centrifugation at $13,000 \times g$ for 20 min at 4°C. The protein concentration of the supernatant was determined using a BCA assay. A total of 1 µg of protein was mixed with 50 mM of the Arg-Ala or Ala-Arg dipeptide (Anygen) or 1000 µM of p62-ZZ ligands in the presence of 100 µM bestatin (Enzo) at room temperature for 2 h. Next, non-reducing 4X LDS sample buffer was added to each sample, heated at 95°C for 10 min, and resolved using 4–20% gradient SDS-PAGE (Bio-Rad). IB analysis was carried out to monitor the conversion of p62 monomers into oligomers or aggregates using anti-myc antibody

***In vivo* oligomerization**

HEK293T cells were transfected with TRIM13-flag using Lipofectamine 2000 and treated with hydroxychloroquine (Sigma) for 24 h. To lyse the cells, the cells were subjected to a cycle of freezing/thawing and centrifuged at 13,000 g for 10 min after 30 min incubation on ice for supernatant collection. Protein concentration was determined using the Pierce BCA Protein Assay Kit (Thermo Fisher Scientific). Next, non-reducing 4X LDS sample buffer was added to sample lysate and followed by boiling for 10 min at 100°C. Samples were loaded on a 3% stacking and 8% separating SDS-PAGE. Immunoblotting assays were performed using anti-Flag antibody (Sigma) to visualize

the oligomeric complexes of TRIM13.

Triton X-100-based insoluble/soluble fractionation

To determine the p62 ligand-degraded fraction of ATZ, cells expressing ectopic ATZ and treated with p62-ZZ ligands were harvested using a cell lysis buffer (20 mM HEPES pH 7.9, 0.2 M KCl, 1 mM MgCl₂, 1 mM EGTA, 1% Triton X-100, 10% glycerol, protease inhibitor and phosphatase inhibitor) and incubated on ice for 15 min. After incubation, cells were centrifuged at 13,000 g for 10 min at 4°C. The supernatant was collected as the soluble fraction and the pellet as the insoluble fraction. The insoluble fraction was thoroughly washed with PBS and solubilized in a SDS-detergent lysis buffer (20 mM HEPES pH 7.9, 0.2 M KCl, 1 mM MgCl₂, 1 mM EGTA, 1% Triton x-100, 1% SDS, 10% glycerol, protease inhibitors and phosphatase inhibitors). The soluble and insoluble samples were added with 5X Laemmli sample buffer, boiled for 10 min at 100°C and loaded on a SDS-PAGE gel.

Subcellular fractionation

To analyze subcellular localization of ER chaperones and their arginylated forms, cells were trypsinized and pelleted by centrifugation at 1,500 x g at 4°C. The plasma membranes of the collected cells were resuspended and permeabilized using 0.01% digitonin (Thermo Fisher Scientific; BN2006) from *Digitalis purpurea* in lysis buffer (110 mM KOAc, 25 mM K-HEPES, pH 7.2, 2.5 mM NaOAc and 1 mM EGTA). After centrifugation for 5 min at 1,000 g, the remaining supernatant was re-centrifuged at 15,000 x g for 10 min at 4°C to obtain a cytosolic fraction in the final supernatant containing soluble cytosolic proteins. The microsome and nuclei fraction was pelleted from the initial centrifugation following digitonin permeabilization. This pellet was then resuspended and permeabilized in RIPA-based buffer (50 mM Tris-HCl, pH 8.0, 150

mM NaCl, 1% NP-40, 0.5% sodium deoxycholate and 0.1% SDS) followed by centrifugation at 5,000 g for 10 min to isolate the nuclei fraction as a pellet and the microsome fraction as the supernatant.

Protein degradation cycloheximide (CHX)-chase assay

To determine the stability of ectopically expressed TRIM13, HeLa cells were transiently co-transfected with TRIM13-flag under siRNA-mediated knockdown of control (Thermo Fisher Scientific), *ATE1* (Thermo Fisher Scientific) or *p62* (Bioneer) for 48 h. Subsequently, the cells were treated with 10 µg/ml cycloheximide (Sigma) and collected at the indicated time points. Cells were completely lysed in a SDS-based 5X Laemmli sample buffer and boiled for 10 min at 100 °C. After boiling, 10 µg of total protein lysate was loaded on a SDS-PAGE gel and analyzed by immunoblotting.

Cell viability assay

Cell viability was quantified using the water-soluble tetrazolium salt-based EZ-Cytox cell viability assay kit (Dojindo Laboratory) according to the manufacturer's instructions. Briefly, following siRNA-mediated knockdown of control or *ATE1* (48 h), HeLa cells in a 96-well plate were treated with the indicated ER stressors. Subsequently, assay reagent solution (10 µL) was added to each well and cells were incubated for 4 h at 37 °C in a CO₂ incubator. Optical density (OD) values were measured at 450 nm using a Evolution 350 UV-Vis Spectrophotometer (Thermo Fisher Scientific).

Transmission electron microscopy (TEM)

For conventional transmission electron microscopy, HEK293T cells were treated with 2.5 µM YOK1104 for 6 h, scraped from culture dish and pelleted by centrifugation.

Pellets were resuspended in 2.5% glutaraldehyde in 0.1M sodium cacodylate buffer (pH 7.4) (Electron Microscopy Sciences) for overnight at 4°C. The fixative was replaced by cacodylate buffer for the last 6 hours, after which cells were embedded in Epon resin. Subsequently, 55-nm sections were cut and stained with uranyl acetate and lead citrate using the Reichert Ultracut S Ultramicrotome (Leica Microsystems) and FEI Vitrobot Mark IV (Thermo Scientific), respectively. Cell sections were examined using the 200 kV transmission electron microscope FEI Tecnai G2-F20 (Thermo Scientific) at the Korea Institute of Science and Technology (KIST) Advanced Analysis Center.

Quantification and Statistical Analysis

For immunocytochemistry assays analyses, cells were deemed to exhibit significant co-localization of two different proteins if more than ten clear puncta structures of the respective proteins showed association or full co-localization. Quantification results are shown as mean \pm S.D. of three independent experiments. For all data shown, stated values represent the mean \pm S.D or S.E.M. of at least three independent experiments. For each experiment, sample size (n) was determined as stated in the figure legends. *P*-values were determined using ANOVA with Prism 6 software (GraphPad) or two-tailed student's *t*-test (degree of freedom = $n-1$). Statistical significance was determined as values of $p < 0.05$ (** $p < 0.001$; ** $p < 0.01$; * $p < 0.05$).

Results

Targeted protein degradation via the autophagy-lysosome system: AUTOTAC (autophagy-targeting chimera)

Development of the AUTOTAC platform

In contrast to the UPS in which each of the 800 E3 ligases possesses a specific clientele of substrates, selective autophagy employs only a handful of receptors for intracellular cargoes, amongst which p62 plays a dominant role. If a bifunctional molecule binds both a target and p62 and activate the otherwise inactive p62, any given proteins could be targeted for autophagic degradation in principle. I therefore developed autophagy-targeting ligands (ATL) that bind and activate p62 into an autophagy-compatible form (Fig. 57A). 3D structure modelling, followed by SAR (structure-activity relationship), was employed on the ZZ domain of p62. Four compounds, YT-8-8, YOK-2204, YOK-1304 and YTK-F105, exhibited efficacy and selectivity to activate p62 as well as pharmacological properties as ATLs (Fig. 57B). When modeled to the p62-ZZ domain, they showed high docking scores based on low/negative energy of the stable system (-5.8, -5.5 and -4.0 kcal/mol for YOK-1304, YOK-2204 and YTK-105, respectively) (Fig. 58). Specific residues of the ZZ domain critical for N-degron recognition, such as Phe168, Arg139, Ile127, Asp129, Asp147 and Asp149, were also identified (Fig. 58).

In vitro pulldown assays using biotinylated ATLs confirmed that p62 bound YT-8-8, YOK-1304, and YTK-1105, as opposed to the negative control V-BiP-biotin peptide (Fig. 59A). The efficacy of ATLs in inducing p62 polymerization, a critical step in cargo collection, was demonstrated using *in vitro* oligomerization assays (Fig. 59B). In co-immunostaining analyses, ATLs induced the formation of p62 and LC3 punctate structures (Fig. 60A and 60B) as well as their co-localization (Fig. 60A and 60C), suggesting that ATLs not only activate and target p62 to autophagic membranes but also facilitate autophagosome biogenesis to receive incoming p62-cargo complexes. When autophagic flux indices were compared based on the ratio of substrate levels in the presence or absence of late-step autophagic inhibitors (Fig. 61B), ATLs enhanced

autophagic turnover of p62 and LC3, indicative of increased autophagy flux (Fig. 61A). These results validate p62-ZZ ligands as ATLs capable of activating p62.

I used these ATLs to synthesize AUTOTACs, composed of TBLs linked to ATLs via a repeating polyethylene glycol (PEG) moiety (Fig. 62A, 77A and 95). I speculated that AUTOTACs would mediate targeted degradation through the following multi-step mechanisms. *First*, AUTOTAC brings a target to p62 via its TBL and ATL, forming a ternary complex. *Second*, normally-inactive p62 is structurally activated for self-oligomerization, forming target-p62 oligomeric complexes. *Third*, ATL facilitates Ub-independent p62-LC3 interaction on autophagic membranes and promotes autophagosome biogenesis on the ER to receive incoming target-p62 complexes. *Fourth*, AUTOTACs are recycled from the lysosome towards other targets in the cytosol, providing a processive nature of degradation. These mechanisms are independent of protein-protein interactions (PPIs) between p62 and targets, as opposed to PROTAC, and thus are generally applicable for a broad range of intracellular proteins.

Targeted degradation of soluble proteins by AUTOTAC

To test the degradative efficacy of AUTOTACs, I sought out to degrade estrogen receptor beta (ER β) using its nonsteroidal and synthetic ligand, PHTPP (Fig. 62B). PHTPP-based AUTOTAC (PHTPP-1304) induced self-oligomerization of p62 (Fig. 63A) and degradation of ER β at half-degrading concentration values (DC₅₀) of 10-50 nM in HEK293T cells (Fig. 64A) and 100 nM in ACHN renal carcinoma (Fig. 64B) and MCF-7 breast cancer (Fig. 64C) cells. Sustained degradation and maximal clearance at the 24 hour mark (D_{max, 24 hr}) values were observed at 10-100 nM (Fig. 64A, 64B and 64C). In contrast, no significant degradation was achieved with counterpart ATL and TBL (Fig. 67A and 67D). Next, I sought out to degrade androgen receptor (AR) and methionine aminopeptidase 2 (MetAP2) using a synthetic derivative of vinclozolin and

fumagillol, a hydrolyzed product of fumagillin (Fig. 62). Fumagillin covalently binds MetAP2 via a spiro-epoxide moiety (91), and vinclozolin derivatives and metabolites inhibit androgen binding to AR (92, 93). As expected, AR and MetAP2 AUTOTACs efficiently induced p62 self-polymerization (Fig. 63B). Moreover, vinclozolin-2204 exhibited DC_{50} of ~200 nM for AR in LNCaP prostate cancer cells (Fig. 65). Fumagillin-105 exhibited DC_{50} of ~0.7 μ M for MetAP2 in HEK293 cells with $D_{max, 24\text{ hr}}$ of ~1-10 μ M (Fig. 66A) and DC_{50} of ~500 nM in U87-MG glioblastoma cells (Fig. 66B). Such degradative efficacy was not observed with their ATLs or TBLs (Fig. 67B, 67C and 67D). These results validate AUTOTAC as a general chemical tool for targeted proteolysis.

Co-localization analysis in LNCaP cells showed that vinclozolin-2204 induced the formation of AR^+p62^+ complexes and AR^+LC3^+ autophagic membranes (Fig. 68). PHTPP-1304 in ACHN cells facilitated dosage-dependent formation of $p62^+ER\beta^+$ puncta subject to autophagic flux when treated with the late-step autophagic flux inhibitor hydroxychloroquine (Fig. 69). Consistently, fumagillin-105 treatment drastically up-regulated the autophagic flux of MetAP2, leading to lysosomal degradation via autophagosomes (Fig. 70). Crucially, the degradation of $ER\beta$ by PHTPP-1304 was completely abolished by RNA interference of either *p62* or *ATG5* (Fig. 71). These results demonstrate that AUTOTAC drives lysosomal degradation of target proteins via p62-dependent macroautophagy.

As an autophagic cargo adaptor, p62 contains a LIR domain for LC3 interaction on autophagic membranes and a UBA domain that binds poly-Ub chains (Fig. 72). Thus, I determined whether AUTOTAC-based proteolysis depends on ubiquitination of target substrate and recognition of Ub chains via the p62-UBA domain. Importantly, AUTOTAC-driven degradation of MetAP2 (Fig. 73A), $ER\beta$ (Fig. 73B) and AR (Fig. 73C) remained not only intact but was even enhanced under *Ubb* interference, possibly

as a consequence of compensatory crosstalk between the UPS and autophagy. These results suggest that Ub-independent proteolysis mediated by AUTOTAC does not require PPI-driven cooperativity as opposed to other types of degraders.

Therapeutic efficacy of AUTOTAC in cancer signaling

To assess the therapeutic efficacy of autophagy-targeting degraders, I compared the downstream signaling of AR and ER β in cells treated with either AUTOTACs or their cognate TBLs. Dihydrotestosterone (DHT) and estradiol (E2) are natural agonists that respectively bind AR and ER β and induce their dimerization and nuclear translocation, resulting in transcriptional activation of downstream proteins (94, 95). When the levels of EGFR and p-Akt/Akt were measured in DHT-activated cells, vinclozolin-2204 inhibited AR pathways approximately 4-folds more efficiently than its TBL (Fig. 74A). Similarly, PHTPP-1304 inhibited ER β -signaling 10-folds more efficiently than its TBL as determined by the levels of EGFR, p-ERK/ERK and p-Akt/Akt in E2-stimulated LNCaP cells (Fig. 74B). Next, I examined the potency of AUTOTACs in cancer cell growth and progression. WST-based viability assays in ACHN cells showed that PHTPP-1304 exerted a ~5-fold higher cytotoxicity (IC₅₀, 3.3 μ M) than those of its ATL (>20 μ M for YOK-1304) or TBL (18 μ M for PHTPP) (Fig. 75A). Vinclozolin-2204 also exhibited higher cytotoxicity (IC₅₀, 4.7 μ M) as compared with its ATL (>100 μ M) and TBL (>100 μ M) (Fig. 75B). When the efficacy of degraders was assessed using wound healing assays, PHTPP-1304 more efficiently inhibited cell migration compared with ATL or TBL (Fig. 76A). Analogous assays targeting MetAP2 revealed that fumagillin-105 more efficiently inhibited the migration of U87-MG glioblastoma cells as early as 4 hours and up to 24 hours post-scratch (Fig. 76B). These data demonstrate the therapeutic advantage of AUTOTACs against cancer cell growth and progression.

AUTOTAC enables the targeting of Ub-conjugated misfolded protein aggregates to the lysosome

Most proteins are misfolded or damaged at least once during their limited lifespans and thus necessitate their turnover via the UPS or autophagy. Soluble misfolded proteins are primarily degraded through the UPS, which involves unfolding into nascent polypeptides and cleavage by the proteasome (96-98). However, the proteasome has an inner diameter as narrow as 13Å whose pore is inaccessible to oligomers and aggregates and clogged by partially misfolded substrates, leaving autophagy as possibly the last line of defense against pathogenic aggregates(19, 99). I therefore applied AUTOTAC for UPS-resistant misfolded proteins and their oligomeric/aggregated species (Fig. 77A).

I first searched for a chemical chaperone that selectively recognizes the exposed hydrophobic regions as a universal signature of misfolded proteins. Screening of various compounds identified 4-phenylbutyric acid (PBA), an FDA-approved drug and chemical chaperone that improves proteostasis and ameliorates misfolding-induced ER stress (100). PBA-1105 and PBA-1106 AUTOTACs (Fig. 77B) efficiently activated p62 and triggered its self-oligomerization in complex with cargoes (Fig. 78A and 78B). Immunoblotting analyses showed that PBA-1105 increased the autophagic flux of Ub-conjugated aggregates under prolonged proteasomal inhibition (Fig. 79A, flux indices 1 vs. 2.2), which was increasingly sustained for at least 48 hours (Fig. 79B). When their intracellular distribution was visualized using immunofluorescence analyses, PBA-1106 facilitated the formation of Ub⁺ cytosolic puncta, the vast majority of which colocalized with p62⁺ puncta (Fig. 80). No such efficacy was observed with PBA alone or ATL (Fig. 78, 79, 80). Thus, AUTOTAC provides a chemical means to target Ub-conjugated, UPS-resistant misfolded protein aggregates to autophagic proteolysis.

In neurodegeneration and other proteinopathies, aggregation-prone misfolded proteins inherently form oligomers that aggregate into fibrillary species. The screening of TBLs that selectively recognize the oligomeric signature of proteins and their aggregates yielded Anle138b, a phase 1 clinical trial compound that binds oligomers and aggregates of neurodegenerative proteinopathies (101, 102). Anle138b-F105 (Fig. 77B) facilitated p62 self-polymerization (Fig. 78) and autophagic flux of Ub-conjugated oligomeric/aggregated proteins (Fig. 81A) via p62-dependent macroautophagy (Fig. 81B). These data validate that AUTOTAC enables autophagic proteolysis of otherwise non-degradable oligomeric or aggregated proteins by recognizing their exposed hydrophobic motifs or oligomeric signature.

Degradation of pathological aggregates of neurodegenerative diseases using AUTOTAC

Neurodegenerative diseases such as Alzheimer's disease are associated with an ever-increasing accumulation of degradation-resistant misfolded hallmark protein aggregates. Traditional approaches for developing ligands that alter the activity of neurodegeneration-associated targets are not applicable for pathological aggregates, leaving degraders as possibly the only therapeutic means. Since PROTAC-based approaches are inherently incapable of degrading large oligomers and aggregates, I tested whether AUTOTACs can target aggregation-prone P301L tau mutant that forms neurofibrillary tangles because of its prion-like seeding behavior (103). PBA-1105 and PBA-1106 AUTOTACs induced autophagic degradation of stably-expressed mutant tau at DC_{50} of ~1-10 nM and $D_{max,24\text{ hr}}$ of 100 nM, followed by a hook effect at higher concentrations (Fig. 82A and 82D). In contrast to PBA AUTOTACs, virtually no degradation was observed with their TBL (Fig. 82B and 82D) or ATLs (Fig. 82C and 82D). Similar to PBA-based degraders, Anle138b-F105 (Fig. 83A and 83D) targeted

tauP301L for lysosomal degradation at DC_{50} of ~3 nM, as opposed to its TBL (Fig. 83B and 83D) or ATL (Fig. 83C and 83D). Autophagy-based targeted degradation was obvious as early as 30 min and reached a sustained maximal effect from 3 hrs onwards (Fig. 84). These data validate the general efficacy of AUTOTACs for tau oligomers and aggregates.

I next confirmed whether AUTOTACs exert their efficacy by directly targeting oligomeric and aggregated species. Co-localization analysis showed that PBA-1105 AUTOTAC selectively induced the sequestration and autophagic targeting of tauP301L in contrast to YTK-1105 or PBA (Fig. 85). Similarly, detergent-based insoluble/soluble fractionation of tauP301L species revealed that only PBA-1105, in contrast to its TBL (Fig. 86A) or ATL (Fig. 86B), promoted autophagic degradation of not only detergent-soluble but critically also detergent-insoluble species. Next, I used the phosphatase inhibitor okadaic acid to examine the efficacy of PBA-based degraders against hyperphosphorylated tau species, which act as a seedbed for tau aggregation. While okadaic acid treatment impaired the autophagic flux of mutant tauP301L (Fig. 87A and 87B), presumably due to hyper-sequestration of tau, PBA-1106 significantly rescued autophagic flux of these otherwise non-digestible species (Fig. 87A and 87B). Detergent-based insoluble/soluble fractionation of okadaic acid-induced hyperphosphorylated tau further confirmed that PBA-1105 not only rescued but drastically accelerated the autophagic flux of both phosphorylated and total tau species (Fig. 87, autophagy flux indices). Consistently, *in vivo* aggregation assays revealed that PBA-1105 effectively eliminated high-molecular weight tau aggregates (Fig. 88). Importantly, co-immunoprecipitation analyses revealed that Anle138b-F105 treatment induced not only the degradation of tauP301L but also its interaction with mutant p62 lacking the UBA domain, which is normally required for the interaction (Fig. 89). These data indicate that AUTOTAC provides a platform to target aggregation-prone misfolded

proteins in neurodegenerative proteinopathies for lysosomal degradation in an ubiquitin-independent manner.

Next, I tested whether AUTOTAC is applicable for other neurodegeneration-associated proteins such as mutant huntingtin. HeLa cells were engineered to stably express wild-type (Q25) or mutant (Q97) huntingtin based on their nuclear localization/export signals (Htt-NLS-GFP or Htt-NES-GFP). Autophagy flux assays showed that PBA AUTOTACs induced lysosomal degradation of both nucleus- and cytosol-resident mutant huntingtin (Htt-NES-Q97 and Htt-NLS-Q97) at DC_{50} of 0.1-1 μ M (Fig. 90A and 90B). Similar degradation efficacy was observed with transiently-expressed mutant huntingtin, HDQ103 (Fig. 90C). PBA AUTOTACs exhibited no significant degradative efficacy against wild-type huntingtin, HttQ25 (Fig. 90D and 90E), further supporting their specificity to mutant Htt. As expected, their ATLs exhibited no efficacy against neither wild-type nor mutant Htt proteins (Fig. 90E). Similar to PBA-based degraders, Anle138b-F105 also showed DC_{50} of ~50 nM against the nuclear subpopulation of Htt (HttQ97-NLS-GFP) 24 hrs post-treatment (Fig. 91A and 91D) in contrast to its TBL or ATL (Fig. 91B, 91C and 91D). These data demonstrate that AUTOTAC is generally applicable for a broad range of pathogenic aggregates in neurodegeneration.

AUTOTAC mediates the eradication of tau aggregates from mouse brains

Increasing evidence points to soluble tau oligomers as causative agents in tau pathology due to their neurotoxic effect and a prion seed-like behavior for self-propagation (104). To date, there are no general methods for targeted degradation of pathological protein oligomers and aggregates in neurodegeneration. I have previously developed hTauP301L-BiFC transgenic mice that express human tauP301L in the brain by employing bimolecular fluorescence complementation to visualize soluble tau oligomers (105) (Fig. 92). I assessed the efficacy of PBA-1105 AUTOTAC to eradicate

misfolded tau aggregates from their brains. The mice were intraperitoneally injected (saline, 20, or 50 mg/kg) three times per week for one month (Fig. 92). Brain hemispheres were subjected to RIPA-based insoluble/soluble fractionation, followed by immunoblotting analyses of both endogenous wild-type murine tau and human tauP301L. I first confirmed that PBA-1105 AUTOTAC did not degrade endogenous wild-type murine tau in either detergent-soluble or -insoluble fractions (Fig. 93A, 93B and 93C). In sharp contrast, PBA-1105 induced marked clearance of detergent-insoluble tauP301L in a dosage-dependent manner (Fig. 93A, 93B and 93C). This reduction in insoluble tau aggregates correlated to an increase in RIPA-insoluble LC3 levels (Fig. 93A and 93B). In contrast to insoluble species, levels of soluble tau species showed little if any reduction (Fig. 93A, 93B and 93C), demonstrating substrate specificity of AUTOTAC towards aggregation-prone tauP301L mutant. Next, I visualized soluble oligomeric htauP301L-BiFC bodies using Sudan Black B staining on the cross sections of murine brains. Notably, PBA-1105 AUTOTAC induced a drastic reduction of total tau oligomers on both the cortex and the CA1 region of the hippocampus sections in a dosage-dependent manner as determined by both the number of tau bodies and their fluorescence signals (Fig. 94A and 94C). Moreover, AT8 staining revealed a marked eradication of soluble bodies of phosphorylated tau-BiFC in the cortex as well as the CA1 region (Fig. 94B and 94C). These results indicate that AUTOTAC provides a platform to eradicate pathological aggregates from the brain.

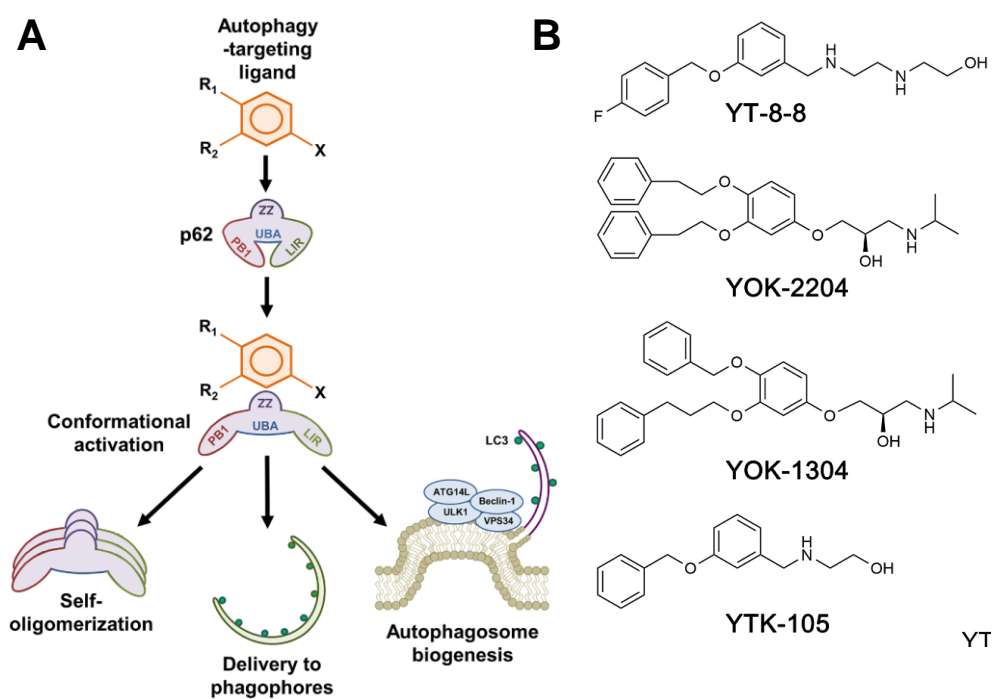


Fig. 57. Mechanism-of-action and chemical structures of autophagy-targeting ligands. (A) A model illustrating the mode of action of autophagy-targeting ligands. **(B)** Chemical structures of autophagy-targeting ligands.

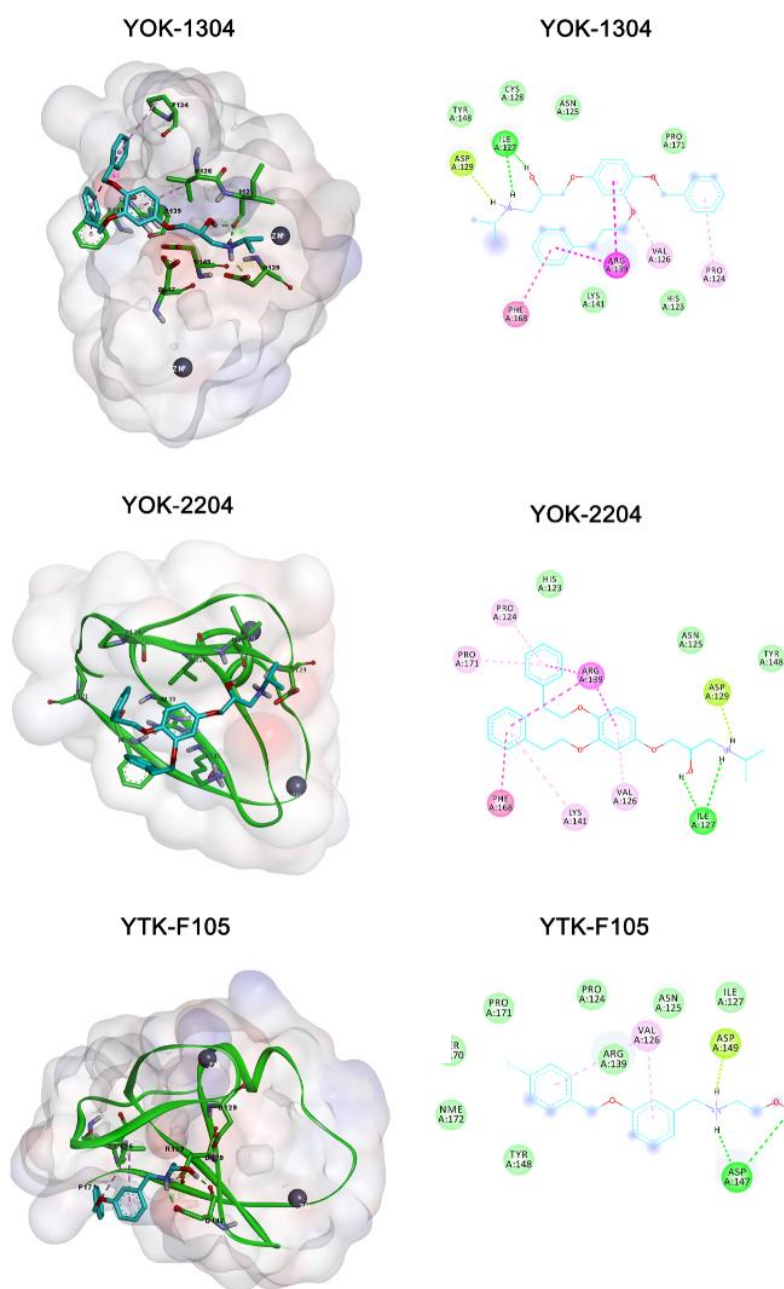


Fig. 58. Molecular docking models of ATLs to the p62-ZZ domain. 3-D modeling and 2-D diagrams of p62 ZZ ligands YOK-1304, YOK-2204 and YTK-105, respectively.

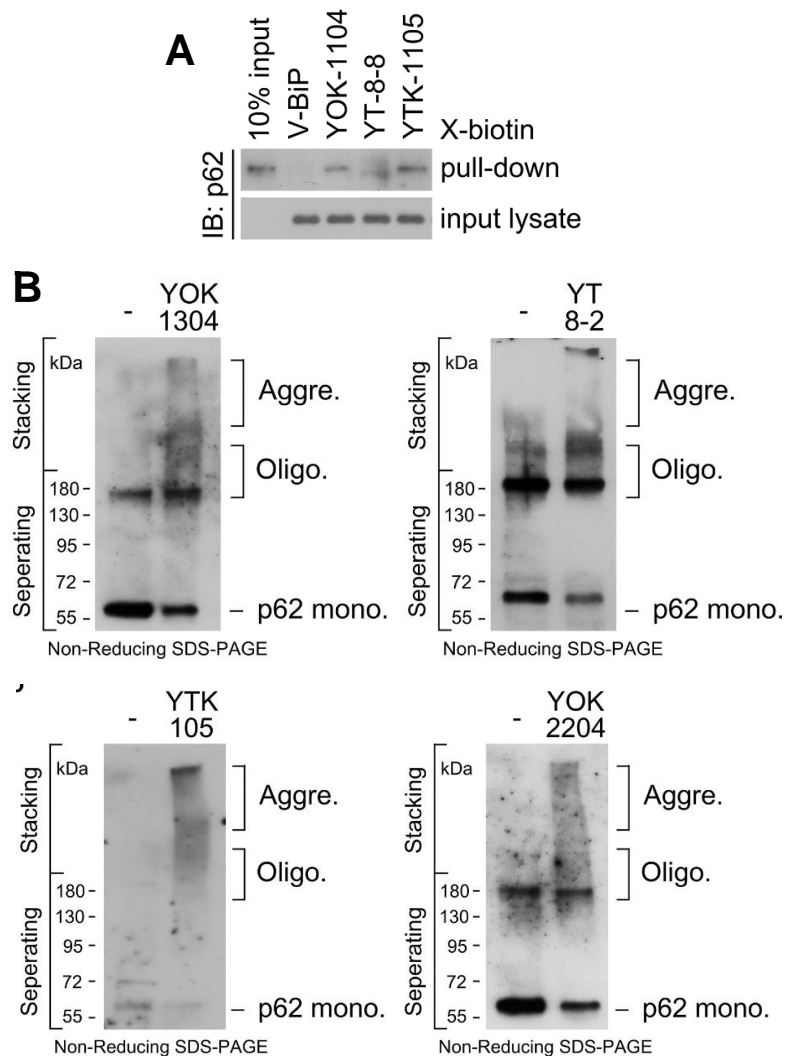


Fig. 59. ATLS bind p62 and induce its self-oligomerization. (A) *In vitro* pull-down assay in HEK293T cells of the 12-mer V-BiP peptide or autophagy-targeting ligands. **(B)** *In vitro* p62 oligomerization assay in HEK293T cells incubated with the p62-ZZ ligands.

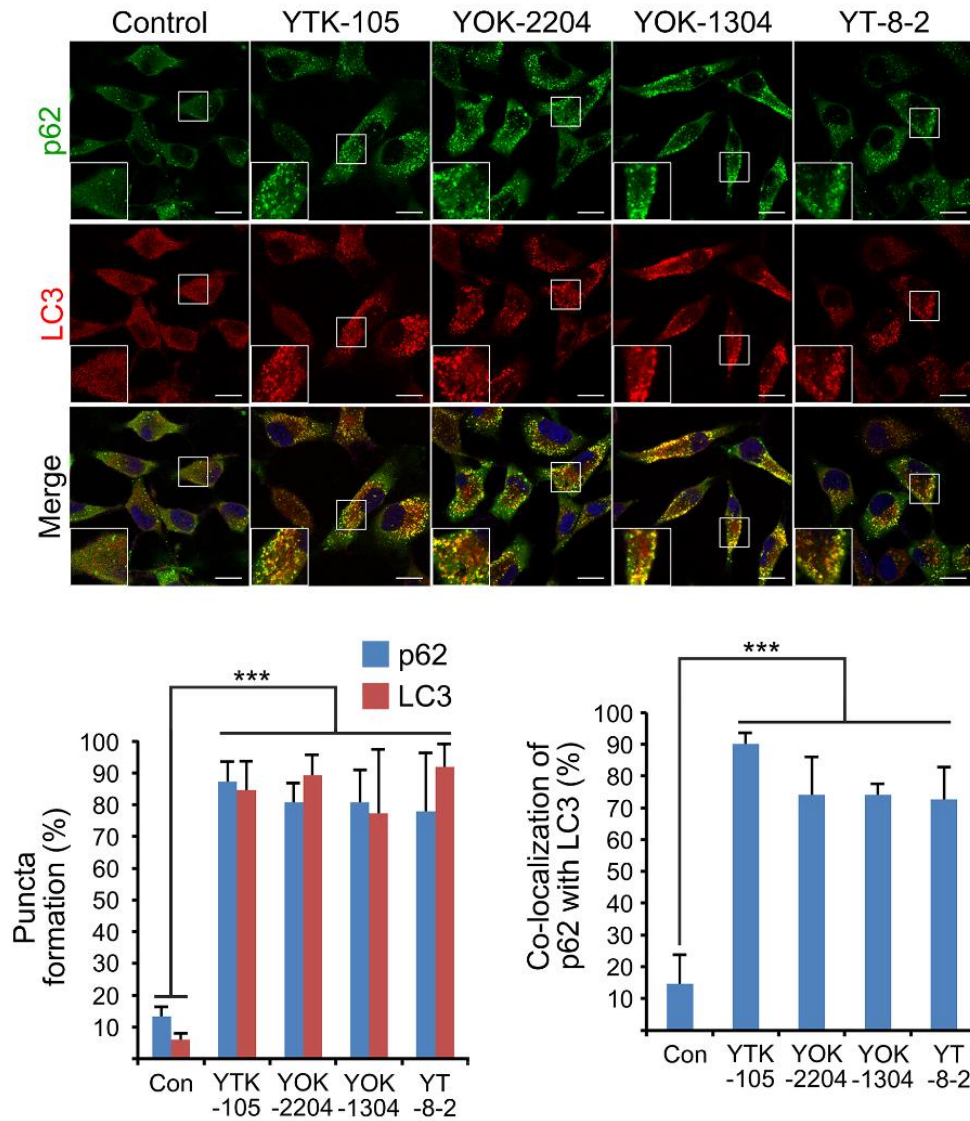


Fig. 60. ATLs induce p62-associated autophagosome formation. ICC of HeLa cells treated with p62-ZZ ligands in **b** (2.5 μ M, 24 h). Scale bar, 10 μ m. Quantification for puncta formation and co-localization, respectively: n=50 cells.

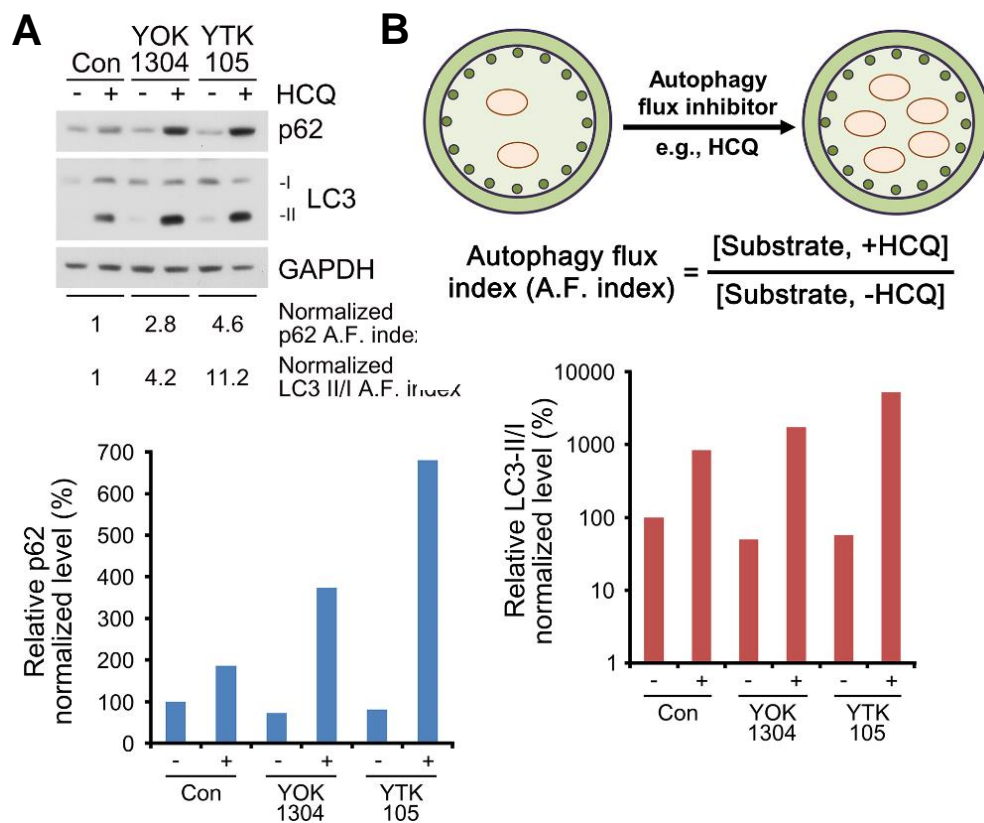


Fig. 61. ATLs induce global autophagic flux and p62 degradation . (A) Autophagic flux assay in HeLa cells treated with YOK-1304 or YTK-105 (2.5 μ M, 24 h) in the presence or absence of HCQ (10 μ M, 24 h). Densitometry of p62 and LC3-II/I levels. **(B)** A schematic/formulae for autophagy flux index.

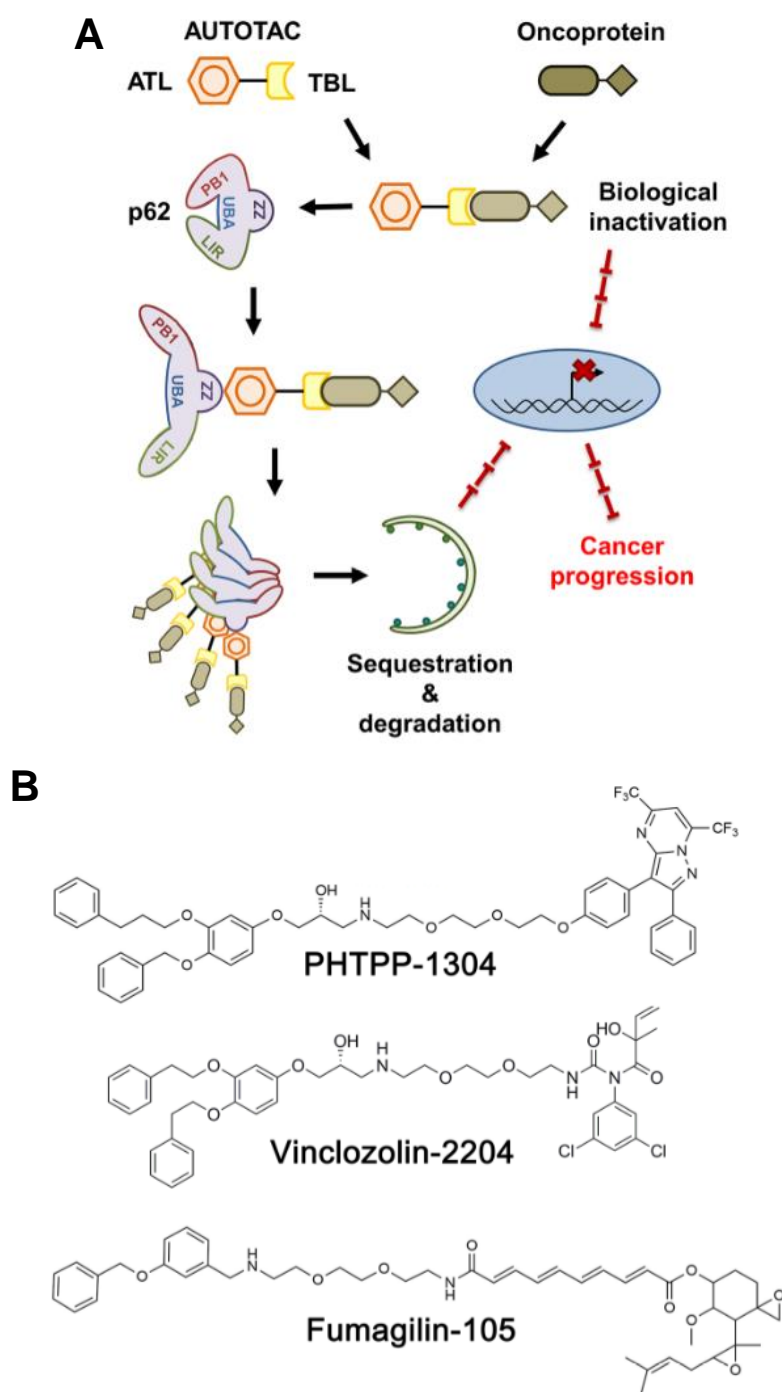


Fig. 62. Mechanism-of-action and chemical structures of oncoprotein-targeting AUTOTACs. (A) A model illustrating oncoproteins-targeting AUTOTAC. **(B)** Chemical structures of oncoprotein-targeting AUTOTAC.

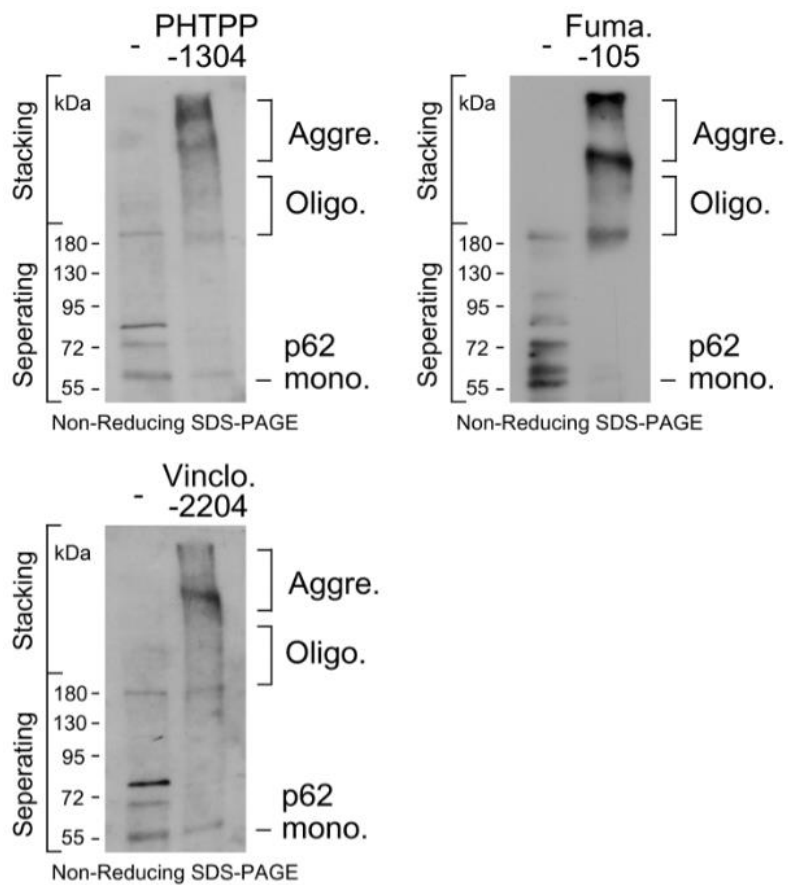


Fig. 63. Oncoprotein-targeting AUTOTACs promote high molecular-weight self-oligomerization of p62. *In vitro* p62 oligomerization assay in HEK293T cells incubated with PHTPP-1304, VinclozolinM2-2204, or Fumagillin-105.

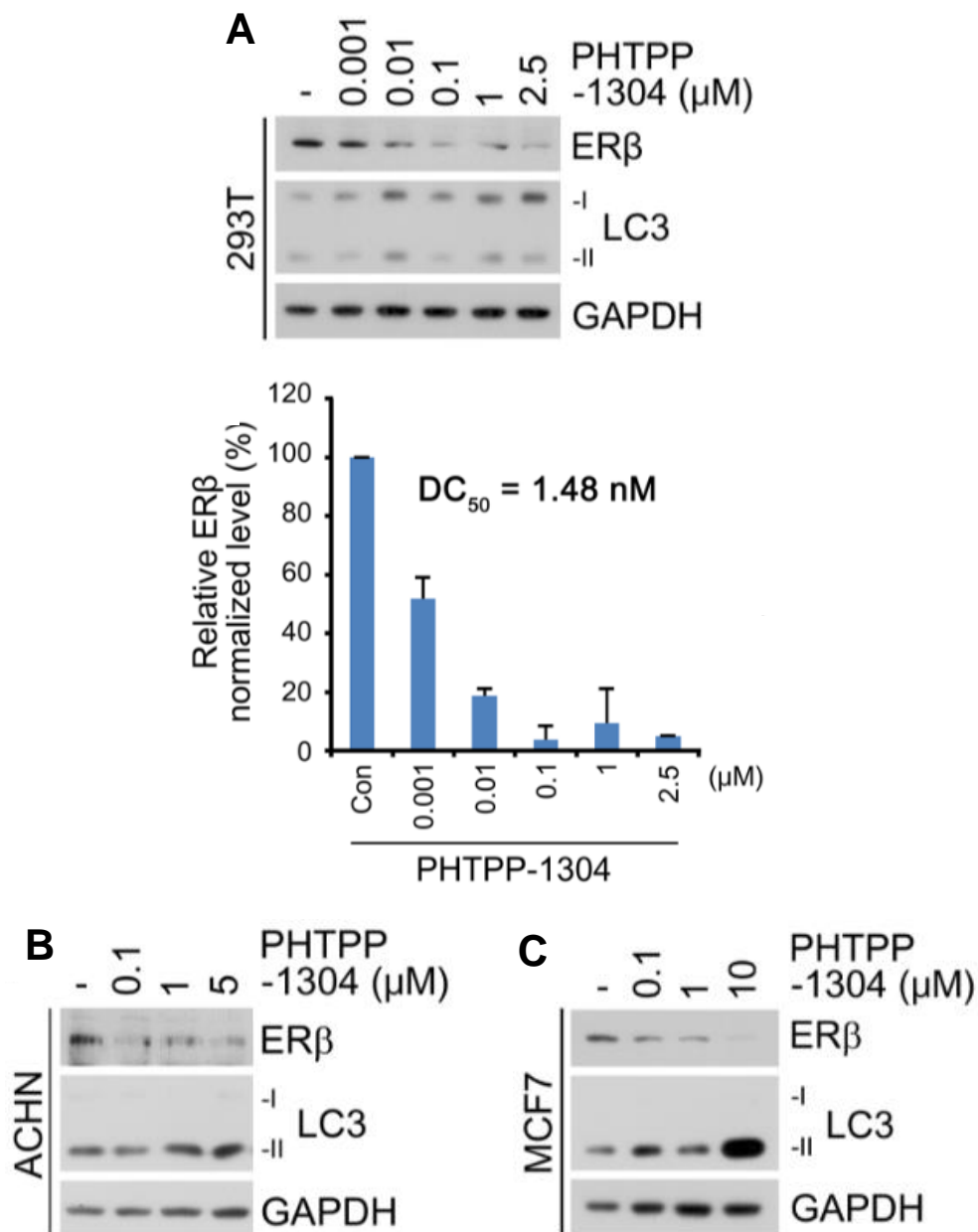


Fig. 64. ER β -targeting AUTOTAC degrades ER β in a dosage-dependent manner. (A) WB in HEK293T cells treated with PHTPP-1304 at the indicated concentrations (24 h). Densitometry of ER β relative to GAPDH (n=3). (B, C). WB in ACHN and MCF7 cells, respectively, treated with PHTPP-1304 at the indicated concentrations (24 h).

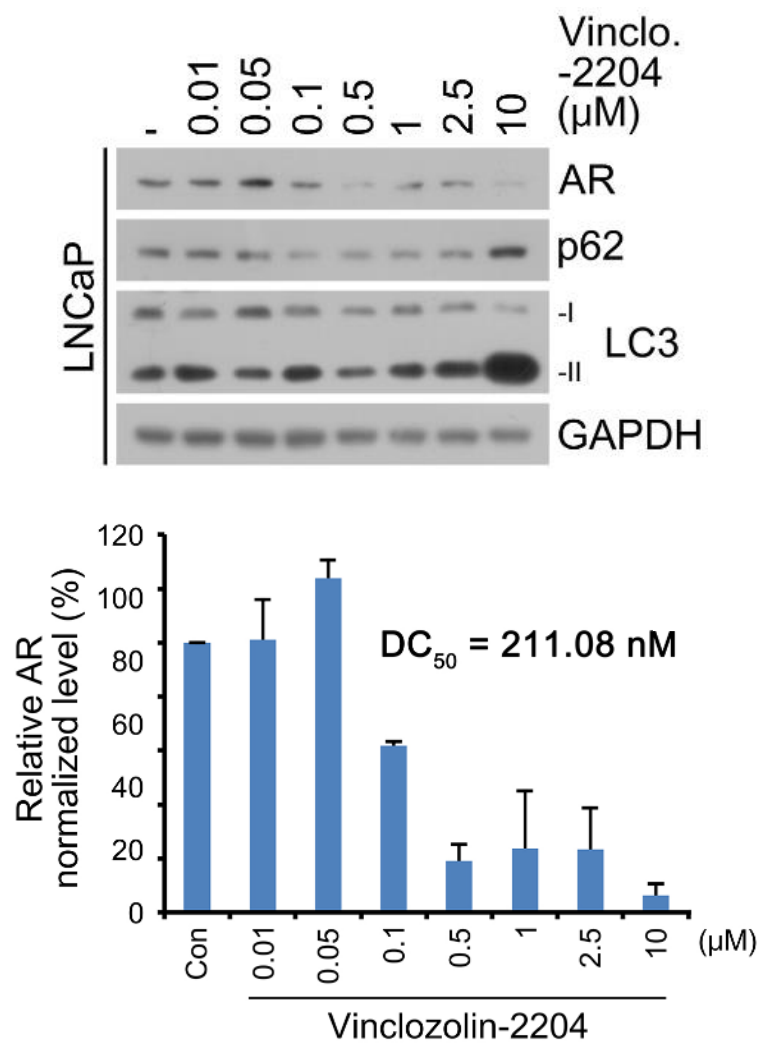


Fig. 65. AR-targeting AUTOTAC degrades AR in a dosage-dependent manner. WB in LNCaP cells treated with VinclozolinM2-2204 at the indicated concentrations. Densitometry of AR relative to GAPDH (n=3).

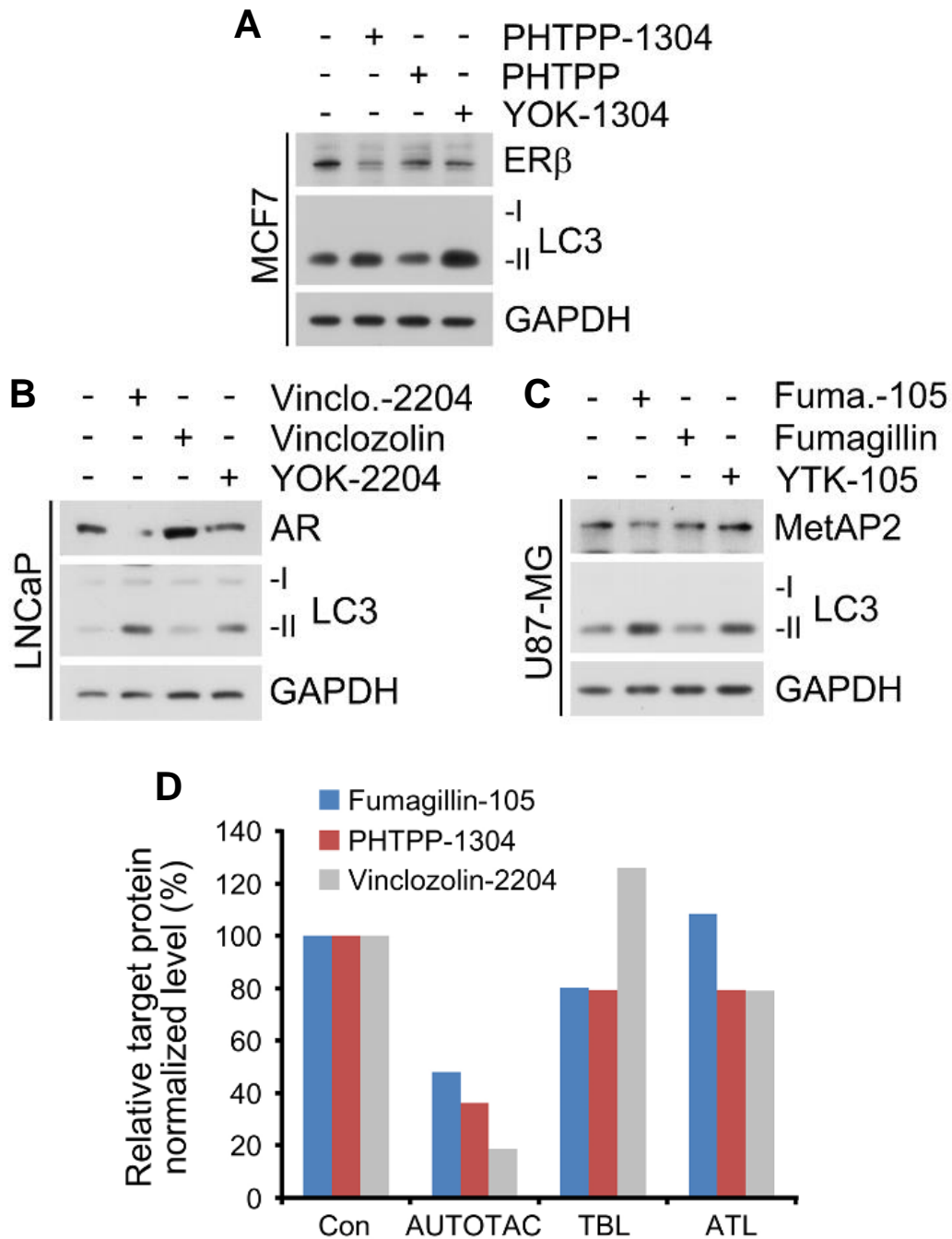


Fig. 67. Oncoprotein-targeting AUTOTACs induce selective degradation of their targets (A) WB in MCF7 cells treated with PHTPP-1304, PHTPP or YOK-1304 (1 μ M, 24hr). (B) WB in LNCaP cells treated with VinclozolinM2-2204, Vinclozolin or YOK-2204 (1 μ M, 24 h). (C) WB in U87-MG cells treated with Fumagillin-105, Fumagillin or YTK-105 (1 μ M, 24 h). (D) Densitometry of target oncoprotein relative to GAPDH,

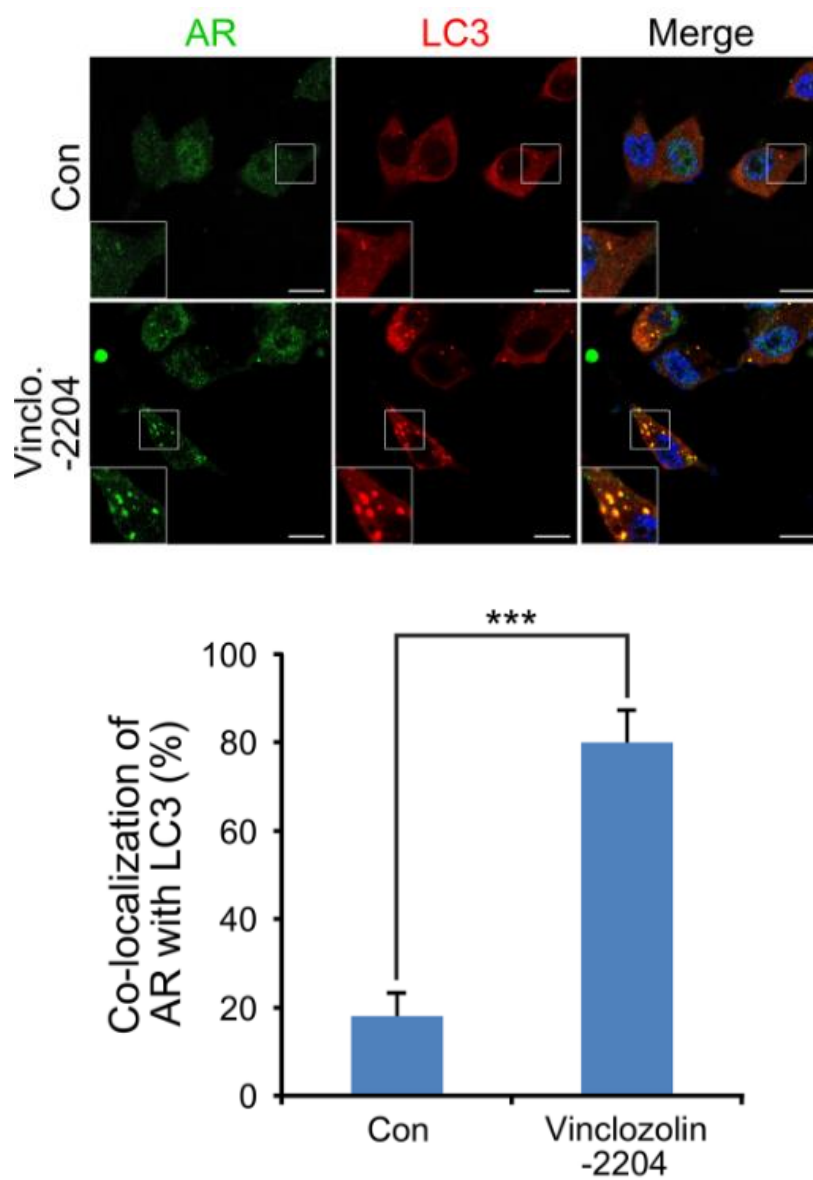


Fig. 68. AR-targeting AUTOTAC targets AR to the autophagosome. ICC of LNCaP cells treated with Vinclo.-2204 (2.5 μ M, 24 h). Scale bar, 10 μ m. Quantification: n=50 cells.

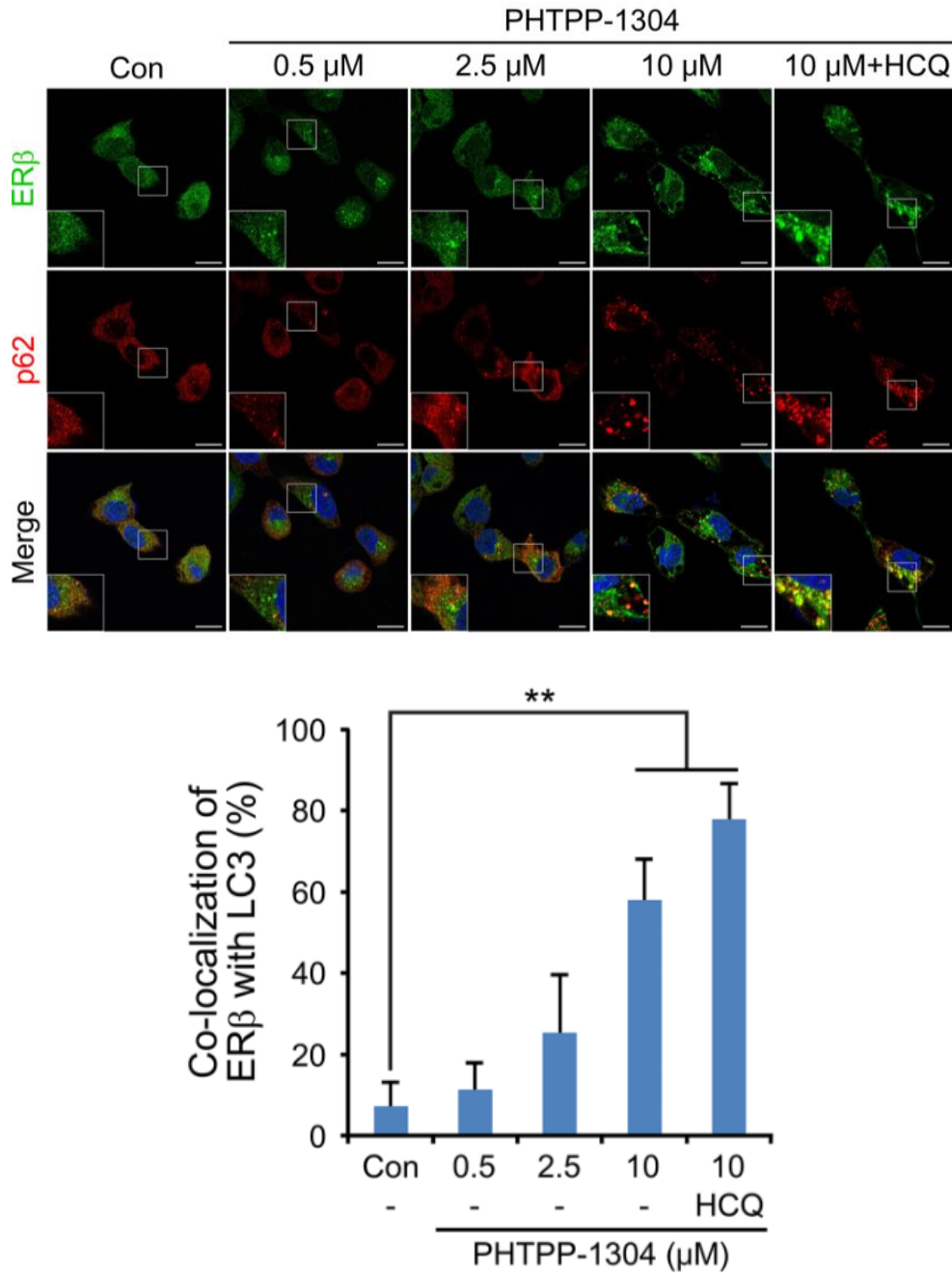


Fig. 69. ER β -targeting AUTOTAC targets ER β and p62 to the autophagosome. ICC of ACHN cells treated with PHTPP-1304 at the indicated concentrations and HCQ (10 μ M) (24 h). Scale bar, 10 μ m. Quantification: n=50 cells.

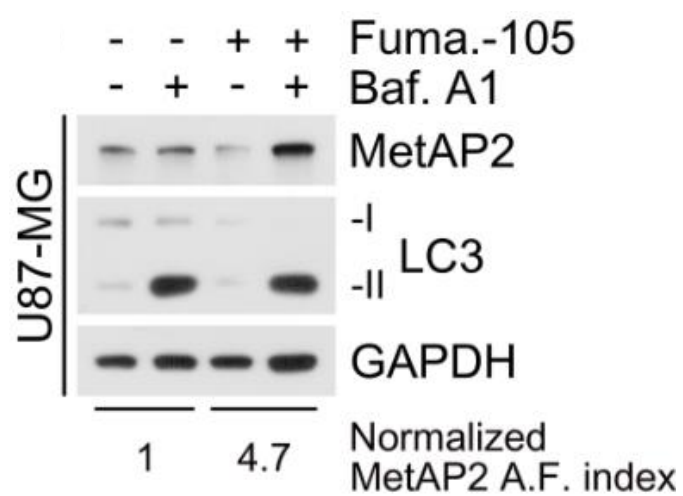


Fig. 70. MetAP2-targeting AUTOTAC accelerates autophagic flux of MetAP2. WB in U-87 MG cells treated with fumagillin-105 (1 μ M, 24 h) with or without bafilomycin A1 (200 nM, 6 h).

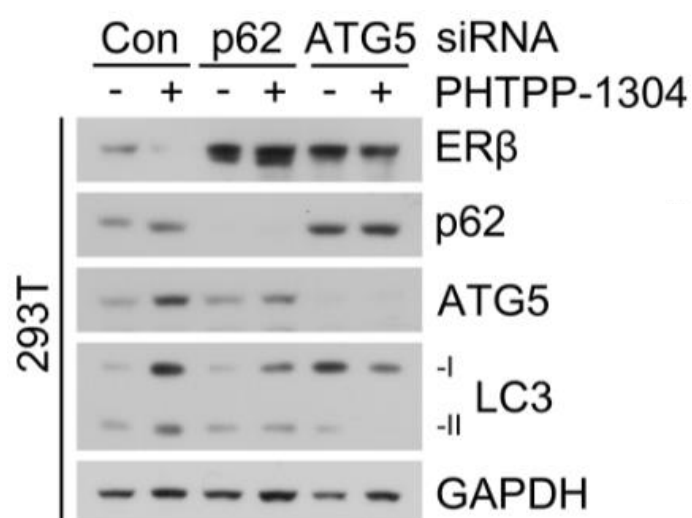


Fig. 71. AUTOTAC-induced degradation is mediated by p62 and macroautophagy. WB in HEK293T cells treated with PHTPP-1304 (0.1 μ M, 24 h) under siRNA-mediated knockdown of *p62* and *ATG5* (40 nM, 48 h).

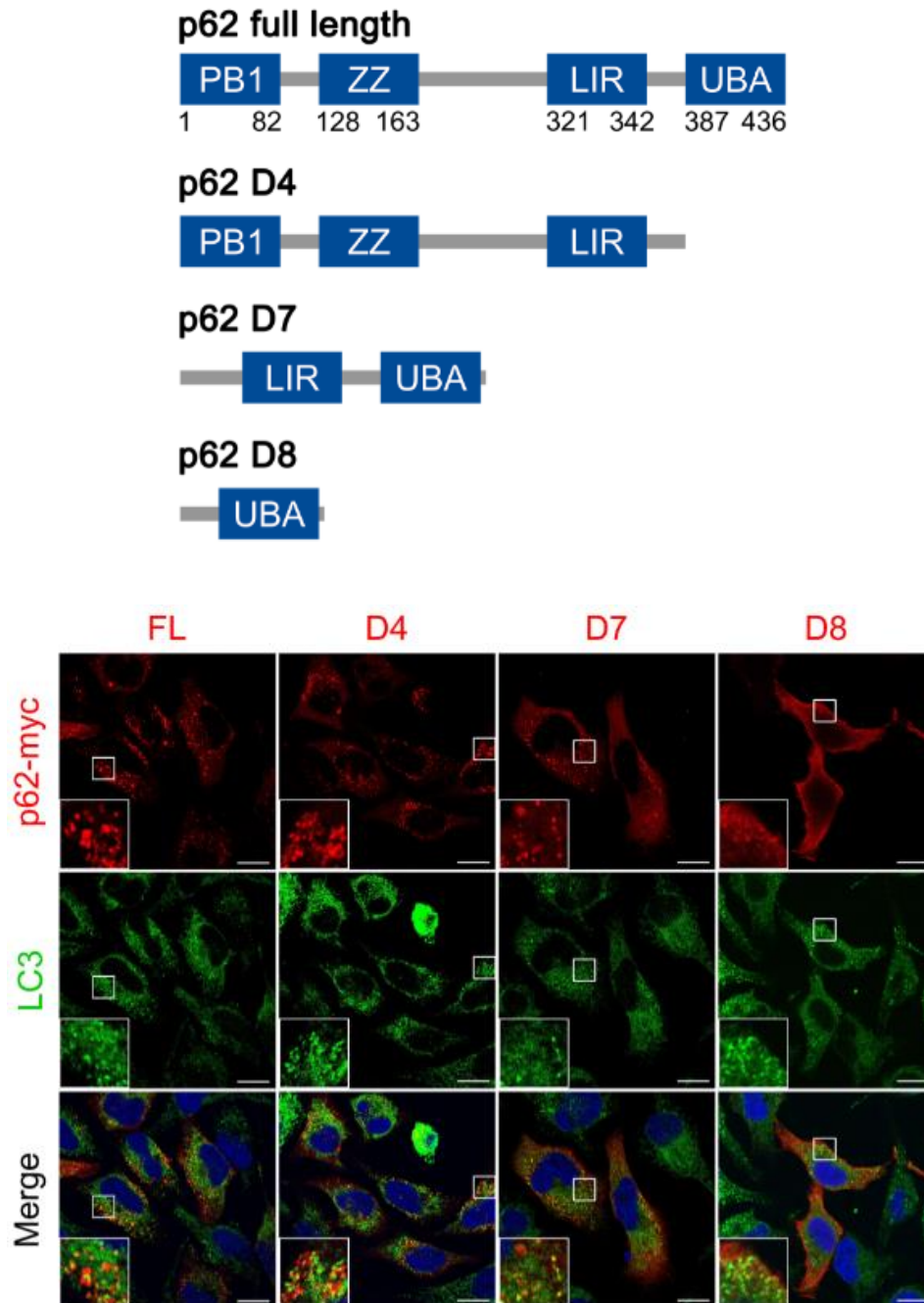


Fig. 72. Domain deletion constructs of p62 and their autophagosomal targeting. ICC in HeLa cells transiently expressing full-length (FL) or domain-deleted (D4, D7 or D8) p62-myc constructs as shown in schematic. Scale bar, 10 μ m.

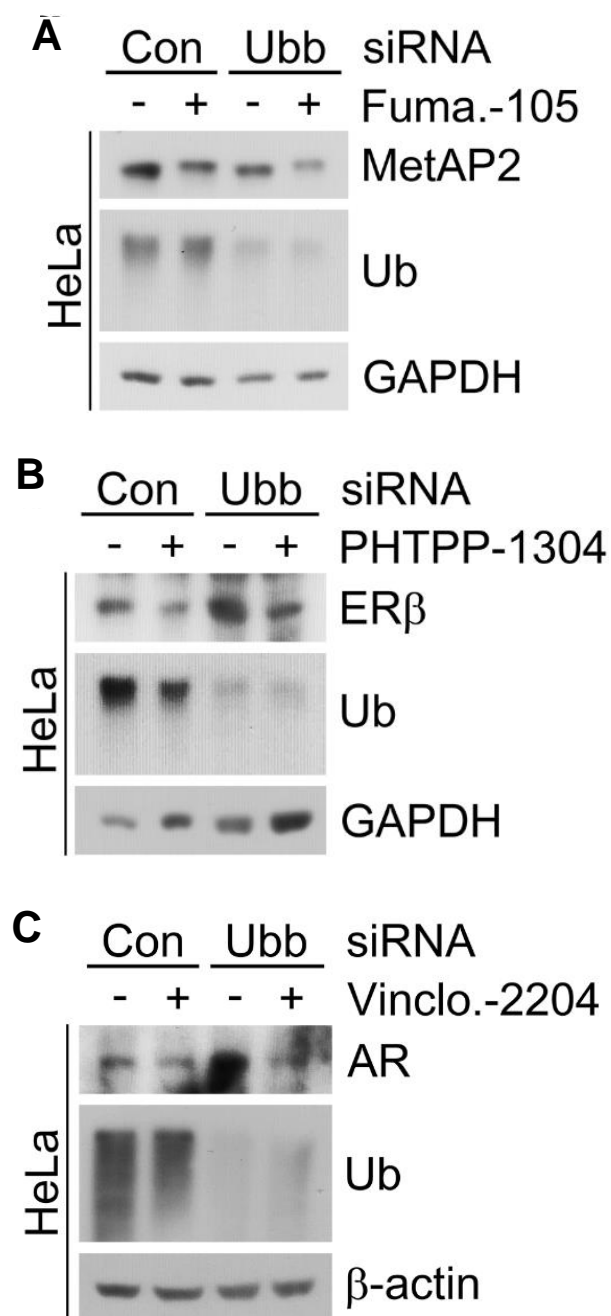


Fig. 73. AUTOTAC-dependent targeted protein degradation does not require ubiquitination. (A) WB in HeLa cells treated with fumagillin-105 (0.1 μ M, 24 h) following RNA interference of *Ubb* (40 nM, 48 h). (B) Identical to A, but with PHTPP-1304 for ER β . (C) Identical to A, but with Vinclo.-2204 for AR.

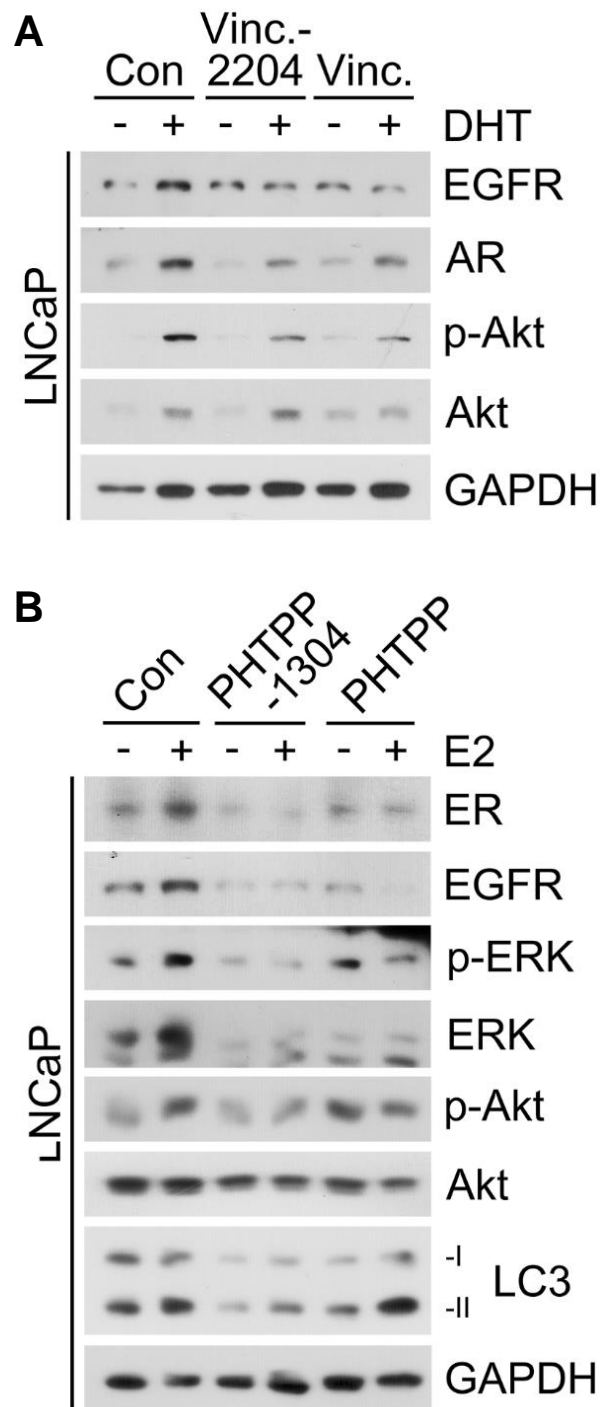


Fig. 74. Oncoprotein-targeting AUTOTACs exhibit enhanced inhibition of oncogenic signaling cascades. (A) WB in LNCaP cells treated with vinclozolinM2-2204 (2.5 μ M) or inclozolin (10 μ M) with or without DHT (15 nM) (24 h). (B) Identical to i but with PHTPP-1304 (0.5 μ M) or PHTPP (5 μ M) with or without E2 (10 nM) (24 h).

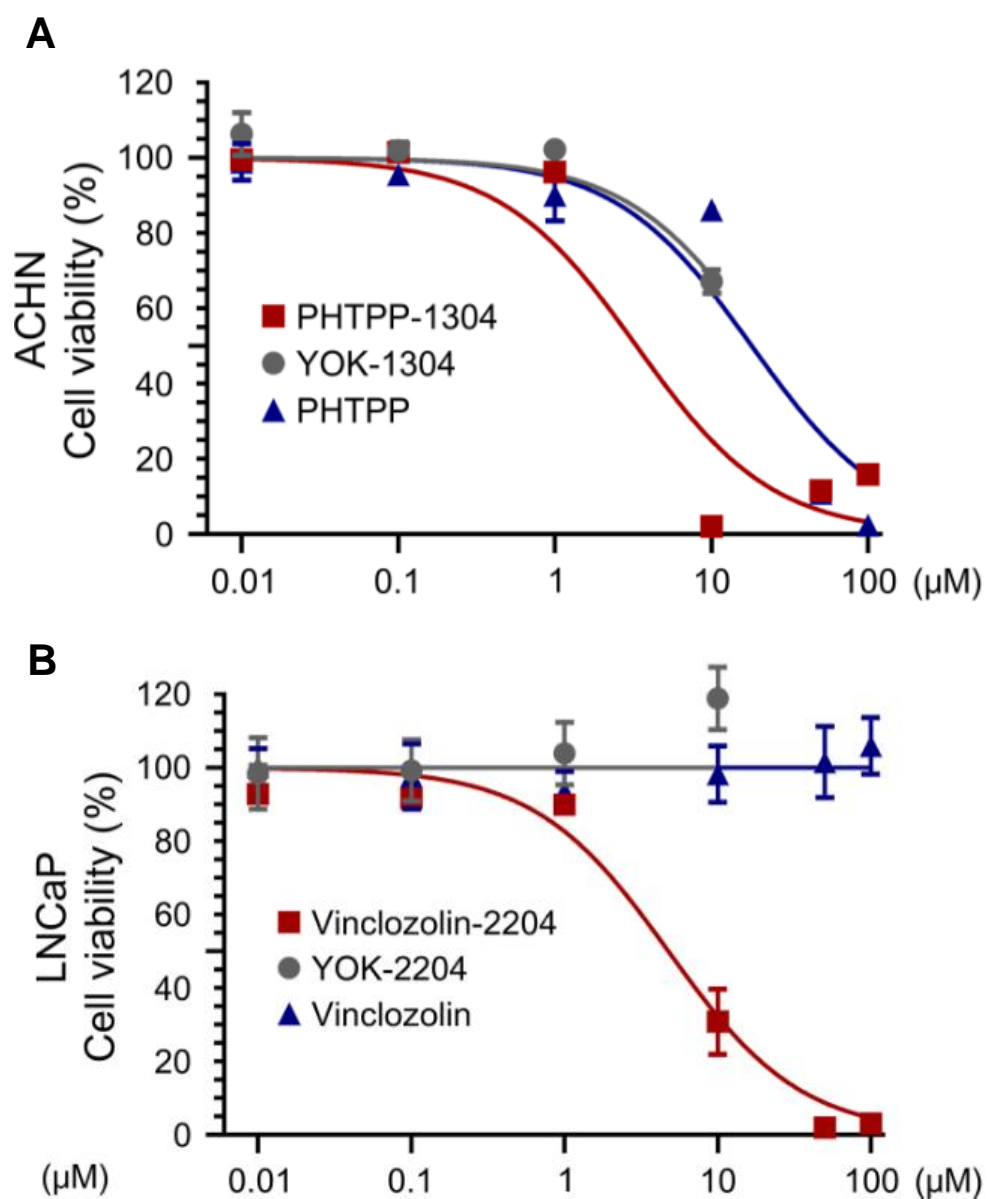


Fig. 75. Oncoprotein-targeting AUTOTACs selectively impede cancer cell proliferation. (A,B) Cell viability assay of ACHN and LNCaP cells treated with the indicated compounds and concentrations (n=2).

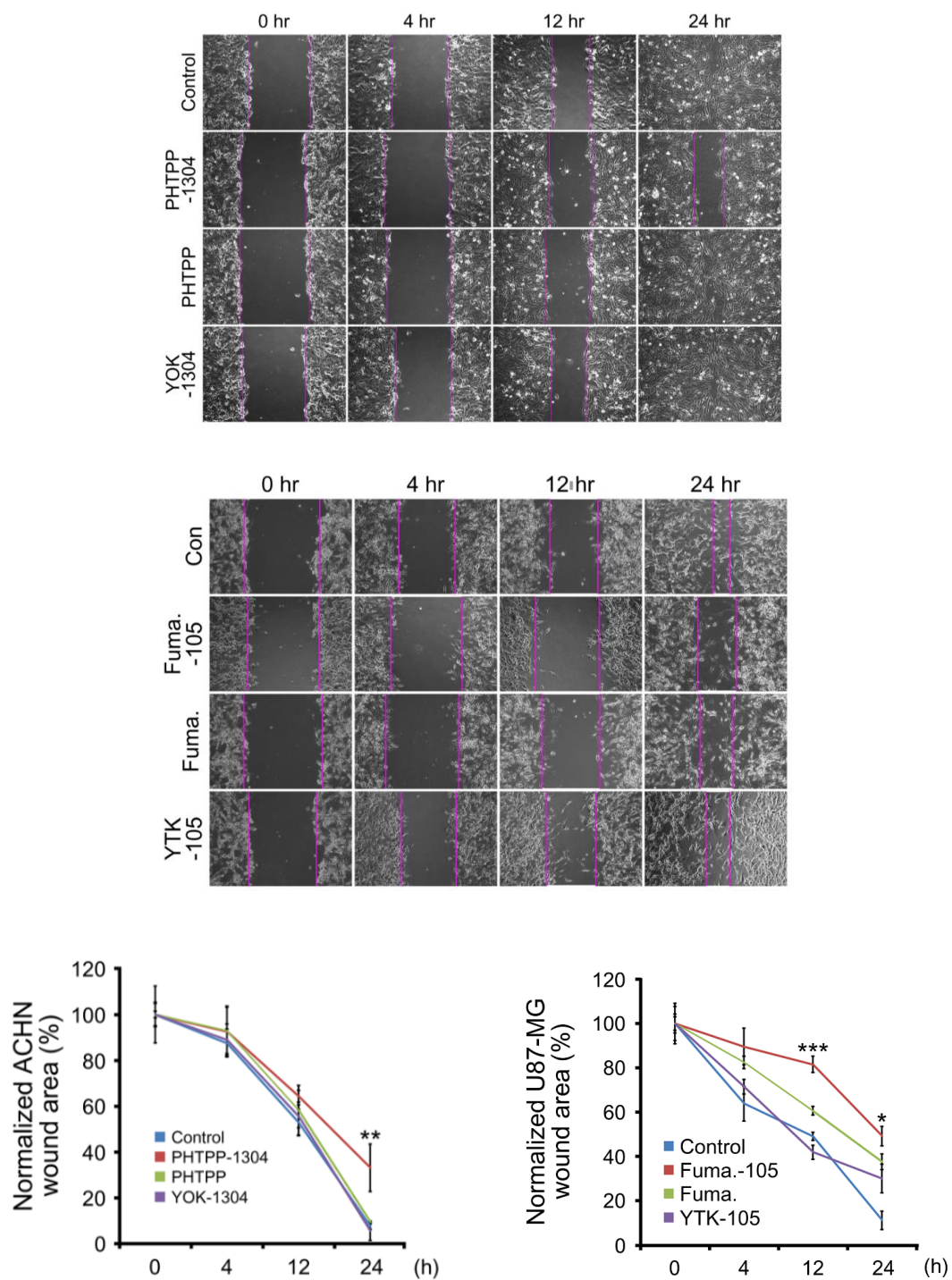


Fig. 76. Oncoprotein-targeting AUTOTACs selectively hinder cancer cell migration. (A) Wound healing assay in ACHN cells treated with PHTPP-1304, PHTPP or YOK-1304 (5 μ M) at the indicated time points. Quantification: n=2 wounds. (B) Identical to A, but with Fumagillin-105, Fumagillin or YTK-105 for MetAP2.

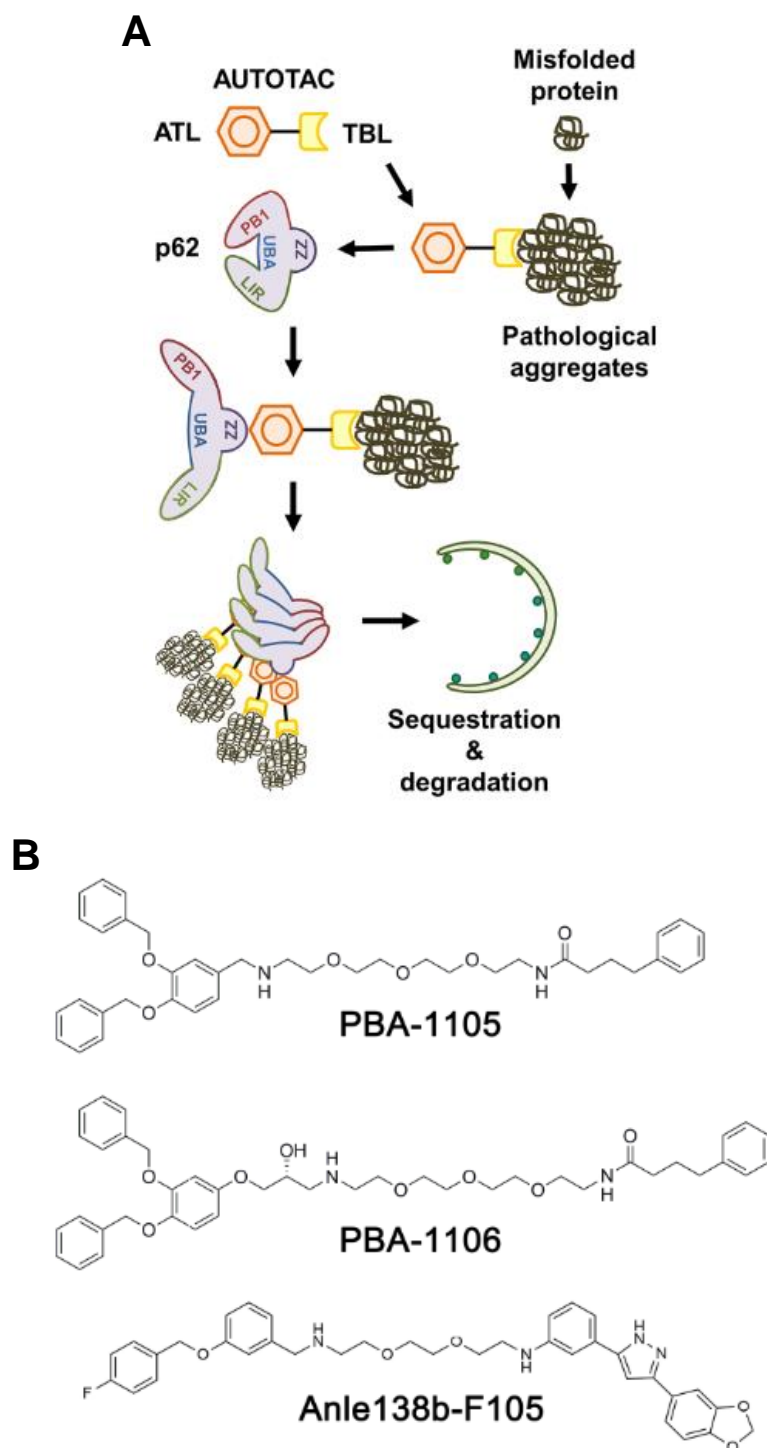


Fig. 77. Mechanism-of-action and chemical structures of proteinopathy-targeting AUTOTACs. (A) A model illustrating the mode of action of aggregate-targeting AUTOTAC. (B) Chemical structures of PBA-1105, PBA-1106, Anle138b-F105 and PBA-1105b.

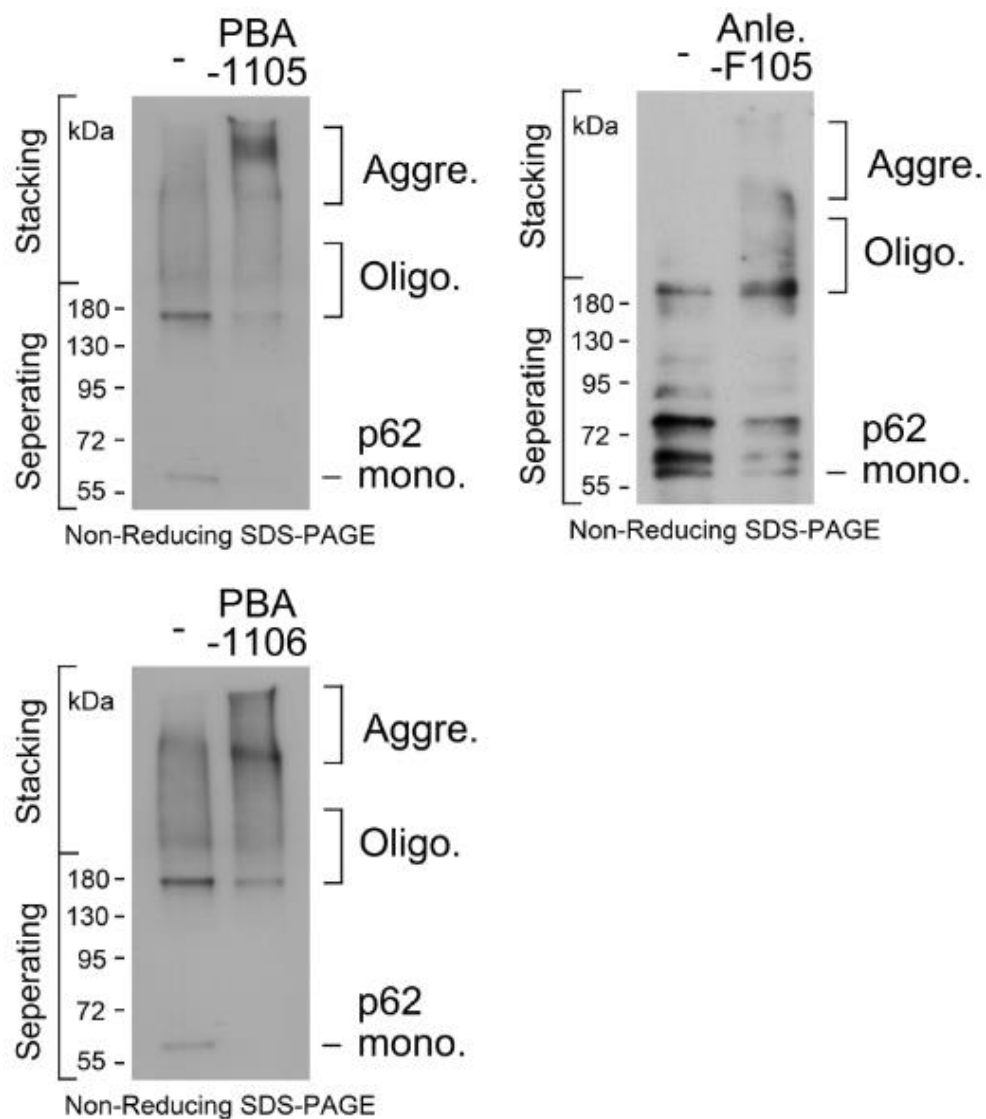


Fig. 78. Chemical chaperone-based AUTOTACs promote high molecular-weight self-oligomerization of p62. *In vitro* p62 oligomerization assay in HEK293T cells incubated with the indicated compounds.

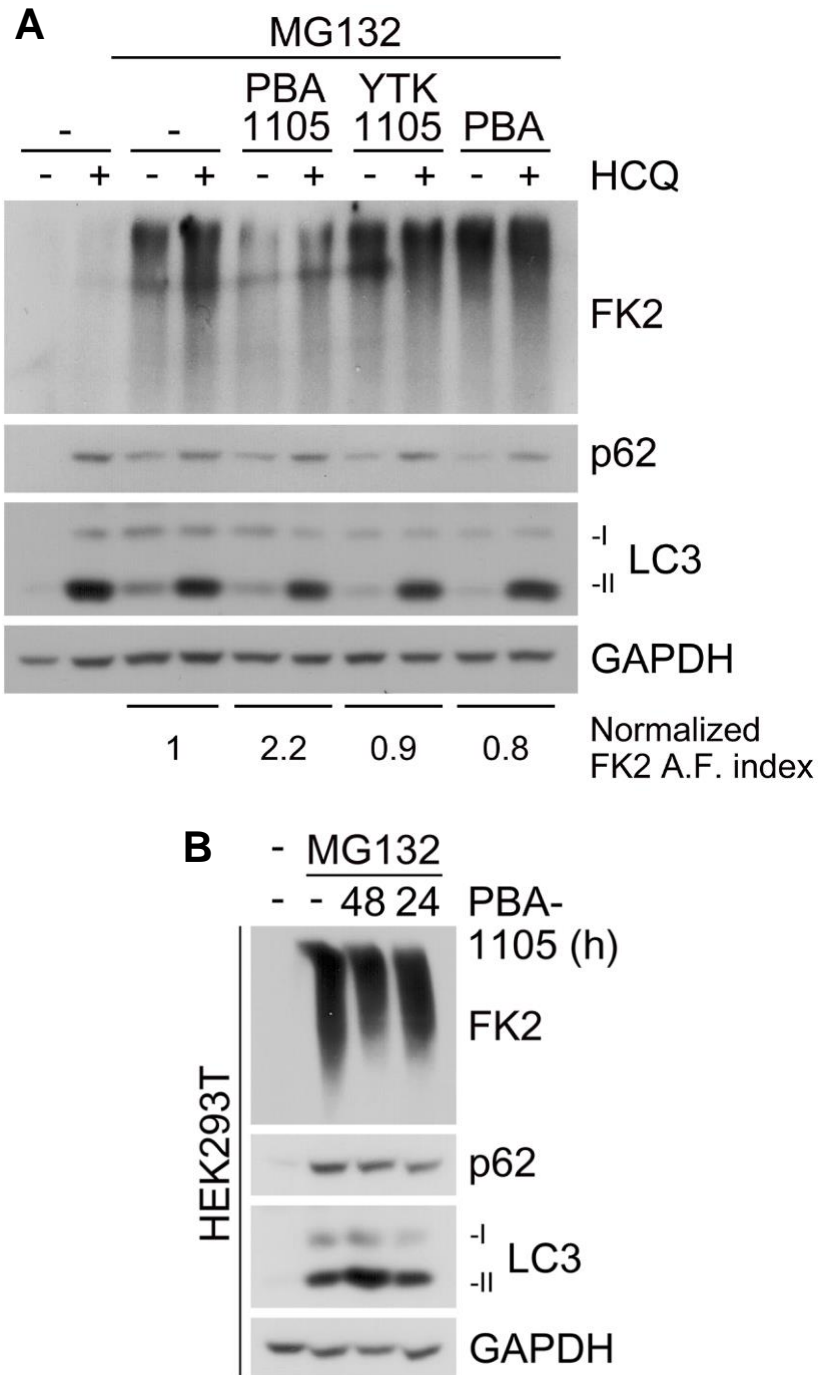


Fig. 79. PBA-based AUTOTACs selectively accelerates. (A) WB in HEK293T cells treated with MG132 (1 μ M, 24 h), HCQ (10 μ M, 24 h), PBA-1105, YTK-1105, and PBA (1 μ M, 24 h). (B) WB in HEK293T cells treated with PBA-1105 (1 μ M) and MG132 (1 μ M, 24 h) at the indicated time points.

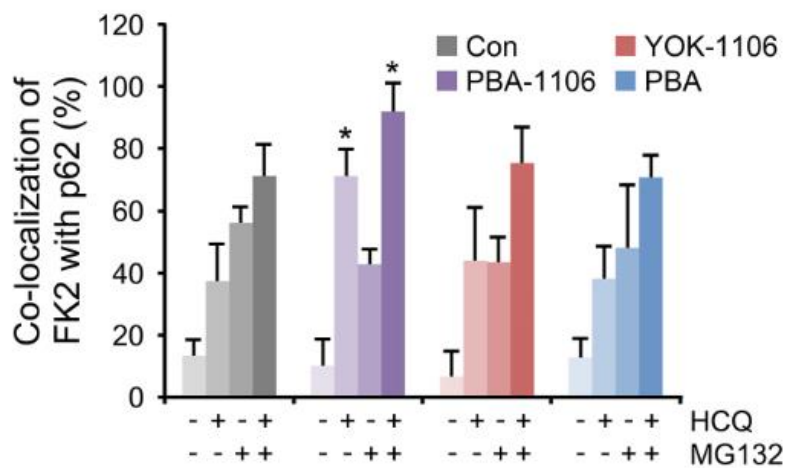
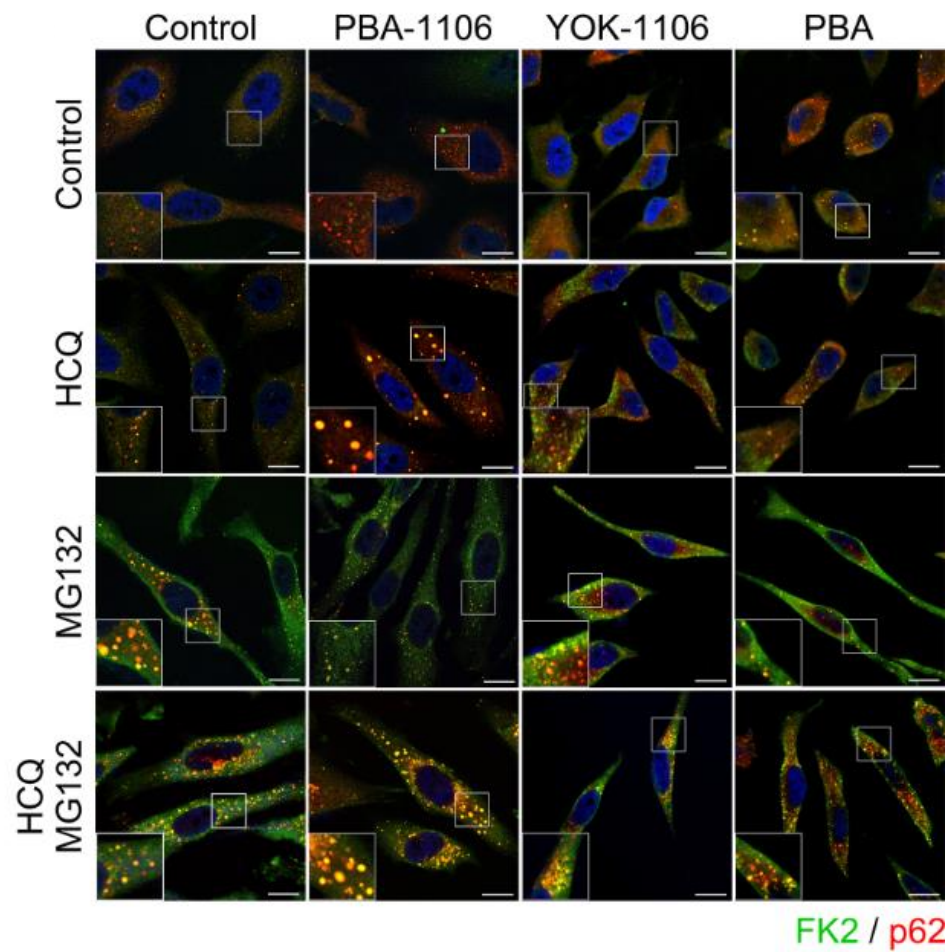


Fig. 80. PBA-based AUTOTACs selectively deliver ubiquitin-conjugated protein aggregates to p62-associated autophagic membranes. ICC of HeLa cells treated with HCQ (10 μ M, 24 h), MG132 (2 μ M, 18 h) or both in the presence of PBA-1106, YOK-1106 or PBA (1 μ M, 24 h). Scale bar, 10 μ m. Quantification: n=50 cells.

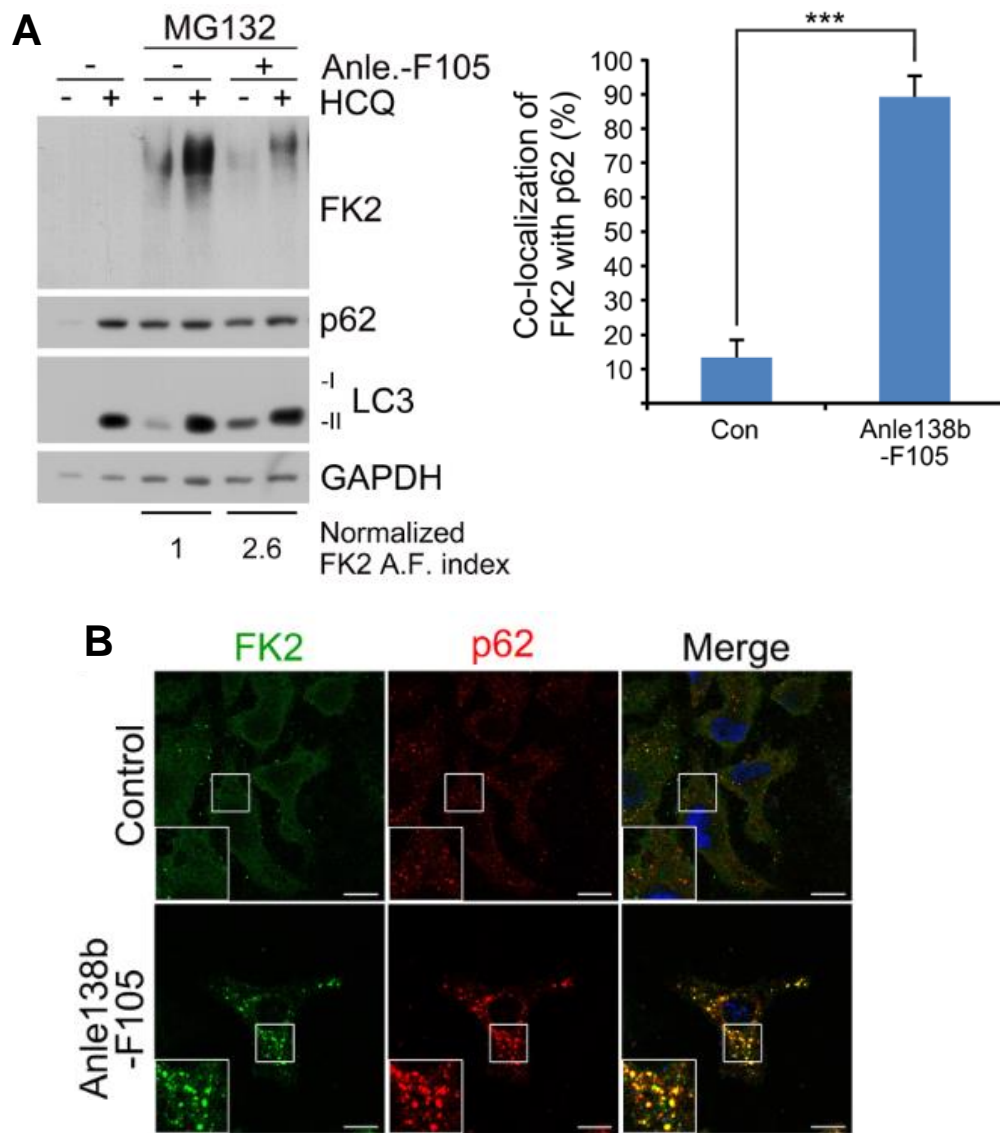


Fig. 81. Anle138b-based AUTOTAC targets ubiquitin-conjugated protein aggregates to p62 bodies for autophagic clearance. (A) WB in HEK293T cells treated with MG132 (1 μ M, 24 h), HCQ (10 μ M, 24 h), and Anle138b-F105 (1 μ M, 24 h). **(B)**

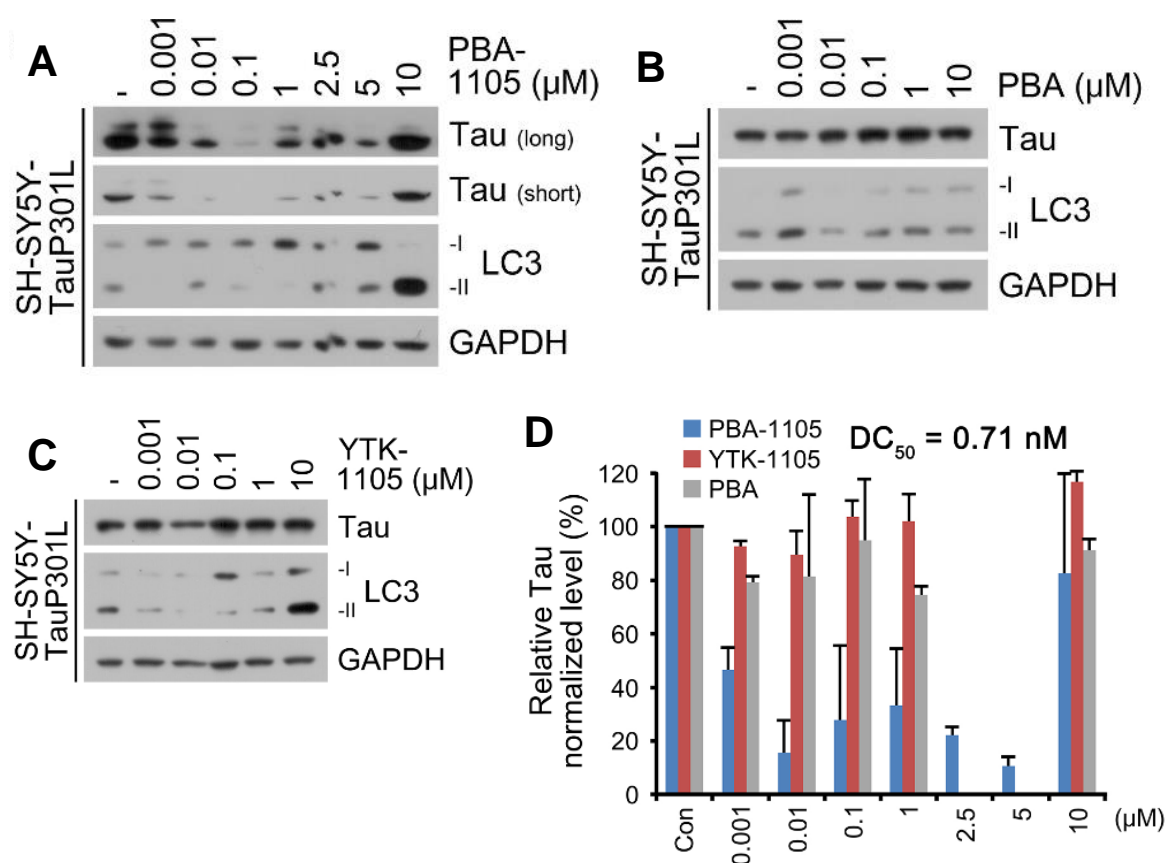


Fig. 82. Dosage-dependent & selective degradation of mutant tauP301L by PBA-based AUTOTACs. (A,B,C,D) WB in SH-SY5Y-tauP301L cells treated with PBA-1105, PBA or YTK-1105 at the indicated concentrations. Densitometry of mutant tauP301L relative to GAPDH (n=3).

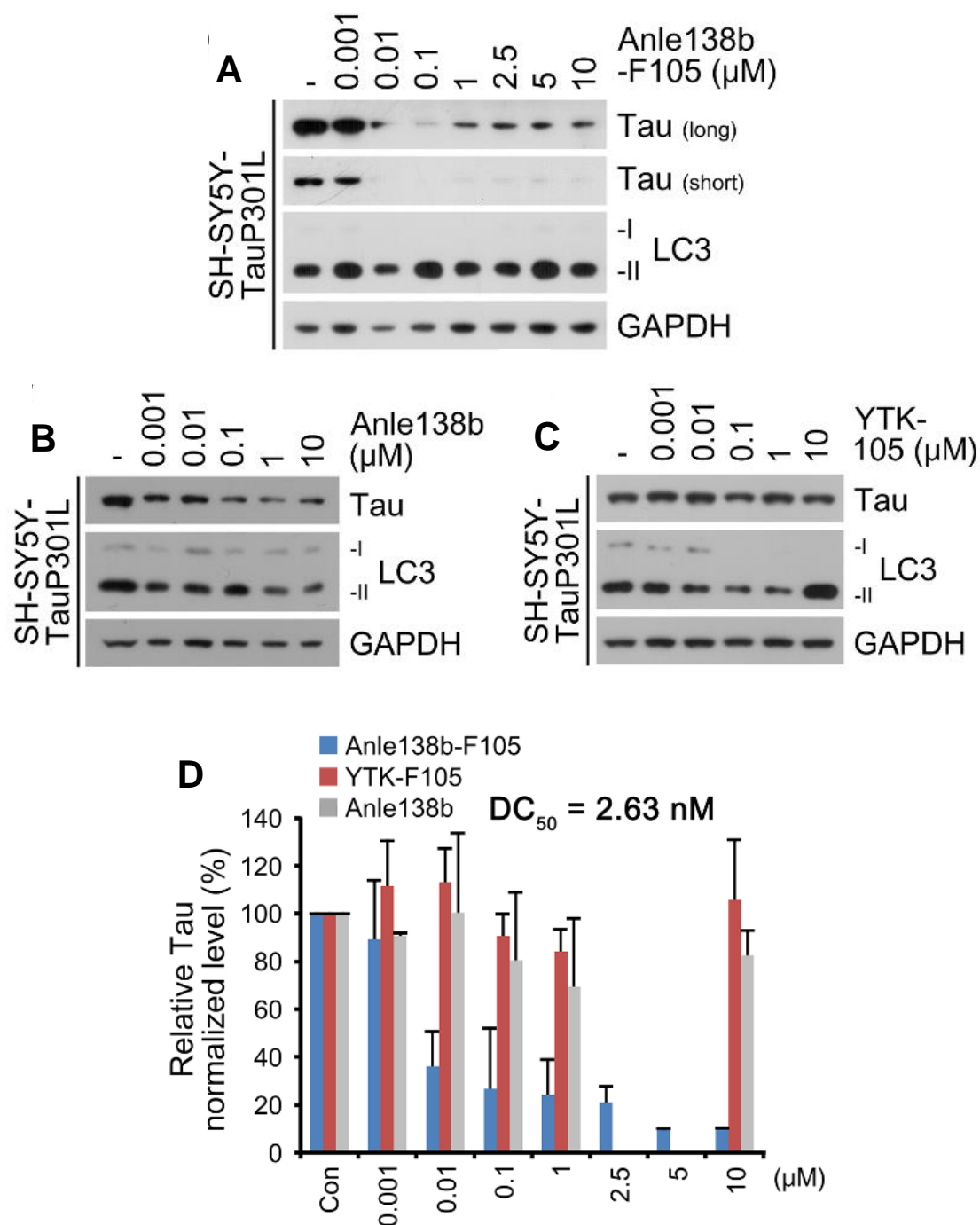


Fig. 83. Dosage-dependent & selective degradation of mutant tauP301L by Anle138b-based AUTOTACs. (A,B,C,D) WB in SH-SY5Y-tauP301L cells treated with Anle138b-F105, Anle138b or YTK-105 at the indicated concentrations. Densitometry of mutant tauP301L relative to GAPDH (n=3).

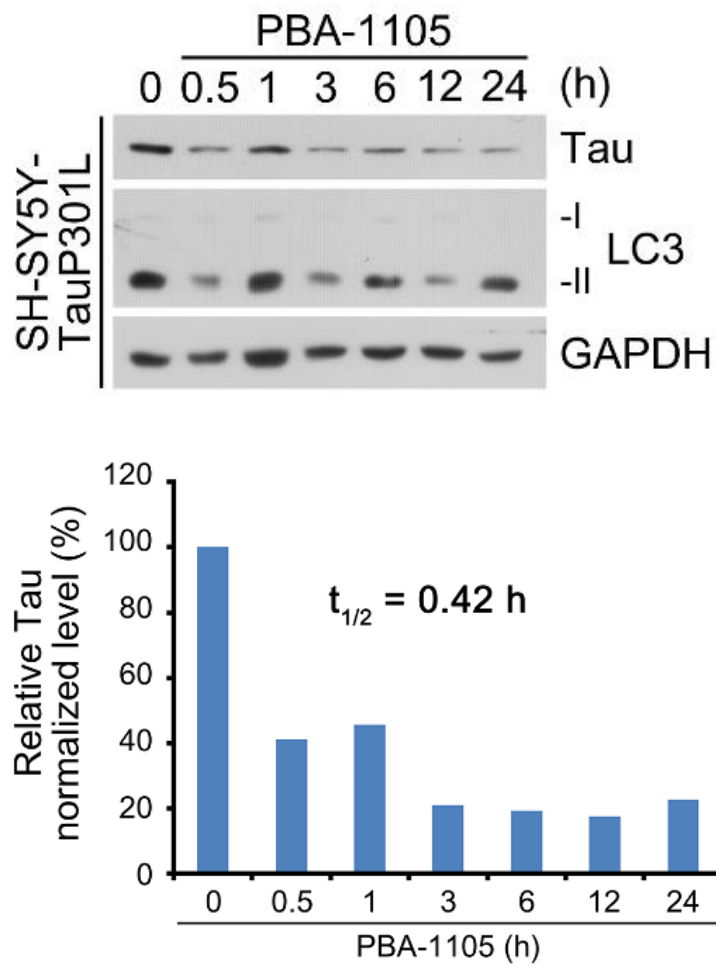


Fig. 84. Anti-aggregate AUTOTACs rapidly degrade mutant tauP301L. WB in SH-SY5Y-tauP301L cells treated with PBA-1105 (0.1 μ M) at the indicated time points. Densitometry of mutant tauP301L relative to GAPDH.

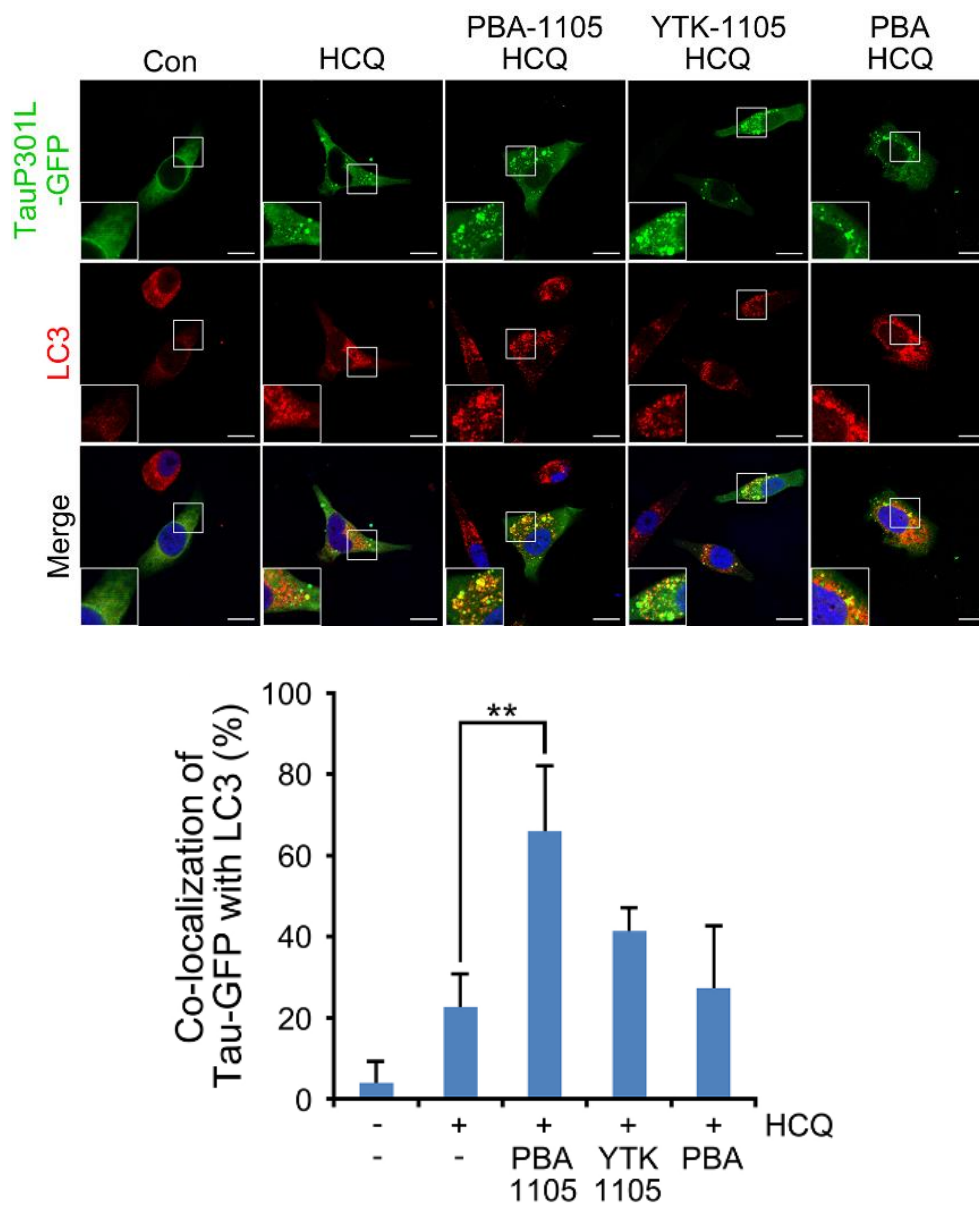


Fig. 85. PBA-based AUTOTACs selectively sequester and target tauP301L for macroautophagy. ICC of HeLa cells expressing recombinant TauP301L-GFP and treated with the indicated compounds (1 μ M, 24 h) and HCQ (10 μ M, 24 h). Scale bar, 10 μ m. Quantification: n=50 cells.

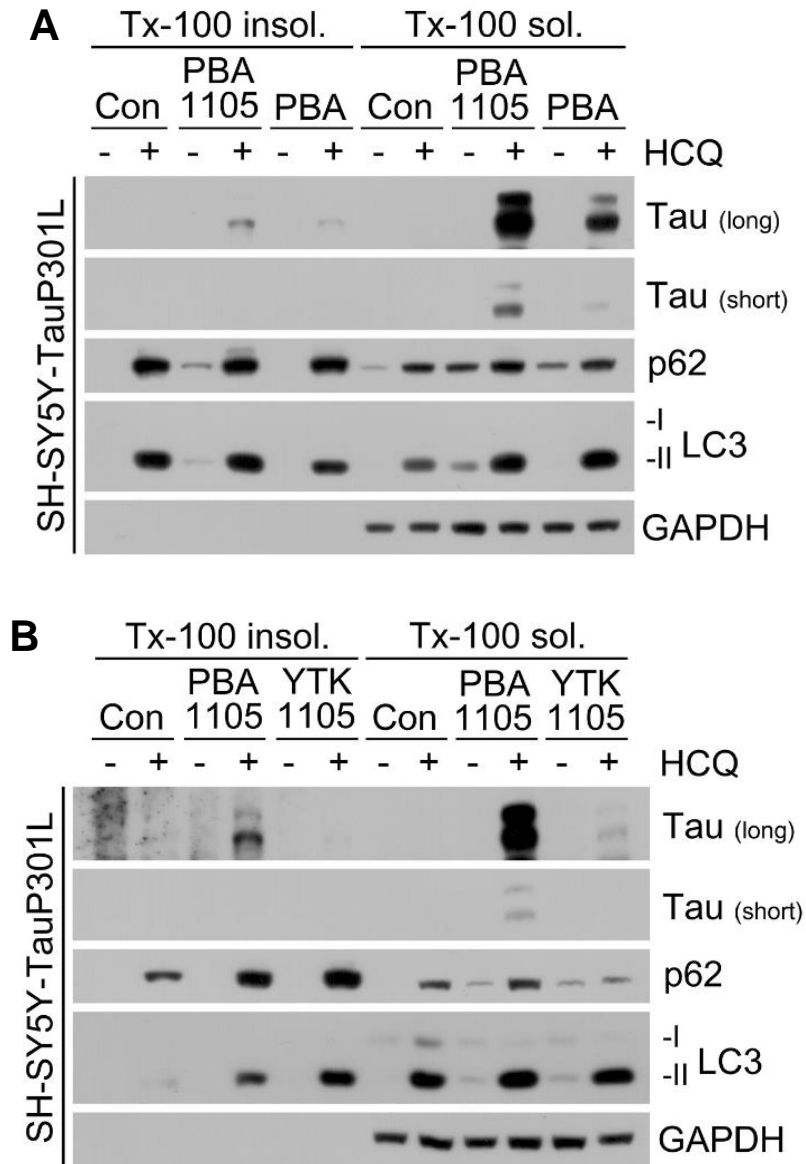


Fig. 86. PBA-based AUTOTACs accelerate lysosomal flux of insoluble mutant tauP301L. (A,B) Triton X-100-insoluble fractionation assay in SH-SY5Y-tauP301L cells treated with PBA-1105 and PBA or YTK-1105 (2.5 μ M, 24 h), respectively and HCQ (10 μ M, 24 h).

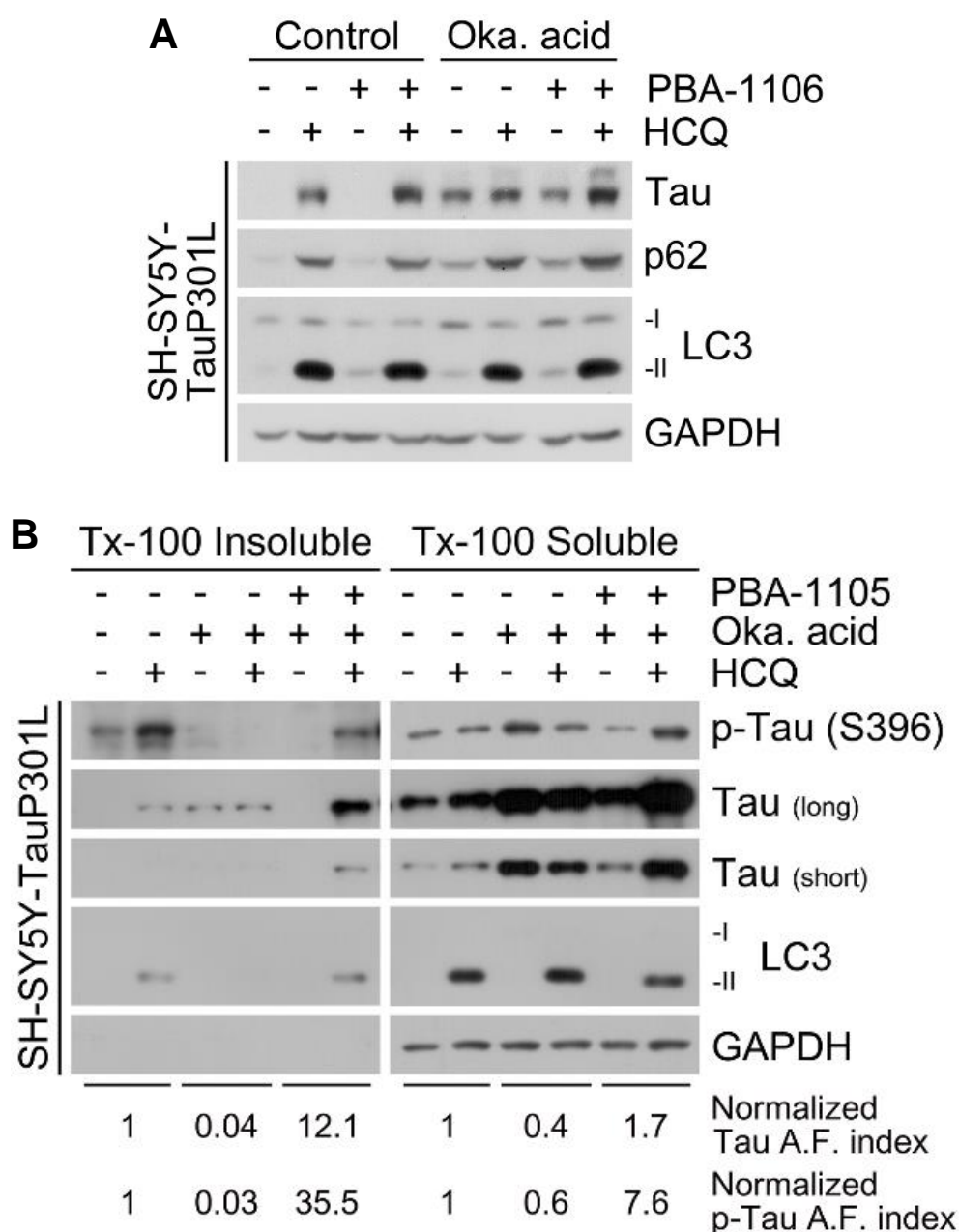


Fig. 87. PBA-based AUTOTACs rescue autophagic flux of hyper-phosphorylated mutant tauP301L. (A) WB in SH-SY5Y-tauP301L cells treated with HCQ (25 μ M, 24 h), okadaic acid (15 nM, 24 h) and PBA-1106 (0.1 μ M, 24 h). (B) Triton X-100-fractionation assay in SH-SY5Y-tauP301L cells treated with a combination of HCQ (10 μ M, 24 h), okadaic acid (15 nM, 24 h) or PBA-1105 (0.1 μ M, 24 h).

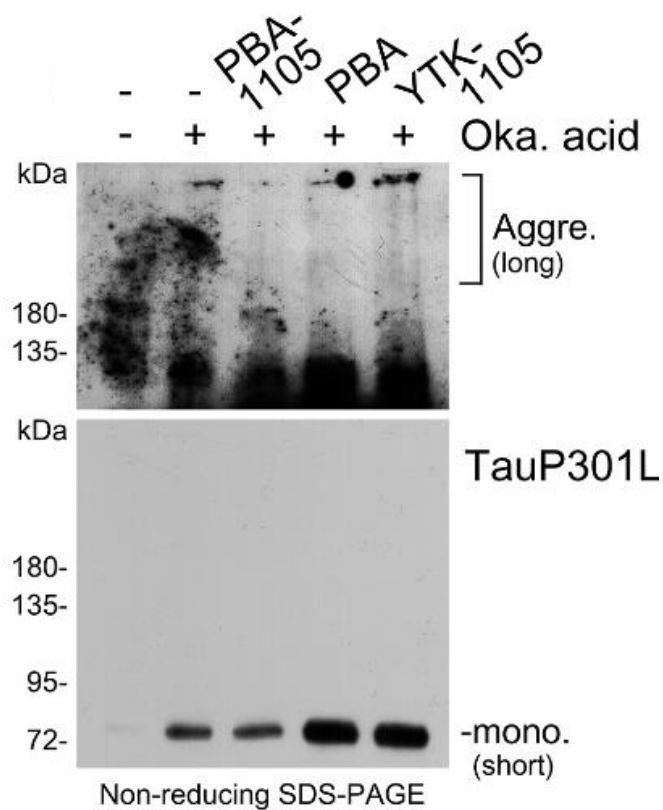


Fig. 88. PBA-based AUTOTACs specifically target high-molecular, aggregated species of mutant tauP301L for degradation. *In vivo* oligomerization assay in SH-SY5Y-tauP301L cells treated with okadaic acid (15 nM, 24 h) and the indicated compounds (0.1 μ M, 24 h).

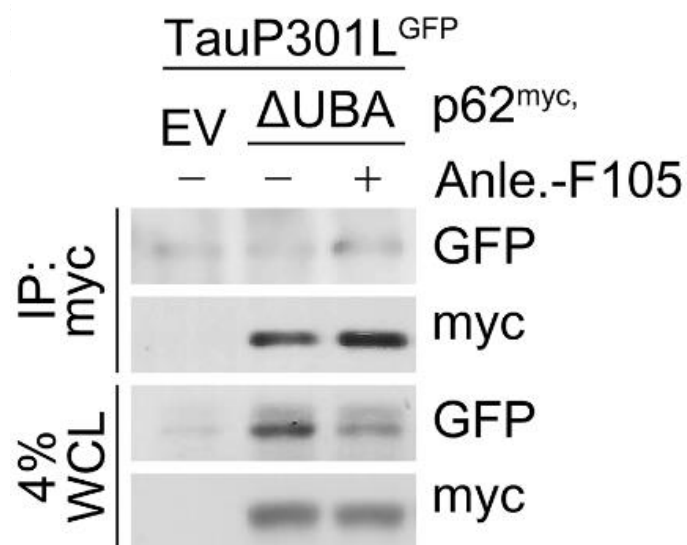


Fig. 89. AUTOTAC-induced interaction between tauP301L and p62 is independent of ubiquitin chain recognition. Co-IP assay in HEK293T cells co-transfected (24 h) with Δ UBA p62-myc and hTauP301L-GFP or negative control empty vector (EV), treated with Anle138b-F105 (1 μ M, 24 h) or negative control.

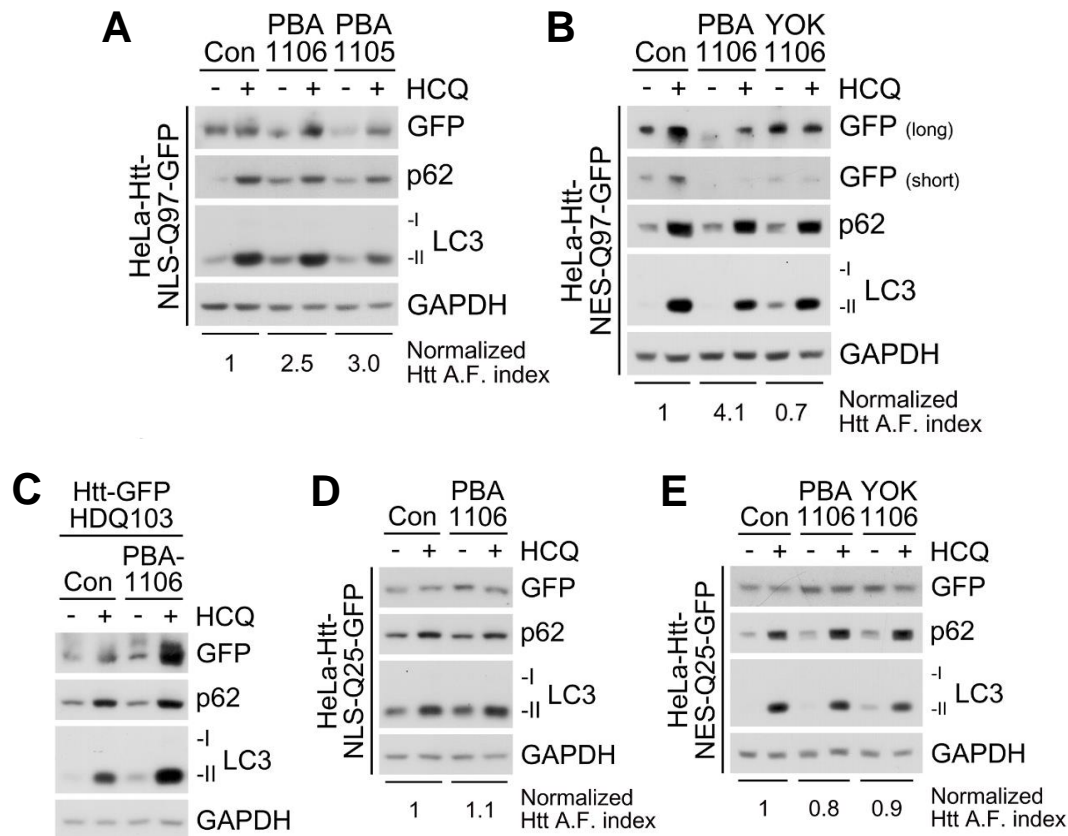


Fig. 90. PBA-based AUTOTACs selectively accelerate autophagic proteolysis of mutant HttQ97 as opposed to wild-type HttQ25. (A) WB in HeLa-Htt-NLS-Q97-GFP cells treated with PBA-1106 or PBA-1105 (2.5 μ M, 24 h) with or without HCQ (25 μ M, 24 h). (B) Identical to A but with YOK-1106 instead of PBA-1105 in HeLa-Htt-NES-Q97-GFP cells. (C) WB in HeLa cells transfected with Htt-GFP-HDQ103 and treated with PBA-1106 (2.5 μ M, 24 h) and HCQ (25 μ M, 24 h). (D) WB in HeLa-Htt-NLS-Q25-GFP cells treated with PBA-1106 (2.5 μ M, 24 h) with or without HCQ (25 μ M, 24 h). (E) Identical to D, but with PBA-1106 and YOK-1106 (2.5 μ M, 24 h) in HeLa-Htt-NES-Q25-GFP cells.

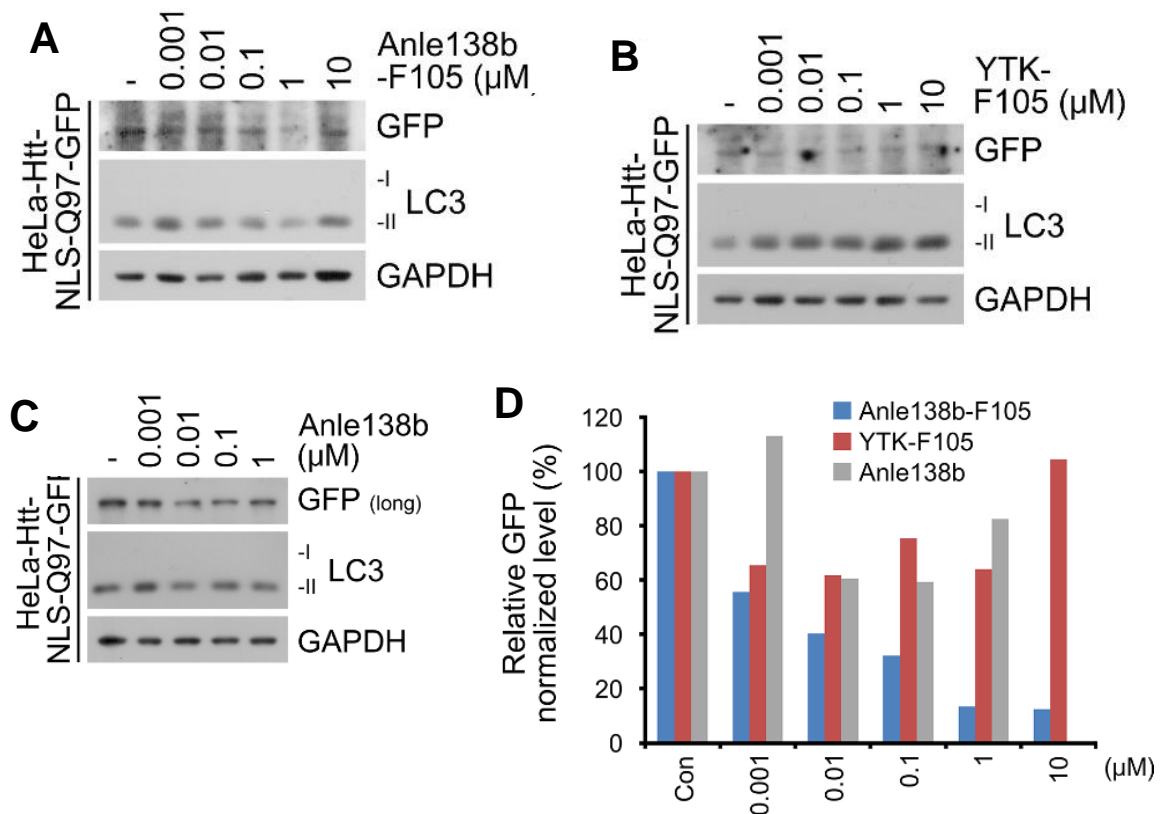


Fig. 91. Dosage-dependent & selective degradation of mutant HttQ97 by Anle138b-based AUTOTAC. (A,B,C,D) WB in HeLa-Htt-NLS-Q97-GFP cells treated resectively with Anle138b-F105, YTK-105 or Anle138b with the indicated concentrations (24 h). Densitometry of mutant Htt-NLS-Q97 relative to GAPDH.

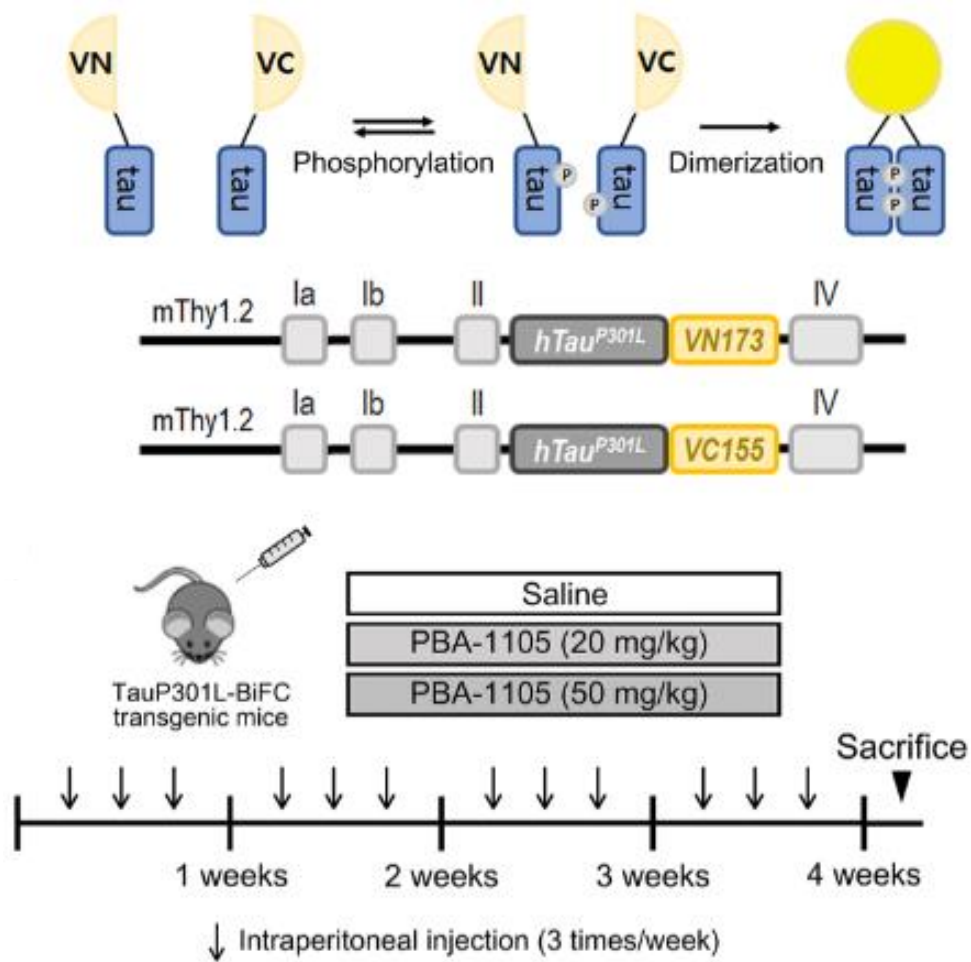


Fig. 92. Schematic illustration of brain-specific hTauP301L-BiFC murine model

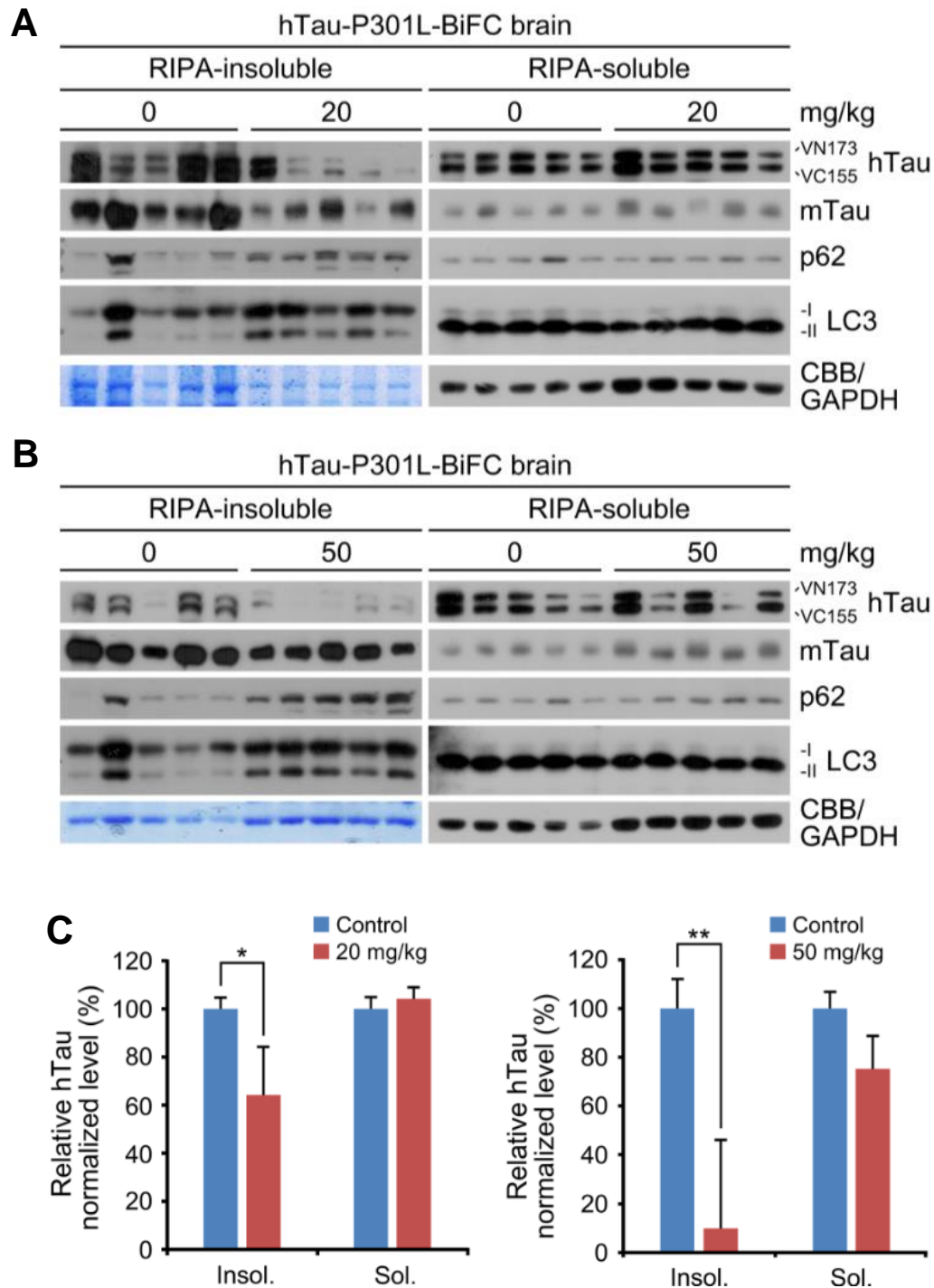
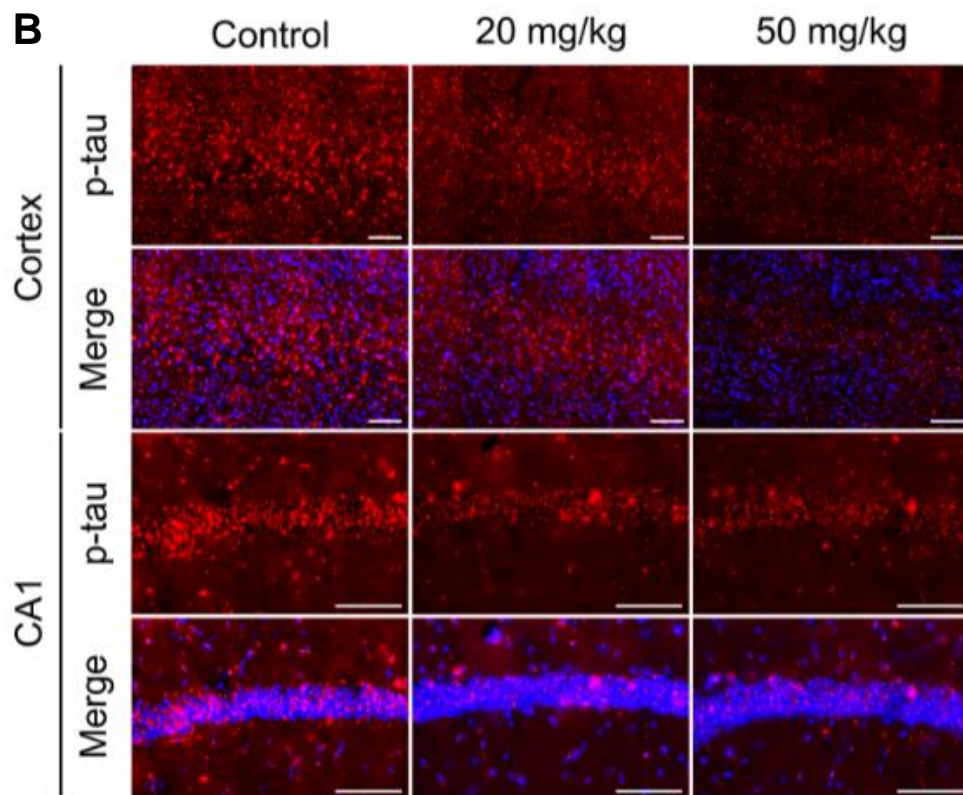
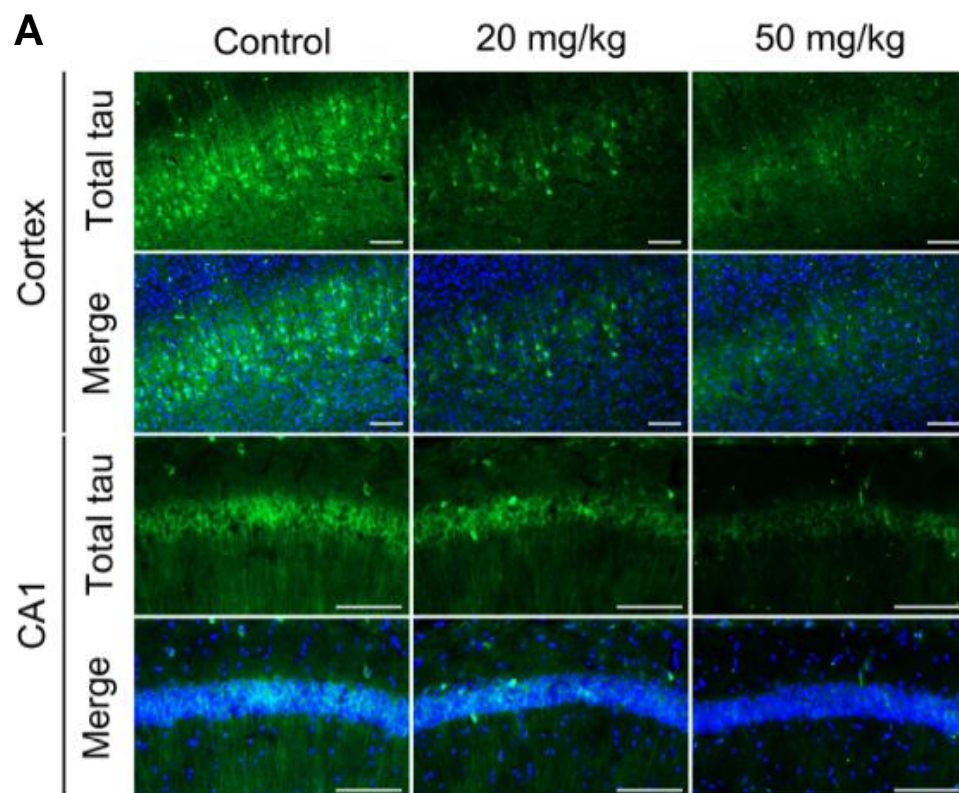


Fig. 93. PBA-based AUTOTAC degrades insoluble mutant tauP301L in murine brains. (A,B,C) RIPA-insoluble fractionation assay in brain tissues of hTauP301L-BiFC mice intraperitoneally injected with PBA-1105 (20 or 50 mg/kg). Normalized densitometry of **A** and **B** for hTau levels, respectively (n=5 mice for 20 or 50 mg/kg).



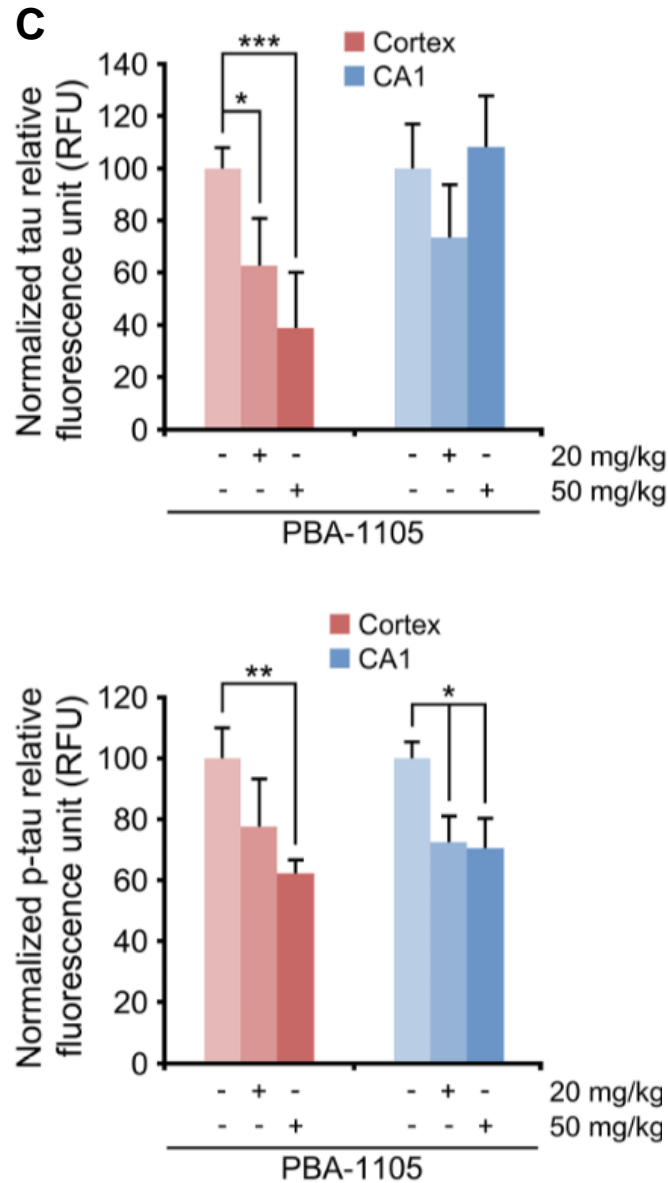


Fig. 94. PBA-based AUTOTAC eliminates both total and phosphorylated mutant tauP301L oligomers and aggregates in murine brains. (A,B) Immunohistochemistry of BiFC fluorescence for total hTau levels or AT8 fluorescence for total phosphorylated levels in hTauP301L-BiFC mice injected with PBA-1105. Scale bar, 100 μ m. (c) Quantification of BiFC or AT8 punctate fluorescence signals in **A** and **B**, respectively (n=7 mice).

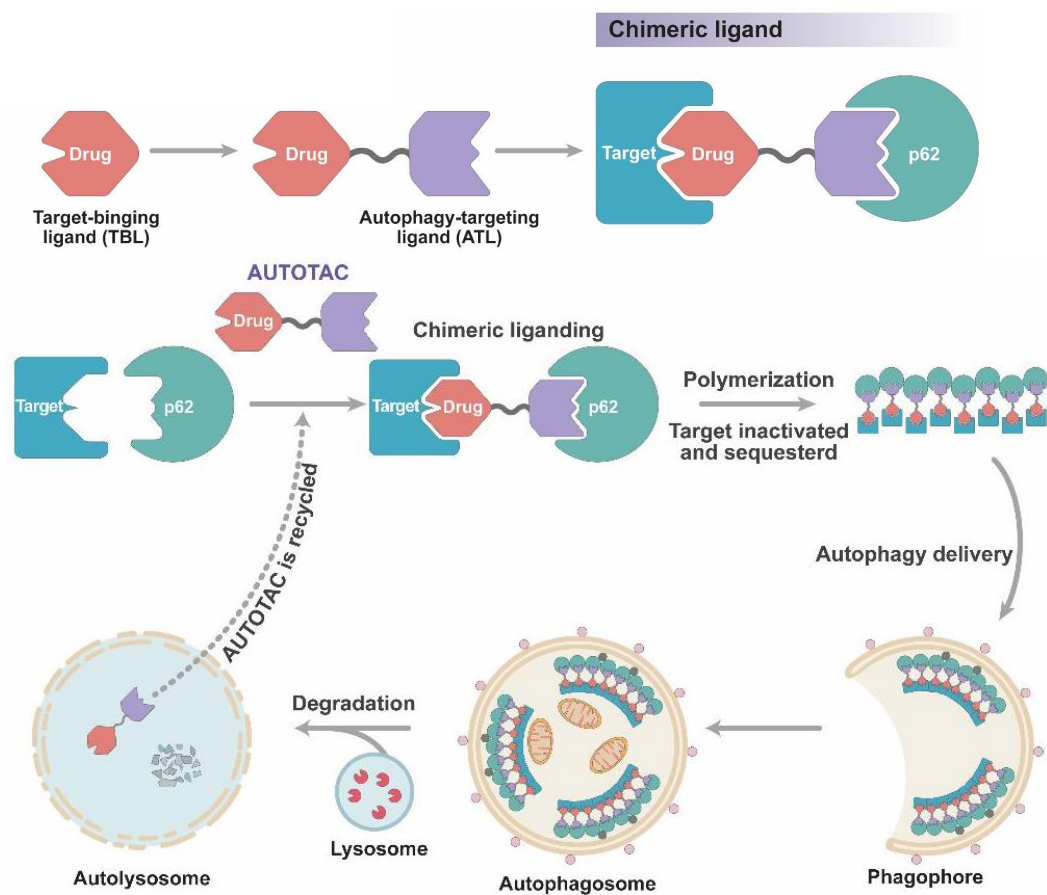


Fig. 95. Schematic of the mechanism-of-action of AUTOTAC

Materials & Methods

Plasmids and other reagents

The recombinant neurodegenerative hallmark protein plasmid was constructed as follow. The GFP tagged Htt-103 plasmid was constructed into pcDNA3.1/*myc*-His plasmid (Thermo Fisher Scientific) at *EcoRI*/*XhoI* sites using PCR amplification. The TauP301L plasmid was a gift from Min Jae Lee (Seoul National University, Korea). These plasmids were transiently transfected using Lipofectamine 2000 or Lipofectamine 3000 (Thermo Fisher Scientific). Other reagents used in this study were bafilomycin A1, hydroxychloroquine, (Sigma); MG132 (Enzo);

Transfection

Plasmids were transfected into HeLa and HEK293T cells using the Lipofectamine 2000 Transfection Reagent according to the manufacturer's instructions (Invitrogen).

RNA interference analysis

Cells in a 12-well plate (0.5×10^6 per well) were transfected with 40 nM siRNA using RNAiMax reagent (Thermo Fisher Scientific). The sequences of pre-designed Silencer Select siRNAs (Thermo Fisher Scientific) against p62, and of pre-designed siRNA (Bioneer) against siubb or siATG5 are as follows: sip62 (sense, 5'-GUGAACUCCAGUCCCUACA-3'; antisense, 5'-UGUAGGGACUGGAGUUCAC-3'), siubb (sense, 5'-CCAGCAGAGGCUCAUCUUU-3'; antisense, 5'-AAAGAUGAGCCUCUGCUGG-3') and siATG5 (sense, 5'-CCUUUCAUUCAGAAGCUGUtt-3'; antisense, 5'-ACAGCUUCUGAAUGAAAGGtc -3').

Antibodies

The antibodies used in this study are as follows: mouse monoclonal anti-p62 (Abcam, ab56416, 1: 10,000), rabbit polyclonal anti-LC3 (Sigma, L7543, 1:10,000), rabbit polyclonal anti-ATE1 (Sigma, HPA038444, 1:1000), mouse monoclonal anti-FK2 specific to Ub-conjugated proteins (Enzo, BML-PW8810, 1:3000), rabbit polyclonal anti-GAPDH (BioWorld, AP0063, 1:20,000), rabbit polyclonal anti-b-actin (BioWorld, AP0060, 1:20,000), mouse monoclonal anti-MetAP2 (Santa Cruz, sc-365637, 1:2000), rabbit polyclonal anti-ER β (Invitrogen, PA1-310B, 1:2000), rabbit polyclonal anti-Androgen Receptor (Cell Signaling, 3202, 1:5000), rabbit polyclonal anti-EGFR (Cell Signaling, 4265, 1:2000), rabbit polyclonal anti-p-Akt (Cell Signaling, 9271, 1:2000), rabbit polyclonal anti-Akt (Cell Signaling, 2920, 1:1000), rabbit polyclonal anti-p-ERK (Cell Signaling, 9101, 1:1000), rabbit polyclonal anti-ERK (Cell Signaling, 9102, 1:1000), rabbit polyclonal anti-ATG5 (Novus, NB110-53818, 1:1000), mouse monoclonal anti-Ub (Santa Cruz, sc-8017, 1:2000), mouse monoclonal anti-GFP (Santa Cruz, sc-9996, 1:2000), mouse monoclonal anti-Tau5 (Invitrogen, AHB0042, 1:5000), rabbit polyclonal anti-p-Tau (Invitrogen, 44-752G, 1:5000). The following secondary antibodies were used: alexa fluor 488 goat anti-rabbit IgG (Invitrogen, A11034, 1:1000), alexa fluor 488 goat anti-mouse IgG (Invitrogen, A11029, 1:1000), alexa fluor 555 goat anti-rabbit IgG (Invitrogen, A32732, 1:1000), alexa fluor 555 goat anti-mouse IgG (Invitrogen, A32727, 1:1000), anti-rabbit IgG-HRP (Cell Signaling, 7074, 1:10,000), and anti-mouse IgG-HRP (Cell Signaling, 7076, 1:10,000).

Cells and cell culture

HeLa, HEK293T, U-87 MG, ACHN, MCF7 and LNCaP cell lines were obtained from ATCC. SH-SY5Y-tau-GFP and HeLa-NLS/NES-Htt-Q25/Q97-eGFP cell lines were a gift from Min Jae Lee (Seoul National University, Korea). HeLa, HEK293T,

SH-SY5Y-tau-GFP, HeLa-NLS/NES-HTT-Q25/Q97-EGFP, U-87 MG, ACHN, MCF7 and LNCaP cell lines were cultured in Dulbecco's Modified Eagle's Medium, MEM medium or RPMI-1640 medium with 10% Fetal Bovine Serum and antibiotics (100 units/mL penicillin and 100 µg/mL streptomycin) in a 5% CO₂ incubator. For stable cell lines, expression of intended tagged target protein(s) was confirmed by immunoblotting and/or immunocytochemistry.

Western blotting (WB)

Adherent cells were washed with phosphate-buffered saline (PBS) and cell pellets were lysed in SDS-based sample buffer (277.8 mM Tris-HCl, pH 6.8, 4.4% LDS, 44.4% (v/v) glycerol) containing beta-mercaptoethanol. Alternatively, cell pellets or protein supernatants were lysed in 5X Laemmli sample buffer. Whole cell lysates were separated using SDS-PAGE, and transferred onto polyvinylidene difluoride membranes at 100 V for 2 h at 4°C. The membrane was incubated with a blocking solution consisting 4% skim milk in PBS solution for 30 min at room temperature and incubated with primary antibodies overnight, followed by incubation with host-specific HRP-conjugated secondary antibodies (1:10000 dilution). For signal detection, the membrane was developed with a mixture of ECL solution (Thermo Fisher Scientific) using X-ray films. Densitometry of developed bands was measured and analyzed with ImageJ (NIH, Bethesda).

Chemical synthesis and analytical data of Nt-Arg-mimicking compounds

Scheme 1: Synthesis of 2-((2-((3-((4-fluorobenzyl)oxy)benzyl)amino)ethyl)amino)ethan-1-ol YT-8-8.

Step 1: To a solution of (3,5)-dihydroxybenzene (50 g, 0.45 mol) in ACN (500 mL) were added K₂CO₃ (112.5 g, 0.81 mol) and (2-bromoethyl)benzene (83.2 g, 0.45 mol).

The mixture was stirred at 60 °C for 10 hrs. The reaction was filtered and concentrated. The crude was purified by column chromatography on silica gel (PE/EA=5:1) to give compound 2-4 (25 g) as yellow oil.

Step 2: To a solution of compound 2-4 (800 mg, 3.48 mmol) in MeOH (4 mL) was added 2-(2-aminoethylamino)ethanol (389 mg, 3.74 mmol). The mixture was stirred at 65 °C for 6 hrs. Then NaBH₄ was added to the reaction at 0 °C. The resulting mixture was stirred at room temperature for 1 hr. The reaction was concentrated, and the residue was purified by Prep-HPLC to give 2-((2-((3-((4-fluorobenzyl)oxy)benzyl)amino)ethyl)amino)ethan-1-ol YT-8-8 (25 mg) as a white solid. ¹H-NMR (CDCl₃, 300 MHz): δ 7.22–7.34 (m, 10H), 6.78 (d, 1H, J = 9.0 Hz), 6.52 (d, 1H, J = 3.0 Hz), 6.38 (dd, 1H, J = 3.0 and 9.0 Hz), 4.09–4.05 (m, 5H), 3.90–3.93 (m, 2H), 2.60 (brs, 2H), 3.13 (t, 2H, J = 6.0 Hz), 3.09 (t, 2H, J = 9.0 Hz), 2.95–2.99 (m, 2H), 2.79 (dd, 1H, J = 9.0 and 12.0 Hz), 1.18 (d, 6H, J = 6.0 Hz); ESIMS m/z: 451 [M+2H]⁺;

Scheme 2: Synthesis of (R)-1-(3,4-diphenethoxyphenoxy)-3-(isopropylamino)propan-2-ol YOK-2204.

Step 1: To the stirred solution of 3, 4-dihydroxybenzaldehyde 1 (0.50 g, 3.62 mmol) in anhydrous DMF (5 mL) added K₂CO₃ (1.50 g, 10.86 mmol), followed by (2-bromoethyl)benzene (1.09 mL, 7.96 mmol). The resulted mixture was heated to 60 °C and continued stirring for 4 h. After completion of the starting material cooled to room temperature. The reaction mixture was partitioned between H₂O and diethyl ether (50 mL each). The organic layer was separated, and the water layer was extracted with ether (3 × 20 mL). The combined organic layers were washed with H₂O (2 × 50 mL) and saturated aqueous NaCl (50 mL) and dried over anhydrous Na₂SO₄ and the solvent was evaporated in vacuo. The obtained crude product was purified by column

chromatography (hexane/EtOAc, 9:1) to give 3,4-diphenethoxybenzaldehyde 2201 (1.10 g, 88%) as white solid.

Step 2: m-Chloroperbenzoic acid (0.78 g, 4.5 mmol) was added to a solution of the 3,4-diphenethoxybenzaldehyde 2201 (1.04 g, 3.0 mmol) in anhydrous dichloromethane (15 mL), and the mixture was stirred at room temperature for 4 h and then diluted with ethyl acetate and washed with saturated aqueous Na₂CO₃ solution and brine and dried over anhydrous Na₂SO₄. The solvent was evaporated in vacuo and the resulted corresponding formiate was dissolved in MeOH (10 mL), added NaOH (6 N). After stirring at room temperature for 30 min, was added HCl (4 N) solution and continued stirring for 30 min. After completion of the starting materials, diluted with ethyl acetate (50 mL), washed with brine, dried over anhydrous Na₂SO₄ and the solvent was evaporated in vacuo. The obtained crude product was purified by column chromatography (hexane/EtOAc, 7:3) furnished the compounds 3,4-diphenethoxyphenol 2202 (0.89 g, 89%) as white solid.

Step 3: To a mixture of 3,4-diphenethoxyphenol 2202 (334 mg, 1.0 mmol) in EtOH (10 mL), aqueous KOH (66 mg, 1.2 mmol) and (R)-epichlorohydrin (410 µL, 5.0 mmol) were added. The resulting mixture was stirred for 5 h at room temperature. The solvent was removed under reduced pressure, and the resulted residue dissolved in ethyl acetate, washed with water, brine and dried over anhydrous Na₂SO₄. The solvent was evaporated to afford the crude product, which were purified by using column chromatography (hexane/EtOAc, 9:1) furnished the epoxide (R)-2-((3,4-diphenethoxyphenoxy)methyl)-oxirane 2203 (312 mg, 80%) as white solid.

Step 4: Isopropyl amine (10 µL, 125 nmol) was added to a stirred solution of 2203 (9.7 mg, 25 nmol) in anhydrous EtOH (1 mL) and the mixture was vigorously stirred at room temperature for 4 h (TLC-monitoring). Then, the solvent was removed in vacuo, added water to the resulted residue and extracted with CH₂Cl₂ (3× 5 mL). The

combined organic layers were washed with brine (5 mL), dried over anhydrous Na₂SO₄ and concentrated in vacuo. The obtained residue was purified by column chromatography (CH₂Cl₂/MeOH, 19:1) to yield (R)-1-(3,4-diphenethoxyphenoxy)-3-(isopropylamino)propan-2-ol YOK-2204 (10 mg, 88%) as white solid.

¹H-NMR (CDCl₃, 300 MHz): δ 7.22–7.34 (m, 10H), 6.78 (d, 1H, J = 9.0 Hz), 6.52 (d, 1H, J = 3.0 Hz), 6.38 (dd, 1H, J = 3.0 and 9.0 Hz), 4.09–4.05 (m, 5H), 3.90–3.93 (m, 2H), 2.60 (brs, 2H), 3.13 (t, 2H, J = 6.0 Hz), 3.09 (t, 2H, J = 9.0 Hz), 2.95–2.99 (m, 2H), 2.79 (dd, 1H, J = 9.0 and 12.0 Hz), 1.18 (d, 6H, J = 6.0 Hz); ESIMS m/z: 451 [M+2H]⁺;

Scheme 3: Synthesis of (R)-1-(4-(benzyloxy)-3-(3-phenylpropoxy)phenoxy)-3-(isopropyl-amino)propan-2-ol YOK-1304.

Step 1: To the stirred solution of 4-benzyloxy-3-hydroxybenzaldehyde 1001 (825 mg, 3.62 mmol) in anhydrous DMF (5 mL) added K₂CO₃ (1.0 g, 7.24 mmol), followed by (3-bromopropyl)benzene (0.82 mL, 5.43 mmol). The resulted mixture was heated to 60°C and continued stirring for 4 h. After completion of the starting material cooled to room temperature. The reaction mixture was partitioned between H₂O and diethyl ether (50 mL each). The organic layer was separated, and the water layer was extracted with ether (3 × 20 mL). The combined organic layers were washed with H₂O (2 × 50 mL), brine (50 mL) and dried over anhydrous Na₂SO₄ and the solvent was evaporated in vacuo. The obtained crude product was purified by column chromatography (hexane/EtOAc, 9:1) to furnish 4-(benzyloxy)-3-(3-phenylpropoxy)benzaldehyde 1301 (1.09 g, 87%) as white solid.

Step 2: m-Chloroperbenzoic acid (260 mg, 1.5 mmol) was added to a solution of the 4-(benzyloxy)-3-(3-phenylpropoxy)benzaldehyde 1301 (346 mg, 1.0 mmol) in anhydrous dichloromethane (10 mL), and the mixture was stirred at room temperature for 4 h and then diluted with ethyl acetate and washed with saturated aqueous Na₂CO₃ solution and

brine and dried over anhydrous Na₂SO₄. The solvent was evaporated in vacuo and the resulted corresponding formiate was dissolved in MeOH (5 mL), added NaOH (6 N). After stirring at room temperature for 30 min, was added HCl (4 N) solution and continued stirring for 30 min. After completion of the starting materials, diluted with ethyl acetate (20 mL), washed with brine, dried over anhydrous Na₂SO₄ and the solvent was evaporated in vacuo. The obtained crude product was purified by column chromatography (hexane/EtOAc, 7:3) furnished the compound 4-(benzyloxy)-3-(3-phenylpropoxy)phenol 1302 (321 mg, 89%) as white solid.

Step 3: To a mixture of 4-(benzyloxy)-3-(3-phenylpropoxy)phenol 1302 (334 mg, 1.0 mmol) in EtOH (5 mL), aqueous KOH (66 mg, 1.2 mmol) and (R)-epichlorohydrin (410 µL, 5.0 mmol) were added. The resulting mixture was stirred for 5 h at room temperature. The solvent was removed under reduced pressure, and the resulted residue dissolved in ethyl acetate, washed with water, brine and dried over anhydrous Na₂SO₄. The solvent was evaporated to afford the crude product, which were purified by using column chromatography (hexane/EtOAc, 9:1) furnished the desired epoxides (R)-2-((4-(benzyloxy)-3-(3-phenylpropoxy)phenoxy)methyl)oxirane 1303 (316 mg, 80%) as white solid.

Step 4: Isopropyl amine (10 µL, 125 nmol) was added to a stirred solution of (R)-2-((4-(benzyloxy)-3-(3-phenylpropoxy)phenoxy)methyl)oxirane 1303 (9.7 mg, 25 nmol) in anhydrous EtOH (1 mL) and the mixture was vigorously stirred at room temperature for 4 h (TLC-monitoring). Then, the solvent was removed in vacuo, added water to the resulted residue and extracted with CH₂Cl₂ (3× 5 mL). The combined organic layers were washed with brine (5 mL), dried over anhydrous Na₂SO₄ and concentrated in vacuo. The obtained residue was purified by column chromatography (CH₂Cl₂/MeOH, 19:1) to yeild target product (R)-1-(4-(benzyloxy)-3-(3-phenylpropoxy)phenoxy)-3-(isopropylamino)propan-2-ol YOK-1304 (9.5 mg, 85%) as a white powder. ¹H-NMR

(CDCl₃, 300 MHz): δ 7.47–7.19 (m, 10H), 6.84 (d, 1H, J = 9.0 Hz), 6.52 (d, 1H, J = 3.0 Hz), 6.36 (dd, 1H, J = 3.0 and 9.0 Hz), 5.07 (s, 2H), 3.98–4.05 (m, 3H), 3.91 (d, 2H, J = 4.0 Hz), 2.71–2.89 (m, 5H), 2.33 (brs, 2H), 2.15 (td, 1H, J = 9.0 and 15.0 Hz), 1.13 (d, 6H, J = 6.0 Hz); ESIMS m/z : 451 [M+2H].

Scheme 4: Synthesis of 2-((3-(benzyloxy)benzyl)amino)ethan-1-ol YTK-105.

Step 1: To the stirred solution of 3-hydroxybenzaldehyde **1** (0.44 g, 3.62 mmol) in anhydrous DMF (5 mL) added K₂CO₃ (1.00 g, 7.24 mmol), followed by Benzyl bromide (0.50 mL, 4.34 mmol) for 101. The resulted mixture was heated to 60°C and continued stirring for 4 h. After completion of the starting material cooled to room temperature. The reaction mixture was partitioned between H₂O and diethyl ether (50 mL each). The organic layer was separated, and the water layer was extracted with ether (3 \times 20 mL). The combined organic layers were washed with H₂O (2 \times 50 mL) and saturated aqueous NaCl (50 mL) and dried over anhydrous Na₂SO₄ and the solvent was evaporated in vacuo. The obtained crude product was purified by column chromatography (hexane/EtOAc, 9:1) to give 3-(benzyloxy)benzaldehyde **101** (0.70 g, 92%).

Step 2: Ethanolamine (15 μ L, 250 nmol) added to a stirred solution of 3-(benzyloxy)benzaldehyde **101** (10.6 mg, 50 nmol) for YTK-105 in anhydrous EtOH (1 mL). The resulted reaction mixture was refluxed for 4 h (TLC-monitoring). Then, cooled down to room temperature and added NaBH₄ (7.6 mg, 0.2 mmol), continued stirring for another 4 h. The solvent was evaporated in vacuum, and the residue was dissolved in water and extracted with ethyl acetate. The combined organic layers were washed with brine and dried with anhydrous Na₂SO₄, filtered, and evaporated in vacuum. The residue was purified by flash column (CH₂Cl₂/MeOH, 19:1) to generate

the desired product 2-((3-(benzyloxy)benzyl)amino)ethan-1-ol YTK-105 (10.4 mg, 81%) as white solids.

Analytical Data for YTK-105: ¹H NMR (CDCl₃, 500 MHz): δ 9.42(brs, 2H), 7.39(d, 2H, J = 7.0 Hz), 7.33(t, 1H, J = 7.0 Hz), 7.30-7.24 (m, 3H), 7.10 (d, 1H, J = 6.0 Hz), 6.95 (d, 1H, J = 8.5 Hz), 5.06 (s, 2H), 4.13 (brs, 2H), 3.89 (brs, 2H), 2.95 (brs, 2H).; LC-MS (ESI): m/z 258.97 (M + H)⁺.

Immunocytochemistry

Cells were cultured on coverslips coated with poly-L-lysine (Sigma) to observe cellular localization of proteins. Using 4% paraformaldehyde in PBS (pH 7.4), the cells were fixed for 15 min at room temperature and washed three times for 5 min with PBS. After fixing, the cells were permeabilized with 0.5% Triton X-100 in PBS solution for 15 min and washed three times with PBS for 5 min. The cells were blocked containing 2% BSA in PBS solution for 1 h at room temperature. Subsequently, the cells were incubated with primary antibody diluted in 2% BSA/PBS solution overnight at 4°C, followed by washing the cells three times for 10 min with PBS and incubated with Alexa Fluor-conjugated secondary antibody diluted in 2% BSA/PBS for 30 min at room temperature. Using a DAPI-containing mounting medium (Vector Laboratories), the coverslips were mounted on glass slides. Confocal images were taken by laser scanning confocal microscope 510 Meta (Zeiss) and analyzed by Zeiss LSM Image Browser (ver. 4.2.0.121). Subsequently, cells were deemed to exhibit significant co-localization if more than ten clear puncta structures of the respective proteins showed association or full co-localization. Quantification results are shown as mean +/- S.D. of three independent experiments.

***In vitro* p62 oligomerization**

HEK293T cells were transiently transfected with a plasmid encoding p62-myc/his fusion proteins. Cells were resuspended in lysis buffer [50 mM HEPES (pH 7.4), 0.15 M KCl, 0.1% Nonidet P-40), 10% glycerol, containing a mixture of protease inhibitors and phosphatase inhibitor (Abcam)]. To lyse the cells, 10 cycles of freezing and thawing was done, followed by centrifugation at $13,000 \times g$ for 20 min at 4°C. Using a BCA assay, the protein concentration of the supernatant was measured. A total of 1 µg of protein was incubated with 1mM of p62-ZZ ligands in the presence of 100 µM bestatin (Enzo) at room temperature for 2 h. After incubation, each sample was mixed with non-reducing 4X LDS sample buffer, heated at 95°C for 10 min, and resolved using 4–20% gradient SDS-PAGE (Bio-Rad). To monitor the conversion of p62 monomers into oligomers or aggregates, IB assay was performed using anti-myc antibody.

***In vivo* oligomerization**

HEK293T cells were transfected with P301L-tau-EGFP plasmid using Lipofectamine 2000. HEK293T and SHSY5Y-tau cells were treated with p62-ZZ ligands for 24 h. After incubation on ice for 30 min for supernatant collection, the cells were lysed by a cycle of freezing/thawing and centrifuged at 13,000 g for 10 min. Protein concentration was determined using the Pierce BCA Protein Assay Kit (Thermo Fisher Scientific). Non-reducing 4X LDS sample buffer was added to sample lysate, followed by boiling at 100°C for 10 min and samples were loaded on a 3% stacking and 8% separating SDS-PAGE. Immunoblotting assays were carried out using anti-GFP antibody (Sigma) to visualize the oligomeric complexes of Tau.

***In vitro* peptide pull-down assay**

A set of synthetic 12-mer peptides corresponding to the N-terminal sequences of the V-BiP (V¹⁹-EEDKKEDVGTK-biotin) and V-RGS4 (V²-KGLAGLPASCLK-biotin) was C-terminally biotin-conjugated. Alternatively, biotinylated versions of YOK-1304, YT-8-2, YTK-1105, PBA were synthesized. To cross-link the above peptides with resin beads, biotin-conjugated peptides and small molecule were mixed with high-capacity streptavidin agarose resin (Thermo Fisher Scientific) at a ratio of 0.5 mg of peptide per 1 mL of settled resin and incubated on a rotator at 4°C overnight. After washing five times with PBS, the peptide/small molecule-bead conjugates were diluted with PBS at a 1:1 ratio. To prepare protein extracts, cells were collected by centrifugation and lysed by freezing and thawing at least 10 times in hypotonic buffer [10 mM KCl, 1.5 mM MgCl₂, and 10 mM HEPES (pH 7.9)] with a protease inhibitor mix (Sigma). After centrifugation at 15,000 rpm 4°C for 15 min, proteins were quantified using a BCA protein assay kit (Thermo Fisher Scientific). Total protein (200 µg) diluted in 300 µL of binding buffer [0.05% Tween-20, 10% glycerol, 0.2 M KCl, and 20 mM HEPES (pH 7.9)] were mixed with 50 µL of peptide/small molecule-bead resin and incubated at 4°C for 2 h on a rotator. The protein-bound beads were collected by centrifugation at 2,400 × g for 3 min and washed five times with binding buffer. The beads were resuspended in 25 µL of SDS sample buffer, heated at 95°C for 5 min, and subjected to SDS/PAGE and immunoblotting.

Co-immunoprecipitation

To study protein interactions, co-immunoprecipitation assays were performed. For exogenous co-IP, HEK293T cells were transfected with recombinant p62, BiP, TRIM13, FAM134B, RTN3 or ATZ using Lipofectamine 2000. For both endogenous and exogenous co-IP, cells were treated after 24 h with specified reagents for indicated incubation times. The cell pellets were scraped and pelleted by

centrifugation, were resuspended and lysed in immunoprecipitation buffer [50 mM Tris-HCl pH 7.5, 150 mM NaCl, 0.5% Triton X-100, 1mM EDTA, 1mM phenylmethylsulfonyl fluoride (PMSF; Roche) and protease inhibitor cocktail (Sigma)] for 30 min on rotator at 4°C. Next, the supernatant and remaining pellet were passed through a 26-gauge 1 mL syringe 15 times and centrifuged at 13,000 g at 4°C and collected for the supernatant, to which we added normal mouse IgG (Santa Cruz) and Protein A/G-Plus agarose beads (Santa Cruz) to preclear the lysate at 4°C on a rotor overnight. Cell lysate was then incubated with M2 FLAG-affinity Gel agarose beads (Sigma) at 4°C on a rotor for 3 h. The gel beads were washed four times with IP buffer, resuspended in 2X Laemmli Sample Buffer, separated by SDS-PAGE and analyzed by immunoblotting with specified antibodies.

Triton X-100-based insoluble/soluble fractionation

SH-SY5Y-tau BiFC cells were treated with PBA-1105, PBA and YTK-1105 to determine the degraded fraction of Tau. Using a cell lysis buffer (20 mM HEPES pH 7.9, 0.2 M KCl, 1 mM MgCl₂, 1 mM EGTA, 1% Triton X-100, 10% glycerol, protease inhibitor and phosphatase inhibitor), the cells were collected and incubated on ice for 15 min, followed by centrifugation at 13,000 g for 10 min at 4°C. The supernatant was collected as the soluble fraction and the pellet as the insoluble fraction. Using PBS, the insoluble fraction was washed 4 times and lysed with a SDS-detergent lysis buffer (20 mM HEPES pH 7.9, 0.2 M KCl, 1 mM MgCl₂, 1 mM EGTA, 1% Triton x-100, 1% SDS, 10% glycerol, protease inhibitors and phosphatase inhibitors). 5X Laemmli sample buffer was added to the soluble and insoluble samples and boiled for 10 min at 100°C and loaded on a SDS-PAGE gel.

Wound healing assay

To analyze cell migration in two dimensions, U-87 MG or ACHN cells were plated to a monolayer. Cells were scratched with a sterile 10 µl pipette tip and the debris was removed using medium. Cells were treated with compounds and incubated for different time to monitor cell behavior. Photographs were obtained using a microscope at different time point.

Cell viability assay

Cell viability was quantified using the water-soluble tetrazolium salt-based EZ-Cytox cell viability assay kit (Dojindo Laboratory) according to the manufacturer's instructions. Briefly, following siRNA-mediated knockdown of control or *ATE1* (48 h), HeLa cells in a 96-well plate were treated with the indicated ER stressors. Subsequently, assay reagent solution (10 µL) was added to each well and cells were incubated for 4 h at 37°C in a CO₂ incubator. Optical density (OD) values were measured at 450 nm using a Evolution 350 UV-Vis Spectrophotometer (Thermo Fisher Scientific).

Flow cytometry

Cell death and cell cycle arrest were quantified by staining cells with propidium iodide for flow cytometry with a BD FACSCalibur (BD Biosciences) according to the manufacturer's instructions. Briefly, 1x10⁶ cells were incubated with fumagillin-105 (1 µM, 48 h) or negative control DMSO. Cells were collected by centrifugation and fixed in 70% ethanol at 4°C for 24 h. Cells were washed with PBS and stained with propidium iodide (10 µg/mL) with RNase treatment at 37°C for 30 min. DNA content at each cell cycle checkpoint was measured and analyzed using BD CellQuest Pro (BD Biosciences) and ModFit LT Systems (Verity Software House).

Animals

hTau-P301L- BiFC mice were bred and housed in a 12:12 light-dark cycle, pathogen-free facility at Korea Institute of Science and Technology. Animal protocols followed the principles and practices outlined in the approved guidelines by the Institutional Animal Care and Use Committee of the Korea Institute of Science and Technology.

Administration of PBA-1105 to TauP301L-BiFC mice

To evaluate the effect of PBA-1105 on tau aggregation in vivo, PBA-1105 was intraperitoneally administered to 9-month-old TauP301L-mice (n=7 per group) with 20 or 50 mg/kg dosage. PBS containing 30% polyethylene glycol (PEG) was used as a vehicle. Twelve total administrations were performed for 4 weeks, three times a week.

Brain tissue preparation

Mice were anesthetized by intraperitoneal injection of 2% avertin (2,2,2-Tribromoethanol). Mice were then perfused with 0.9% saline. Brains were rapidly extracted and fixed with PBS containing 4% paraformaldehyde for 48 hr. For cryprotection, the brains were infiltrated with PBS containing 30% sucrose at 4°C until they sunk. For cryosectioning, the brains were embedded with O.C.T (Leica, Germany) and serially cut in the coronal plane into 30-μm thick sections on a cryostat microtome (Leica). Tissue slices were transferred to PBS containing 0.05% sodium azide as a preservative and stored at 4°C.

Sudan Black B stain and BiFC image acquisition

To reduce autofluorescence of brain tissues, Sudan Black B stain was performed.

Brain tissue slices were mounted onto glass slides and were stained with Sudan Black B solution (70% ethanol containing 0.05% Sudan Black B) for 10 min. Then, to eliminate excessive stain, the slides were dipped in PBS containing 0.1% Triton X-100 three times and washed with distilled water after. For nuclei counter-stain, brain tissues were stained with 0.5 µg/mL Hoechst in distilled water for 30 min. BiFC fluorescence ($\lambda_{\text{ex}} = 460\text{--}490$ nm and $\lambda_{\text{em}} = 500\text{--}550$ nm) of brain slices were imaged using ZEISS® Axio Scan.Z1 (Zeiss, Germany). Fluorescence and total area of each puncta were measured using ImageJ (NIH, Bethesda).

Statistical analysis

For all data shown, stated values represent the mean \pm S.D or S.E.M. of at least three independent experiments. For each experiment, sample size (n) was determined as stated in the figure legends. *P*-values were determined using ANOVA or two-tailed student's *t*-test (degree of freedom = *n*-1) with Prism 6 software (GraphPad). Statistical significance was determined as values of $p < 0.05$ (** $p < 0.001$; ** $p < 0.01$; * $p < 0.05$).

Data availability

All data relating to the finding of this study is available within the article and its associated files, or are available from the authors upon request.

Discussion

Summary & follow-up

In this thesis, I first provided a general introduction on protein quality control and focus on the mechanisms by which proteolysis is achieved, and its role in the cell. I then expound on how substrate selectivity is achieved for cellular degradation, noting the crosstalk and interplay between the ubiquitin-proteasome system and the autophagy-lysosome pathway. Next, I describe how the Arg/N-degron pathway can mediate both proteasomal and lysosomal degradation of its substrates, and the recent discovery that p62 can induce autophagy via its function as an autophagic N-recognin.

As the starting point of my thesis to investigate the role of the autophagic Arg/N-degron pathway for general proteostasis, I show that the N-degron pathway mediates ER-phagy. During this process, the ER transmembrane E3 ligase TRIM13, which may already bind p62 directly or indirectly via the PB1 domain, self-ubiquitinates itself with K63 linkage chains, further recruiting p62. As an N-recognin, p62 also binds, via its ZZ domain, the Nt-Arg of arginylated substrates such as R-BiP and undergoes oligomerization in complex with TRIM13. TRIM13 also recruits the Beclin-1/VPS34 complex, which are responsible for ER membrane curvature and autophagosome biogenesis. Given that p62, by virtue of its LIR domain, binds LC3 on autophagic membranes, the above interactions promote the targeting of TRIM13-associated ER compartments to autophagic membranes generated by VPS34 complexes. Chemical mimicry of the interaction between the Nt-Arg and p62-ZZ domain recapitulates p62/Nt-Arg/TRIM13-dependent ER-phagy. In stressed conditions such as misfolded ER protein accumulation/aggregation (e.g., ATZ) or prolonged ERAD inhibition, levels of Nt-arginylation are greatly boosted following induction and cytosolic retrotranslocation of Nt-arginylation-permissive ER chaperones, thereby leading to greater N-degron-mediated oligomerization and autophagic flux of p62 via its ZZ domain. Simultaneously, TRIM13 is also up-regulated in these stress conditions, which presumably induces not only more auto-ubiquitination and self-oligomerization but also increased recruitment of

p62 and the mammalian PI3K complex, facilitating ER-phagy at a heightened degree. In this sense, N-degron-regulated ER-phagy is required for ER homeostasis as a basal constitutive pathway but also as an ER stress response system by dynamically regulating Nt-Arg and TRIM13 levels.

Recent studies showed that ER-phagy can be mediated by a set of ER transmembrane proteins who directly interact with phagophores for ER-phagy (40-43). However, the mechanisms and pathways for an Ub-dependent ER-phagy have not been yet elucidated. My work establishes the role of K63-linked Ub on TRIM13 as an autophagic degron for ER-phagy that enables autophagic flux of the p62-TRIM13 complex. TRIM proteins, numbering more than 80 in humans, represent a large subfamily of the RING-type E3 Ub ligase family (81). TRIM proteins regulate autophagy by serving as platforms on which autophagy regulator proteins (ATG proteins) mediate autophagosome biogenesis as well as by interacting with autophagy cargo adaptors for autophagy flux (81, 82). Indeed, these results are consistent with this paradigm and indicate TRIM13 as an inducer of autophagy by recruiting the Beclin-1/VPS34 complex. However, whether TRIM proteins regulate cellular autophagy via their E3 ligase activities remains unclear (74, 81). My findings indicate that the E3 ligase activities of TRIM13, specifically its self-ubiquitination of K63-linked chains, promote ER-phagy. My work opens a line of research exploring possible crosstalk between Ub-mediated and LIR domain receptor-mediated ER-phagy,

Another question concerns the functional role of oligomerization of the TRIM13-p62 complex. My results suggest that p62 binds K63-ubiquitinated TRIM13 independent of its binding to the Nt-Arg. However, the interaction of p62 with TRIM13 as monomers may not be sufficient to initiate ER-phagy. One possible explanation is that the successful initiation of ER-phagy may require the oligomerization of p62 and its increased interaction with LC3 modulated by the N-degron Nt-Arg, as well as self-

oligomerization of TRIM13. This is not unlikely given the fact that TRIM proteins require CC domain-dependent dimerization for their autoubiquitination (106) and that TRIM13 likely depends on its oligomerization (via its CC domain) for self-ubiquitination since TRIM13 oligomers rather than monomers are subject to autophagy. Even so, it remains to be seen whether the interaction between TRIM13 and p62 depends on their oligomerization. Despite the requirement of the PB1 domain for p62-TRIM13 binding, it is not yet clear whether this is a direct interaction between TRIM13 and the p62-PB1 domain, or an indirect interaction between oligomeric p62 and oligomeric TRIM13. Furthermore, since both the ZZ and UBA domains on p62 are required for autophagic flux of p62-TRIM13 complexes, it remains to be seen whether the binding of each domain to its respective target (i.e., Nt-Arg to the ZZ domain or Ub to the UBA domain) is affected by that of the other. Possibly, the binding of Nt-Arg to the p62-ZZ domain may trigger a conformational change, allowing efficient recognition of Ub chains. I propose that since TRIM13 recruits the Beclin-1/VPS34 complex, which regulate ER membrane curvature and phagophore nucleation from the omegasome, oligomeric TRIM13-p62 complexes may mark the site of ER-phagy. Although it remains to be seen whether monomeric or oligomeric TRIM13 recruits the mammalian PI3K complex, the above increased recruitment of Beclin-1/VPS34 complexes would mean that maturing phagophores are physically near the TRIM13-marked and curved ER compartments and be energetically advantageous for ER-phagy. If so, oligomerization of organellar receptors may be a general signal to trigger autophagic removal of organelles and subcellular structures, especially since oligomerization of scaffolding proteins can also induce lipid membrane curvature and tubulation (83, 107). It will be interesting to determine whether the Nt-Arg degron generally binds autophagic receptors for their 'oligomeric activation' and hence mediate other types of organellophagy for global organelle quality.

The ER stress response is a critical factor in the pathogenesis of a myriad of proteinopathies including metabolic disorders and even those whose hallmark proteins are not of ER origins, such as neurodegenerative diseases (54). Modulating the ER stress response by degradation of unfolded or misfolded proteins that accumulate within the ER lumen thus continues to be a major therapeutic target (88, 108). In this study, I developed four synthetic ligands to the ZZ domain of p62 (Figure S4). Using these chemical mimics of the Nt-Arg, I confirmed that N-degron-mediated ER-phagy directly ameliorates ER stress and maintains ER homeostasis via autophagic degradation of ER-resident pathological aggregates, such as insoluble ATZ, and of the ER itself. Although the general efficacy of p62 ZZ ligands should be further evaluated, my results suggest that modulation of the Arg branch of the N-degron pathway for ER proteostasis can provide a novel avenue of therapeutic targeting against ER stress and treatment for related metabolic proteinopathies.

In the next part of my thesis as an extension of the pharmacological modulation of the autophagic Arg/N-degron pathway for proteostasis, I report the development of AUTOTACs as a generally applicable chemical platform that enables targeted degradation of a variety of cellular proteins. Bifunctional AUTOTAC compounds simultaneously bind a target and the ZZ domain of an otherwise inactive p62 by virtue of their TBL and ATL, respectively. Central to this chemical platform is the ability of ATL to activate an otherwise inactive p62 to an autophagy-compatible form via a conformational change. Upon binding to ATL, p62 exposes its PB1 domain for self-polymerization in complex with TBL-bound cargoes (effectively sequestering target cargoes) and its LIR domain for interaction with LC3 on autophagic membranes. Through this allosteric alteration, AUTOTAC can mediate targeted degradation of not only monomeric oncoproteins (whose oncogenic signaling was functionally silenced) but also oligomeric species of aggregation-prone proteins, including hallmark substrates

of neurodegenerative proteinopathies. Therapeutic efficacy of a misfolded protein-targeting AUTOTAC was further confirmed in a brain-specific murine model expressing transgenic human mutant pathological tau. These results substantiate AUTOTACs as first-in-class heterobifunctional chimeric degraders for Ub-independent and p62-mediated autophagic clearance of intracellular target proteins.

Among proteinopathies with gain-of-function toxicity, a large subset is defined as protein misfolding/aggregation disorders wherein misfolded proteins, from their monomeric to oligomeric and aggregated species, are pathological(96, 98). Due to the inherent size and substrate-conformation limitations of a proteasome, any conformationally stable subspecies of a protein beyond its monomeric form is not only non-degradable by the UPS but can even clog the pores of proteasomal subunits(19, 97). While several recent efforts using PROTACs have succeeded in degrading pathological and aggregation-prone tau, it is most likely that the targeted species were monomeric and that the anti-aggregate efficacy, if any, is more of a prevention than a treatment(62). In this sense, AUTOTACs provide a direct means to target not only the monomeric but also the oligomeric and aggregated species of these pathological hallmark proteins.

Another advantage that AUTOTAC offers over current TPD modalities is in its promiscuity. Notably, the requirement of ligand-induced proximity to achieve spatial and temporal colocalization between E3 and target substrate using PROTACs necessitates extremely specific linker lengths and types for ternary complex formation, subject to change for each of the numerous E3 ligase-substrate combinations(60, 64, 65). Moreover, despite the initial promising outlook on ‘hijacking’ E3 ligases to ubiquitinate non-native substrates, it is becoming increasingly clear that the current spectrum of E3 ligases used in PROTAC technology exhibits restricted substrate specificities, and that a ‘pan-ubiquitinating’ E3 ligase is yet to be found(69, 109). In this study, we discovered that the degradative efficacy of AUTOTACs was dramatically

enhanced in the absence of Ub, indicating that their mode-of-action, by directly tethering to an autophagic cargo adaptor protein, is Ub-independent. Moreover, the variety of structurally distinct ATLs used in AUTOTACs to successfully eradicate equally numerous and diverse target proteins highlight p62 as a ‘pan-autophagy receptor,’ capable of targeting non-native or autophagy-resistant substrates such as MetAP2 or hyper-phosphorylated mutant tau. Thus, this work opens a line of clinical research exploring alternative avenues of targeting the human proteome for degradation.

Critical remaining questions from this study involves the pharmacological and mechanistic properties of AUTOTACs. For example, it remains to be seen whether and how AUTOTACs can be recycled for multiple rounds of degradation. While PROTACs and similar degraders are naturally salvaged due to their localization in the cytosol following the dissociation of the E3 ligase-substrate ternary complex formation, AUTOTACs (and other autophagy-based degraders) are likely to occupy the lysosomal lumen at the end of each degradation ‘round.’ I observed that AUTOTAC-mediated silencing of a target protein and its downstream signaling is several folds more effective than that of the target-binding inhibitor alone. Also, given that small-molecule cytotoxic drugs of antibody-drug conjugates (ADCs) can translocate from the lysosome to the cytosol, it is highly likely that AUTOTACs manifest sub-stoichiometric degradation by repeatedly entering and exiting the lysosome(110). Another question concerns the autophagic sequestration mode-of-action possibly unique to AUTOTACs. I show that AUTOTACs, through its p62-ZZ ligand arm, not only deliver the target substrate to the autophagosome but also induce the high-molecular weight self-oligomerization/aggregation of p62. Given that each monomer of these high-molecular weight p62 species are potentially tethered by AUTOTACs to the target substrate, it is highly likely that the target substrate is sequestered and trapped (and thus unable to carry out its endogenous function) in an intracellular body comprised of itself and p62

oligomers/aggregates. Thus, I propose that AUTOTACs exhibit their biological silencing downstream of a target protein not only through degradation but also by sequestration. Although the general efficacy of AUTOTACs have yet to be fully evaluated, my results suggest that activating the p62-ZZ domain in an Arg/N-degron-dependent manner for targeted proteolysis can provide a novel avenue of research and therapeutic investigation into a myriad of diseases.

REFERENCES

1. N. Berner, K. R. Reutter, D. H. Wolf, Protein Quality Control of the Endoplasmic Reticulum and Ubiquitin-Proteasome-Triggered Degradation of Aberrant Proteins: Yeast Pioneers the Path. *Annu Rev Biochem* 10.1146/annurev-biochem-062917-012749 (2018).
2. A. Ciechanover, Y. T. Kwon, Protein Quality Control by Molecular Chaperones in Neurodegeneration. *Frontiers in neuroscience* **11**, 185 (2017).
3. K. McCaffrey, I. Braakman, Protein quality control at the endoplasmic reticulum. *Essays Biochem* **60**, 227-235 (2016).
4. M. Griesemer, C. Young, A. S. Robinson, L. Petzold, BiP clustering facilitates protein folding in the endoplasmic reticulum. *PLoS Comput Biol* **10**, e1003675 (2014).
5. A. Chakrabarti, A. W. Chen, J. D. Varner, A review of the mammalian unfolded protein response. *Biotechnol Bioeng* **108**, 2777-2793 (2011).
6. J. Kaur, J. Debnath, Autophagy at the crossroads of catabolism and anabolism. *Nature reviews. Molecular cell biology* **16**, 461-472 (2015).
7. G. L. Grice, J. A. Nathan, The recognition of ubiquitinated proteins by the proteasome. *Cellular and molecular life sciences : CMLS* **73**, 3497-3506 (2016).
8. D. Scott, N. J. Oldham, J. Strachan, M. S. Searle, R. Layfield, Ubiquitin-binding domains: mechanisms of ubiquitin recognition and use as tools to investigate ubiquitin-modified proteomes. *Proteomics* **15**, 844-861 (2015).
9. A. L. Anding, E. H. Baehrecke, Cleaning House: Selective Autophagy of Organelles. *Dev Cell* **41**, 10-22 (2017).
10. Y. Feng, D. He, Z. Yao, D. J. Klionsky, The machinery of macroautophagy. *Cell research* **24**, 24-41 (2014).
11. C. H. Ji, Y. T. Kwon, Crosstalk and Interplay between the Ubiquitin-Proteasome System and Autophagy. *Mol Cells* **40**, 441-449 (2017).
12. K. N. Swatek, D. Komander, Ubiquitin modifications. *Cell research* **26**, 399-422 (2016).
13. A. Ciechanover, The unravelling of the ubiquitin system. *Nature reviews. Molecular*

- cell biology* **16**, 322-324 (2015).
14. S. T. Shibutani, T. Yoshimori, A current perspective of autophagosome biogenesis. *Cell research* **24**, 58-68 (2014).
 15. P. K. Kim, D. W. Hailey, R. T. Mullen, J. Lippincott-Schwartz, Ubiquitin signals autophagic degradation of cytosolic proteins and peroxisomes. *Proc Natl Acad Sci U S A* **105**, 20567-20574 (2008).
 16. D. Senft, Z. A. Ronai, UPR, autophagy, and mitochondria crosstalk underlies the ER stress response. *Trends Biochem Sci* **40**, 141-148 (2015).
 17. S. Pankiv, T. H. Clausen, T. Lamark, A. Brech, J. A. Bruun, H. Outzen, A. Overvatn, G. Bjorkoy, T. Johansen, p62/SQSTM1 binds directly to Atg8/LC3 to facilitate degradation of ubiquitinated protein aggregates by autophagy. *J Biol Chem* **282**, 24131-24145 (2007).
 18. G. Bjorkoy, T. Lamark, A. Brech, H. Outzen, M. Perander, A. Overvatn, H. Stenmark, T. Johansen, p62/SQSTM1 forms protein aggregates degraded by autophagy and has a protective effect on huntingtin-induced cell death. *J Cell Biol* **171**, 603-614 (2005).
 19. A. Ciechanover, Y. T. Kwon, Degradation of misfolded proteins in neurodegenerative diseases: therapeutic targets and strategies. *Exp Mol Med* **47**, e147 (2015).
 20. F. Ohtake, H. Tsuchiya, The emerging complexity of ubiquitin architecture. *Journal of biochemistry* **161**, 125-133 (2017).
 21. R. Yau, M. Rape, The increasing complexity of the ubiquitin code. *Nature cell biology* **18**, 579-586 (2016).
 22. J. R. Morris, A. J. Garvin, SUMO in the DNA Double-Stranded Break Response: Similarities, Differences, and Cooperation with Ubiquitin. *Journal of molecular biology* 10.1016/j.jmb.2017.05.012 (2017).
 23. J. S. Seeler, A. Dejean, SUMO and the robustness of cancer. *Nature reviews. Cancer* **17**, 184-197 (2017).
 24. K. Yamano, N. Matsuda, K. Tanaka, The ubiquitin signal and autophagy: an orchestrated dance leading to mitochondrial degradation. *EMBO reports* **17**, 300-316 (2016).

25. M. Akutsu, I. Dikic, A. Bremm, Ubiquitin chain diversity at a glance. *Journal of cell science* **129**, 875-880 (2016).
26. Z. Deng, K. Purtell, V. Lachance, M. S. Wold, S. Chen, Z. Yue, Autophagy Receptors and Neurodegenerative Diseases. *Trends in cell biology* **27**, 491-504 (2017).
27. A. Varshavsky, N-degron and C-degron pathways of protein degradation. *Proc Natl Acad Sci U S A* **116**, 358-366 (2019).
28. T. Tasaki, L. C. Mulder, A. Iwamatsu, M. J. Lee, I. V. Davydov, A. Varshavsky, M. Muesing, Y. T. Kwon, A family of mammalian E3 ubiquitin ligases that contain the UBR box motif and recognize N-degrons. *Mol Cell Biol* **25**, 7120-7136 (2005).
29. Y. T. Kwon, A. S. Kashina, I. V. Davydov, R. G. Hu, J. Y. An, J. W. Seo, F. Du, A. Varshavsky, An essential role of N-terminal arginylation in cardiovascular development. *Science* **297**, 96-99 (2002).
30. Y. T. Kwon, A. S. Kashina, A. Varshavsky, Alternative splicing results in differential expression, activity, and localization of the two forms of arginyl-tRNA-protein transferase, a component of the N-end rule pathway. *Mol Cell Biol* **19**, 182-193 (1999).
31. T. Tasaki, S. T. Kim, A. Zakrzewska, B. E. Lee, M. J. Kang, Y. D. Yoo, H. J. Cha-Molstad, J. Hwang, N. K. Soung, K. S. Sung, S. H. Kim, M. D. Nguyen, M. Sun, E. C. Yi, B. Y. Kim, Y. T. Kwon, UBR box N-recognin-4 (UBR4), an N-recognin of the N-end rule pathway, and its role in yolk sac vascular development and autophagy. *Proc Natl Acad Sci U S A* **110**, 3800-3805 (2013).
32. H. Cha-Molstad, J. E. Yu, Z. Feng, S. H. Lee, J. G. Kim, P. Yang, B. Han, K. W. Sung, Y. D. Yoo, J. Hwang, T. McGuire, S. M. Shim, H. D. Song, S. Ganipiseti, N. Wang, J. M. Jang, M. J. Lee, S. J. Kim, K. H. Lee, J. T. Hong, A. Ciechanover, I. Mook-Jung, K. P. Kim, X. Q. Xie, Y. T. Kwon, B. Y. Kim, p62/SQSTM1/Sequestosome-1 is an N-recognin of the N-end rule pathway which modulates autophagosome biogenesis. *Nat Commun* **8**, 102 (2017).
33. V. Kirkin, T. Lamark, Y. S. Sou, G. Bjorkoy, J. L. Nunn, J. A. Bruun, E. Shvets, D. G. McEwan, T. H. Clausen, P. Wild, I. Bilusic, J. P. Theurillat, A. Overvatn, T. Ishii, Z. Elazar, M. Komatsu, I. Dikic, T. Johansen, A role for NBR1 in autophagosomal

- degradation of ubiquitinated substrates. *Mol Cell* **33**, 505-516 (2009).
34. M. Lazarou, D. A. Sliter, L. A. Kane, S. A. Sarraf, C. Wang, J. L. Burman, D. P. Sideris, A. I. Fogel, R. J. Youle, The ubiquitin kinase PINK1 recruits autophagy receptors to induce mitophagy. *Nature* **524**, 309-314 (2015).
 35. V. Cohen-Kaplan, I. Livneh, N. Avni, B. Fabre, T. Ziv, Y. T. Kwon, A. Ciechanover, p62- and ubiquitin-dependent stress-induced autophagy of the mammalian 26S proteasome. *Proc Natl Acad Sci U S A* **113**, E7490-E7499 (2016).
 36. L. Liu, D. Feng, G. Chen, M. Chen, Q. Zheng, P. Song, Q. Ma, C. Zhu, R. Wang, W. Qi, L. Huang, P. Xue, B. Li, X. Wang, H. Jin, J. Wang, F. Yang, P. Liu, Y. Zhu, S. Sui, Q. Chen, Mitochondrial outer-membrane protein FUNDC1 mediates hypoxia-induced mitophagy in mammalian cells. *Nature cell biology* **14**, 177-185 (2012).
 37. I. Novak, V. Kirkin, D. G. McEwan, J. Zhang, P. Wild, A. Rozenknop, V. Rogov, F. Lohr, D. Popovic, A. Occhipinti, A. S. Reichert, J. Terzic, V. Dotsch, P. A. Ney, I. Dikic, Nix is a selective autophagy receptor for mitochondrial clearance. *EMBO reports* **11**, 45-51 (2010).
 38. S. Hara-Kuge, Y. Fujiki, The peroxin Pex14p is involved in LC3-dependent degradation of mammalian peroxisomes. *Exp Cell Res* **314**, 3531-3541 (2008).
 39. J. W. Harper, A. Ordureau, J. M. Heo, Building and decoding ubiquitin chains for mitophagy. *Nature reviews. Molecular cell biology* **19**, 93-108 (2018).
 40. M. D. Smith, M. E. Harley, A. J. Kemp, J. Wills, M. Lee, M. Arends, A. von Kriegsheim, C. Behrends, S. Wilkinson, CCPG1 Is a Non-canonical Autophagy Cargo Receptor Essential for ER-Phagy and Pancreatic ER Proteostasis. *Dev Cell* **44**, 217-232 e211 (2018).
 41. P. Grumati, G. Morozzi, S. Holper, M. Mari, M. I. Harwardt, R. Yan, S. Muller, F. Reggiori, M. Heilemann, I. Dikic, Full length RTN3 regulates turnover of tubular endoplasmic reticulum via selective autophagy. *Elife* **6** (2017).
 42. A. Khaminets, T. Heinrich, M. Mari, P. Grumati, A. K. Huebner, M. Akutsu, L. Liebmann, A. Stolz, S. Nietzsche, N. Koch, M. Mauthe, I. Katona, B. Qualmann, J. Weis, F. Reggiori, I. Kurth, C. A. Hubner, I. Dikic, Regulation of endoplasmic reticulum

- turnover by selective autophagy. *Nature* **522**, 354-358 (2015).
43. F. Fumagalli, J. Noack, T. J. Bergmann, E. Cebollero, G. B. Pisoni, E. Fasana, I. Fregno, C. Galli, M. Loi, T. Solda, R. D'Antuono, A. Raimondi, M. Jung, A. Melnyk, S. Schorr, A. Schreiber, L. Simonelli, L. Varani, C. Wilson-Zbinden, O. Zerbe, K. Hofmann, M. Peter, M. Quadroni, R. Zimmermann, M. Molinari, Translocon component Sec62 acts in endoplasmic reticulum turnover during stress recovery. *Nature cell biology* **18**, 1173-1184 (2016).
 44. B. M. Gardner, D. Pincus, K. Gotthardt, C. M. Gallagher, P. Walter, Endoplasmic reticulum stress sensing in the unfolded protein response. *Cold Spring Harb Perspect Biol* **5**, a013169 (2013).
 45. B. Y. Jang, H. D. Ryoo, J. Son, K. C. Choi, D. M. Shin, S. W. Kang, M. J. Kang, Role of Drosophila EDEMs in the degradation of the alpha-1-antitrypsin Z variant. *Int J Mol Med* **35**, 870-876 (2015).
 46. K. W. Park, G. Eun Kim, R. Morales, F. Moda, I. Moreno-Gonzalez, L. Concha-Marambio, A. S. Lee, C. Hetz, C. Soto, The Endoplasmic Reticulum Chaperone GRP78/BiP Modulates Prion Propagation in vitro and in vivo. *Sci Rep* **7**, 44723 (2017).
 47. K. J. Travers, C. K. Patil, L. Wodicka, D. J. Lockhart, J. S. Weissman, P. Walter, Functional and genomic analyses reveal an essential coordination between the unfolded protein response and ER-associated degradation. *Cell* **101**, 249-258 (2000).
 48. M. Bi, C. Naczki, M. Koritzinsky, D. Fels, J. Blais, N. Hu, H. Harding, I. Novoa, M. Varia, J. Raleigh, D. Scheuner, R. J. Kaufman, J. Bell, D. Ron, B. G. Wouters, C. Koumenis, ER stress-regulated translation increases tolerance to extreme hypoxia and promotes tumor growth. *EMBO J* **24**, 3470-3481 (2005).
 49. L. Haataja, T. Gurlo, C. J. Huang, P. C. Butler, Islet amyloid in type 2 diabetes, and the toxic oligomer hypothesis. *Endocr Rev* **29**, 303-316 (2008).
 50. T. Katayama, K. Imaizumi, T. Manabe, J. Hitomi, T. Kudo, M. Tohyama, Induction of neuronal death by ER stress in Alzheimer's disease. *J Chem Neuroanat* **28**, 67-78 (2004).
 51. L. Salvado, X. Palomer, E. Barroso, M. Vazquez-Carrera, Targeting endoplasmic reticulum stress in insulin resistance. *Trends Endocrinol Metab* **26**, 438-448 (2015).

52. N. Mimura, M. Fulciniti, G. Gorgun, Y. T. Tai, D. Cirstea, L. Santo, Y. Hu, C. Fabre, J. Minami, H. Ohguchi, T. Kiziltepe, H. Ikeda, Y. Kawano, M. French, M. Blumenthal, V. Tam, N. L. Kertesz, U. M. Malyankar, M. Hokenson, T. Pham, Q. Zeng, J. B. Patterson, P. G. Richardson, N. C. Munshi, K. C. Anderson, Blockade of XBP1 splicing by inhibition of IRE1alpha is a promising therapeutic option in multiple myeloma. *Blood* **119**, 5772-5781 (2012).
53. S. Saxena, E. Cabuy, P. Caroni, A role for motoneuron subtype-selective ER stress in disease manifestations of FALS mice. *Nat Neurosci* **12**, 627-636 (2009).
54. C. Hetz, S. Saxena, ER stress and the unfolded protein response in neurodegeneration. *Nat Rev Neurol* **13**, 477-491 (2017).
55. H. O. Rashid, R. K. Yadav, H. R. Kim, H. J. Chae, ER stress: Autophagy induction, inhibition and selection. *Autophagy* **11**, 1956-1977 (2015).
56. C. M. Greene, S. J. Marciniak, J. Teckman, I. Ferrarotti, M. L. Brantly, D. A. Lomas, J. K. Stoller, N. G. McElvaney, alpha1-Antitrypsin deficiency. *Nat Rev Dis Primers* **2**, 16051 (2016).
57. N. Hamdan, P. Kritsiligkou, C. M. Grant, ER stress causes widespread protein aggregation and prion formation. *J Cell Biol* **216**, 2295-2304 (2017).
58. M. Boettcher, M. T. McManus, Choosing the Right Tool for the Job: RNAi, TALEN, or CRISPR. *Mol Cell* **58**, 575-585 (2015).
59. T. Christofi, A. Zaravinos, RNA editing in the forefront of epitranscriptomics and human health. *J Transl Med* **17**, 319 (2019).
60. S. Moon, B. H. Lee, Chemically Induced Cellular Proteolysis: An Emerging Therapeutic Strategy for Undruggable Targets. *Mol Cells* **41**, 933-942 (2018).
61. S. L. Fisher, A. J. Phillips, Targeted protein degradation and the enzymology of degraders. *Curr Opin Chem Biol* **44**, 47-55 (2018).
62. M. C. Silva, F. M. Ferguson, Q. Cai, K. A. Donovan, G. Nandi, D. Patnaik, T. Zhang, H. T. Huang, D. E. Lucente, B. C. Dickerson, T. J. Mitchison, E. S. Fischer, N. S. Gray, S. J. Haggarty, Targeted degradation of aberrant tau in frontotemporal dementia patient-derived neuronal cell models. *Elife* **8** (2019).

63. J. Hu, B. Hu, M. Wang, F. Xu, B. Miao, C. Y. Yang, M. Wang, Z. Liu, D. F. Hayes, K. Chinnaswamy, J. Delproposto, J. Stuckey, S. Wang, Discovery of ERD-308 as a Highly Potent Proteolysis Targeting Chimera (PROTAC) Degradar of Estrogen Receptor (ER). *J Med Chem* **62**, 1420-1442 (2019).
64. M. Schapira, M. F. Calabrese, A. N. Bullock, C. M. Crews, Targeted protein degradation: expanding the toolbox. *Nat Rev Drug Discov* **18**, 949-963 (2019).
65. M. Pettersson, C. M. Crews, PROteolysis TArgeting Chimeras (PROTACs) - Past, present and future. *Drug Discov Today Technol* **31**, 15-27 (2019).
66. S. Roth, L. J. Fulcher, G. P. Sapkota, Advances in targeted degradation of endogenous proteins. *Cell Mol Life Sci* **76**, 2761-2777 (2019).
67. N. Ohoka, G. Tsuji, T. Shoda, T. Fujisato, M. Kurihara, Y. Demizu, M. Naito, Development of Small Molecule Chimeras That Recruit AhR E3 Ligase to Target Proteins. *ACS Chem Biol* **14**, 2822-2832 (2019).
68. C. Zhao, X. Chen, D. Zang, X. Lan, S. Liao, C. Yang, P. Zhang, J. Wu, X. Li, N. Liu, Y. Liao, H. Huang, X. Shi, L. Jiang, X. Liu, Z. He, Q. P. Dou, X. Wang, J. Liu, A novel nickel complex works as a proteasomal deubiquitinase inhibitor for cancer therapy. *Oncogene* **35**, 5916-5927 (2016).
69. D. Takahashi, J. Moriyama, T. Nakamura, E. Miki, E. Takahashi, A. Sato, T. Akaike, K. Itto-Nakama, H. Arimoto, AUTACs: Cargo-Specific Degraders Using Selective Autophagy. *Mol Cell* **76**, 797-810 e710 (2019).
70. Y. D. Yoo, S. R. Mun, C. H. Ji, K. W. Sung, K. Y. Kang, A. J. Heo, S. H. Lee, J. Y. An, J. Hwang, X. Q. Xie, A. Ciechanover, B. Y. Kim, Y. T. Kwon, N-terminal arginylation generates a bimodal degron that modulates autophagic proteolysis. *Proc Natl Acad Sci U S A* **115**, E2716-E2724 (2018).
71. H. Cha-Molstad, K. S. Sung, J. Hwang, K. A. Kim, J. E. Yu, Y. D. Yoo, J. M. Jang, D. H. Han, M. Molstad, J. G. Kim, Y. J. Lee, A. Zakrzewska, S. H. Kim, S. T. Kim, S. Y. Kim, H. G. Lee, N. K. Soung, J. S. Ahn, A. Ciechanover, B. Y. Kim, Y. T. Kwon, Amino-terminal arginylation targets endoplasmic reticulum chaperone BiP for autophagy through p62 binding. *Nature cell biology* **17**, 917-929 (2015).

72. A. Varshavsky, Ubiquitin fusion technique and related methods. *Methods Enzymol* **399**, 777-799 (2005).
73. D. Tomar, P. Prajapati, L. Sripada, K. Singh, R. Singh, A. K. Singh, R. Singh, TRIM13 regulates caspase-8 ubiquitination, translocation to autophagosomes and activation during ER stress induced cell death. *Biochim Biophys Acta* **1833**, 3134-3144 (2013).
74. D. Tomar, R. Singh, A. K. Singh, C. D. Pandya, R. Singh, TRIM13 regulates ER stress induced autophagy and clonogenic ability of the cells. *Biochim Biophys Acta* **1823**, 316-326 (2012).
75. M. Lerner, M. Corcoran, D. Cepeda, M. L. Nielsen, R. Zubarev, F. Ponten, M. Uhlen, S. Hober, D. Grander, O. Sangfelt, The RBCC gene RFP2 (Leu5) encodes a novel transmembrane E3 ubiquitin ligase involved in ERAD. *Mol Biol Cell* **18**, 1670-1682 (2007).
76. Y. S. Yang, S. M. Strittmatter, The reticulons: a family of proteins with diverse functions. *Genome Biol* **8**, 234 (2007).
77. N. Zurek, L. Sparks, G. Voeltz, Reticulon short hairpin transmembrane domains are used to shape ER tubules. *Traffic* **12**, 28-41 (2011).
78. N. Mizushima, A Dual Binding Receptor for ER-phagy. *Dev Cell* **44**, 133-135 (2018).
79. K. Mochida, Y. Oikawa, Y. Kimura, H. Kirisako, H. Hirano, Y. Ohsumi, H. Nakatogawa, Receptor-mediated selective autophagy degrades the endoplasmic reticulum and the nucleus. *Nature* **522**, 359-362 (2015).
80. S. A. Tooze, T. Yoshimori, The origin of the autophagosomal membrane. *Nature cell biology* **12**, 831-835 (2010).
81. S. Hatakeyama, TRIM Family Proteins: Roles in Autophagy, Immunity, and Carcinogenesis. *Trends Biochem Sci* **42**, 297-311 (2017).
82. M. A. Mandell, A. Jain, J. Arko-Mensah, S. Chauhan, T. Kimura, C. Dinkins, G. Silvestri, J. Munch, F. Kirchhoff, A. Simonsen, Y. Wei, B. Levine, T. Johansen, V. Deretic, TRIM proteins regulate autophagy and can target autophagic substrates by direct recognition. *Dev Cell* **30**, 394-409 (2014).
83. N. Nguyen, V. Shteyn, T. J. Melia, Sensing Membrane Curvature in Macroautophagy.

Journal of molecular biology **429**, 457-472 (2017).

84. H. Zhang, J. Hu, Shaping the Endoplasmic Reticulum into a Social Network. *Trends in cell biology* **26**, 934-943 (2016).
85. D. H. Perlmutter, Alpha-1-antitrypsin deficiency: importance of proteasomal and autophagic degradative pathways in disposal of liver disease-associated protein aggregates. *Annu Rev Med* **62**, 333-345 (2011).
86. A. Tzakis, Early recognition of alpha-1 antitrypsin deficiency and considerations for liver transplantation. *Gastroenterol Hepatol (N Y)* **9**, 110-112 (2013).
87. E. E. Cummings, L. P. O'Reilly, D. E. King, R. M. Silverman, M. T. Miedel, C. J. Luke, D. H. Perlmutter, G. A. Silverman, S. C. Pak, Deficient and Null Variants of SERPINA1 Are Proteotoxic in a *Caenorhabditis elegans* Model of alpha1-Antitrypsin Deficiency. *PLoS One* **10**, e0141542 (2015).
88. T. Hidvegi, M. Ewing, P. Hale, C. Dippold, C. Beckett, C. Kemp, N. Maurice, A. Mukherjee, C. Goldbach, S. Watkins, G. Michalopoulos, D. H. Perlmutter, An autophagy-enhancing drug promotes degradation of mutant alpha1-antitrypsin Z and reduces hepatic fibrosis. *Science* **329**, 229-232 (2010).
89. T. Kamimoto, S. Shoji, T. Hidvegi, N. Mizushima, K. Umebayashi, D. H. Perlmutter, T. Yoshimori, Intracellular inclusions containing mutant alpha1-antitrypsin Z are propagated in the absence of autophagic activity. *J Biol Chem* **281**, 4467-4476 (2006).
90. L. Feng, J. Zhang, N. Zhu, Q. Ding, X. Zhang, J. Yu, W. Qiang, Z. Zhang, Y. Ma, D. Huang, Y. Shen, S. Fang, Y. Yu, H. Wang, Y. Shen, Ubiquitin ligase SYVN1/HRD1 facilitates degradation of the SERPINA1 Z variant/alpha-1-antitrypsin Z variant via SQSTM1/p62-dependent selective autophagy. *Autophagy* **13**, 686-702 (2017).
91. T. Heinrich, J. Seenisamy, B. Blume, J. Bomke, M. Calderini, U. Eckert, M. Friesen-Hamim, R. Kohl, M. Lehmann, B. Leuthner, D. Musil, F. Rohdich, F. T. Zenke, Discovery and Structure-Based Optimization of Next-Generation Reversible Methionine Aminopeptidase-2 (MetAP-2) Inhibitors. *J Med Chem* **62**, 5025-5039 (2019).
92. W. Al-Khyatt, C. Tufarelli, R. Khan, S. Y. Iftikhar, Selective oestrogen receptor

- antagonists inhibit oesophageal cancer cell proliferation in vitro. *BMC Cancer* **18**, 121 (2018).
93. C. L. Galli, C. Sensi, A. Fumagalli, C. Parravicini, M. Marinovich, I. Eberini, A computational approach to evaluate the androgenic affinity of iprodione, procymidone, vinclozolin and their metabolites. *PLoS One* **9**, e104822 (2014).
 94. K. Dalal, F. Ban, H. Li, H. Morin, M. Roshan-Moniri, K. J. Tam, A. Shepherd, A. Sharma, J. Peacock, M. L. Carlson, E. LeBlanc, C. Perez, F. Duong, C. J. Ong, P. S. Rennie, A. Cherkasov, Selectively targeting the dimerization interface of human androgen receptor with small-molecules to treat castration-resistant prostate cancer. *Cancer Lett* **437**, 35-43 (2018).
 95. J. Ding, C. R. Yeh, Y. Sun, C. Lin, J. Chou, Z. Ou, C. Chang, J. Qi, S. Yeh, Estrogen receptor beta promotes renal cell carcinoma progression via regulating LncRNA HOTAIR-miR-138/200c/204/217 associated CeRNA network. *Oncogene* **37**, 5037-5053 (2018).
 96. I. Dikic, Proteasomal and Autophagic Degradation Systems. *Annu Rev Biochem* **86**, 193-224 (2017).
 97. T. A. Thibaut, R. T. Anderson, D. M. Smith, A common mechanism of proteasome impairment by neurodegenerative disease-associated oligomers. *Nat Commun* **9**, 1097 (2018).
 98. F. M. Menzies, K. Moreau, D. C. Rubinsztein, Protein misfolding disorders and macroautophagy. *Curr Opin Cell Biol* **23**, 190-197 (2011).
 99. S. Hashimoto, Y. Matsuba, N. Kamano, N. Mihira, N. Sahara, J. Takano, S. I. Muramatsu, T. C. Saido, T. Saito, Tau binding protein CAPON induces tau aggregation and neurodegeneration. *Nat Commun* **10**, 2394 (2019).
 100. L. Cortez, V. Sim, The therapeutic potential of chemical chaperones in protein folding diseases. *Prion* **8** (2014).
 101. A. Heras-Garvin, D. Weckbecker, S. Ryazanov, A. Leonov, C. Griesinger, A. Giese, G. K. Wenning, N. Stefanova, Anle138b modulates alpha-synuclein oligomerization and prevents motor decline and neurodegeneration in a mouse model of multiple system

- atrophy. *Mov Disord* **34**, 255-263 (2019).
102. J. Wagner, S. Ryazanov, A. Leonov, J. Levin, S. Shi, F. Schmidt, C. Prix, F. Pan-Montojo, U. Bertsch, G. Mitteregger-Kretzschmar, M. Geissen, M. Eiden, F. Leidel, T. Hirschberger, A. A. Deeg, J. J. Krauth, W. Zinth, P. Tavan, J. Pilger, M. Zweckstetter, T. Frank, M. Bahr, J. H. Weishaupt, M. Uhr, H. Urlaub, U. Teichmann, M. Samwer, K. Botzel, M. Groschup, H. Kretzschmar, C. Griesinger, A. Giese, Anle138b: a novel oligomer modulator for disease-modifying therapy of neurodegenerative diseases such as prion and Parkinson's disease. *Acta Neuropathol* **125**, 795-813 (2013).
 103. K. H. Strang, C. L. Croft, Z. A. Sorrentino, P. Chakrabarty, T. E. Golde, B. I. Giasson, Distinct differences in prion-like seeding and aggregation between Tau protein variants provide mechanistic insights into tauopathies. *J Biol Chem* **293**, 4579 (2018).
 104. G. Ghag, N. Bhatt, D. V. Cantu, M. J. Guerrero-Munoz, A. Ellsworth, U. Sengupta, R. Kaye, Soluble tau aggregates, not large fibrils, are the toxic species that display seeding and cross-seeding behavior. *Protein Sci* **27**, 1901-1909 (2018).
 105. S. Shin, D. Kim, J. Y. Song, H. Jeong, S. J. Hyeon, N. W. Kowall, H. Ryu, A. N. Pae, S. Lim, Y. K. Kim, Visualization of soluble tau oligomers in TauP301L-BiFC transgenic mice demonstrates the progression of tauopathy. *Prog Neurobiol* 10.1016/j.pneurobio.2020.101782, 101782 (2020).
 106. M. G. Koliopoulos, D. Esposito, E. Christodoulou, I. A. Taylor, K. Rittinger, Functional role of TRIM E3 ligase oligomerization and regulation of catalytic activity. *EMBO J* **35**, 1204-1218 (2016).
 107. J. C. Stachowiak, C. C. Hayden, D. Y. Sasaki, Steric confinement of proteins on lipid membranes can drive curvature and tubulation. *Proc Natl Acad Sci U S A* **107**, 7781-7786 (2010).
 108. F. Puls, I. Goldschmidt, H. Bantel, C. Agne, V. Brocker, M. Dammrich, U. Lehmann, J. Berrang, E. D. Pfister, H. H. Kreipe, U. Baumann, Autophagy-enhancing drug carbamazepine diminishes hepatocellular death in fibrinogen storage disease. *J Hepatol* **59**, 626-630 (2013).
 109. L. H. Gallo, J. Ko, D. J. Donoghue, The importance of regulatory ubiquitination in

- cancer and metastasis. *Cell Cycle* **16**, 634-648 (2017).
110. P. L. Salomon, E. E. Reid, K. E. Archer, L. Harris, E. K. Maloney, A. J. Wilhelm, M. L. Miller, R. V. J. Chari, T. A. Keating, R. Singh, Optimizing Lysosomal Activation of Antibody-Drug Conjugates (ADCs) by Incorporation of Novel Cleavable Dipeptide Linkers. *Mol Pharm* 10.1021/acs.molpharmaceut.9b00696 (2019).

초록

지창훈
의과학과, 의과학
서울대학교 대학원

N-말단 법칙(N-degron pathway)은 단백질의 N-말단 아미노산 잔기 혹은 N-말단의 번역 후 수정 (post-translational modification)에 따라 그 단백질의 생체내 분해가 결정되는 시스템이다. 이러한 N-말단 법칙의 다양한 분과들 중, 알지닐화 (arginylation) 분과의 경우, N-말단 알지닌 (Nt-Arg) 아미노산 잔기를 이용해 프로테아좀과 오토파지를 이용한 단백질 분해를 유도한다. 이러한 과정들을 통해 Arg/N-말단 법칙은 세포 내 총체적 단백질대사를 조절하게 된다.

이 논문에서는 세포 내 단백질 분해와 품질관리 (protein quality control)의 기전과 더불어 이 기전과 Arg/N-말단 법칙의 연관성에 대해 구체적으로 다룬다. 대표적인 두가지 분해 기전인 유비퀴틴-프로테아좀 시스템 (UPS) 와 오토파지-리소좀 경로 (ALP)는 각자 프로테아좀과 리소좀을 이용하여 단백질을 분해하게 된다. 그 중에서도 오토파지의 경우, DNA부터 세포 소기관과 병원체까지 사실상 모든 세포 내 물질들의 선택적 분해를 가능케 함으로서 세포내 방어와 유지에 필수적인 기전이다.

이러한 Arg/N-말단 법칙의 분자적 기전과 생리학적 영향이 세포 내 단백질 항상성, 특히 소포체(ER)의 선택적 분해를 통한 소포체 내 단백질 품질 관리와 항상성을 유지함에 대한 내용을 다룬다. 유비퀴틴과 Arg/N-말단 법칙을 통해 일어나는 ER-phagy(소포체-파지)가 소포체 막(ER

membrane), 내강(ER lumen)뿐만 아니라 내부에 포함된 단백질들의 격리와 분해를 일으키며, 이러한 기전을 통해 프로테아좀을 통한 분해가 불가능했던 소포체 내부의 쌓이고 뭉쳐진 병증 단백질들의 표적이 가능케 함으로서, 소포체 단백질병증 치료에 대한 새로운 장을 열었다.

추가적으로, Arg/N-말단 법칙을 통해 소포체 자가포식을 생화학적으로 저절하는 저분자량 p62 리간드를 이용해 신규 표적 단백질 분해(targeted protein degradation; TPD) 플랫폼을 제안한다. 이 플랫폼은 병리학적 단백질의 표적분해에 특징점을 가지며 이를 오토텍 (AUTOPhagy-TArgeting Chimera; AUTOTAC)이라 명명한다. RNA간섭을 이용한 유전자 침묵이나 항체를 이용한 테라피들 대비, 표적 단백질 분해 플랫폼은 약학적, 생리적 측면에서 크나큰 이점을 가진다. 또한 단백질 표적 분해에 있어 표적하는 단백질을 오토파지 막으로 배달하는 오토파지를 이용한 일반적 분해제들과는 달리 오토텍은 단백질 배달-분해와 동시에 세포 내 오토파지 자체를 신장시키는 특징적 양상을 가진다.

마지막으로, 상기 연구 결과들에 대한 개괄적 요약과 고찰을 통해 논문을 마무리한다. 오토파지를 관장하는 Arg/N-말단 법칙의 분자 생화학적 기전 연구를 통해 세포 내 단백질 항상성 유지와 단백질병증 타파에 대한 틀을 제공할 것이다.

Keywords : 아르기닌/N-말단 법칙, 단백질 품질 관리, 선택적 자가포식, 소포체 자가포식, 표적 단백질 분해, 오토텍

Student Number : 2014-25075

Acknowledgments

While no number of words would do justice in expressing the amount of help I have received and the gratitude I owe to all the people who have empowered me on my journey as a doctor of philosophy, I would like to express my heartfelt thanks to the following people:

Dr. Yong Tae Kwon, for his endless patience and support in me as not only a scientist but also a leader and a person of worth. His enduring insight and wisdom into the subject matter has been a constant source of learning. I hope to one day be as great a scientist, leader, role model and mentor as you have been to me.

The committee members of my doctoral thesis - Dr. In Hee Mook-Jung, Dr. Sang Kyu Ye, Dr. Min Jae Lee and Dr. Cheol Yong Choi – for their vast wisdom and expertise into the subject matter, for which I am indebted both professionally and personally.

Ah Jung Heo, for her ceaseless and fiery commitment, ceaseless friendship and advice. None of this would have been possible without you next to me – knowing you and being your best friend have been one of the greatest joys and learning experiences I have had the pleasure of enjoying.

Su Hyun Lee, Min Ju Lee, Su Bin Kim, Seong Eon Roh, Su Jin Lee, Ji Soo Lee, Hee Yeon Kim, Young Jae Park, for all their individual contributions, which are too numerous to list here. Thank you so much for everything.

Mom, Dad and Seiyen, for their unconditional and unbreakable love, without which I would have been broken beyond repair. I will never be able to repay the love you have given me or wipe the tears it took to raise this prodigal son, but I hope to spend the rest of my life trying.

Last but greatest – Lord, thank you for everything. This would have been literally impossible to begin, let alone finish, without you, my Provider. You were with me when I started this, and are still with me as I finish. In every victory, let it be said of me that my source of strength, my source of hope is Christ alone. Come, Lord Jesus, and wipe away every tear from my eyes. Soli Deo Gloria.